HARVARD
Kenneth C. Griffin

GRADUATE SCHOOL
OF ARTS AND SCIENCES

THESIS ACCEPTANCE CERTIFICATE

The undersigned, appointed by the

Department of Physics

have examined a dissertation entitled

Towards A Programmable Nanomechanical Interface for Mediating Spin-Spin Interactions

presented by Long Fung Frankie Fung

candidate for the degree of Doctor of Philosophy and hereby certify that it is worthy of acceptance.

Signature _____

Typed name: Prof. Mikhail Lukin

Signature _____

Typed name: Prof. Marko Lončar

Signature _____

Typed name: Prof. Philip Kim

Date: April 17, 2025

Towards A Programmable Nanomechanical Interface for Mediating Spin-Spin Interactions

A dissertation presented

by

Long Fung Frankie Fung

to

The Department of Physics

in partial fulfillment of the requirements

for the degree of

Doctor of Philosophy

in the subject of

Physics

Harvard University

Cambridge, Massachusetts

April 2025

© 2025 Long Fung Frankie Fung
All rights reserved.

Dissertation Advisor: Professor Mikhail Lukin Long Fung Frankie Fung

Towards A Programmable Nanomechanical Interface for Mediating Spin-Spin Interactions

Abstract

Solid state spin qubits are promising candidates for quantum information processing. In particular, the nitrogen vacancy (NV) center in diamond is known to have coherence times exceeding milliseconds even at room temperature. However, due to the limits of qubit fabrication and the short-range nature of magnetic dipolar interactions, it remains difficult to generate programmable interactions between a large number of NV centers. To address this challenge, it has been proposed to use nanomechanical resonators as a mesoscopic interface between solid state spin qubits. In this thesis, I will describe experimental efforts in building a scanning probe platform, where individual NV centers in diamond nanopillars are coupled to magnetially functionalized silicon nitride mechanical resonators. The scanning probe configuration enables programmable connectivity via mechanical transport of the nanopillars. Proof-of-principle measurements show that the coherence of the NV center is preserved despite relative movement in a magnetic field gradient, by utilizing the nitrogen nuclear spin as a quantum memory. I will also describe measurements of the spin-mechanical coupling via both DC and AC magnetometry. Finally, I present some preliminary results related to sensing of a single NV center with the mechanical resonator, which demonstrate the high level of control over each subsystem. With realistic improvements to several system parameters, high spin-mechanical cooperativities are feasible, offering a new avenue towards scalable quantum information processing with spin qubits.

Contents

Title Page i
Copyright ii
Abstract iii
Table of Contents vii
Acknowledgments xxv
Citations to Previously Published Works xxix

1 Introduction **1**
1.1 Background 1
1.2 Longitudinal Coupling between an NV Center and a Mechanical Resonator . 4
1.3 The Field of Spin Mechanics 6

2 Spin-mechanics on a Flip-Chip Device **8**
2.1 Introduction 8
2.2 Device Characterization 9
2.2.1 Mechanics Characterization 9
2.2.2 NV center characterization 11
2.3 Challenges 14
2.3.1 Standoff Issues 14
2.3.2 Demagnetization from Laser 16
2.4 Conclusion and Outlook 17

3 A New Cryogenic Scanning Probe Experimental Platform **21**
3.1 Introduction 21
3.2 Cryogenic Setup 22
3.2.1 Sample Mount 24
3.2.2 Probe Mount 26
3.2.3 Electrical Connections 28
3.3 Vacuum system 30
3.4 Temperature and Helium Flow Control 31
3.5 Confocal Microscope 33

3.5.1 Optical Path for NV Measurements . . . 37
3.5.2 Optical Path for the Interferometer . . . 38
3.6 Microwave Electronics . . . 39
3.7 Pulse Timing . . . 40
3.8 External Bias Field . . . 40
3.9 Laboratory Environment . . . 42

4 Scanning Probe Magnetometry Measurements for Gradient Characterization 46
4.1 Introduction . . . 46
4.2 Magnetic Field Scans . . . 48
4.3 Magnetic Iso-field Scans . . . 51
4.4 Investigation of Low Remanence of Neodymium Micromagnets . . . 54
4.5 Field Misalignment and Compensation with External Bias Field . . . 59
4.6 Demagnetization Issues . . . 65
4.6.1 Temperature-related Demagnetization Issues . . . 65
4.6.2 Laser-related Demagnetization Issues . . . 70

5 Towards Programmable Quantum Processors based on Spin Qubits with Mechanically-Mediated Interactions and Transport 73
5.1 Introduction . . . 73
5.2 Experimental Setup and Static Magnetic Field Characterization . . . 76
5.3 Preservation of Spin Coherence in Proximity of a Transported Micromagnet 78
5.4 Mechanical Motion and Single-phonon Coupling Strength . . . 80
5.5 Discussion and Outlook . . . 82
5.6 Acknowledgements . . . 84

6 Characterization of High-Q Mechanical Resonators 86
6.1 Introduction . . . 86
6.2 Frequency Drift at Cryogenic Temperatures . . . 86
6.3 Magnetically Functionalized Soft-Clamped Resonators . . . 94
6.3.1 Hierarchical Resonators . . . 94
6.3.2 Nanobeam Resonators with Torsional Supports . . . 99

7 Nanomechanical Sensing of a Single NV Center 102
7.1 Introduction . . . 102
7.2 High Gradients with Iron Thin Film Magnets . . . 104
7.2.1 Coupling Measurement . . . 104
7.2.2 Additional Gradient Measurements . . . 110
7.3 General Detection Scheme . . . 110

7.3.1 Pulse Sequence . . . 110
7.3.2 Sideband Modulation . . . 113
7.3.3 Spurious Classical Effects of Microwave and Laser Pulses . . . 117
7.3.4 Pulse Sequences to Mitigate Classical Spurious Effects . . . 124
7.4 Preliminary Results . . . 131

References **134**

Appendix A Fabrication of Mechanical Resonator Chip **147**
A.1 Coplanar Waveguide Fabrication . . . 147
A.1.1 Cleaning . . . 147
A.1.2 Spinning Resist . . . 148
A.1.3 Optical Lithography . . . 148
A.1.4 Metal Deposition . . . 149
A.1.5 Liftoff . . . 149
A.2 Nanobeam Definition . . . 150
A.2.1 Spinning Resist . . . 150
A.2.2 E-beam Lithography . . . 150
A.2.3 Nitride Etching . . . 150
A.3 Magnet Definition and Deposition . . . 151
A.3.1 Spinning Resist . . . 151
A.3.2 Defining Micromagnets . . . 151
A.3.3 Magnet Deposition . . . 152
A.3.4 Liftoff . . . 153
A.4 Nanobeam Release . . . 153

Appendix B Magnetic Functonalization of Nanobeams with Neodymium Microspheres **155**
B.1 Setup and Components . . . 155
B.2 Preparation . . . 156
B.3 Applying Glue to Needle . . . 157
B.4 Applying Epoxy to Sample . . . 157
B.5 Picking up a Micromagnet . . . 158
B.6 Curing the Epoxy (heat) . . . 159
B.7 Curing the Epoxy (UV) . . . 160

Appendix C Attempts to revive diamond probes **161**

Appendix D Experimental Setup and Methods for Chapter 5 **165**
D.1 Experimental setup 165
D.2 Sample Fabrication 165
D.3 Magnetic Field Imaging 167
D.4 Analytical Form of Hahn Echo Contrast in the Presence of Mechanical Motion 168
D.5 Preservation of Coherent Information while Moving inside a Field Gradient 170
D.5.1 Experimental Setup 170
D.5.2 Nuclear and Electronic Spin Control 171
D.5.3 Pulse Sequence for ESR Measurements during Movement Sequence . 172
D.5.4 Pulse Sequence for Coherence Measurement 173
D.5.5 Phase Information $\phi(\tau)$ 176
D.6 NV center Electronic and Nuclear Spin Coherence Times 177
D.7 Comparisons of Cooperativity for Previous Works 178

List of Tables

2.1 Four nanobeams are subjected to green laser illumination either directly on the micromagnet or somewhere else on the nanobeam. For each nanobeam, the laser power is slowly increased from $\sim$ 100 µW and the laser focus is swept along the optical axis until the nanobeam is destroyed. Note that the nanobeams in this measurement are functionalized manually with neodymium magnets. We have noticed that nanobeams with iron thin film magnets also break with similar laser powers. 19

3.1 Description of each part labeled in Fig. 3.1. 22

4.1 List of magnetic materials and their respective remanences. 54

6.1 Drift rates (absolute and relative) are tabulated alongside the dimensions and functionalization details of each resonator shown in Fig. 6.1. 88

D.1 Comparison of spin-mechanical cooperativities with previous works. Optimistic estimates (highlighted) are given for unreported values. We also note the large coupling strength ($>$ 700 Hz) reported in a related work where a cantilever is coupled to unpaired electron spins [127]; however, the spin coherence time and quality factor were not reported. 178

List of Figures

2.1 (a) Schematic of the flip-chip geometry. NV centers in the diamond is coupled to the motion of the micromagnet on the nanobeam underneath. (b) Photo of the completed device, consisting of the diamond (transparent square) placed on top of a chip containing mechanical resonators. The chip contains a coplanar waveguide, and is wirebonded to a printed circuit board (PCB) with SMP connectors for microwave delivery to manipulate the NV center's spin state. 9

2.2 Diagram (top-down view) showing some relevant dimensions of the nanobeam along a coplanar waveguide (CPW). The CPW can be used to deliver microwaves to manipulate the NV center's spin state, and also to excite the nanobeam. The red rectangle is the micromagnet consisting of an iron thin film. This micromagnet can also be a manually placed neodymium micropshere. 10

2.3 (a) Resonance frequency of the nanobeam as a function of the pressure inside the vacuum chamber. (b) Mechanical quality factor of the nanobeam as a function of the pressure. The quality factor is calculated using the linewidth extracted from fitting the resonance spectrum to a Lorentzian. 11

2.4 Duffing nonlinearity of the nanobeam. Sweeping the frequency of the piezo drive, we see that the response of the nanobeam no longer follows a Lorentzian lineshape for high drive amplitudes and depends on the direction of the sweep. 12

2.5 (a) Typical confocal image, where NV centers can be resolved down to the diffraction limit. (b) Electron spin resonance (ESR) measurement, which gives the resonance frequencies of the NV center. Here an external magnetic field of $\sim 50\,\mathrm{G}$ gives rise to a splitting of $\sim 272\,\mathrm{MHz}$. (c) Rabi oscillations. With the on-chip coplanar waveguide (CPW), Rabi frequencies exceeding $10\,\mathrm{MHz}$ can be achieved without saturating the microwave amplifier. (d) Spin echo measurement, where clear collapses and revivals can be observed. The revivals happen with a period of $16\,\mu\mathrm{s}$, as a result of the Larmor precession of background ^{13}C nuclear spins in an external field of $\sim 52\,\mathrm{G}$. Fitting to the envelope of decay, we extract a coherence time of $80\,\mu\mathrm{s}$. 13

2.6 Interferometer measurement before and after diamond placement. The clear resonance at 1.68 MHz is missing after the placement, suggesting that it is stuck to the diamond. 15
2.7 (a) Confocal image of NV centers near an iron micromagnet fabricated on top of a nanobeam. The bright vertical line is the nanobeam (1 µm wide), interrupted by a dark region that is the iron micromagnet. Red (green) circles indicate NV centers for which there was no (some) ESR splitting. (b) ESR of the NV center indicated by the thick green circle in (a), showing a splitting of ~ 38 MHz corresponding to an on-axis field about 7 G. 16
2.8 Photon counts from light reflected off a nanobeam while the green laser is focused close to the micromagnet. The sharp drop indicates when the nanobeam breaks. The time axis is likely in units of 0.1 s (incomplete documentation). . 17
2.9 (a) SEM image of a nanobeam compromised to a permanent end, indicated by the gap in middle where the micromagnet used to be. (b) Zoom-in of the breaking point. (c,d) Additional images of other broken resonators. 18
2.10 SEM image of a nanobeam which appears to have broken not at the micromagnet (rectangle on the left), but on the bare nitride. 19

3.1 Cross-section view of the cryostat, with some parts such as screws and KF clamps omitted for clarity. See Table 3.1 for the parts list. 23
3.2 Chamber pressure and temperatures of the heat exchanger and sample during the first hour of a cooldown. After the initial cooldown, a feedback loop is initiated to keep the heat exchanger temperature typically at 13 K. The temperature of the nanopillar mount is not shown, but it is typically kept above 80 K. 25
3.3 Side and top view of the sample mount and cryostat. 27
3.4 (a) Close-up view of the AFM chip holding the diamond nanopillar, glued to the custom copper probe mount. (b) Close-up view of the diamond probe glued to a bare cantilever. 27
3.5 (a) Photo of a QZabre scanning probe clamped to our custom-made copper probe mount (bottom-up view). Typically we make electrical contact between the SEM clip and the leg of the tuning fork holding the diamond to avoid charge issues. (b) Mechanical drawing (top-down view). 28

3.6 Photo of the column with integrated heater (part 14 in Fig. 3.1)). The nanopillar mount (not shown) will be fastened on top of this column. The two G10 spacers thermally isolate the nanopillar (80 K) from the heat exchanger (13 K), reducing unnecessary heat load on the cryostat from having to keep the nanopillar at high temperature. The cartridge heater is secured inside the column using Stycast epoxy. The column is made of aluminum for easy machining; in the future, a different material should be chosen for matching thermal expansion coefficients to maintain a stable NV-magnet distance. . . 32
3.7 Large swings in fluorescence counts from the NV center due to instability in the helium flow. As the helium flow rate changes, the sample moves relative to the optical setup, leading to count fluctuations. 33
3.8 Full schematic of the optical setup and microwave connections. 34
3.9 Photo of the optics setup. The cryostat vacuum shroud is open for room-temperature characterization measurements. The entire confocal microscope consists of two levels. The bottom level contains components such as the APD and fiber launchers for the green laser and fluorescence collection, while the top level contains components such as the galvo mirrors, servo motor-actuated mirror, and fiber launcher for the IR laser. The top level can be moved in three axes using large translation stages. The Z-axis translation stage is shown, while the stages for the other two axes (green arrows) are hidden. To ensure that the microscope stays aligned during translations, the stages are arranged such that the translation axes are always parallel to the light path. 35
3.10 Fourier transform of the drive current for one of the galvo mirrors, showing a broad peak around 2 kHz. A similar peak shows up in the Fourier transform of the reflected light intensity. 38
3.11 Fourier transform of the intensity of IR light reflected off a sample. This was measured on an interferometer in a different experiment also using a galvo scanner, and it shows a similar peak around 2 kHz. 39
3.12 Inward extension for the cryostat vacuum shroud. The bias field magnet can be fitted inside and stay close to the NV center while remaining in atmosphere, allowing for easy adjustments. 41
3.13 (a) Current-carrying coil for generating a tunable bias magnetic field. (b) Characterization of the current coil. A maximum of 23 G, or an ESR shift of 64 MHz, can be applied to the NV center. The current through the coil can be calculated by dividing the voltage by the resistance of 2.6 Ω. 42
3.14 An example of huge swings ($> 3\,^{\circ}$C) in the lab temperature, which make NV and mechanics measurements virtually impossible. The temperature in the lab and inside the enclosure are plotted in red and blue respectively. 43

3.15 Taking the Fourier transform of the fluorescence counts from the NV center, we see some noise peaks at $\sim$ 30 Hz, which we attribute to the natural resonances of the optical setup. Depending on the lab conditions, the area under these vibration peaks can lead to classical measurement noise on the same order as shot noise. These peaks were greatly reduced after replacing the polystyrene panels with fabric. 44
3.16 (a) Original enclosure with walls made of polystyrene panels, which turned out to be sensitive to external disturbances. (b) Current enclosure with the polystyrene panels replaced with blackout fabric. 45

4.1 (a) Magnetic field scan of a neodymium spherical micromagnet. The dipole field distribution can be clearly seen. (b) Photo of the nanobeam and micromagnet, taken with an optical microscope. This particular sample was overetched in the release process for the nanobeam, which occurred before the micromagnet placement. 49
4.2 (a) Magnetic field scan of a square iron micromagnet. The four corners of the magnet show up as high field regions. (b) Photo of the nanobeam and micromagnet, taken with an optical microscope. 50
4.3 Direct gradient measurement. The left plot shows a field scan with the sample at $Z = 0$ nm. In the middle plot, we raise the sample to $Z = 210$ nm using the nanopoistioners, thus bringing the micromagnet closer to the NV center. In the right plot, we take the difference between the left and middle plots and divide by the sample displacement of 210 nm to obtain the magnetic field gradient distribution. We see that the point of maximum gradient matches quite well with the point of maximum field. 52
4.4 (a) A typical contour scan of a neodymium micromagnet. Since the micromagnet is spherical, the contour usually takes on an ovular shape. In this scan, the microwave frequency is fixed at 2.835 GHz, corresponding to a magnetic field along the NV center's axis of 13 G. (b) Contour scan of the same square iron micromagnet in Fig. 4.2, taken at the same NV-magnet separation. . . . 53

4.5 Left: field scans of a micromagnet (1.3 µm diameter) on a nanobeam, with each scan taken at a different NV-micromagnet separation z. The fitting parameters are shown on the upper left of the plot, θ_{magnet} and ϕ_{magnet} being the azimuthal and polar angles of the micromagnet's magnetization orientation (with the Z axis pointing out of the page), x_{magnet} and y_{magnet} being the lateral position of the micromagnet's center, B_0 being the remanent magnetization, and B_{bias} being the background bias field. The fitting parameters are obtained by fitting all three scans together (global fitting). The step size in z between each scan is a fixed parameter (from calibration of the nanopositioner's displacement), but the offset is obtained from fitting. Right: residuals, i.e. the difference between the fit and data. 55
4.6 Field scan of a micromagnet (1.0 µm diameter) on a nanobeam. Unlike Fig. 4.5, this plot only contains one scan at a fixed NV-micromagnet distance. 56
4.7 Left: field scans of a micromagnet (3.0 µm diameter) on a bare patch of silicon nitride (not on a nanobeam), with each scan taken at a different NV-micromagnet separation z. The fitting parameters are shown on the upper left of the plot, θ_{magnet} and ϕ_{magnet} being the azimuthal and polar angles of the micromagnet's magnetization orientation (with the Z axis pointing out of the page), x_{magnet} and y_{magnet} being the lateral position of the micromagnet's center, B_0 being the remanent magnetization, and B_{bias} being the background bias field. The fitting parameters are obtained by fitting all two scans together (global fitting). The step size in z between each scan is a fixed parameter (from calibration of the nanopositioner's displacement), but the offset is obtained from fitting. Right: residuals, i.e. the difference between the fit and data. . . 58
4.8 Field scan of a micromagnet (1.8 µm diameter) on a nanobeam. Unlike Fig. 4.7, this plot only contains one scan at a fixed NV-micromagnet distance. 59
4.9 Left: field scans of a micromagnet (2.3 µm diameter) on a bare patch of silicon nitride (not on a nanobeam), with each scan taken at a different NV-micromagnet separation z. The fitting parameters are shown on the upper left of the plot, θ_{magnet} and ϕ_{magnet} being the azimuthal and polar angles of the micromagnet's magnetization orientation (with the Z axis pointing out of the page), x_{magnet} and y_{magnet} being the lateral position of the micromagnet's center, B_0 being the remanent magnetization, and B_{bias} being the background bias field. The fitting parameters are obtained by fitting all two scans together (global fitting). The step size in z between each scan is a fixed parameter (from calibration of the nanopositioner's displacement), but the offset is obtained from fitting. Right: residuals, i.e. the difference between the fit and data. . . 60

4.10 Field scan of a micromagnet (1.5 µm diameter) on a nanobeam. Unlike Fig. 4.5, this plot only contains one scan at a fixed NV-micromagnet distance. 61
4.11 Plot of the effective magnetic remanences of spherical neodymiyum micromagnets as a function of their diameters. The effective magnetic remanence is defined as the remanence assuming that the entire micromagnet is magnetized uniformly, and is extracted from dipole fitting of the field scans. There is a clear dependence of the effective remanence on magnet diameter. Given that even larger micromagnets have shown effective remanences of $\sim 0.7\,\mathrm{T}$ (data not shown), it is likely that the reduced remanence for small micromagnets is due to a constant layer of surface oxidation with reduced/no magnetism. . . 61
4.12 (a) Contour scan above a spherical neodymium micromagnet, with the microwave frequency fixed at 2.720 GHz, corresponding to a field of about 50 G. A high-contrast contour is visible, alongside another one on the bottom right with lower contrast. The low-contrast contour is due to a second NV center in the nanopillar in the same confocal volume. The dark blob in the middle right indicates a region with low NV spin contrast. (b) After decreasing the NV-magnet distance, the dark blob indicating low spin contrast expands in size. Note the different microwave frequency of 2.390 GHz, which corresponds to a field of about 170 G. 62
4.13 (a) Normalized contour scan in the same scan area as Fig. 4.12. The contour disappears in the same region as the dark blob in Fig. 4.12. (b,c) Zoom-in of the tail of the contour, where it disappears due to low spin contrast. 64
4.14 (a) Contour scan showing a large region where the NV center experiences large off-axis fields from the micromagnet. (b) Using fitted parameters from a field scan (see 4.2), we compute the expected off-axis fields from the micromagnet. We see that the off-axis fields can exceed 200 G in the right part of the plot. This matches qualitatively with the dark region in (a). The red cross indicates the point of maximum gradient, where the off-axis field exceeds 100 G. 65
4.15 With an external bias field, the contour scan changes dramatically, with a bright spot appearing at the center of the contour in Fig. 4.14(a). The bright spot indicates where the off-axis field from the micromagnet is canceled by the external field, leading to a recovery in NV fluorescence. 66
4.16 Experimental setup to demonstrate cancellation of off-axis fields from the micromagnet using an external bias field. To make this configuration compatible with the cryostat, a pocket inside the cryostat vacuum shroud was added to accommodate the external magnet (Fig. 3.1). 67

4.17 (a) Contour scan after retracting the sample away from the NV center by $\sim 200\,\text{nm}$, which resulted in a change to the shape of the cancellation region. (b) Contour scan after positioning the external magnet at the opposite side of the sample, which results in a much larger cancellation region where the ESR contrast recovers to 20%. 68
4.18 (a) Contour scan of a spherical neodymium magnet, with the microwave frequency fixed at 2.83 GHz, corresponding to an on-axis field of 14 G. (b) Contour scan of the same micromagnet, with the same microwave frequency. The NV-magnet distance is also smaller than in (a), as evidenced by the onset of optical effects (dark spot) near the center of the scan associated with small separations. 69
4.19 (a) Measurements of the NV center's ESR splitting as a function of laser duty cycle. The ESR measurement sequence is kept constant at 5 µs. To illustrate the irreversible and reversible effects of the laser pulses, the measurements are connected with arrows, with the initial and final measurement marked with green and blue dots respectively. With higher laser duty cycle, the ESR splitting decreases, suggesting demagnetization of the micromagnet due to laser heating. (b) The measurement in (a) is repeated after repositioning the micromagnet to regain a larger splitting. This time, even with a laser duty cycle > 0.5, changes in the ESR splitting appears reversible. (c) The ESR measurement sequence duration is changed to 7.5 µs. Interestingly, the ESR splitting increases with the laser duty cycle. (d) The ESR splitting is measured as a function of laser power, while the sequence duration is kept constant at 7.5 µs. 72

5.1 (a) Conceptual diagram for programmable interactions within arrays of nanopillars containing spin qubits. Spin qubits (orange) can be micromanipulated (black arrows) to interact with a common mechanical mode of a magnetically-functionalized resonator (turquoise), enabling mechanically-mediated spin-spin interactions. (b) Our current experimental realization: a diamond nanopillar containing a single NV center at its tip is positioned above an NdFeB spherical micromagnet at the center of a doubly clamped silicon nitride nanobeam. A coplanar waveguide on the same chip facilitates coherent microwave control of the NV center's electronic spin. The chip is mounted on a 3-axis nanopositioner stack, while the diamond nanopillar is kept fixed. (c) False-color scanning electron microscope image of the nanobeam (turquoise lines, two shown) with a micromagnet (red sphere) placed on a pad at the antinode of motion. Gold area at the bottom of the image is the coplanar waveguide. Inset: zoom-in image of the micromagnet. 75

5.2 Magnetic field imaging of a micromagnet. (a) Magnetic field near the micromagnet, with a vertical NV-magnet separation of about 1 µm. For each position of the diamond nanopillar, we measure the electron spin resonance (ESR) frequencies, from which we extract the magnetic field along the NV center's axis [1]. The field from the spherical micromagnet is well-approximated by a dipole model, with the fit (contours) deviating from the measured fields by less than 3 G at any point. The orientations of the NV center and magnet are consistent with the fabrication process of the nanopillar and magnetization direction respectively. These measurements were performed in air at room temperature, without any external driving of the mechanical resonator. Inset: Diagram showing the scanning area around the micromagnet on the nanobeam. (b) Reconstructed magnetic field gradients based on fit to dipole model. The maximum gradient is $\sim 1.5 \times 10^4$ T/m. 77

5.3 Preservation of spin coherence in proximity of a transported micromagnet. (a) The nanobeam along with the micromagnet is moved $1.7(2)\,\mu m$ from the NV center and then back to its original position over 1.7 ms. Pulsed ESR measurements at different times during the movement sequence show the changing field from the moving micromagnet. The 3 MHz hyperfine splitting from the NV center's intrinsic ^{15}N nuclear spin is clearly visible; an additional hyperfine splitting from a nearby ^{13}C nuclear spin is not shown here due to the microwave pulse duration used [1]. (b) Pulse sequence used to demonstrate storage and retrieval of coherent information, synchronized with the movement sequence shown in (a). (c) Fixing the phase accumulation time $\tau = 900\,ns$, we measure the coherence of the nuclear spin at the end of the movement sequence by varying the rotation axis angle θ of the final $\pi/2$-pulse, for both cases where the micromagnet is moved (orange) and kept stationary (blue). 79

5.4 Sensing the mechanical motion of the nanobeam. (a) Power spectral density (PSD) of the mechanical mode, measured using an interferometer. From the Lorentzian fit (black line) we extract a resonance frequency of $\sim 1.4\,MHz$ and a linewidth of $\kappa/2\pi = 1.5(2)\,Hz$. (b) After switching off an external drive from a piezoelectric chip, we measure the amplitude decay of the mechanical motion and obtain $Q = 8.25(6) \times 10^5$. **(c)** Sensing of the mechanical motion with the NV center. We perform a Hahn echo pulse sequence on the NV center with and without the mechanical drive, and plot their ratio (black circles) such that we can neglect the NV center's decoherence in our model for the fit ($\chi(\tau)$, blue line). We fit the signal $S(\tau, \lambda, \Delta_x)/e^{-\chi(\tau)}$ (see eq. (5.1)) to find $\lambda/2\pi = 7.7(9)\,Hz$. Due to drift in the cryogenic setup, the sweep of τ is limited to 700 ns to capture the first collapse in coherence due to the effect of the mechanical motion. 81

6.1 Frequency drift of four nanobeams with varying geometries and magnetic functionalization at cryogenic temperatures ($\sim 20\,K$). The resonance frequency is tracked by repeatedly taking frequency sweeps and fitting the mechanical response to a Lorentzian lineshape. 87

6.2 Drift rate of the mechanical frequency plotted against their initial frequencies. 88

6.3 The mechanical frequency of a nanobeam is plotted over about 22 h, alongside the cryostat temperature. Note that data for the sample mount temperature was unavailable at the time of the measurement; it can be estimated as an intermediate value between the temperature of the heat exchanger and the radiation shield. The abrupt temperature changes are due to user intervention in attempts to affect the frequency drift. 89
6.4 Measurement of the frequency drift over time, interrupted by scans of the nanobeam with the same laser used for the interferometer measurements (1064 nm). The setting for the laser is 20 mW, corresponding to several hundred µW at the objective back focal plane. 90
6.5 Upon cooling the cryostat from 30 K to 20 K, the resonator frequency momentarily increases before resuming its downward drift. 92
6.6 (a) Photo of the radiation shield extension. (b) The frequency drift rate is reduced by 2 orders of magnitude for the same nanobeam after the installation of the shield extension. 93
6.7 Photo of a fractal resonator fabricated in Simon Gröblacher's group, taken with an optical microscope. A coplanar waveguide is fabricated on the same chip, with constrictions near the center of the resonator, to deliver microwaves for manipulating the NV center's spin state. 96
6.8 Ringdown measurements of a bare (not functionalized) resonator at room and cryogenic temperatures. 96
6.9 Quality factors of multiple fractal resonators functionalized with neodymium micromagnets. The micromagnets are attached with different types of epoxy, or simply with electrostatic forces. In particular, the two epoxies are 8329TCS (MG Chemicals), which is heat-cured and has high thermal conductivity, and Loctite 349, which is UV-cured. For about half of the functionalized resonators, the quality factor approaches or even exceeds 1×10^7 at ~ 10 K. . 97
6.10 (a) The quality factor of a magnetically functionalized (with neodymium microsphere) fractal resonator is plotted as a function of the interferometer's laser power and the laser spot's position relative to the center of the resonator. We see that with increasing laser power and a laser spot close to the magnet, the quality factor is at its maximum (i.e. laser has an anti-damping effect). (b) The same measurement is repeated at cryogenic temperature (~ 14 K), showing an opposite effect. The quality factor is maximized with low laser power and the laser spot far away from the magnet (i.e. laser has a damping effect). 98

6.11 The measurements in Fig. 6.10 are repeated for a bare resonator at room temperature (a) and $\sim 14\,\mathrm{K}$ (b). No clear relationship is observed between the quality factor and the laser power and spot position. 99
6.12 (a) Design of a double fractal resonator. The width of the nanobeam at the center is 1 μm. The rectangle at the center of the nanobeam is the iron thin-film magnet, measuring 2 μm long and 1 μm wide. (b) Ringdown measurement of a double fractal resonator, with quality factor of 3×10^6 at 14 K. 101

7.1 (a,b,c) A series of Contour scans of the iron micromagnet during the NV-magnet approach (NV-magnet distance reduces from top to bottom). Two separate contours emerge, corresponding to two corners of the rectangular magnet. 106
7.2 By monitoring the NV center's ESR frequency as we decrease the NV-magnet distance, we can measure changes in the magnetic field and therefore the field gradient. 107
7.3 (a,b) ESR measurements for different drive amplitudes of the nanobeam. As the nanobeam is driven with a higher drive amplitude, the oscillating micor-magnet causes the ESR lineshape to broaden. For the two drive amplitudes 20 mV (a) and 25 mV (b), we can fit the broadened lineshape to determine the magnetic field oscillation amplitude to be 9.2 G and 11.5 G respectively. (c) Plotting the magnetic field oscillation amplitude as a function of the external piezo drive, we can fit the results using a linear function with zero intercept. 108
7.4 (a,b) Spin-echo measurement of the mechanical motion. As the amplitude of the mechanical drive is increased (1 mV and 2 mV for (a) and (b) respectively), the effect of the oscillating micromagnet has a more prominent effect on the echo signal. The baseline measurement is taken with the mechanical drive turned off. 109
7.5 Normalized spin-echo signal, with a drive amplitude of 2 mV, which corresponds to a nanobeam displacement amplitude of 0.92 nm. Fitting the normalized signal to an analytical function, we obtain a coupling strength of 30 Hz. 110

7.6 (a,b) By monitoring the NV center's ESR frequency as we change the NV-magnet distance, we can measure changes in the magnetic field and therefore the field gradient. To avoid misleading measurements due to drift during the gradient measurement, we measure the gradient as we approach (a) and then retract (b) the nanopillar from the micromagnet. By confirming that both field curves look similar, we can also confirm that "snap-in" did not occur at the rightmost data point, where the nanopillar is the closest to the magnet. "Snap-in" is a phenomenon in AFM where the tip snaps into contact with the sample at small separation distances [141]. In the context of this experiment, "snap-in" would result in misleadingly large gradients. If "snap-in" did occur, the field will instead remain "stuck" at the maximum value in the retraction curve. 111

7.7 Basic pulse sequence (LX Y X Y) for performing spin flips to excite the mechanical resonator. At each mechanical half-period, a trigger signal (gray dashed line) is sent to the pulse generator, which sends a combination of laser and MW π pulses.The phase of the MW pulses is alternated by 90° (X and Y) to mitigate pulse errors. Laser pulses are applied periodically to correct for pulse errors and mitigate lifetime decay of the spin state. Note that they must be applied every even number of mechanical half-periods, such that the reinitialization to spin state $|0\rangle$ is in sync with the spin drive. 112

7.8 Spin signal in phase space and the frequency domain. Left: The external coherent drive for the PLL is shown in blue. Flipping the NV center's magnetic moment at twice the mechanical frequency results in an additional excitation of the mechanical resonator, indicated by the red arrow. The phase of the "spin drive" relative to the PLL drive is denoated ϕ, and can be adjusted with the delay of the MW π pulses on the NV center. To maximize the spin signal, ϕ should be either 0° or 180°. Right: Mechanical motion in the frequency domain. The thermal motion is shown as a Lorentzian (black), and the excitations from the PLL and spin drives are shown in blue and red respectively. 115

7.9 Amplitude modulation of the spin signal. Left: The additional excitation from the spin is turned on and off periodically at frequency f_{mod}, as indicated by the dashed red arrow. Right: Because of the amplitude modulation of the spin drive, the spin signal now appears as two symmetrical sidebands around the coherent PLL drive. 116

7.10 Phase modulation of the spin signal. Left: The phase of the spin drive is toggled at frequency f_{mod} between ϕ and $\phi + 180°$, as indicated by the bright and dark red arrows. This effectively doubles the spin signal. 116

7.11 Phase modulation of spin control sequence. Every $1/2f_{mod}$, the pulse sequence skips over one mechanical half-period (indicated by the empty pulse labeled 0). Since the laser pulse always initializes the spin to the $|0\rangle$ state, it sets the phase of the spin drive relative to the mechanical motion. By shifting the pulse sequence (and therefore the laser pulses) by one mechanical half-period, the spin drive changes its phase by 180°. 117
7.12 (a) A 80 ns MW pulse is sent every mechanical period. There are no laser pulses. The gray dashed line indicates when the pulse generator is triggered. (b) Phase dependence of the vibration amplitude of the mechanical resonator, with the phase being that between the mechanical motion and the pulse train. The different colors correspond to measurements with varying MW power. (c) MW power dependence of the peak-to-peak amplitude of the phase-dependent driven amplitude in (b). 119
7.13 (a) A 80 ns MW pulse is sent every mechanical half-period (X-X). There are no laser pulses. The gray dashed line indicates when the pulse generator is triggered. (b) Phase dependence of the vibration amplitude of the mechanical resonator, with the phase ϕ being that between the mechanical motion and the pulse train. Blue (orange): MW pulses are disabled (enabled). Note that we also drive the mechanical resonator with a piezo in a PLL to sync the pulse train with the mechanics, hence the non-zero amplitude even with the microwaves disabled (blue). (c) The measurement in (b) is repeated with different drive amplitudes of the piezo. Blue (orange): total driven amplitude at $\phi = 132°$ with MW pulses disabled (enabled). 120
7.14 Mechanical parametric amplification. A coherent excitation $\sin(2\pi ft + \phi)$ is amplified by a parametric pump at $\sin(4\pi ft)$. The gain G varies from amplification ($G > 1$ to deamplfication (limited to $1 > G > 0.5$). Plot reproduced from reference [128]. 121
7.15 (a) A laser pulse is sent every n mechanical half-periods (L0 0^{n-1}). (b) For each value of n, we plot the driven amplitude of the mechanical resonator. . 122
7.16 (a) A laser pulse is sent every n mechanical half-periods. (b) For each value of n, we plot the spectrum of the mechanical motion. Note that the mechanical resonance has been demodulated to 50 Hz, and that the data for $n = 3$ was taken twice. It is clear that when $n = 2$, the excitation from the laser pulses raises the noise floor significantly above the thermal noise. 123
7.17 XYYX pulse sequence. The order of the XY pulses is flipped periodically, which leads to self-cancellation of the excitation due to the MW pulses. . . . 124

7.18 (a) The mechanical motion is measured with a lock-in amplifier and demodulated down to 10 Hz, such that both sides of the thermal spectrum can be seen in the Fourier transform. Symmetric sidebands at f_{mod} around the resonance can be seen, where f_{mod} is the modulation frequency of the MW pulse frequency. The sidebands can be seen even when the NV center is far away ($\sim 1\,\mu$m) from the micromagnet, indicating that they are due to classical spurious excitation from the laser and MW pulses. (b) The Fourier transform of the PLL's frequency is plotted. A peak is also seen at f_{mod} (2 Hz in this measurement). However, just as with the amplitude sideband in (a), this signal in the mechanical frequency's FFT also persists when the NV center is far away from the micromagnet. 126
7.19 (a) The power contained in the sideband (due to MW frequency modulation) in the mechnaical amplitude and frequency FFT is shown as a function of the MW center frequency. The measurements were taken at ~ 14 K with the NV center close to the resonator with a magnetic field gradient of $\sim 1 \times 10^5$ T/m. The red line indicates the ESR frequency. (b) The power contained in the sideband is shown as a function of the MW center frequency, with data taken at room temperature, with the NV center placed far away from the micromagnet on the mechanical resonator. 128
7.20 The LX $(\mathrm{Y\ X})^{\mathrm{n}}$ sequence, with $n = 1$. As clearly shown, in the first repetition block of LX (Y X), the spin state is $|0\rangle$ when the mechanical displacement is positive (in phase), whereas in the second repetition block, the spin state is $|1\rangle$ when the mechanical displacement is positive (in phase). This leads to self-cancellation of the spin's effect on the mechanics. 129
7.21 The monitoring sequence given by LX $(\mathrm{Y\ X})^{\mathrm{n}}$ L0 $(\mathrm{Y\ X})^{\mathrm{n}}$, with $n = 1$. Unlike the LX (Y X) sequence shown in Fig. 7.20, the spin state in this sequence always flips with the same phase (in phase in this figure) relative to the mechanical motion, which results in a spin-induced change in the overall motion. Additionally, the spin state can be read out at the beginning of each laser pulse before it gets fully reinitialized to the $|0\rangle$ state. 130
7.22 Zigzag pattern in the NV fluorescence collected from the monitoring sequence ($n = 20$), indicating that the spin is flipped continuously with decent fidelity. For this particular measurement, 2×10^5 laser pulses were used, with a single read-out performed for each pulse. The fluorescence data is then divided into sets of 20 successive measurements, stacked together and then averaged to give the plot shown. Because of this method of averaging, the zigzag pattern indicates that spin flips maintain their phase throughout 4×10^6 flips. 131

7.23 (a) The spin contrast is measured using the monitoring sequence ($n = 20$) as the MW pulse frequency is varied. For a π time of 90 ns, the monitoring sequence appears to be effective at inducing spin flips within 10 MHz of the ESR frequency. (b) The spin contrast is measured with the same monitoring sequence, while the MW power is swept. 132
7.24 Preliminary results suggesting the detection of single-spin backaction on the mechanical resonator. The color indicates the sideband amplitude (a.u.) in the amplitude FFT, after row-wise mean subtraction followed by column-wise mean subtraction. 133

A.1 A neodymium magnet is placed next to the sample inside the e-beam evaporator to magnetize the deposited iron thin-film in-situ. 152

B.1 Micromanipulator setup 156

C.1 (a) A diamond probe (on copper probe mount) and a beaker of hot water are enclosed in a "sauna". (b) Condensation on the diamond probe and probe holder. 162
C.2 (a) The same micromanipulator setup used for placing micromagnets on nanobeams (Sec. B) can also be used for "acid-cleaning" diamond nanopillars. (b) Pulsed ESR contrast reaches 26% after acid-cleaning and scanning the laser over the NV center for a few hours. 164

D.1 Schematic of the interferometer. A 1064 nm laser is split into a sample and reference arm. Power in the sample arm is reflected off a nanobeam and then recombined with the reference arm. The light is then split off again by a polarization beam splitter to be detected by a balanced photoreceiver (Newport 2117-FC), where the output is sent for lock-in detection (Zurich Instruments HF2) and also used to phase-stabilize the reference arm against low-frequency noise. 166
D.2 Ringdown measurements of a bare resonator (left) and a functionalized resonator (right, same as Fig. 4(b) of the main text), taken at cryostat base temperature of 20 K and 10 K respectively. 167
D.3 Hahn echo contrast without normalizing to a baseline measurement (without driving mechanical resonator), ... 170

D.4 Pulsed ESR measurement taken with the NV center being near a stationary micromagnet and an external field. We see four dips as a result of hyperfine interactions with both the ^{15}N and ^{13}C nuclear spins. We choose frequencies $MW_{\downarrow}$ and $MW_{\uparrow}$ such that they are equally detuned from the two nearby hyperfine transitions attributed to a nearby ^{13}C nuclear spin. 172
D.5 Pulse sequence for taking ESR measurements during movement. For each microwave frequency, we divide the total movement time by a number of time segments (number of pixels along the x-axis). In each time segment we run the pulse sequence shown inside the gray box. 173
D.6 Full pulse sequence for the measurements in Fig. 3(c) in the main text, with the part between the dashed lines corresponding to the pulse sequence in Fig. 3(b). 174
D.7 Pulsed ESR taken after nuclear spin polarization. 174
D.8 Estimation of the phase accumulated on the ^{15}N nuclear spin during the movement sequence. From the ESR plot in Fig. 3(a) in the main text, one can integrate the magnetic field change over time to obtain the total phase accumulated on the nuclear spin. 175
D.9 (a) Pulse sequence for determining the optimal time of the ^{15}N nuclear spin echo π-time. (b) We observe fringes in the readout contrast as we sweep T_π, where the maxima correspond to times when the phase accumulation is cancelled out to 0 by the nuclear π-pulse. The contrast is defined as the difference between the readout fluorescence when the final $\pi/2$-pulse rotation axis is set to $+x$ and $-x$. 176
D.10 Phase information stored inside the nuclear spin. The fringe contrast is not degraded by movement inside the magnetic field gradient. 177
D.11 Left: coherence of a single NV in the nanopillar, measured using a Hahn echo sequence, showing collapse and revivals of the 13C bath due to an external bias magnetic field. Middle: coherence times measured using different dynamic decoupling sequences. The electron spin T_1 is also plotted (black) for comparison. Right: coherence of the nuclear spin, measured using a Hahn echo sequence. 178

Acknowledgments

First and foremost, I would like to thank my adviser Misha for guiding me for the past seven years. You have always encouraged me to dream big while staying focused on the main objective of the experiment. I appreciate the freedom you gave me to pursue my own ideas, and I realize that it is a privilege not granted to every graduate student in science. Thank you for encouraging me to believe in myself, which can sometimes be difficult given the many challenges of this experiment. I also appreciate the enthusiasm and optimism you bring to our regular update meetings, whether the experiment was producing results or going through one equipment failure after another.

This thesis would not be possible without my labmates in LISE B26. Emma and Aaron were there when I first joined the lab, and set great examples as senior graduate students. Aaron taught me a lot of my cleanroom fabrication skills, and Emma was always very patient in answering my questions about key concepts in the experiment. Emma also had great scientific foresight, initiating some changes that greatly benefited the experiment in the long run. DaLi and I started in B26 around the same time, and I respect him a lot for the hard work he did to revamp the levitation experiment despite the myriad technical challenges. Trisha brought a lot of fabrication expertise to the team and has made solid contributions since the day she joined. I am confident that under her leadership, the levitation experiment will produce many more exciting results in the years to come. Yiqi joined around the time I started attempts to measure single-spin backaction, and I appreciate his expertise in mechanics and eye for detail. We had a lot of fun designing different pulse sequences, and while there was a lot of emotional whiplash from the experiment working very well one day and completely falling apart the next, it was made a lot easier by your sense of humor.

Binhan and Addison are the newest additions to the lab, and I sincerely hope you two will take both the nanobeam and levitation experiments to new heights in the future. A special mention goes to Florian. While you were in B26 only for a short exchange program, I had a great time working with you and hope you find success in whatever you set your mind to. Finally, I want to thank the previous generations of people who worked on this

project, such as Arthur Safira and Jan Gieseler. While we did not overlap that much (or at all), your hard work laid a strong foundation for the project, and I benefited tremendously from your notes and old messages on the #nanomech Slack channel.

I would like to thank our collaborators at TU Delft, namely Simon, Jin, and Jingkun. You have been very patient in answering our questions and requests for more samples. I will not forget the excitement I had from witnessing a twenty-second ringdown on one of your samples for the first time. In particular, I appreciate Jin's optimism and colorful Slack messages. I would like to acknowledge our collaborators at Harvard, namely Amir Yacoby and Tony Zhou. In particular, I am thankful to Tony for his scientific and career advice, not to mention the superb coherence times of the nanopillars he has provided for the collaboration.

I was fortunate to work with the many talented and good-natured people in the Lukin group. In particular, I would like to thank Brandon and Eric for the many fun conversations we had over these years. Thank you to Allen, for commiserating with me over our regular lunches at the law school. I would also like to thank all the other group members who have provided valuable advice and support over the years: Trond Anderson, Nabeel Aslam, Mihir Bhaskar, Dolev Bluvstein, Sambuddha Chattopadhyay, Tamara Dordevic, Pavel Dolgirev, Bo Dwyer, Gurudev Dutt, Haoyang Gao, Tim Guo, Yan Qi Huan, Alexander Keesling, Erik Knall, Can Knaut, Hoang Le, Harry Levine, Xiaoling Liu, Bart Machielse, Eirini Mandopoulou, Paloma Ocola, Po Samutpraphoot, Danilio Shchepanovich, Pieter-Jan Stas, Pavel Stroganov, Aziza Suleymanzade, Tamara Sumarac, Elana Urbach, Katherine Van Kirk, Tout Wang, Yan-Cheng Wei, Ralf Reidinger, Hengyun Zhou, Sasha Zibrov (Sr), and Sasha Zibrov (Jr).

I must also thank my labmates from my time at the University of Chicago. I had a very wonderful time in Professor Cheng Chin's lab, and during rough patches in graduate school I would think back to his words of encouragement. Misha Usatyuk (not to be confused with Misha Lukin), my lab partner back then, is one of the funniest people I know and I think you will have a bright career ahead as a comedian. Thank you also for introducing me to the

world of bodybuilding. My time with Cheng and Misha showed me how fun experimental physics could be, and you two were a big reason I decided to apply to graduate school programs.

To all my friends (and foes), I thank you all for your support (and motivation). In particular, I am very grateful for the friendships that have endured since my time in Chicago. Seeing you guys again always brings me great joy.

To my parents and sister, I would like to thank you all for making me who I am today. Both of my parents are hard-working people and they taught me that a lot of shortcomings can be overcome with hard work and sheer will. I know that you probably would still prefer me to be a real doctor, but hopefully a Doctor of Philosophy counts for something.

Finally, I would like to thank Brigitte for being by my side during this long journey. I look forward to the many adventures we will have together in the future.

To the person reading this

Citations to Previously Published Works

The contents of Chapter 5 and Appendix D have been published as:

F. Fung, E. Rosenfeld, J. D. Schaefer, A. Kabcenell, J. Gieseler, T. X. Zhou, T. Madhavan, N. Aslam, A. Yacoby, and M. D. Lukin. Toward programmable quantum processors based on spin qubits with mechanically mediated interactions and transport. *Phys. Rev. Lett.*, 132:263602, Jun 2024.

Chapter 7 forms the basis of a manuscript currently being prepared.

Chapter 1

Introduction

1.1 Background

Quantum computing leverages the phenomenon of superposition and entanglement to perform computation tasks that would be otherwise intractable for a classical computer. While a classical computer operates on bits that are either 0 or 1, a quantum computer operates on quantum bits, or qubits, which can exist simultaneously in both 0 and 1 states. Moreover, quantum correlations can exist between different qubits, a phenomenon known as entanglement. A collection of entangled qubits can exist in a definite collective state, but each individual qubit still exists in a superposition of states. These two unique properties of qubits allow a quantum computer to perform, in a sense, parallel computing over a large parameter space.

Richard Feynman's speech in 1981 is often credited as the start of the field of quantum computing [49]. In it, he talked about the problem of "simulating physics with computers". It is believed that there are classes of quantum systems that cannot be simulated efficiently with a classical computer. In principle, a quantum simulator can perform programmable simulations of large many-body quantum systems, which has the potential for advances such as better understanding of high-temperature superconductivity and the development of new drugs [74, 94, 28, 31, 54, 32].

Since then, quantum algorithms have been proposed to solve a variety of difficult problems. The most famous one, Shor's algorithm, allows a quantum computer to factor large numbers which are products of prime numbers, potentially breaking much of today's data encryption [135]. Other quantum algorithms promise significant speedups to complex optimization problems, with potential economic and societal benefits [44, 48, 105].

Different quantum systems are currently being explored as qubit candidates for quantum computers. Each qubit candidate has its advantages and disadvantages. For example, consider two of the leading qubit candidates: neutral atoms and superconducting qubits. While neutral atoms have longer coherence times, their gate speeds are also lower. It is quite possible that a useful quantum computer can eventually take the form of a hybrid system, which takes advantage of the strengths of its constituent subsystems [83].

To connect these subsystems, an interconnect is needed. Photons have traditionally served this role as a flying qubit capable of low loss over long distances [42, 71, 24, 35, 121]. However, mechanical resonators have recently emerged as an alternative interconnect. Importantly, mechanical resonators can be functionalized for a wide variety of interactions, including electric fields, magnetic fields, and gravity [159, 154, 53, 96, 148, 120, 5]. Recent advances have proven mechanical resonators to be highly coherent systems, as evidenced by their high quality factors Q, which can be as high as 1×10^{10} [19, 39, 21, 23].

Other than serving as an interconnect, the mechanical resonator can also act as a one of the two constituents in a hybrid system, alongside a two-level system acting as a qubit. The nonlinearity of the qubit can be used to create non-Gaussian mechanical states and cool the mechanical mode to its ground state [115, 107]. On the other hand, the mechanical mode can also be used to manipulate the qubit state, and even act as an alternative readout mechanism for the qubit [127, 124].

In this thesis, we will consider a hybrid quantum system between nitrogen vacancy (NV) center(s) in diamond and a mechanical resonator. NV centers are defects in the diamond lattice that have several properties making them favorable for quantum information processing. They have long coherence times up to milliseconds even at room temperature,

and unlike neutral atoms, they cannot escape from their "trap" inside the diamond lattice [16]. The NV center is also surrounded by a variety of even longer-lived nuclear spins, which together with the NV center can form a spin register [43, 30, 6, 144].

However, interfacing a large number of NV centers remains challenging for a number of reasons. NV centers can interact with each other via magnetic dipole-dipole coupling, but the range of such interactions is very short-ranged, on the order of tens of nanometers. It is also difficult to deterministically fabricate an array of such closely spaced defects in the diamond lattice [34]. To date, spin registers in diamond have been limited to about ten spins [125, 6].

Mechanical resonators can act as a mesoscopic interface between distant spins and enable scalable spin-spin interactions [118, 124, 51, 132, 82]. For example, it has been proposed that NV centers can be coupled to cantilevers which in turn are capacitatively coupled to an electrical circuit [118]. In this geometry, long-range electrical interactions between the cantilevers mediate interactions between distant spins. However, such proposals have yet been realized experimentally, due to the high coupling strength, quality factor, and spin coherence required.

In this thesis, I will describe experimental efforts that bring us closer to the goal of generating mechanically-mediated interactions between solid-state spins. As a starting point, we focus on coupling a single NV center to a single mechanical resonator. This is done on a home-built scanning probe platform, where individual NV centers in diamond nanopillars are coupled to magnetially functionalized silicon nitride mechanical resonators. In this scanning probe configuration, nanopillars can be physically moved, enabling programmable, mechanically-mediated connectivity between NV centers. I will discuss a number of technical challenges that we overcame, and successful measurements of the spin-mechanical coupling via both DC and AC magnetometry. The large magnetic field gradients exceeding $1 \times 10^5\,\mathrm{T/m}$ and the correspondingly high coupling strength mean that the effect of the single NV center can be detected by the mechanical resonator. I present some preliminary results showing such a measurement, which demonstrates the high level of control over each

subsystem. With realistic improvements to several system parameters, we believe that our system can be extended to enable scalable quantum information processing with solid-state spin qubits.

1.2 Longitudinal Coupling between an NV Center and a Mechanical Resonator

As mentioned earlier, NV centers can be coupled to mechanical resonators via various interactions. Throughout the rest of this thesis, we will consider mostly magnetic coupling between a single NV center and a mechanical resonator. This hybrid system can be described by the following Hamiltonian:

$$\mathcal{H} = \hbar\omega_0 S^z + \omega_r a^\dagger a + \gamma \vec{S} \cdot \vec{B} \tag{1.1}$$

where S is the spin operator for the NV center, a and $a^\dagger$ are the annihilation and creation operators of the mechanical mode respectively, and $\hbar$ is the reduced Planck's constant. While the NV center is a spin-1 system, by applying a bias field to lift the degeneracy between the $|m_s = 1\rangle$ and $|m_s = -1\rangle$ states and only addressing the $|m_s = 0\rangle \leftrightarrow |m_s = -1\rangle$ transition, we can effectively consider the NV center as a spin-1/2 system with an energy splitting of ω_0. The magnetic coupling is given by the Zeeman term $\gamma \vec{S} \cdot \vec{B}$, where $\gamma \approx 2.7\,\mathrm{MHz/G}$ is the NV center's gyromagnetic ratio and $\vec{B}$ is the magnetic field at the NV center's location. Finally, ω_r is the mechanical mode frequency, and g_i is the coupling strength between the NV center and the mechanical resonator's displacement $a + a^\dagger$.

For there to be a spin-mechanical coupling, the magnetic coupling term must have a dependence on the mechanical resonator's displacement. This can be achieved by magnetically functionalizing the resonator, such that the NV center's energy levels change as the mechanical resonator vibrates. The Zeeman interaction term can then be expanded in terms of the resonator's displacement $z_p(a + a^\dagger)$, where $z_p = \sqrt{\frac{\hbar}{2m\omega_r}}$ is the mechanical zero-point motion, with m being the effective mass of the resonator:

$$\begin{aligned}\mathcal{H} &= \hbar\omega_0 S^z + \omega_r a^\dagger a + \gamma(\vec{S}\cdot\vec{\nabla}B)z_p(a+a^\dagger) \\ &= \hbar\omega_0 S^z + \omega_r a^\dagger a + \sum_{i=x,y,z} g_i S^i (a+a^\dagger)\end{aligned} \tag{1.2}$$

where $g^i = \gamma\vec{\nabla}Bz_p$ is the coupling strength between the mechanical motion and each spin component S^i, with $\vec{\nabla}B$ being the magnetic field gradient at the NV center's location. Due to symmetry, we can also drop the S^y term to simplify the analysis:

$$\mathcal{H} = \hbar\omega_0 S^z + \omega_r a^\dagger a + g_z S^z(a+a^\dagger) + + g_x S^x(a+a^\dagger) \tag{1.3}$$

For the spin-mechanical system in this thesis, ω_0 is typically $> 2.0\,\text{GHz}$, while ω_r is typically $\approx 1\,\text{MHz}$. This big disparity in the energy levels of the two systems allows us to simplify the interaction term by going into the interaction picture $\tilde{\mathcal{H}} = U\mathcal{H}U^\dagger - \mathcal{H}_0$, where $U = e^{i\mathcal{H}_0 t/\hbar}$ and $\mathcal{H}_0 = \hbar\omega_0 S^z + \omega_r a^\dagger a$:

$$\tilde{\mathcal{H}} = g^z S^z(ae^{-i\omega_r t} + a^\dagger e^{i\omega_r t}) + + \frac{g_x}{2}(S^+ e^{i\omega_0 t} + S^- e^{-i\omega_0 t})(ae^{-i\omega_r t} + a^\dagger e^{i\omega_r t}) \tag{1.4}$$

Given that $\omega_0 >> \omega_r, g_x$, all the terms proportional to g^x are rotating rapidly and can be dropped according to the rotating-wave approximation (RWA). This leaves us with a Hamiltonian with only longitudinal coupling:

$$\mathcal{H} = \hbar\omega_0 S^z + \omega_r a^\dagger a + g_z S^z(a+a^\dagger) \tag{1.5}$$

From now on, we will refer to g_z simply as g. Note that if $\omega_0 \approx \omega_r$, the RWA will give us a transverse interaction term $S^+a + S^-a^\dagger$, which is the Jaynes-Cummings Hamiltonian describing direct energy exchange between the spin and mechanical resonator. With the Hamiltonian relevant to this work, the coupling term $g_z S^z(a+a^\dagger)$ is longitudinal, allowing for spin-mechanical interactions without direct energy exchange. This property is significant because it underlies schemes to generate mechanically-mediated spin-spin entanglement, despite the mechanical mode typically having phonon occupancies exceeding 10^5 even at

4 K [117, 132, 124].

1.3 The Field of Spin Mechanics

An often-used figure of merit is the spin-mechanical cooperativity C [83]:

$$C = \frac{g^2}{n_{th}\gamma\Gamma} \tag{1.6}$$

where $n_{th} \approx \frac{k_B T}{\hbar\omega_r}$ is the thermal occupation number, with k_B and T being Boltzmann's constant and the environment temperature respectively, $\gamma = \omega_r/2\pi Q$ is the mechanical linewidth, and $\Gamma = 1/T_2$, with T_2 being the spin coherence time. One can see that the cooperativity is the ratio between the coherent coupling g and the two deocherence channels of each subsystem: $n_{th}\gamma$ being the rate at which a phonon leaks from the environment into the mechanical mode, and Γ being the spin decoherence rate.

$C > 1$ marks the onset of coherent spin-mechanical coupling, where information is coherently transferred between the two subsystems at a rate faster than decoherence. However, all experimental work done on NV-mechanics systems thus far has fallen short of this threshold, as it is often a balancing act between maximizing the coupling and minimizing the decoherence. For example, a hybrid system has been demonstrated where a nanocrystal containing an NV center is attached to the end of a silicon carbide (SiC) nanowire, with the spin-mechanical coupling arising from an external magnetic field gradient [11]. Such a system has demonstrated impressive coupling strength exceeding 100 Hz, owing to the combination of high gradient and low mass of the nanowire, but the cooperativity is limited by the short coherence times of the NV center inside the nanocrystal. Apart from magnetic field gradient coupling, the NV center can also be coupled to the mechanics via strain. This is typically achieved by implanting NV centers inside a diamond mechanical resonator. However, the coupling strength for such systems has been limited to about 1 Hz, due to the low NV strain susceptibility [106, 102].

Our proposed NV-mechanics system consists of a magnetically functionalized nanobeam

coupled to a nearby NV center inside a diamond nanopillar. This configuration has multiple advantages: the small footprint of the nanopillar allows for nanoscale distances between the NV center and the nanobeam and therefore high magnetic field gradients; the doubly-clamped nanobeam has high quality factors due to dissipation dilution; the nanopillar fabrication process is not as detrimental to the NV center's long coherence times, compared to that of diamond nanocrystals. As we will discuss later in this thesis, given our latest parameters, the cooperativity of our system is on the order of 1×10^{-3}, which is higher than previous works on NV-mechanics systems. There is also a realistic path towards $C > 1$. For maximum coupling strength, the integration of well-established AFM technology should allow stable NV-magnet separation of tens of nanometers over meaningfully long measurement times. On the other hand, the mechanical decoherence rate can be greatly reduced by incorporating the latest developments in high-Q dissipation-diluted nanomechanical resonators. Finally, with adjustments to the NV implantation depth, we believe that there is likely room for improvement in the spin coherence times without sacrificing too much in the coupling strength. The justifications as well as caveats to these claims will be discussed throughout this thesis.

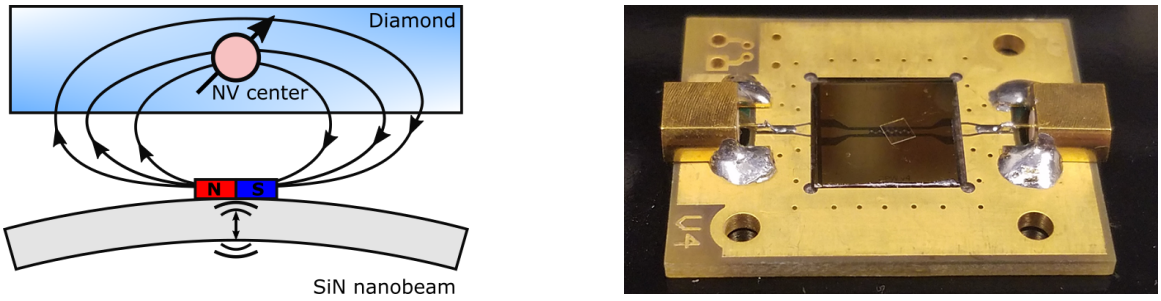
Chapter 2

Spin-mechanics on a Flip-Chip Device

2.1 Introduction

As discussed in the thesis introduction, our goal is to couple individual NV centers to nanomechanical resonators using magnetic field gradients. Our first approach uses a "flip-chip" design, where a diamond slab containing NV centers is placed directly on top of a chip containing mechanical resonators (Fig. 2.1a), which are functionalized with iron thin-film magnets (see Sec. A.3 and Sec. 7.2). This ensures a small vertical distance between NV centers and the micromagnet on the mechanical resonator. This approach comes with other advantages. Firstly, the use of slab diamonds gives us predictable NV properties and avoids the technical challenges of fabricating diamond nanostructures, which typically result in lower NV coherence times. Given a typical implantation energy of 20 keV, the NV centers are expected to be around 30 nm below the surface, which is expected to give long spin coherence times approaching those of NV centers in bulk. Secondly, in this "flip-chip" geometry the diamond will make physical contact at multiple points with the mechanical resonator chip, thus one can expect high stability in the distance between the NV center and micromagnet.

A complete device is shown in Fig. 2.1b. The mechanical resonator chip is wirebonded to a printed circuit board with SMP connectors. The diamond slab is placed using vacuum



(a) (b)

Figure 2.1: (a) Schematic of the flip-chip geometry. NV centers in the diamond is coupled to the motion of the micromagnet on the nanobeam underneath. (b) Photo of the completed device, consisting of the diamond (transparent square) placed on top of a chip containing mechanical resonators. The chip contains a coplanar waveguide, and is wirebonded to a printed circuit board (PCB) with SMP connectors for microwave delivery to manipulate the NV center's spin state.

tweezers (Ted Pella) such that the side with implanted NV centers faces the chip. To maintain mechanical stability during subsequent sample handling, a small amount of Crystalbond is sometimes applied afterwards to the diamond edges to affix it to the chip. The complete device is finally transferred to a vacuum chamber (Janis ST-500 flow cryostat with a faulty helium line).

2.2 Device Characterization

2.2.1 Mechanics Characterization

In this section we discuss some characterization measurements of the mechanics before putting the diamond slab on top of the chip. The geometry of the silicon nitride (SiN) nanobeam mechanical resonator is illustrated in Fig. 2.2. In the case where the restoring force is dominated by tension, the frequency f of a nanobeam is given by: [114]

$$f = \frac{n}{2L}\sqrt{\frac{\sigma}{\rho}} \tag{2.1}$$

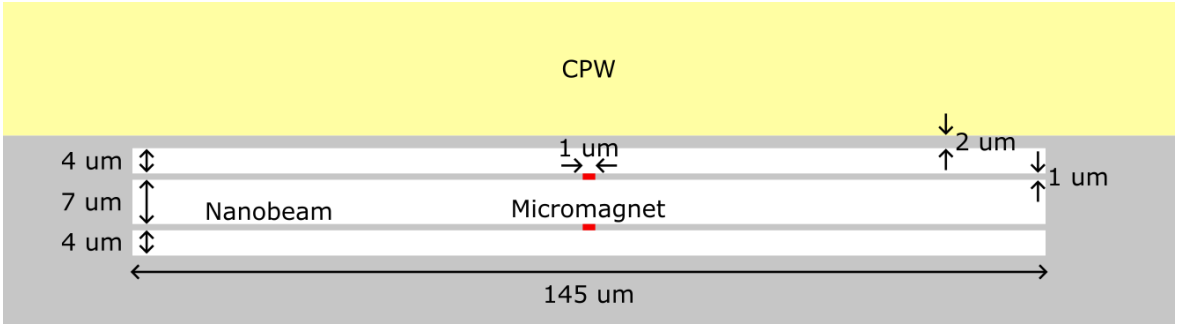


Figure 2.2: Diagram (top-down view) showing some relevant dimensions of the nanobeam along a coplanar waveguide (CPW). The CPW can be used to deliver microwaves to manipulate the NV center's spin state, and also to excite the nanobeam. The red rectangle is the micromagnet consisting of an iron thin film. This micromagnet can also be a manually placed neodymium micropshere.

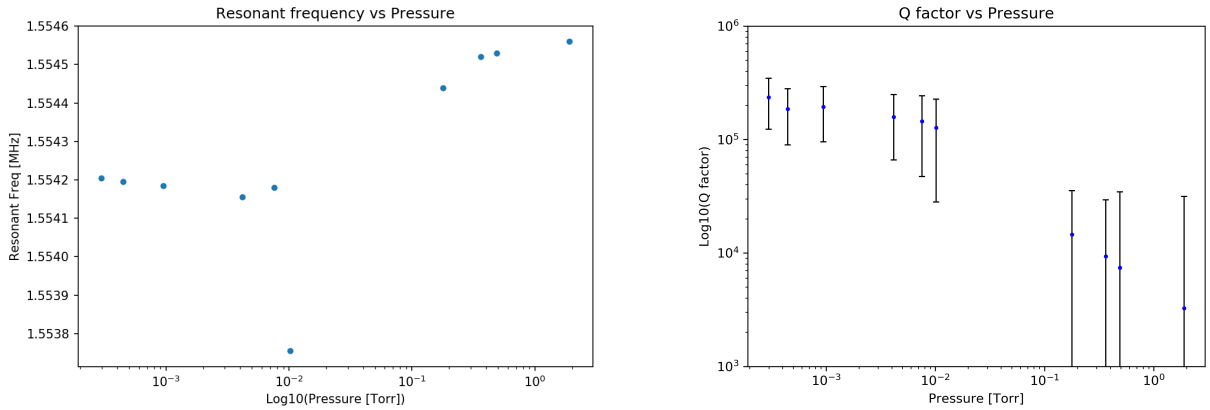
where n is the mode number, L is the beam length, σ is the thin film stress, and ρ is the mass density of the beam. In our design, where $L = 145\,\mu\text{m}$, $\sigma \approx 800\,\text{MPa}$, and $\rho = 3170\,\text{kg/m}^3$, we can estimate the fundamental frequency to be $f \approx 1.74\,\text{MHz}$.

Our mechanical characterization shows rough agreement with the above estimate. Fig. 2.3b shows the variation of the mechanical frequency and quality factor Q as a function of the pressure inside the vacuum chamber. We see that Q plateaus at around 2×10^5 below 1×10^{-3} Torr at room temperature.

At large driven amplitudes, the restoring force no longer simply follows Hooke's law and nonlinear terms become significant. The potential of an anharmonic oscillator can be described by the following:

$$\begin{aligned} V(x) &= \frac{1}{2}kx^2 + Bx^4 \\ &= \frac{1}{2}k(1 + \frac{2B}{k}x^2)x^2 \end{aligned} \tag{2.2}$$

where k is the spring constant and B is the coefficient for the nonlinearity contribution. Note that we have neglected the x^3 term to enforce the symmetry of the potential. As made explicit in Eq. 2.2, the effective spring constant and mechanical frequency are now modified by a term proportional to the displacement, i.e. the resonator exhibits a Duffing



(a) **(b)**

Figure 2.3: (a) Resonance frequency of the nanobeam as a function of the pressure inside the vacuum chamber. (b) Mechanical quality factor of the nanobeam as a function of the pressure. The quality factor is calculated using the linewidth extracted from fitting the resonance spectrum to a Lorentzian.

nonlinearity. For a positive (negative) coefficient B, the resonator is said to exhibit "stiffening" ("softening").

Fig. 2.4 shows frequency sweeps of the resonator response with varying drive amplitudes. As the drive increases, the amplitude as a function of drive frequency no longer follows a Lorentzian curve. Notably, the response exhibits hysteresis based on the direction of the frequency sweep; there exists a frequency range in which the response takes on two possible values, i.e. the system exhibits bistability. Proposals have been made to leverage this property to create a nanomechanical memory element [14, 101, 62]. For measurements presented in this thesis, we generally work in the regime where the displacement of the nanobeam is much smaller than its thickness, such that the Duffing nonlinearity can be neglected.

2.2.2 NV center characterization

Some typical characterization measurements are shown in Fig. 2.5. Note that the measurements shown in the figure were performed on NV centers not directly on top of the

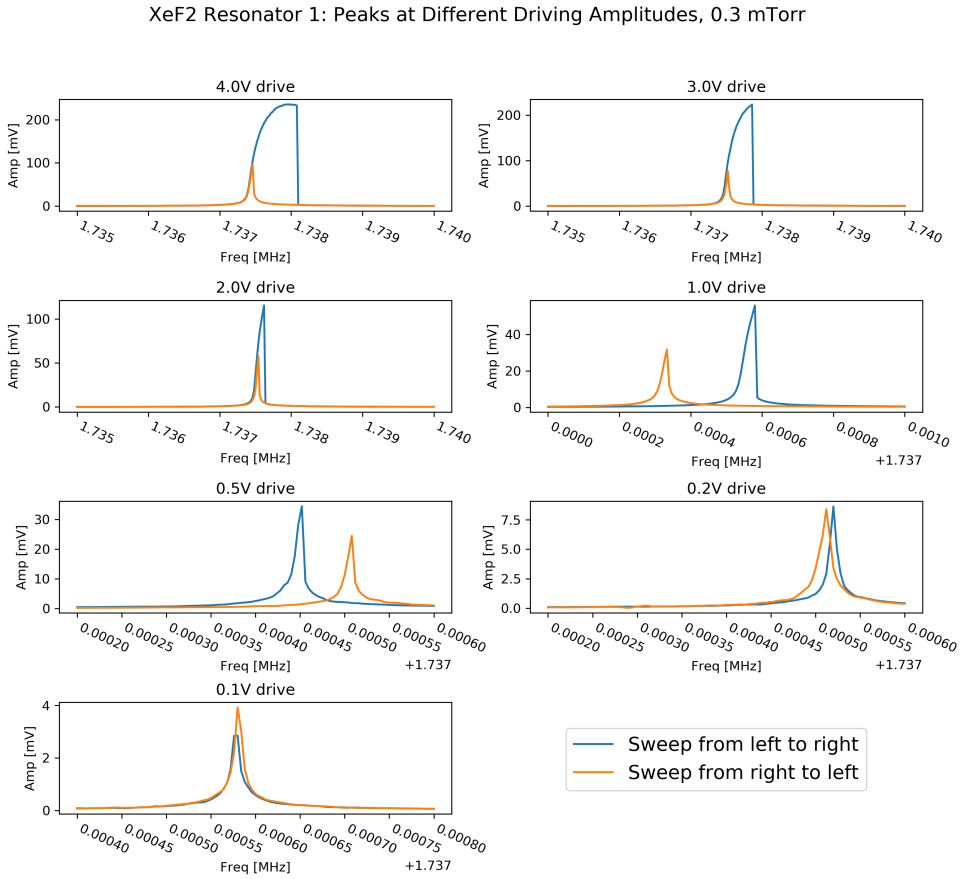


Figure 2.4: Duffing nonlinearity of the nanobeam. Sweeping the frequency of the piezo drive, we see that the response of the nanobeam no longer follows a Lorentzian lineshape for high drive amplitudes and depends on the direction of the sweep.

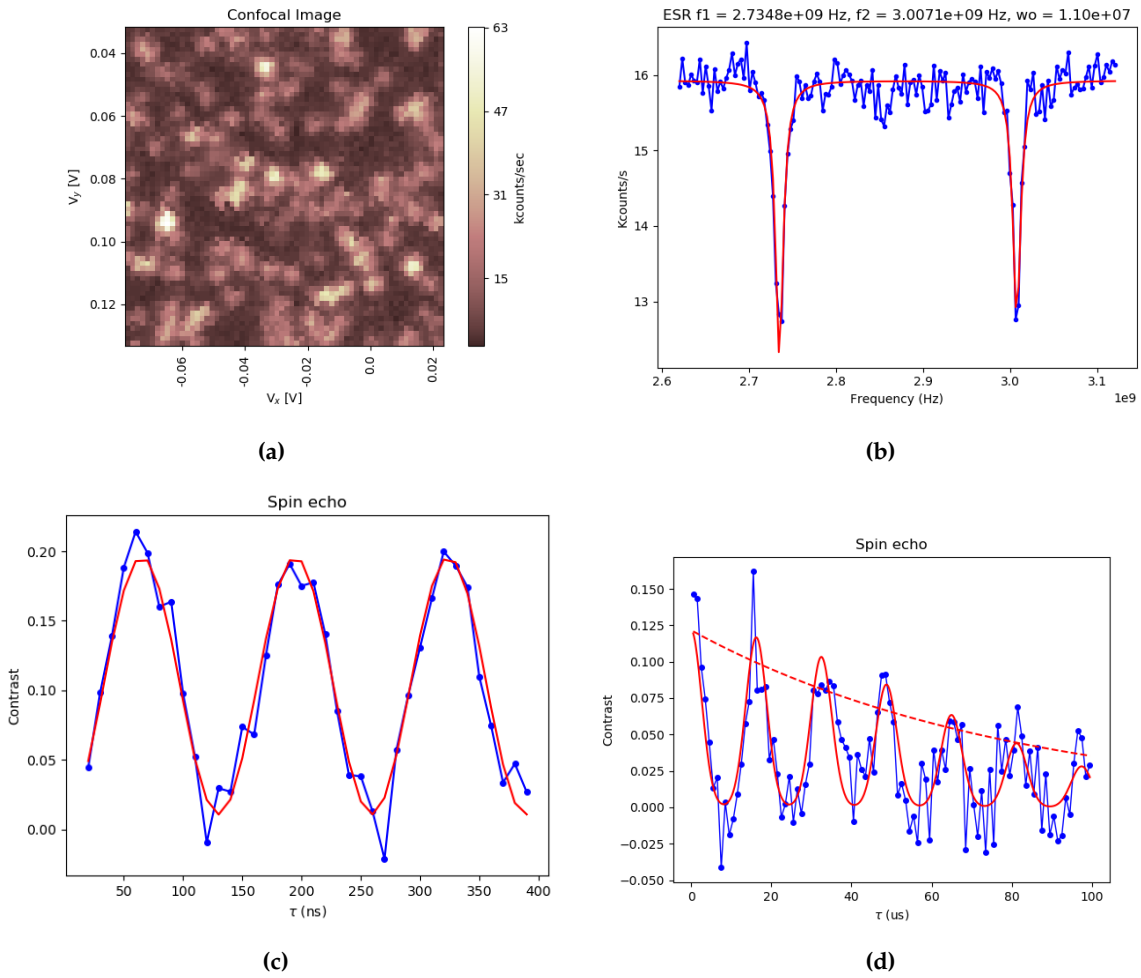


Figure 2.5: (a) Typical confocal image, where NV centers can be resolved down to the diffraction limit. (b) Electron spin resonance (ESR) measurement, which gives the resonance frequencies of the NV center. Here an external magnetic field of $\sim 50\,\mathrm{G}$ gives rise to a splitting of $\sim 272\,\mathrm{MHz}$. (c) Rabi oscillations. With the on-chip coplanar waveguide (CPW), Rabi frequencies exceeding 10 MHz can be achieved without saturating the microwave amplifier. (d) Spin echo measurement, where clear collapses and revivals can be observed. The revivals happen with a period of 16 µs, as a result of the Larmor precession of background ^{13}C nuclear spins in an external field of $\sim 52\,\mathrm{G}$. Fitting to the envelope of decay, we extract a coherence time of 80 µs.

mechanical resonator.

2.3 Challenges

Unfortunately, this "flip-chip" approach comes with two critical technical issues: lack of control over distance between the micromagnet and NV center, and the micromagnets being demagnetized by the green laser used to reinitialize and read out the NV center's spin state. While these two issues are not fundamental and can be mitigated with fabrication improvements, they motivated us to redesign the experiment using a scanning probe approach, as described in the subsequent chapter.

2.3.1 Standoff Issues

In the "flip-chip" geometry, the distance between the micromagnet and NV center is fixed after the device is completed, i.e. the diamond is placed on top of the mechanical chip. It is completely up to chance whether an NV center is located close enough to the micromagnet laterally to have an appreciable spin-mechanical coupling.

On the other hand, the vertical distance between the NV center and micromagnet is also rather unpredictable. In our first devices, we did not fabricate any spacers on the mechanical chip, believing that any debris on the chip can serve that purpose. After placing the diamond on top of the mechanical chip, we notice from camera images that some resonators are stuck to the diamond. This is confirmed by the fact that we can no longer detect mechanical resonances after diamond placement, an example being shown in Fig. 2.6.

Even for resonators that are not stuck to the diamond (i.e. display a mechanical resonance), there is still significant difficulty finding an NV center close enough to the micromagnet that there is an appreciable ESR splitting. Fig. 2.7a shows a typical measurement where we measure the ESRs of multiple NV centers near the micromagnet. Out of 17 NV centers, only 2 show a detectable splitting. One such measurement is shown in Fig. 2.7b, where the NV center experiences a small field of $\sim 7\,\mathrm{G}$ from the micromagnet. Approximating the iron micromagnet as a sphere with similar volume (giving a diameter of $1\,\mu\mathrm{m}$), and assuming a magnetic remanence of $0.1\,\mathrm{T}$ for iron, we can estimate the gradient at the NV location to be only $900\,\mathrm{T/m}$, corresponding to a coupling strength of $0.4\,\mathrm{Hz}$.

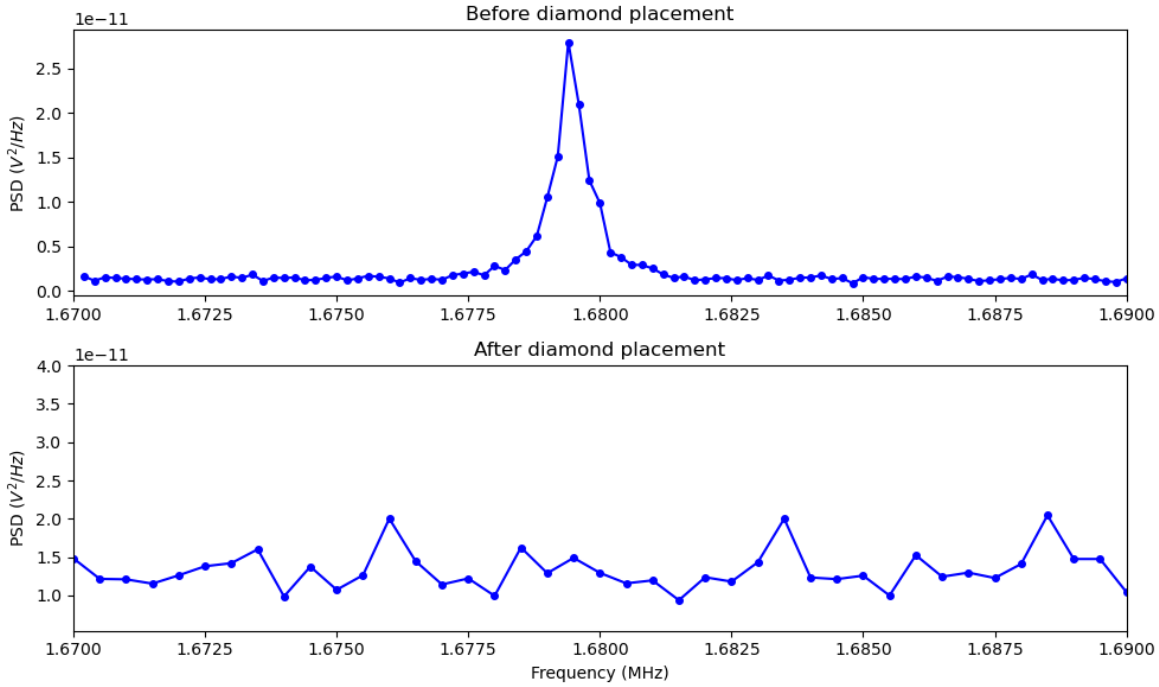
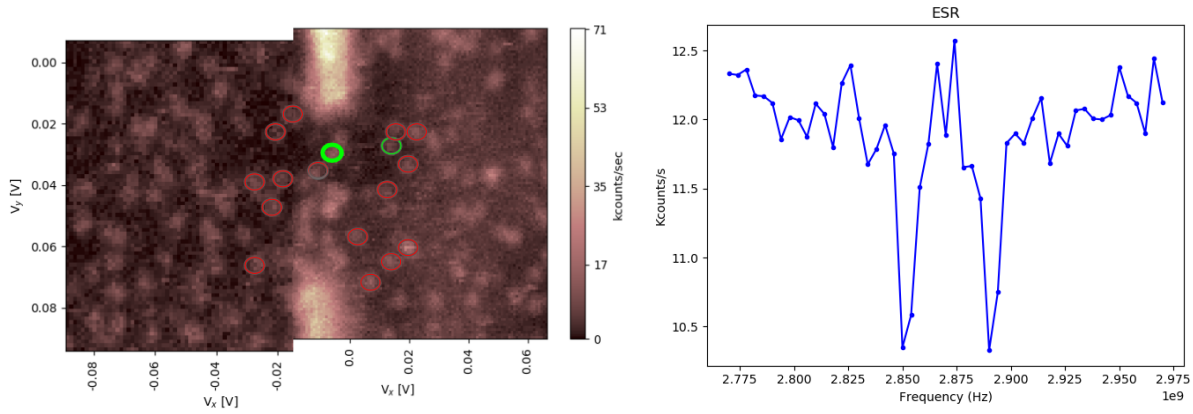


Figure 2.6: Interferometer measurement before and after diamond placement. The clear resonance at 1.68 MHz is missing after the placement, suggesting that it is stuck to the diamond.



(a) (b)

Figure 2.7: (a) Confocal image of NV centers near an iron micromagnet fabricated on top of a nanobeam. The bright vertical line is the nanobeam (1 µm wide), interrupted by a dark region that is the iron micromagnet. Red (green) circles indicate NV centers for which there was no (some) ESR splitting. (b) ESR of the NV center indicated by the thick green circle in (a), showing a splitting of ~ 38 MHz corresponding to an on-axis field about 7 G.

2.3.2 Demagnetization from Laser

Another major technical challenge arises from the micromagnet's vulnerability to being demagnetized by the green laser, which is necessary for initializing and reading out the NV center's spin state. Given that the device is situated in vacuum to avoid gas-damping, laser light absorbed by the micromagnet is not easily dissipated, heating it up beyond its Curie temperature and demagnetizing it. Confocal scans like that in Fig. 2.7a are necessary to locate NV centers, but they run the risk of demagnetizing the micromagnet. Moreover, we have seen NVs that initially exhibit ESR splittings, which disappear in subsequent measurements, once again suggesting demagnetization caused by the laser.

Adding to the problem, we have noticed that laser heating is sometimes so drastic that the micromagnet melts and completely destroys the nanobeam. Fig. 2.8 shows the photon counts from the light reflected off a nanobeam while the laser spot is parked close to the micromagnet; the sharp drop in counts indicates the time when the nanobeam breaks, which is later confirmed with a camera image. Example scanning electron microscopy (SEM) images in Fig. 2.9 show the extent of physical and emotional destruction caused by

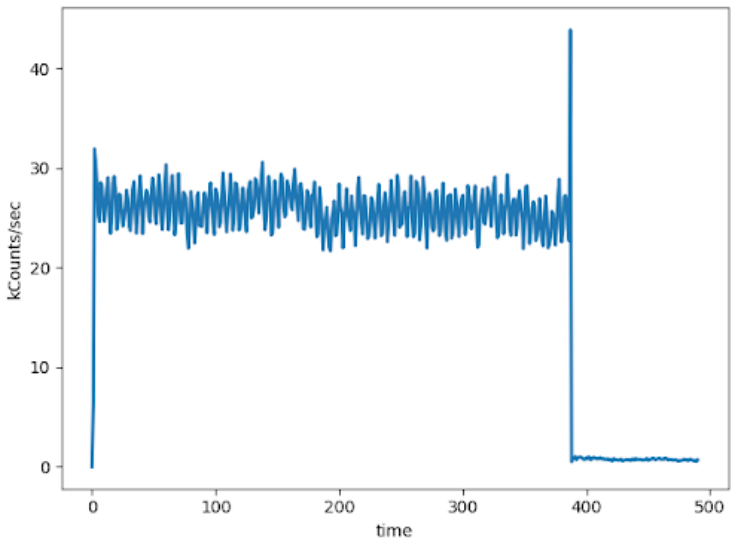


Figure 2.8: Photon counts from light reflected off a nanobeam while the green laser is focused close to the micromagnet. The sharp drop indicates when the nanobeam breaks. The time axis is likely in units of 0.1 s (incomplete documentation).

overheating from the green laser.

We have also seen cases where the nanobeam appears to have broken not at the micromagnet (Fig. 2.10), as well as cases of nanobeams breaking despite not even having a micromagnet. We attribute this to light-absorbant surface contaminants (e.g. residual photoresist). This issue is resolved after using PG Remover (Kayaku) (instead of acetone) for photoresist-stripping steps in the fabrication process.

As a note, the infrared (IR) laser used for interferometer measurements also causes similar overheating. However, while the NV center (and therefore the green laser spot) must be close to the micromagnet, the IR laser spot can simply be moved to a different point on the nanobeam away from the micromagnet to avoid demagnetization.

2.4 Conclusion and Outlook

The two aforementioned technical issues constitute major obstacles towards realizing a reliable spin-mechanics experimental platform. Despite years of effort, we have not been

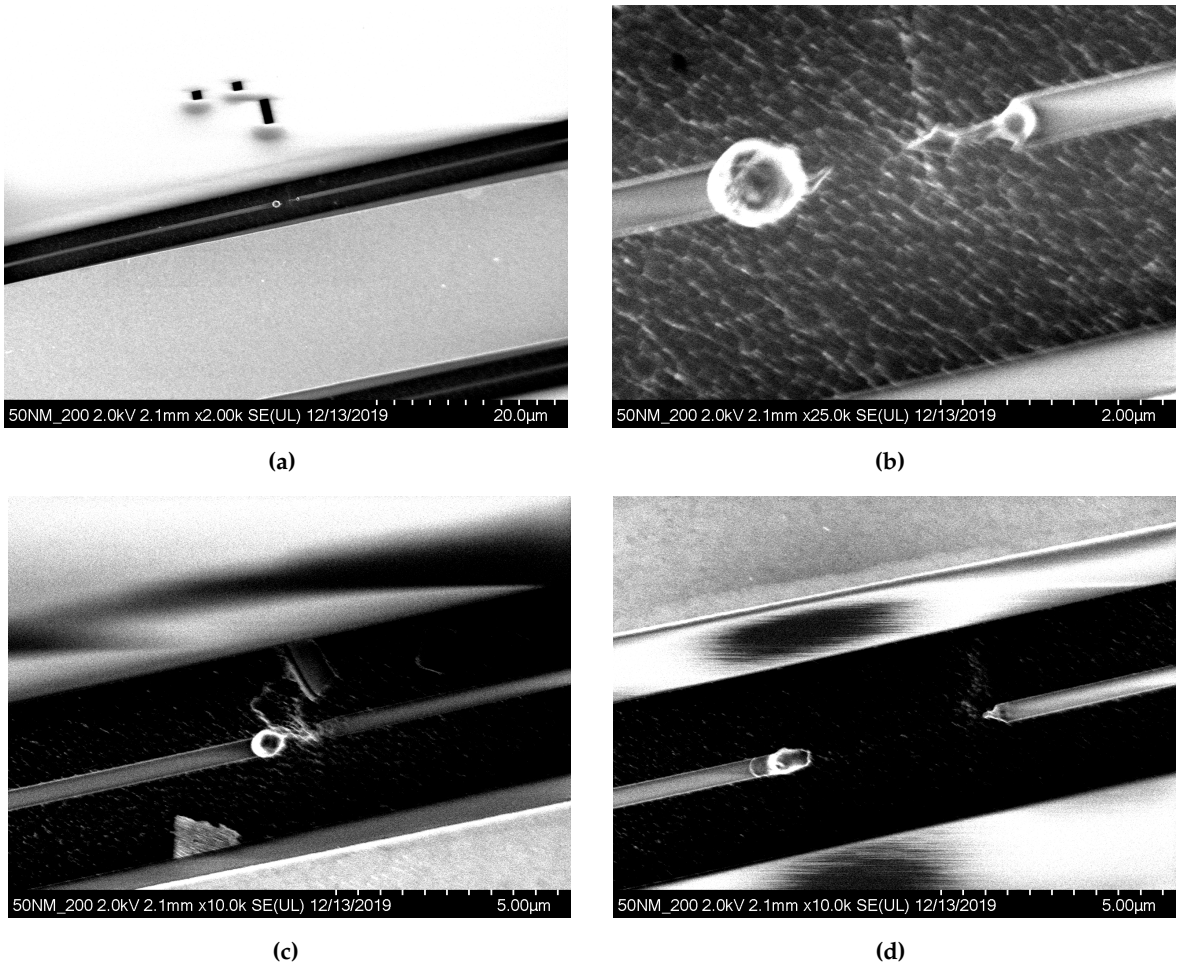


Figure 2.9: (a) SEM image of a nanobeam compromised to a permanent end, indicated by the gap in middle where the micromagnet used to be. (b) Zoom-in of the breaking point. (c,d) Additional images of other broken resonators.

able to measure any coupling between the NV center and the mechanical resonator. The lack of control over the NV center's location relative to the micromagnet over all three dimensions excludes any possibility to optimize the spin-mechanical coupling after diamond placement. It also greatly reduces the number of diagnostic tools at our disposal. For example, it is hard to determine if a small ESR splitting is caused by the magnetic field from the micromagnet, or other effects like hyperfine splitting or strain [145, 137]. This ambiguity can be eliminated if we can monitor the ESR splitting as a function of the NV-magnet distance.

The issue of demagnetization from the laser can in principle be mitigated by reducing the

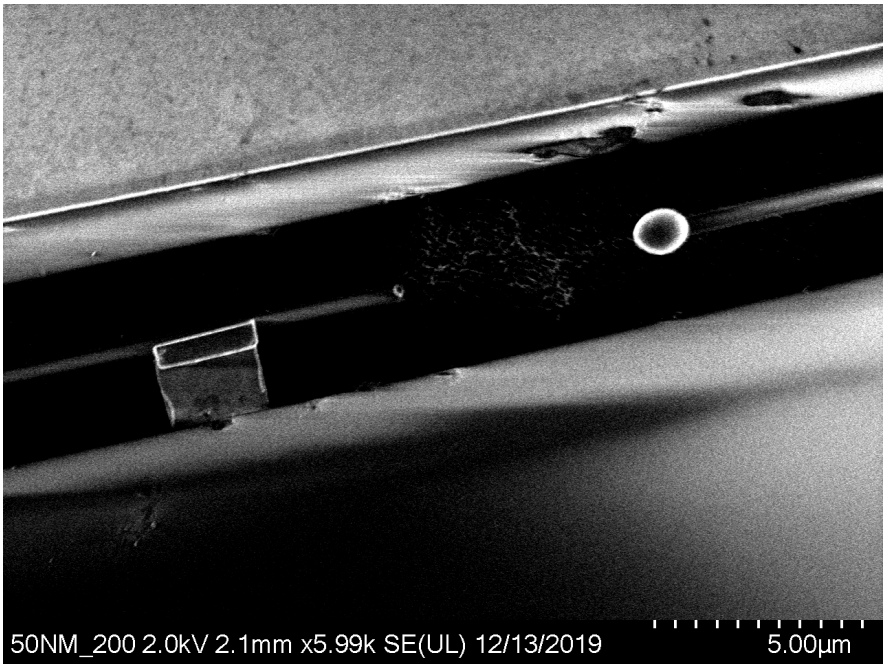


Figure 2.10: SEM image of a nanobeam which appears to have broken not at the micromagnet (rectangle on the left), but on the bare nitride.

Laser power needed to destroy nanobeam (uW)	Laser focused on micromagnet	Laser focused on nanobeam (nitride)
110	✓	
210		✓
220	✓	
530	✓	

Table 2.1: Four nanobeams are subjected to green laser illumination either directly on the micromagnet or somewhere else on the nanobeam. For each nanobeam, the laser power is slowly increased from $\sim 100\,\mu W$ and the laser focus is swept along the optical axis until the nanobeam is destroyed. Note that the nanobeams in this measurement are functionalized manually with neodymium magnets. We have noticed that nanobeams with iron thin film magnets also break with similar laser powers.

laser duty cycle throughout all experiments in vacuum. However, given the low fluorescence counts, this will make the measurement times unbearably long. Table 2.1 shows that there is no clear threshold laser power above which a nanobeam will be destroyed by the laser, making it difficult to determine a safe laser power for an individual resonator. There is a clear conflict between experimental requirements: achieving high coupling requires using an NV center very close to the micromagnet, but that would necessarily entail higher chance of the laser demagnetizing it. Finally, the laser for the interferometer has to travel through the diamond twice, which greatly reduces the SNR of mechanics measurements.

As we will see in the subsequent chapter, moving the experiment to a scanning probe geometry mostly resolves these two issues. However, the scanning probe geometry also has its own disadvantages, such as susceptibility to drift, especially at gradients approaching $1 \times 10^6\,\mathrm{T/m}$. In the future, one might consider revisiting the flip-chip design, but with some significant changes. For example, the vertical distance can be well-controlled by on-chip or pick-and-place spacers with thickness below 100 nm [64]. Also, the diamond size can be reduced significantly to avoid any debris on the mechanical chip acting as unintentional standoffs, and a set of micromanipulators can be used to make nanoscale adjustments to the diamond's position. To reduce the adjustment needed, one should characterize multiple NV centers in the diamond beforehand, choosing the one with the longest coherence times and most favorable orientation. Diamond placement can then be done by aligning markers on both the diamond and mechanical chip. To reduce laser heating, one can increase the photon-collection efficiency through the use of integrated solid immersion lenses [122, 67] while preserving long NV center coherence times [6].

Chapter 3

A New Cryogenic Scanning Probe Experimental Platform

3.1 Introduction

The shortcomings of the "flip-chip" approach described in the previous chapter led us to consider a different approach. Given the small NV-magnet distance required to achieve high coupling, a scanning probe geometry is a promising alternative, given the mature field of atomic force microscopy (AFM), where probe-sample distances on the order of tens of nanometers are routinely achievable. We are also encouraged by advances in the field of scanning probe magnetometry, where diamond scanning probes containing NV centers have been commercialized by companies such as QZabre and Qnami [2, 3].

In this section, we describe the details of the redesigned experimental setup. The two main technical challenges in the "flip-chip" approach, namely lack of control of the NV-magnet distance and laser-induced demagnetization, are mostly mitigiated by the scanning probe geometry. Additionally, the scanning probe geometry grants a whole new control knob that enables new magnetometry measurements, allowing us to characterize the micromagnets and diagnose any issues. These advantages enabled the first spin-mechanical coupling measurements in the history of this experiment.

Label	Description
1	ST-500 vacuum shroud
2	Vacuum shroud extension (Janis)
3	Adapter plate for bellows
4	ST-500 radiation shield
5	50 Ω heater ring (Janis)
6	3-axis nanopositioner stack
7	Radiation shield (lower)
8	Radiation shield (upper)
9	Heat exchanger extension
10	Adapter plate for radiation shield
11	Sample mount and sample chip
12	Inward extension for external magnet
13	Permanent magnet (in atmosphere)
14	Column with integrated heater
15	Garolite spacer
16	Probe holder with diamond probe
17	NW-50 bellows
18	NW-50 o-ring
19	Objective
20	Lens tube (Thorlabs SM1)

Table 3.1: Description of each part labeled in Fig. 3.1.

3.2 Cryogenic Setup

The experiment was moved from a vacuum chamber to a helium flow cryostat. A diagram showing different components of the setup is shown in Fig. 3.1. The cryostat is a heavily modified continuous flow cryostat (Janis ST-500) with a factory-made vacuum extension shroud. Liquid helium is transferred from a 100 L dewar to the cryostat via a vacuum-insulated transfer line, with pressure from the dewar provided by natural boil-off and regulated at $\sim$ 2 PSI. Inside the cryostat, the helium flows through an internal line that forms a coil inside a heat exchanger (not shown, directly below part 9 in Fig. 3.1) before boiling off into gaseous form. The cold helium gas is then circulated through a larger coil which acts as a radiation shield (part 4), before leaving the cryostat through an exhaust port. To conserve helium, which is becoming increasingly expensive, the exhaust helium is directed to a recovery system in the laboratory building. To avoid contamination of the

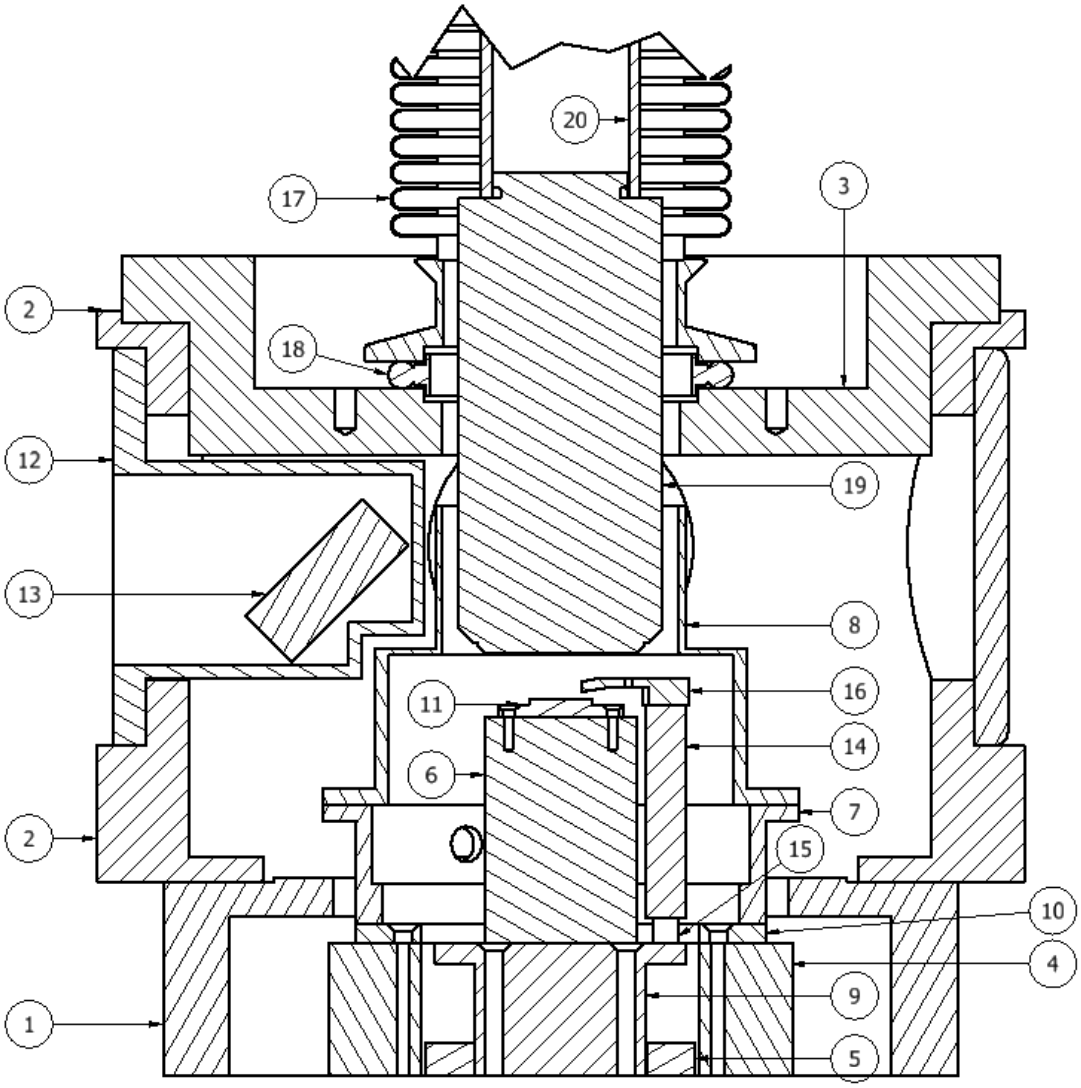


Figure 3.1: Cross-section view of the cryostat, with some parts such as screws and KF clamps omitted for clarity. See Table 3.1 for the parts list.

recovery system, care must be taken to seal off the recovery line when the cryostat is not in use.

The radiation shield (parts 4, 7, and 8 in Fig. 3.1) serves to shield the sample area from radiation from the room-temperature exterior of the cryostat. It reaches a temperature of $\sim 20\,\mathrm{K}$ after the cryostat is fully cooled down. Importantly, it also serves as a cryopump that reduces adsorption onto the mechanical resonators (see Sec.6.2).

The operating time of the cryostat is limited by the volume of liquid helium in the 100 L dewar. While the cryostat is capable of reaching a sample temperature of 5 K, we typically operate the cryostat at a base temperature of about 13 K. Under these conditions, the cryostat exhausts $\sim 600\,\mathrm{SL/h}$ of helium gas, which given the helium gas-to-liquid volume ratio of 745, corresponds to an operating time of 5 days. In reality, we seldom begin a cooldown with a completely full dewar, and the cryostat temperature starts to rise when there is only about 10 L left in the dewar, so the actual operating time is only about 4 days. This limited operation time can be challenging, given the time needed to safely approach the sample with the diamond nanopillar and locate the area of highest magnetic field gradient, not to mention the time needed for any subsequent measurements, such as spin-echo measurements for AC magnetometry or sensing single-spin backaction. However, this time pressure has also proved to be a reliable motivator pushing the experiment forward and has encouraged many technical improvements in measurement efficiency.

3.2.1 Sample Mount

The sample chip is mounted on a custom mount made of copper 101 (part 11 in Fig. 3.1). To ensure good thermalization, a thin layer of vacuum grease (Apiezon N grease) is applied to the sample mount before the sample chip is placed on top. After the chip is wirebonded to the two PCBs also on the sample mount, the entire assembly is mounted on top of the nanopositioner stack (2 ANPx101s and 1 ANPz101 from Attocube, part 6 in Fig. 3.1), which allows control of the sample's position in 3 dimensions. The nanopositioners are made of titanium which are poor thermal conductors; to ensure good thermalization of the

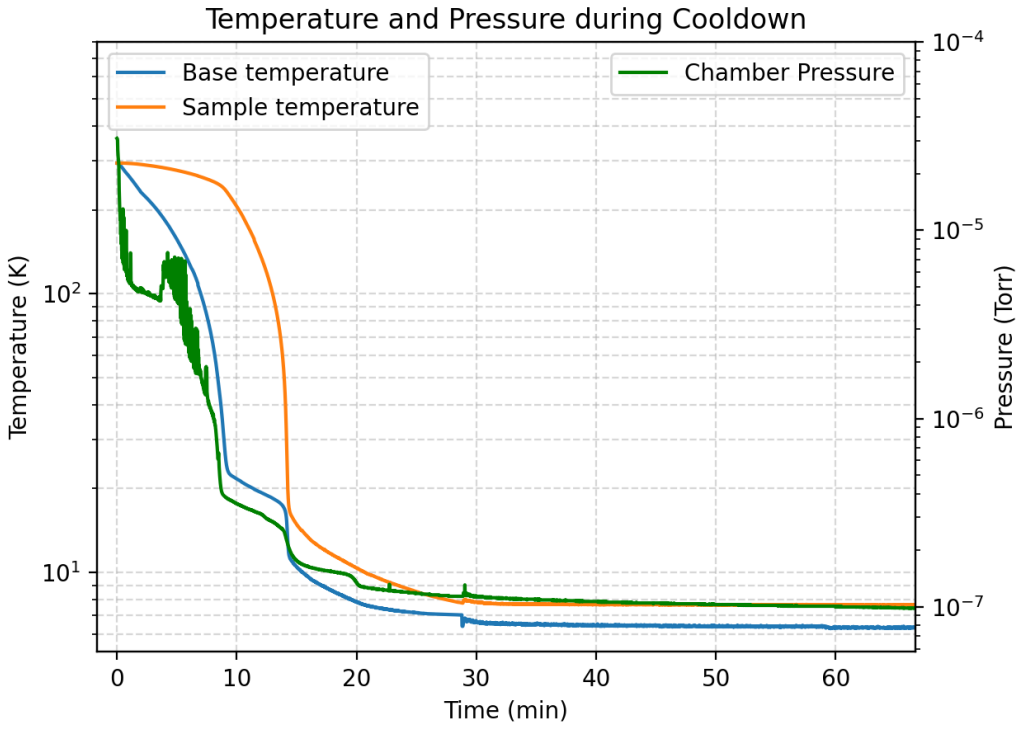


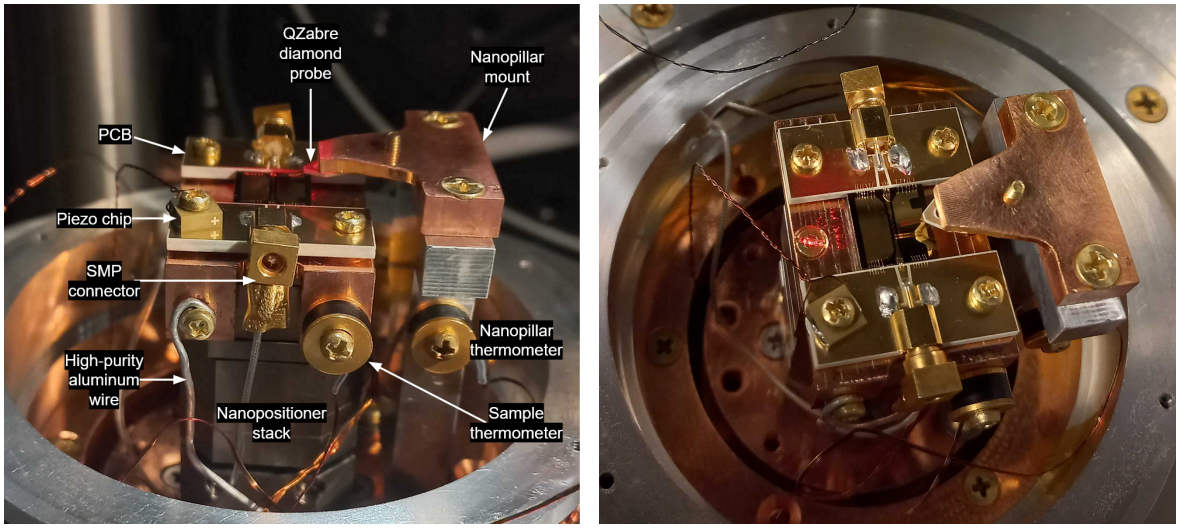
Figure 3.2: Chamber pressure and temperatures of the heat exchanger and sample during the first hour of a cooldown. After the initial cooldown, a feedback loop is initiated to keep the heat exchanger temperature typically at 13 K. The temperature of the nanopillar mount is not shown, but it is typically kept above 80 K.

sample, two 99.9999% (6N) purity, 1 mm-diameter aluminum wires (Laurand Associates) are used to connect the sample mount and the heat exchanger. The high purity of the aluminum gives it high thermal conductivity and the wires are soft enough to not impede the movement of the nanopostioners [160, 157]. In the past, we have also tried using copper braids and foil as thermal links, but they did not bring meaningful improvements to the sample temperature. The sample mount also contains threaded holes to hold a silicon diode thermometer (Lakeshore DT670-CU) and a piezoelectric chip (Thorlabs PA4FEH3) for exciting the mechanical resonators.

3.2.2 Probe Mount

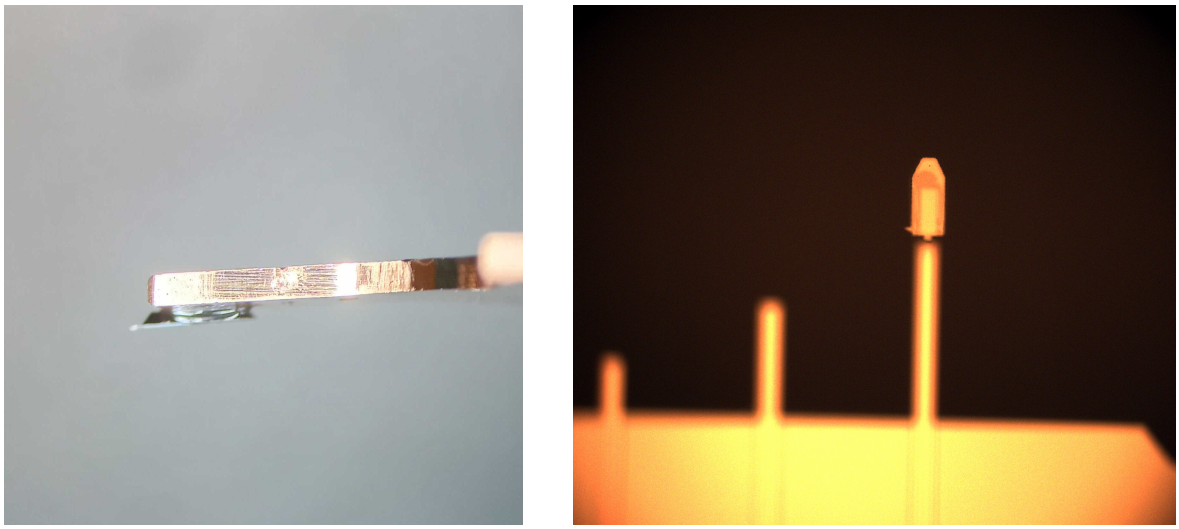
Two types of diamond probes are used in this work. The first type is fabricated by Prof. Amir Yacoby's group and comes with the diamond already glued to a tipless cantilever on a standard atomic force microscopy (AFM) chip [163]. Initially the AFM chip was secured to the probe mount using adhesive (Fig. 3.4). Different adhesives were used, such as Stycast, crystal bond, and GE varnish. However, with every adhesive we tried, the thermal cycles between room and low temperatures eventually caused the AFM chip to fall off from the probe mount. The failure time is unpredictable and ranges from two thermal cycles to more than ten cycles over a year.

The second type of diamond probe is purchased from QZabre [2], which consists of the diamond glued to an Akiyama tuning fork with a PCB [7]. The tuning fork's vibration frequency changes as the diamond nanopillar approaches a surface, which can be used to perform AFM feedback to stabilize the probe-to-sample distance. A new custom mount (part 16 in Fig. 3.1) has been designed to hold these QZabre probes, shown in Fig. 3.5. The main feature is that the PCB is now clamped down with a hand-trimmed SEM clip, which has proven to be robust against thermal cycling (no failures in the past two years). Note that the probe mount is not designed for electrical connections to the PCB, so the probe is operated without AFM feedback using the tuning fork (for tuning fork operation, we have built another room temperature characterization setup, not covered in this thesis).



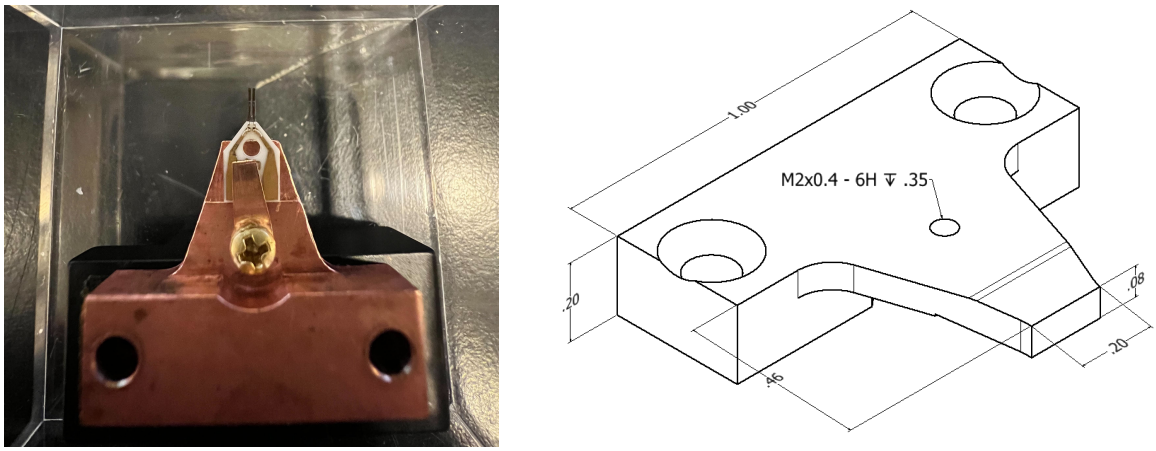
(a) **(b)**

Figure 3.3: Side and top view of the sample mount and cryostat.



(a) **(b)**

Figure 3.4: (a) Close-up view of the AFM chip holding the diamond nanopillar, glued to the custom copper probe mount. (b) Close-up view of the diamond probe glued to a bare cantilever.



(a) **(b)**

Figure 3.5: (a) Photo of a QZabre scanning probe clamped to our custom-made copper probe mount (bottom-up view). Typically we make electrical contact between the SEM clip and the leg of the tuning fork holding the diamond to avoid charge issues. (b) Mechanical drawing (top-down view).

Furthermore, the probe mount is designed such that the tuning fork is at a 10° angle relative to the sample surface, which ensures that the diamond nanopillar is the closest object to the sample.

3.2.3 Electrical Connections

The stack of nanopositioners is controlled with a high-voltage controller (Attocube ANC300) equipped with 3 modules (Attocube ANM300). These modules allow for operating the nanopositioners in both stepping and scanning modes. In the stepping mode, the nanopositioners are excited with a sawtooth voltage signal, which leads to slip-stick motion, allowing each of them to move over a range of 5 mm. This range is sufficient to cover all of the mechanical resonators on a single chip. In the scanning mode, a slow or DC voltage can be applied to the nanopositioners, such that they behave like a simple piezoelectric chip, allowing for smooth displacements over a range of about 3 µm at room temperature. Typically, the stepping mode is used to position a chosen resonator under the diamond probe, and the scanning mode is used to make sub-micron adjustments or for scanning magnetometry

experiments. In particular, care is taken to avoid using the stepping mode in the vertical (Z) direction when the nanopillar is close to the resonator, as each step can excite the resonances of both the tuning fork and experimental setup, with the risk of crashing the probe into the sample. If vertical stepping is necessary with the nanopillar above the sample, a stepping frequency (period of the sawtooth voltage signal) is chosen to minimize these excitations beforehand.

The piezoelectric chip (Fig. 3.3(a)) for exciting the mechanical resonators is controlled by a lock-in amplifier (Zurich Instruments HF2LI), which is also responsible for tasks such as measuring the mechanical motion and triggering other signal generators. Depending on the quality factor, usually a voltage of less than 100 mV is enough to excite the mechanical resonator above the measurement noise floor.

The three thermometers are read out using a temperature controller (Lakeshore Model 336). Just like with the sample chip, care is taken to apply a thin layer of grease to thermalize the thermometers properly with the underlying surface. Furthermore, each thermometer's wires are wrapped around a copper bobbin, the radiation shield (part 7 in Fig. 3.1), or both to reduce thermal leakage from the cryostat exterior to the cold parts. Based on the temperature readings, the controller supplies a varying amount of current to the two heaters in the heat exchanger and aluminum column to maintain their temperature setpoints.

Microwave signals are delivered via two flexible coaxial cables (Lakeshore) terminating in SMP connectors (Amphenol SMP-FR-C06). The cables are soldered to the SMP connectors in lab. One cable delivers amplified microwave signals into the chip, while the other carries the return signal and is typically terminated outside the cryostat with a 50 Ω terminator. Shorting the two cables together and bypassing the chip, we have discovered a loss of about 5 dB from each cable inside the cryostat. In the future, the soldering method should be revisited, or the cable assemblies should be replaced with professionally-made versions to avoid such losses.

To reduce heat load from the room-temperature exterior of the cryostat, where the electrical feedthrough ports are located, all wires going into the sample area are thermally

anchored at least once to the radiation shield. To thermally anchor wires, we either tie them down using dental floss or tape them down using Kapton tape. Tying down loose wires is also important to avoid any unexpected movement when different parts contract during a cooldown, especially when we approach the sample with the diamond nanopillar. Wires are also generally twisted together to maintain mechanical integrity and reduce cross-talk.

3.3 Vacuum system

The interior of the cryostat is kept under high vacuum to eliminate heat load from gas conduction and convection with the cryostat exterior. A turbopump (Pfeiffer HiCube 80) brings the vacuum level down to 10^{-5} – 10^{-6} Torr, which takes between a day and a few, depending on whether the chamber has been recently exposed to air. To reduce outgassing, parts are sonicated in Citranox (or Alconox), acetone, and IPA for 5 min each before being installed in the chamber. O-rings are lightly lubricated with Apiezon L grease to ensure that they are properly seated in their grooves, while KF o-rings are ungreased (a point of contention and a hill I shall perish upon).

After the vacuum has reached $< 10^{-5}$ Torr, the cooldown procedure is initiated. As the temperature inside the chamber decreases, residual gas in the chamber condenses and adsorbs onto the cold surfaces. This phenomenon, known as cryopumping, further reduces the pressure down to 10^{-7} Torr. Note that this pressure is measured using a cold cathode gauge (Pfeiffer PKR 251) attached somewhere between the turbopump and the cryostat, so the pressure inside the cryostat is likely even lower. Typical temperatures and pressure during a cooldown is shown in Fig. 3.2.

Ideally the cryostat should be valved off from the turbopump after it has been fully cooled down, and the vacuum can be maintained with just cryopumping. The rationale is that the pressure inside the cryostat will be likely lower than that at the turbopump, and leaving the two systems connected run the risk of cont aminants from the turbopump getting cryopumped into the cryostat. However, we have discovered a substantial leak of about 1×10^{-5} Torr L/s from the helium line inside the cryostat, which only shows up at

low temperature. As a result, we always keep pumping the cryostat while it is cold.

3.4 Temperature and Helium Flow Control

There are a total of three temperature sensors in the cryostat. The heat exchanger (the coldest part of the cryostat) and the sample mount (part 11 in Fig. 3.1) are monitored with individual silicon diodes (Lakeshore DT670-CU), while the nanopillar mount is monitored with a Cernox sensor (Lakeshore). A feedback loop controls the heat exchanger temperature via the resistive ring heater (part 5). As mentioned earlier, the cryostat base temperature can be as low as 5 K, but to conserve helium and extend operation time, we typically reduce the flow rate and use a proportional-integral (PI) loop to keep the heat exchanger temperature at 13 K. The second feedback loop uses a cartridge heater (50 W, 25 Ω Firerod from Watlow) to maintain the nanopillar mount at a temperature above 80 K, to avoid loss of NV contrast [47]. Without any microwaves sent into the sample, the temperature at the heat exchanger is stable to about ~ 10 K, while the temperatures at the sample mount and nanopillar mount are stable to about ~ 5 K.

To maintain a stable flow rate of liquid helium, we maintain the dewar pressure at about 2 PSI using a regulator at the dewar exhaust port. After going through the cryostat, the helium goes through a mass flow controller, which we use to maintain the flow rate at about 500 SL/h. Additionally, the dewar is placed on top of a weight scale while the cryostat is in operation, which allows us to estimate the amount of helium left inside.

During the cooldown, we have occasionally noticed large swings (up to 50% every few seconds) in the helium flow rate, which also lead to large oscillations in the cryostat temperature and pressure. We attribute these oscillations to impedance mismatch in the helium exhaust path. We are usually able to resolve this issue by closing the needle valve in the transfer line completely, then very slowly reopen it over half a minute or more to "reset" the helium flow.

We have also encountered instability in the flow rate likely due to the recovery system. This results in large swings in the fluorescence counts from the NV center 3.7, as the cryostat

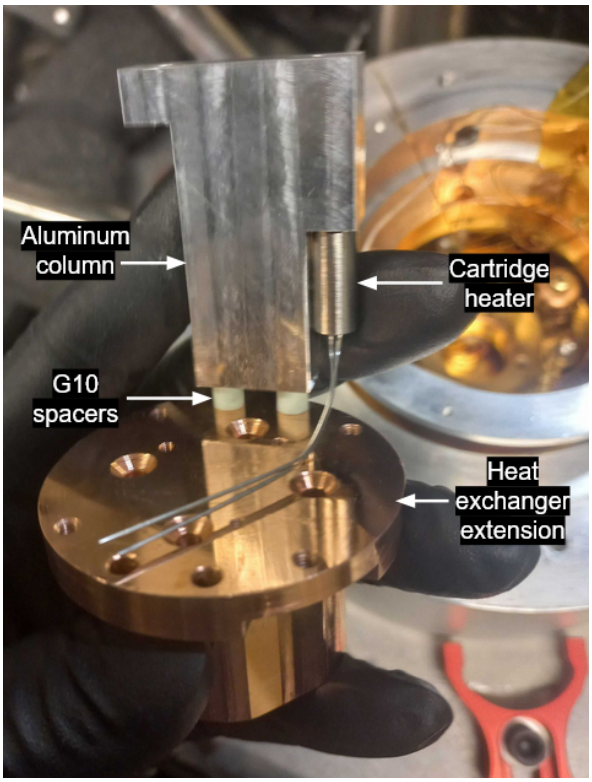


Figure 3.6: Photo of the column with integrated heater (part 14 in Fig. 3.1)). The nanopillar mount (not shown) will be fastened on top of this column. The two G10 spacers thermally isolate the nanopillar (80 K) from the heat exchanger (13 K), reducing unnecessary heat load on the cryostat from having to keep the nanopillar at high temperature. The cartridge heater is secured inside the column using Stycast epoxy. The column is made of aluminum for easy machining; in the future, a different material should be chosen for matching thermal expansion coefficients to maintain a stable NV-magnet distance.

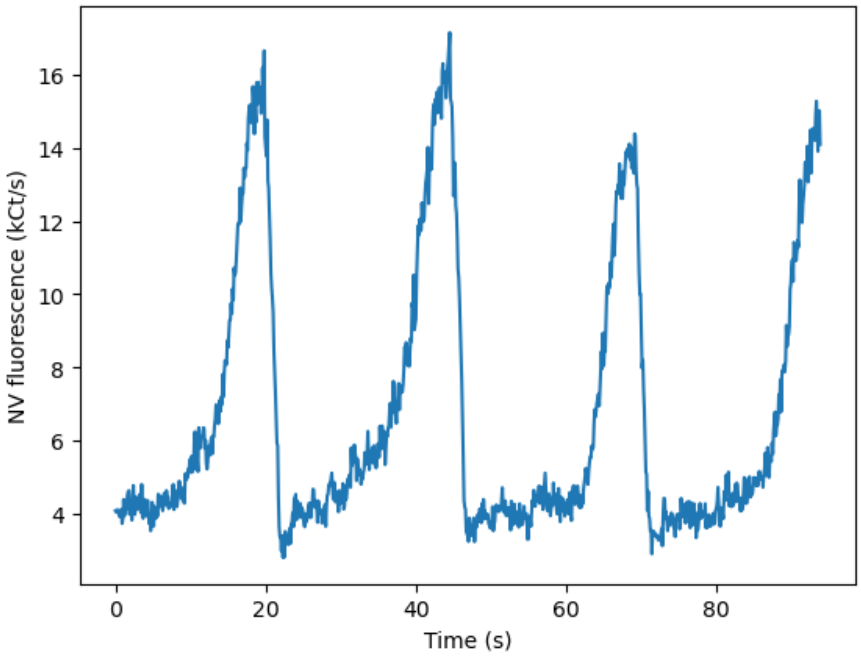


Figure 3.7: Large swings in fluorescence counts from the NV center due to instability in the helium flow. As the helium flow rate changes, the sample moves relative to the optical setup, leading to count fluctuations.

appears to "breathe" in and out visibly even on the camera. These large swings drastically increase the averaging time needed for all NV measurements. This issue (fortunately it does not happen often) is typically resolved by venting the exhaust helium to atmosphere instead of the recovery system.

3.5 Confocal Microscope

A scanning confocal microscope directs different laser beams into the cryostat and allows us to read out the NV center and mechanical motion (Fig. 3.8 and 3.9). For raster scanning, collimated laser beams are deflected with a pair of galvo mirrors (Thorlabs GVSK2), sent through a 4f lens system before entering an objective (100X NIR HR, Mitutoyo) focused onto the NV center or the mechanical resonator. The 4f lens system consists of a pair of 2 in-diameter achromatic lens (Edmund Optics 49-391) which have anti-reflection coatings

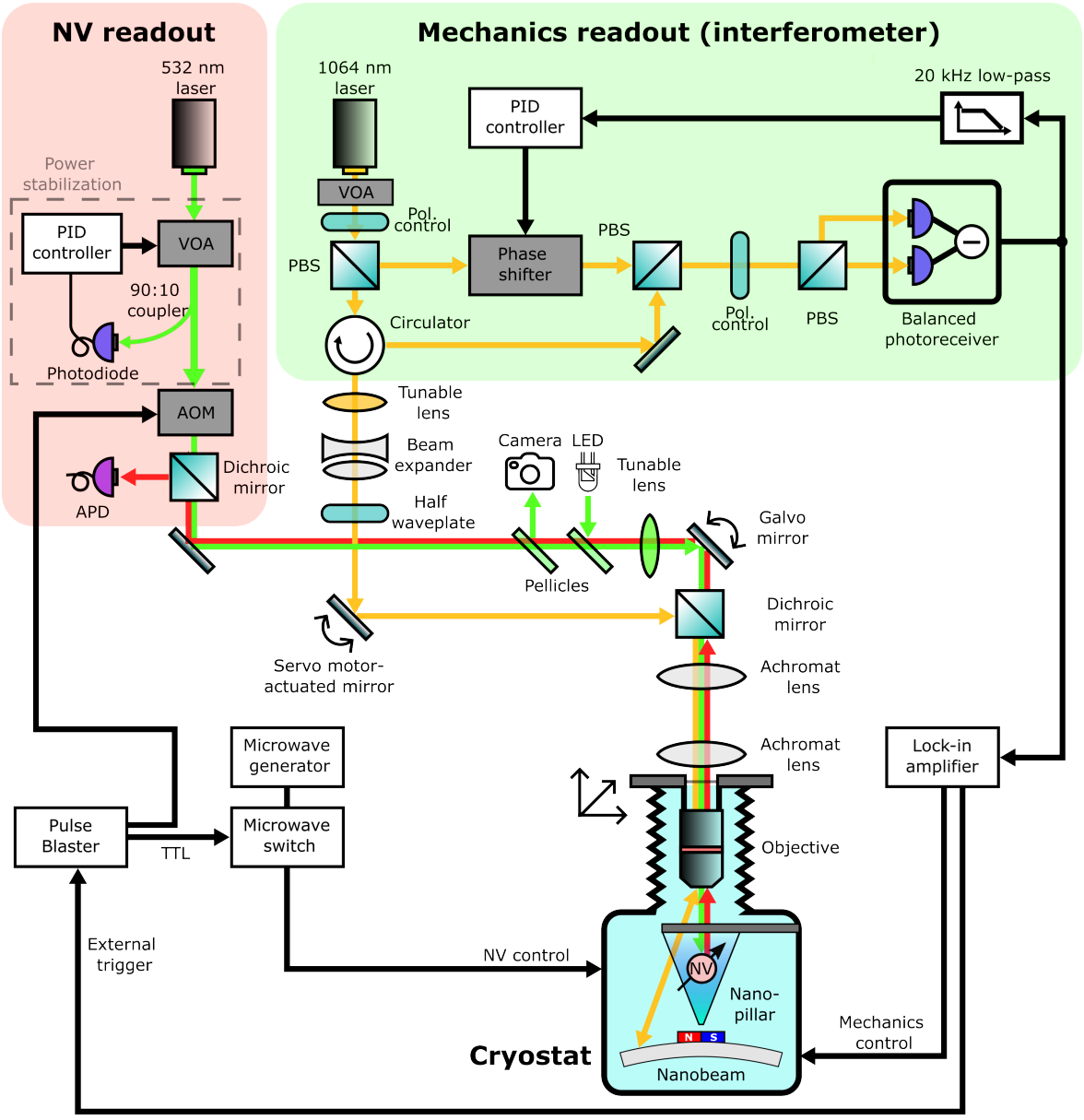


Figure 3.8: Full schematic of the optical setup and microwave connections.

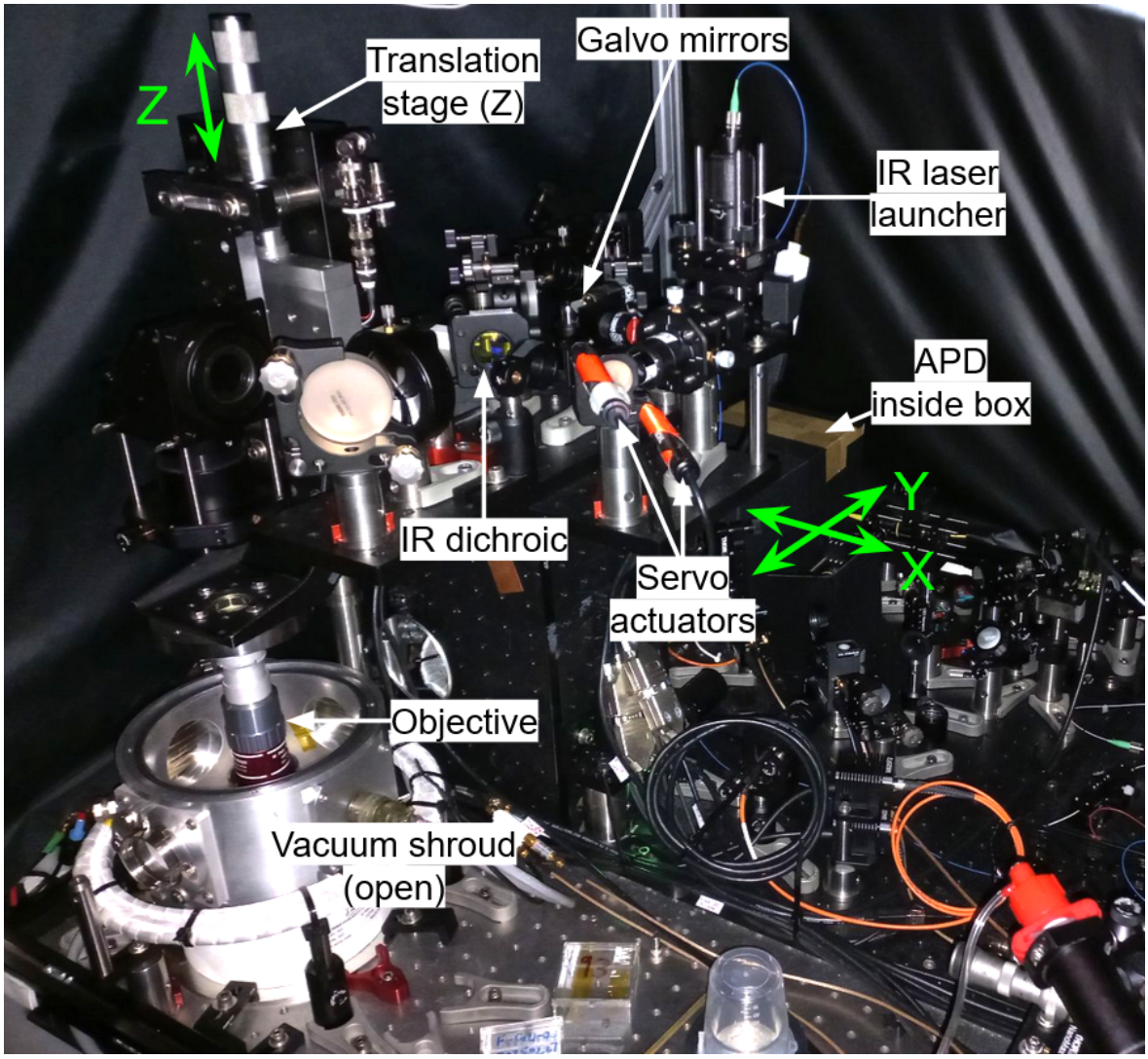


Figure 3.9: Photo of the optics setup. The cryostat vacuum shroud is open for room-temperature characterization measurements. The entire confocal microscope consists of two levels. The bottom level contains components such as the APD and fiber launchers for the green laser and fluorescence collection, while the top level contains components such as the galvo mirrors, servo motor-actuated mirror, and fiber launcher for the IR laser. The top level can be moved in three axes using large translation stages. The Z-axis translation stage is shown, while the stages for the other two axes (green arrows) are hidden. To ensure that the microscope stays aligned during translations, the stages are arranged such that the translation axes are always parallel to the light path.

for wavelengths between 400 to 1000 nm. The first lens is located at one focal length (1f) from the galvo mirrors and the second is located at two focal lengths from the first. This configuration ensures that the light coming out of the second lens is collimated before entering the objective placed another 1f away. The 4f system also ensures that there is a $1:1$ mapping between the galvo mirror deflection angle and the angle of the laser beam entering the galvo scan.

The objective is coated for a wavelength range of 480 – 1800 nm. Importantly, it is designed such that the focus does not change appreciably over this range. This is crucial for performing simultaneous measurements of the NV center and the mechanical resonator, which require both the green and infrared lasers being focused at roughly the same focal plane. Moreover, the objective has a very generous working distance of 1 cm, which loosens the design requirements of the probe holder and decreases the risk of crashing the objective into the diamond nanopillar.

The diamond nanopillar is fixed relative to the cryostat. To locate the nanopillar and NV center, we cannot move the nanopillar around and have to adjust the confocal microscope instead. The galvo mirrors give a limited scan range of less than 100 µm in each lateral direction in the sample plane, so we physically move parts of the confocal microscope using a set of 3 translation stages (Newport UMR12.63). The objective is kept under vacuum to avoid any aberrations from vacuum viewports. To be able to move the objective, we designed the cryostat such that the objective is housed inside a vacuum bellows attached to a translation stage via an L-bracket. To avoid breaking the vacuum, care must be taken not to move the confocal microscope too much in any of the 3 directions. This configuration gives us a total range of about 1 cm in each direction, which is sufficient to find any feature on a 1 cm^2 sample chip.

In what follows, we describe how the confocal microscope allows us to address both the NV center and the mechanical resonator.

3.5.1 Optical Path for NV Measurements

A green (532 nm) laser (Edmund Optics 19-486) is used to excite the NV center for both initialization and readout of its spin state. The laser beam is first coupled into a single-mode fiber, sent through a laser power stabilization circuit and an acousto-optic modulator (AOM) (G&H Fiber-Q) before being launched into free space on the optics table. The AOM has a bandwidth of 200 MHz with a rise time of 25 ns. By sending TTL pulses to a homebuilt AOM driver, we are able to create short laser pulses.

Inside the power stabilization circuit, the laser light goes through a variable optical attenuator (Thorlabs V450F) before entering a 90:10 fiber coupler. The optical power in the tap output is measured with a photodiode. A PID controller (Moku:Go, Liquid Instruments) adjusts the attenuation of the optical attenuator so that the photodiode output matches a user-defined setpoint. The laser power is adjusted by either changing the setpoint of the stabilization circuit, or using a filter wheel containing multiple neutral-density filters on the optics table. For most NV measurements, the laser power measured at the back aperture of the objective is about 50 – 100 µW.

Light from the sample or NV center travel back along the same path as the green laser until it is diverted to an avalanche photodetector (APD) by a dichroic mirror (Semrock FF560-FDi01). To collect only fluorescence from the NV center, we add a long-pass filter before the APD. For "reflection" scans, which are useful to locate which part of the sample we are looking at, the long-pass filter is omitted.

The focus of the green laser is adjusted using two methods. The first one relies on a 150 V co-fired piezoelectric actuator (Thorlabs) attached to the Z-axis translation stage holding the objective, which allows us to adjust the focus by about 15 µm. The second one relies on a electric tunable lens (ETL) (EL-10-30-TC-VIS-12D) placed immediately before the galvo mirrors. While the piezo changes the focus of the other laser beams going through the objective, the ETL allows for independent control over the focus of the green laser.

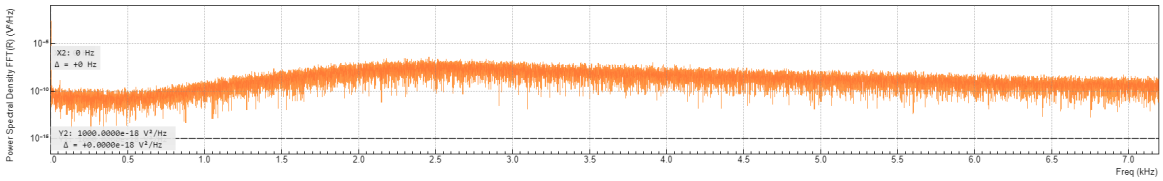


Figure 3.10: Fourier transform of the drive current for one of the galvo mirrors, showing a broad peak around 2 kHz. A similar peak shows up in the Fourier transform of the reflected light intensity.

3.5.2 Optical Path for the Interferometer

An infrared (1064 nm) laser (Koheras BASIK) is used for interferometer measurements of the mechanical resonator. The interferometer follows a homodyne Mach-Zehnder configuration. Light in the signal arm goes through a fiber circulator (Thorlabs CIR1064PM-APC) and gets launched onto the optics table. Afterwards, it follows a similar configuration as the green laser path. It first encounters a mirror actuated with a pair of servo motors (Thorlabs Z906), which serves the same role as the galvo mirrors in the green laser path. After this scanning mirror, the IR light enters the 4f lens system and joins the green laser path via a dichroic mirror. The servo motor-actuated mirrors are chosen over another galvo scanner because we have found that the latter suffers from oscillations at ~ 2 kHz due to its internal feedback circuit (Fig. 3.10).

To turn on and off the IR laser, we toggle a control voltage signal for a VOA inserted before the interferometer. As in the case of the green laser path, to control the focal plane of the IR laser, an ETL is added right before the servo motor-actuated mirror. To optimize the coupling of the reflected light into the optical fiber, a beam expander/condenser consisting of two lenses is used to adjust the beam waist immediately after the ETL. Given that the width of the nanobeam is only 1 µm, comparable to the laser wavelength, a half-waveplate is also inserted after the ETL to rotate the polarization of the laser light to align it to the nanobeam and maximize the reflected power.

The reflected light from the mechanical resonator travels back along the same path into the optical circulator and back into the signal arm of the interferometer, where it is interfered

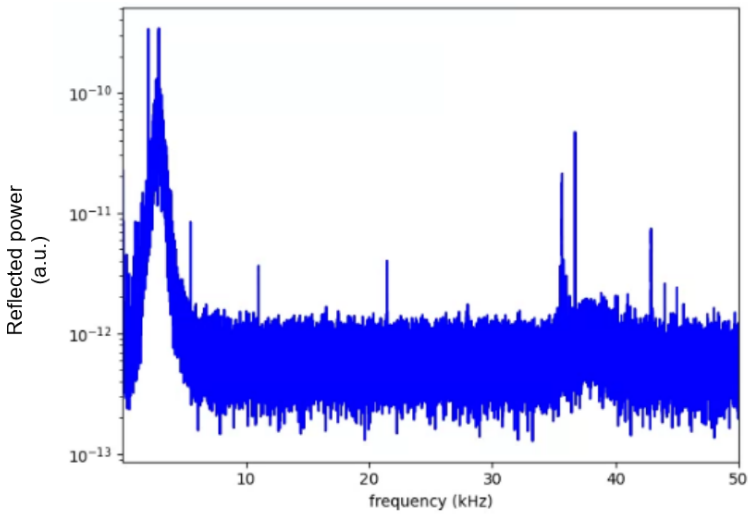


Figure 3.11: Fourier transform of the intensity of IR light reflected off a sample. This was measured on an interferometer in a different experiment also using a galvo scanner, and it shows a similar peak around 2 kHz.

with the reference arm and then measured using a balanced photoreceiver (Newport 2117-FC). Finally, the unfiltered voltage signal from the photoreceiver is sent to a lock-in amplifier, which allows us to detect any small voltage oscillations at the mechanical frequency. To compensate for slow drift in the length of the interferometer arms, the photoreceiver signal is branched off, sent through a 20 kHz low-pass filter, and the resulting voltage is used as part of a feedback loop to control a fiber phase shifter (FPS-001-10-90, Luna) in the reference arm.

3.6 Microwave Electronics

Microwave signals are required to manipulate the NV center's spin states. The configuration of microwave electronics has evolved over the time during which the work in this thesis was performed. In general, microwave signals are generated by a signal generator (SRS SG384). To generate microwave pulses, the microwave signals are gated by a high-speed microwave switch (Mini-Circuits ZASWA-2-50DRA+) with a switching time of 20 ns, and then gets amplified by 45 dB (Mini-Circuits ZHL-16W-43-S+). To avoid reflections damaging

the amplifier, the amplified signal goes through a circulator, before entering the cryostat via an SMA feedthrough. In general, we can achieve Rabi frequencies up to 10 MHz, with about 20 dBm of microwave power going into the cryostat.

3.7 Pulse Timing

As mentioned earlier, a switch is used to gate microwave signals to generate pulses as short as 10 ns. The switch is controlled with TTL signals, which are generated by a 21-channel pulse generator (SpinCore PulseBlasterESR-PRO 500 MHz). The PulseBlaster allows programming of loops (max $\sim$ 1 million iterations), subroutines, and external triggering. Apart from generating TTL signals for microwave switches, the PulseBlaster is also used for triggering other devices such as AOMs, data acquisition modules, and other function generators, and is indispensable for combining multiple instruments for pulse sequences.

3.8 External Bias Field

In most of our measurements, we rely on the micromagnet's magnetic field to lift the degeneracy of the $m_s = \pm 1$ spin levels. However, an external bias magnetic field is still useful because its known orientation lets us obtain information about the NV center's orientation. Furthermore, it can also be used to cancel off-axis fields from the micromagnet, and as shown in Sec. 4.5, can be used to modulate the spin-induced mechanical signal.

Two bias field sources are used. The first one is a permanent neodymium magnet (1.25 in diameter, 0.5 in). An extension "pocket" (part 12 in Fig. 3.1) for the cryostat vacuum shroud was designed such that the magnet can be brought within $\sim$ 4 cm of the NV center (giving an on-axis field of $\sim$ 200 G) while remaining in atmosphere for easy adjustments (Fig. 3.12).

The second bias field source is a pair of current-carring coils stacked together such that the current is flowing in the same direction. The resistance of this combined coil is $\sim 2.6\,\Omega$. Using a home-built current driver, we are able to send in a maximum current of 3.7 A, which generates a bias field of 23 G along the axis of the NV center used in Fig. 3.13b.

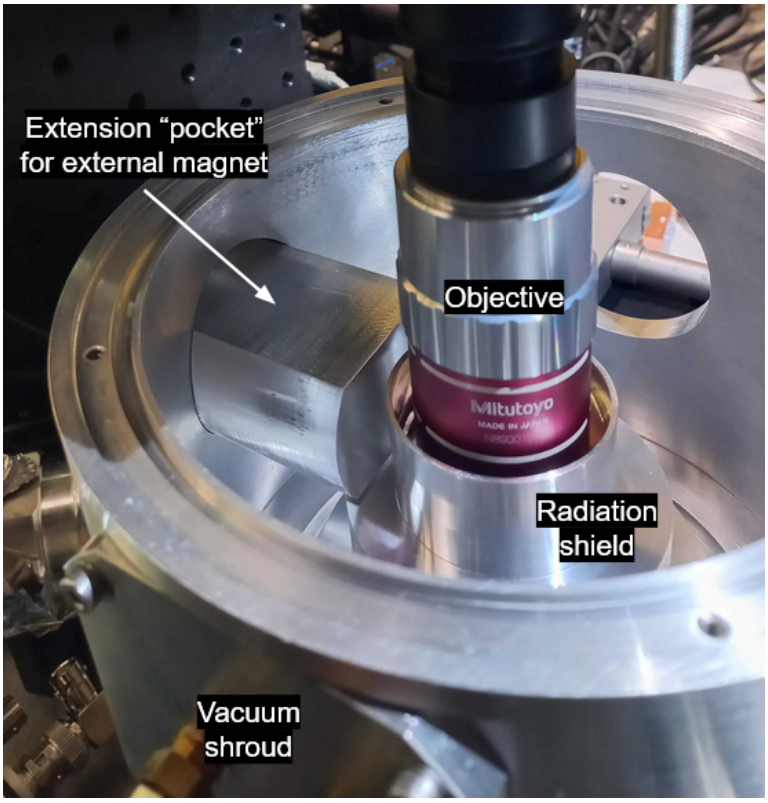
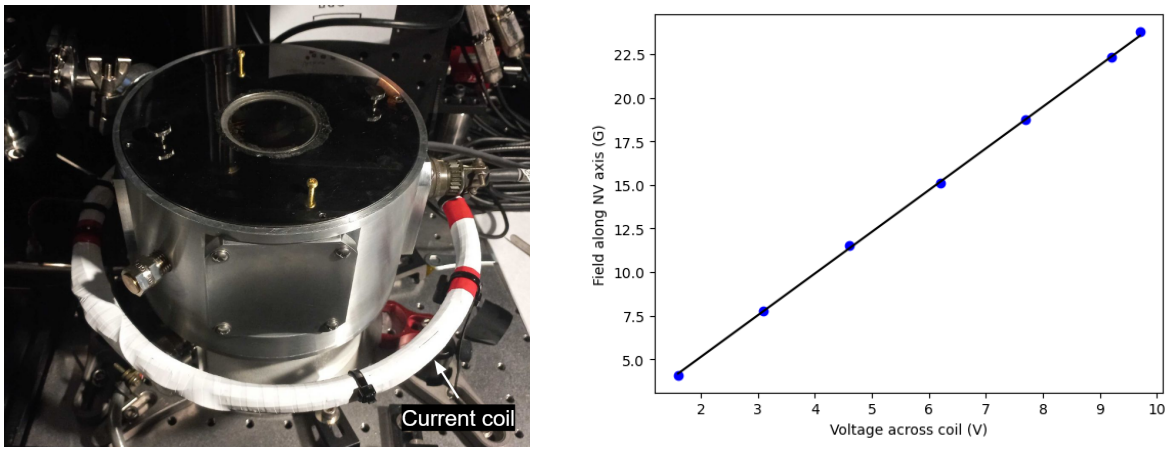


Figure 3.12: Inward extension for the cryostat vacuum shroud. The bias field magnet can be fitted inside and stay close to the NV center while remaining in atmosphere, allowing for easy adjustments.



(a) **(b)**

Figure 3.13: (a) Current-carrying coil for generating a tunable bias magnetic field. (b) Characterization of the current coil. A maximum of 23 G, or an ESR shift of 64 MHz, can be applied to the NV center. The current through the coil can be calculated by dividing the voltage by the resistance of 2.6 Ω.

3.9 Laboratory Environment

The cryostat and the optical setup are located on the same optics table. It is important to avoid vibrations and temperature fluctuations, which can introduce classical measurement noise and drift. To reduce vibrations, the table floats on pneumatic supports, which are pressurized with air from the building supply. However, for sensitive measurements, we switch the air supply to an isolated cylinder (Airgas), which appears to lead to slightly less vibrations.

To avoid temperature fluctuations, we have built an enclosure above the optics table. The frame was built using a combination of 25 mm and 1 in T-slotted rails (Thorlabs and McMaster Carr), Initially, to isolate the optics from the external temperature fluctuations, the walls of the enclosure were chosen to be 1 in-thick polystyrene panels (McMaster 9255K1). While this provided good thermal isolation, it turns out (after an exhausting search) that the large surface area of the panels mean that they readily pick up external vibrations, which then excite the resonances of the optical setup (Fig. 3.15. After this discovery, we replaced the panels with nylon fabric (Thorlabs BK5), which decreased the vibrations noticeably.

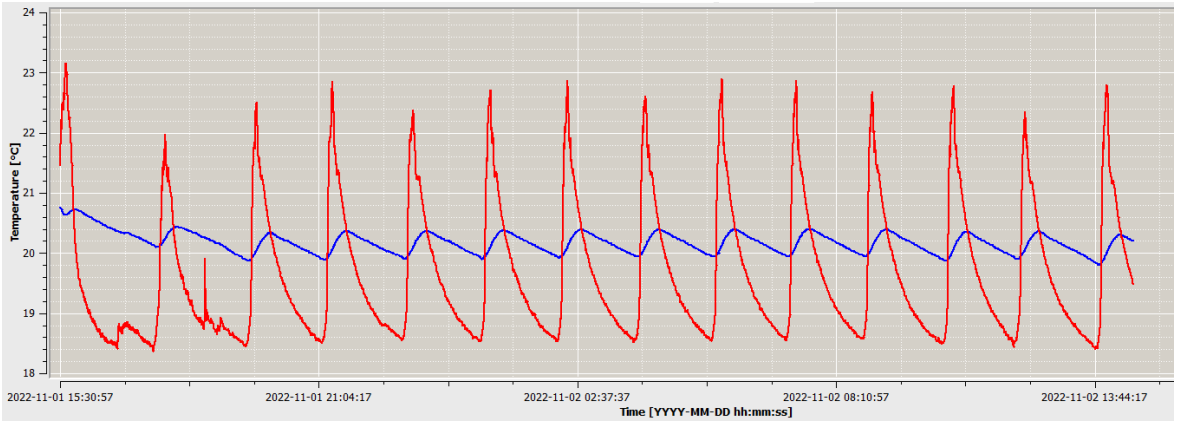


Figure 3.14: An example of huge swings ($> 3\,^{\circ}\mathrm{C}$) in the lab temperature, which make NV and mechanics measurements virtually impossible. The temperature in the lab and inside the enclosure are plotted in red and blue respectively.

Unfortunately, the thermal isolation from the enclosure is not enough to insulate the setup from the occasional large temperature fluctuations from the building's ventilation system. These large fluctuations tend to happen during seasonal transitions, when the building changes the method of heating or cooling, leading to large changes in the cooling/heating power and destabilizing the PID loop. A particularly egregious example is shown in Fig. 3.14, where the $3\,^{\circ}\mathrm{C}$ swing in lab temperature is enough to make the laser spot drift off the NV center in a matter of minutes. We have found some success in reducing the occurrences of these large instabilities by disabling the PID loop altogether.

Care must also be taken to isolate all possible sources of vibration. In particular, confirmed sources of vibrations are the fans of the microwave amplifier, the walls of the lab, and the turbopump. As a result, all amplifiers and power supplies are moved off the shelves to the floor, and we avoid any direct physical connections between the table and the wall. To avoid air currents, the air vent above the optics table is blocked with fabric. All cables are tied down with strain relief, and optical fibers are taped down to the walls or table. The vacuum bellows connecting the turbopump and the cryostat is also routed through a large bucket containing 200 lbs of sand, and the turbopump is placed on a sorbothane mat.

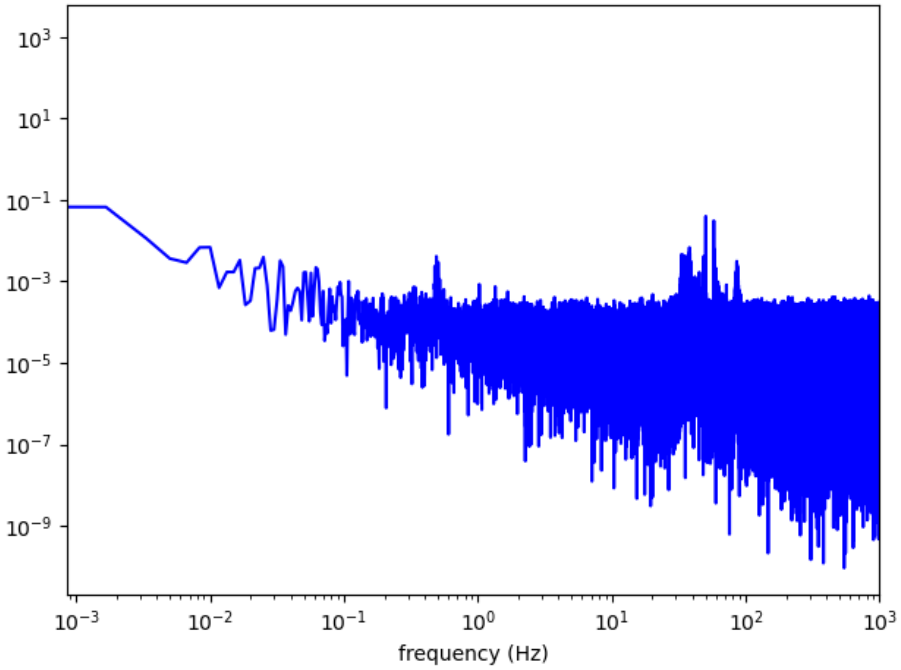


Figure 3.15: Taking the Fourier transform of the fluorescence counts from the NV center, we see some noise peaks at $\sim 30\,\text{Hz}$, which we attribute to the natural resonances of the optical setup. Depending on the lab conditions, the area under these vibration peaks can lead to classical measurement noise on the same order as shot noise. These peaks were greatly reduced after replacing the polystyrene panels with fabric.



(a) **(b)**

Figure 3.16: (a) Original enclosure with walls made of polystyrene panels, which turned out to be sensitive to external disturbances. (b) Current enclosure with the polystyrene panels replaced with blackout fabric.

Chapter 4

Scanning Probe Magnetometry Measurements for Gradient Characterization

4.1 Introduction

In essence, a scanning probe microscope consists of a tip that scans over a sample, and an image is created based on the spatially-varying interaction between the tip and the sample. The field of scanning probe microscopy (SPM) is well-established and has enabled many scientific advances. For example, scanning tunneling microscopy (STM) measures the tunneling current between a sharp conductive tip and the underlying conductive sample. Because of the high-sensitivity of the tunneling current to the tip-sample distance, it allows imaging of materials with an unprecedented resolution – down to single atoms. STM also allows researchers to drag and rearrange individual atoms, offering the intriguing possibility of building "perfect" nanostructures atom by atom [33]. For inventing STM, Gerd Binnig and Heinrich Rohrer were awarded the Nobel Prize in Physics in 1986 [27].

Another well-established subfield of SPM is atomic force microscopy (AFM), which measures the repulsive/attractive forces between the scanning tip and sample. The scanning

tip is typically a cantilever, and its frequency shifts based on the tip-sample interaction. Using a feedback system to maintain this frequency shift by adjusting the tip-sample distance, one can image the sample's topology, sometimes down to atomic-scale resolution [103]. AFM has the added advantage that it does not require a conductive sample or even a vacuum environment, which makes it an indispensable tool in biology [109, 59, 98]. Furthermore, the AFM tip can be functionalized for measurements of different forces, such as electrostatic and magnetic forces [69].

A more recent development is scanning probe magnetometry using NV centers. A tip containing single or multiple NV centers is used as the scanning tip, and the magnetic field can be detected via fluorescence measurements of the NV center(s). For sample-tip distance feedback, the diamond tip is mounted on either a conventional AFM tip or a tuning fork, and the vibration frequency is measured either optically or electrically. Just like AFM, scanning NV magnetometry can be performed under ambient conditions, though it is also possible in UHV and at temperatures as low as 350 mK [131, 130]. For static fields, the sensitivity is on the order of a few $\mu T/\sqrt{Hz}$; for AC fields, the sensitivity is higher, on the order of 50 nT [75]. Depending on the NV-sample distance, spatial resolutions of less than 100 nm are possible [75].

Early demonstrations used probes consisting of a diamond nanocrystal glued to an AFM tip [15, 40, 123, 146]. However, this approach suffers drawbacks such as the short coherence times and low light collection efficiency of NV centers inside nanocrystals, both of which limit the magnetic sensitivity. These problems were greatly reduced with the fabrication of diamond nanopillars [10] which contain single NV centers near the apex. The nanopillar acts as a waveguide for emitted photons from the NV center, enabling significantly higher light collection efficiencies, with fluorescence counts exceeding 1×10^6 kCt/s [70, 93]. Furthermore, NV centers in nanopillars have longer coherence times compared to those in nanocrystals and can be fabricated in large batches with predictable properties. Such is the success of diamond nanopillars for scanning magnetometry that they have been the basis of two commercial spinoffs, namely QZabre and Qnami [3, 2].

In this chapter, we will discuss some of the scanning magnetometry measurements performed on the new experimental platform described in 3. These measurements allow us to characterize and diagnose issues with the micromagnets, such as demagnetization from the laser and surface oxidation. Importantly, they also allow us to maximize parameters such as the spin-mechanical coupling and field alignment to the NV center's quantization axis. We will also discuss efforts to increase the measurement efficiency of such experiments.

4.2 Magnetic Field Scans

To characterize the field distribution around the micromagnet, one can scan the diamond probe in a rectangular grid over it and measure the electron spin resonance (ESR) at each point. The ESR measurement can be done via CW or pulsed ODMR. The ESR frequencies give vector information of the field distribution, for it not only gives the magnetic field magnitude along the NV center's quantization axis, but also the magnitude of the off-axis component. Example scans of a spherical neodymium micromagnet and a rectangular iron micromagnet are shown in Fig. 4.1 and Fig. 4.2. Note that for this chapter, unless otherwise specified, the micromagnet is a neodymium alloy microsphere.

For a uniformly magnetized spherical micromagnet, the field distribution is described by a dipole model:

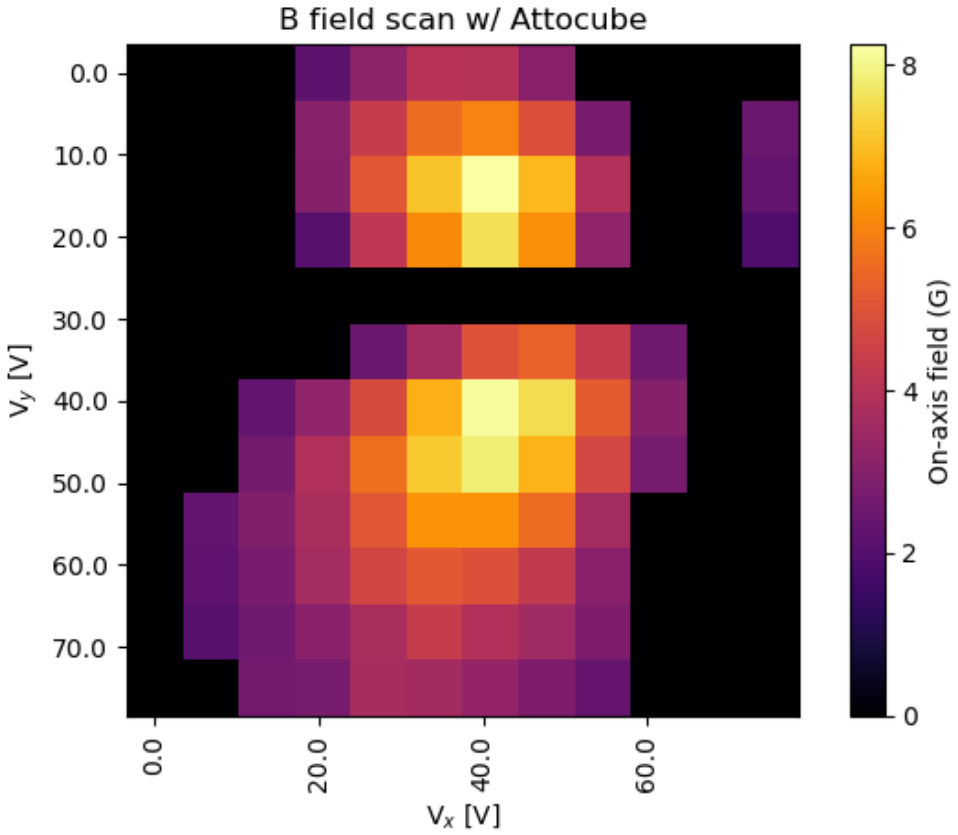
$$\vec{B}(\vec{r}) = \frac{\mu_0}{4\pi}\left(\frac{3\vec{r}(\vec{m}\cdot\vec{r})}{r^5} - \frac{\vec{m}}{r^3}\right) \tag{4.1}$$

where μ_0 is the vacuum magnetic permeability, and $\vec{m}$ is the magnetic moment, given by:

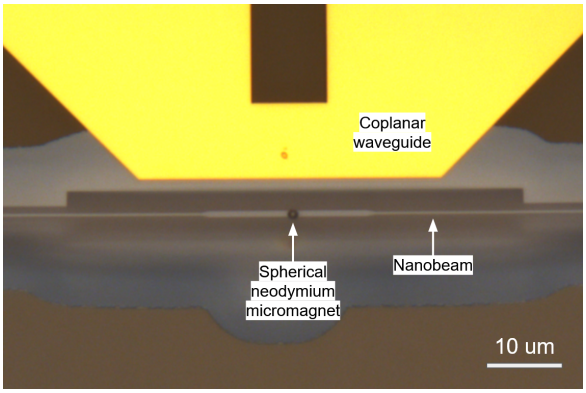
$$\frac{B_0}{\mu_0}\frac{4}{3}\pi a^3 \tag{4.2}$$

for a sphere with radius a and magnetic remanence B_0. The spherical micromagnets used in this work are made of an NdFeB alloy with an expected remanence of $B_0 = 0.7\,\mathrm{T}$, and typically have a diameter of $\sim 1\,\mu\mathrm{m}$.

With the fitting parameters, it is straightforward to differentiate Eq. 4.1 and calculate the magnetic field gradient distribution, as shown in Fig. 4.1(b). In the shown plot, the

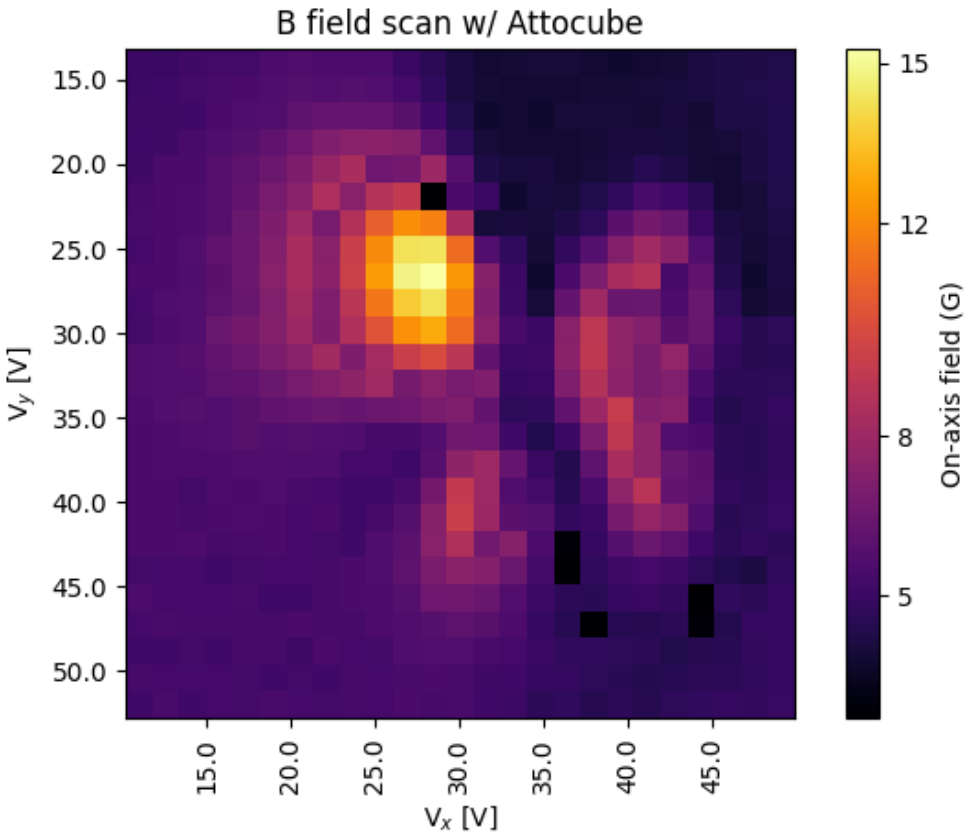


(a)

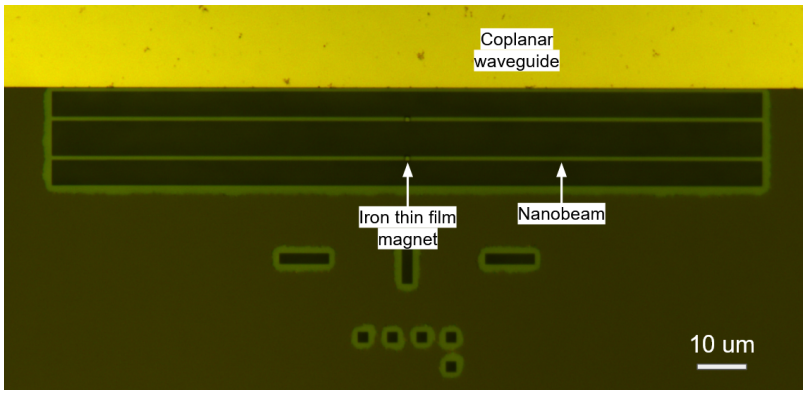


(b)

Figure 4.1: (a) Magnetic field scan of a neodymium spherical micromagnet. The dipole field distribution can be clearly seen. (b) Photo of the nanobeam and micromagnet, taken with an optical microscope. This particular sample was overetched in the release process for the nanobeam, which occurred before the micromagnet placement.



(a)



(b)

Figure 4.2: (a) Magnetic field scan of a square iron micromagnet. The four corners of the magnet show up as high field regions. (b) Photo of the nanobeam and micromagnet, taken with an optical microscope.

maximum gradient is around 1.5×10^4 T/m, corresponding to an expected spin-mechanical coupling strength of 5 Hz.

Fig. 4.1 is one of the first field scans in this work. It contains 15×15 pixels and took about 5.5 h to complete. Since then, numerous improvements have been made to reduce the measurement time. A major improvement was obtained by simply reducing the frequency scan range of each ESR measurement and recentering the scan range at the ESR frequency of the adjacent pixel. Other improvements include software upgrades to reduce the overhead time from reading the fluorescence counts from the data acquisition modules. As a result of these improvements, the scan in Fig. 4.2, which contains 25×25 pixels, took only 1.5 h to complete, representing a speedup of $\sim 10\times$.

With the reductions in measurement time, we can take multiple field scans in a reasonable amount of time. For example, Fig. 4.3 shows two back-to-back field scans (left two plots) taken at different NV-sample separations. By taking the difference between the two scans, we can obtain the field gradient directly (rightmost plot). This is useful for non-spherical micromagnets, for which the magnetic field gradients cannot be calculated by fitting the field scans to a dipole model. From these scans on micromagnets with various shapes, we have also noticed that the point of maximum gradient usually coincides with the point of maximum field within about 100 nm. This knowledge greatly reduces the amount of time spent locating the point of maximum gradient.

4.3 Magnetic Iso-field Scans

The above method of magnetic field scans provides information about the field along the NV center's axis at each point in the scan grid. However, the method is also time-consuming. In some scenarios, such as during the initial approach of the nanopillar towards the micromagnet, we are only interested in the approximate location of the micromagnet and qualitative information about the field distribution. Considering the limited run-time of the flow cryostat, it is desirable to use a faster method for magnetic field imaging whenever possible.

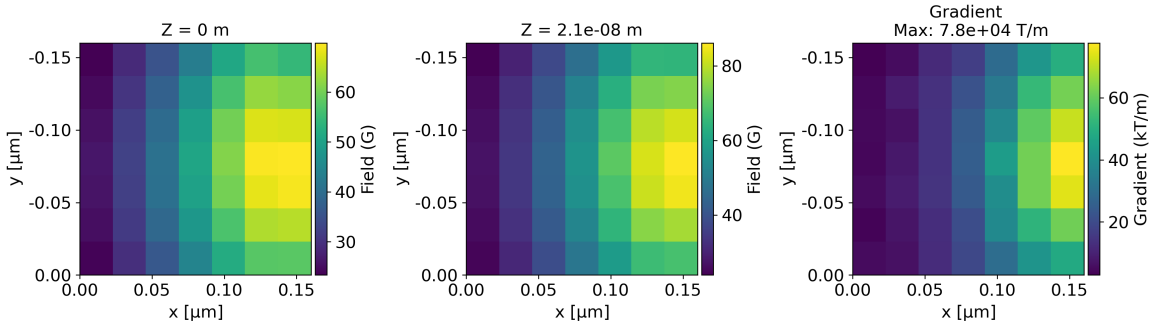
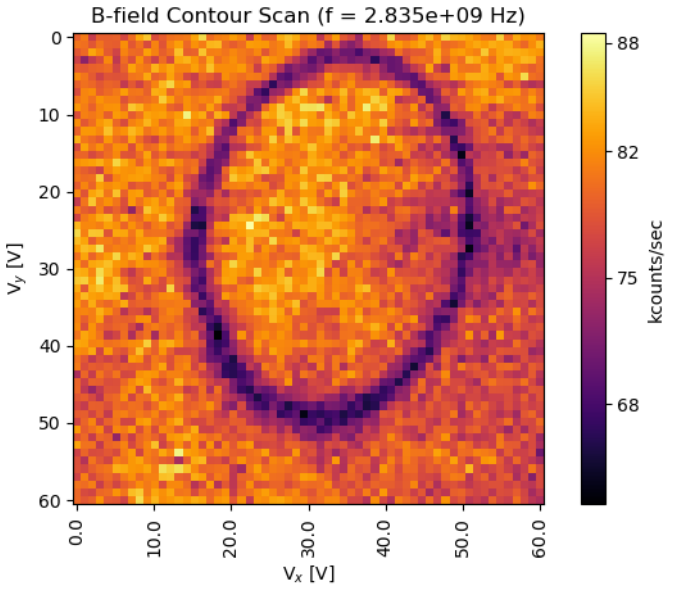


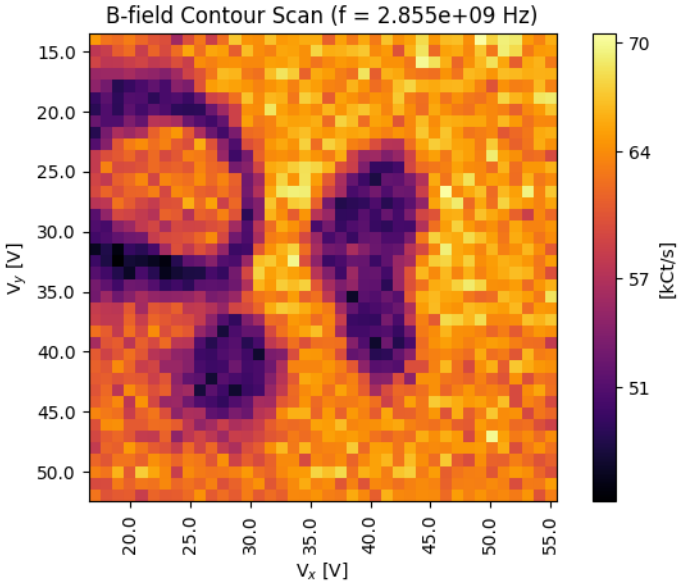
Figure 4.3: Direct gradient measurement. The left plot shows a field scan with the sample at $Z = 0$ nm. In the middle plot, we raise the sample to $Z = 210$ nm using the nanopoistioners, thus bringing the micromagnet closer to the NV center. In the right plot, we take the difference between the left and middle plots and divide by the sample displacement of 210 nm to obtain the magnetic field gradient distribution. We see that the point of maximum gradient matches quite well with the point of maximum field.

An alternative method is to perform magnetic field contour scans, or "iso-field scans" as known in literature. Instead of sweeping the microwave frequency to find the ESR at each point, the microwave frequency is kept fixed throughout the entire scan. As the NV center is scanned over the sample, the ESR frequency will change due to the spatially varying magnetic field. At certain points, however, the ESR frequency will coincide with the applied microwave frequency, resulting in a decrease in the NV center's fluorescence. These points form a contour along which the magnetic field along the NV center's quantization axis is constant (assuming small off-axis fields), i.e. an iso-field contour. Because of Gauss's law for magnetism ($\vec{\nabla} \cdot \vec{B} = 0$), these magnetic field contours are always closed. An example contour scan is shown in Fig.4.4.

Just like for the magnetic field scans in the previous section, contour scans can be performed in CW or pulsed mode. In CW mode, the microwaves and laser are kept on while the NV center's fluorescence is monitored throughout the scan. In pulsed mode, a π pulse followed by a laser pulse for readout is repeatedly applied on the NV center. For most of the work in this thesis, the contour scans were performed in pulsed mode to reduce the microwave and laser duty cycle, which reduces sample heating and minimizes the risk of demagnetization from the laser.



(a)



(b)

Figure 4.4: (a) A typical contour scan of a neodymium micromagnet. Since the micromagnet is spherical, the contour usually takes on an ovular shape. In this scan, the microwave frequency is fixed at 2.835 GHz, corresponding to a magnetic field along the NV center's axis of 13 G. (b) Contour scan of the same square iron micromagnet in Fig. 4.2, taken at the same NV-magnet separation.

Material	Magnetic remanence (T)
NdFeB	0.7–1.5 [68]
SmCo	0.8–1.0 [66]
PrFeB	0.95 [58]
NiFe	0.15 [143]

Table 4.1: List of magnetic materials and their respective remanences.

4.4 Investigation of Low Remanence of Neodymium Micromagnets

Maximizing the field from the micromagnet is key to maximizing the magnetic field gradient and spin-mechanical coupling. To do this, a common approach in the field of magnetic resonance force microscopy (MRFM) is to choose a micromagnet material with a high saturation magnetization, and apply an external magnetic field to saturate the magnetization [86]. Given that our current experimental setup does not allow for such large external fields ($> 1\,\mathrm{T}$), we choose a magnetic material that has a high magnetic remanence instead. A list of magnetic materials and their magnetic remanences is given in Table 4.1.

Neodymium alloy is initially chosen for this work because of its high remanence and commercial availability. It also commonly comes in the form of microspheres, which makes for straightforward modeling with a dipole model. However, we have found from parameter fitting that the magnetic remanence is consistently much lower than the vendor specification. Example field scans of micromagnets placed on nanobeams are shown in Fig. 4.5 and 4.6. To improve the accuracy of the fitting, multiple field scans at different NV-micromagnet separations are fitted with the same parameters (global fitting). The step size in z between each scan is a fixed parameter (from calibration of the nanopositioner's displacement), but the offset is obtained from fitting. From the dipole fitting, while parameters such as the NV center orientation and magnet location are consistent with expectations, we find that the remanences are typically only $< 0.3\,\mathrm{T}$.

The measurements in Fig. 4.5 and 4.6 were performed at room temperature in air, so it is unlikely that the magnet was demagnetized by heating from the green laser used for initialization and readout of the NV center, a problem we have seen in vacuum in

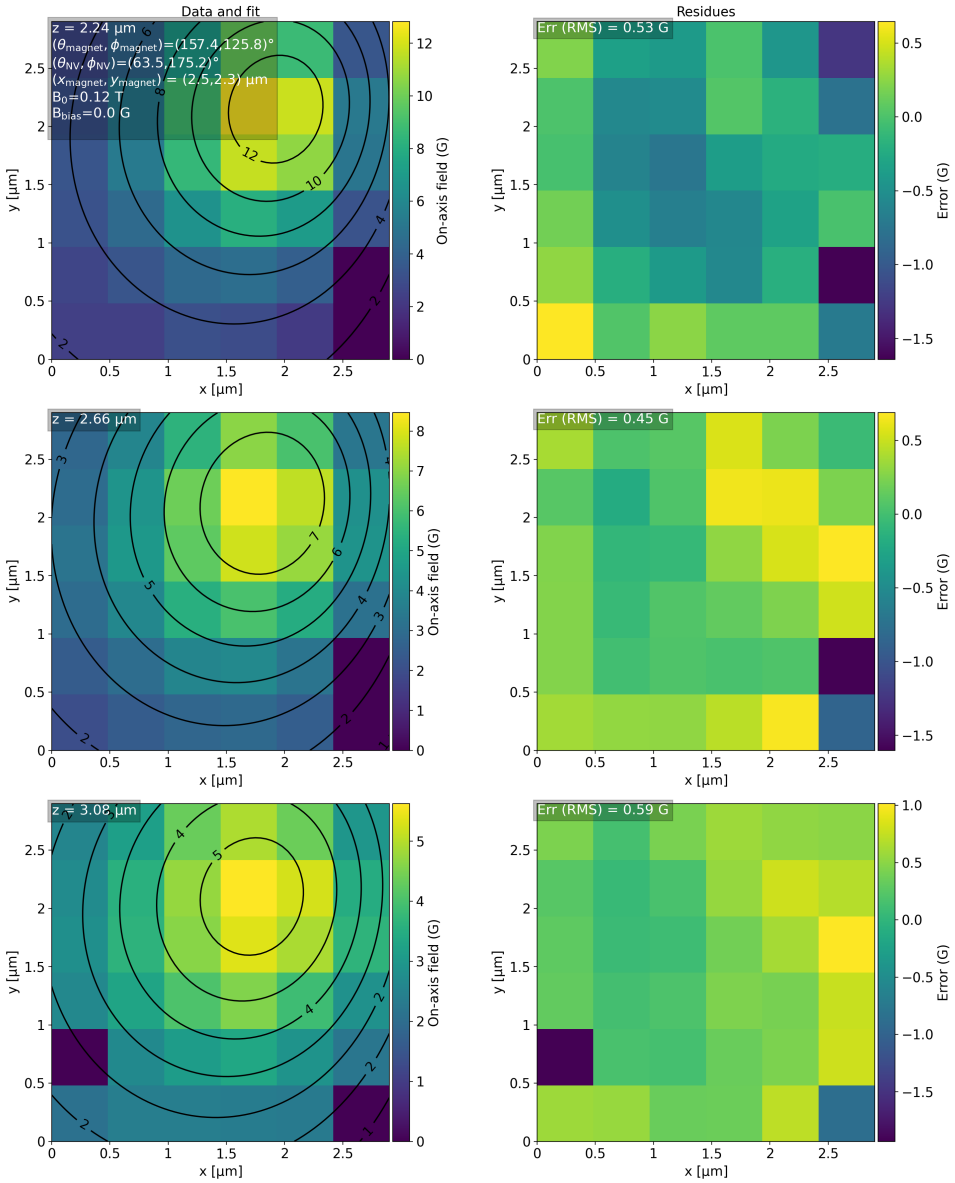


Figure 4.5: Left: field scans of a micromagnet (1.3 μm diameter) on a nanobeam, with each scan taken at a different NV-micromagnet separation z. The fitting parameters are shown on the upper left of the plot, θ_{magnet} and ϕ_{magnet} being the azimuthal and polar angles of the micromagnet's magnetization orientation (with the Z axis pointing out of the page), x_{magnet} and y_{magnet} being the lateral position of the micromagnet's center, B_0 being the remanent magnetization, and B_{bias} being the background bias field. The fitting parameters are obtained by fitting all three scans together (global fitting). The step size in z between each scan is a fixed parameter (from calibration of the nanopositioner's displacement), but the offset is obtained from fitting. Right: residuals, i.e. the difference between the fit and data.

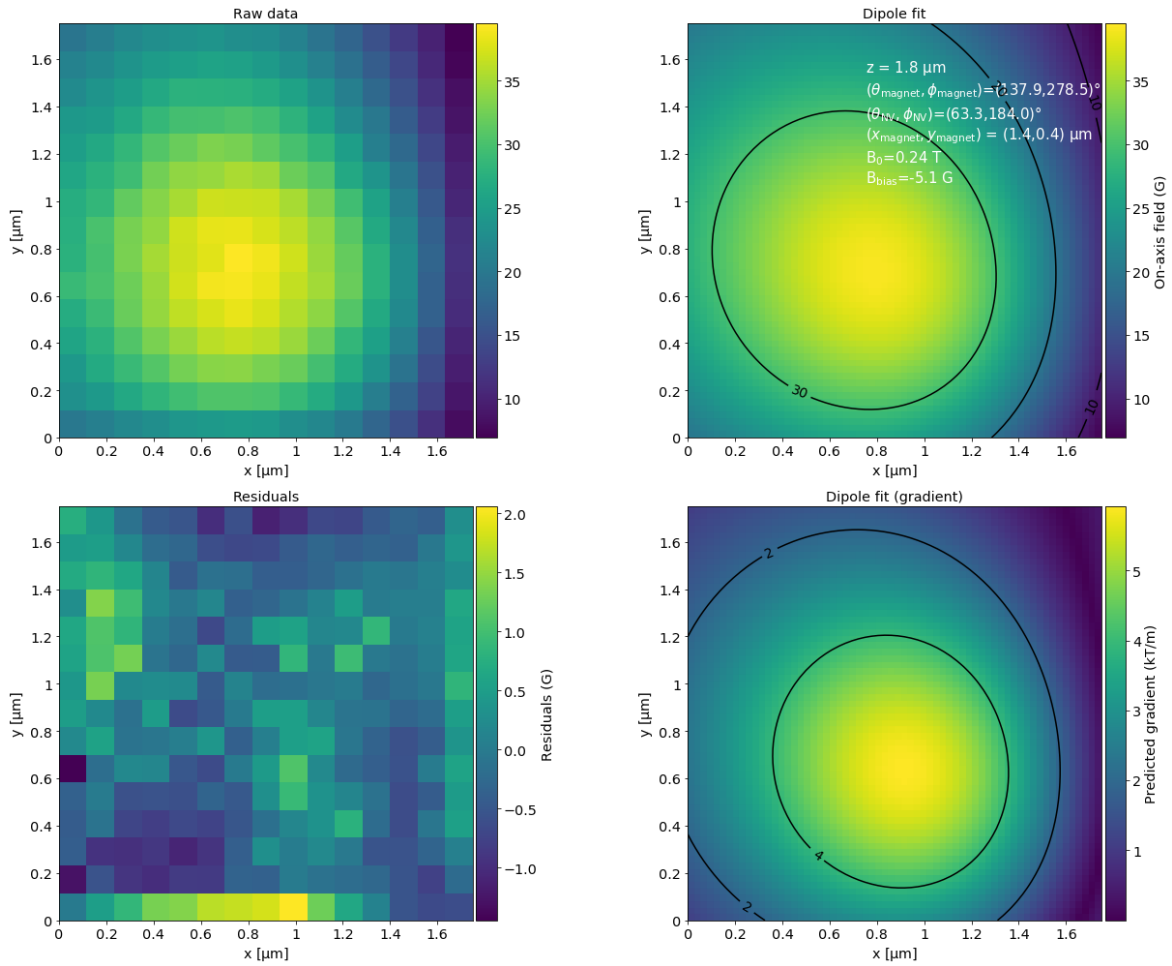


Figure 4.6: Field scan of a micromagnet (1.0 µm diameter) on a nanobeam. Unlike Fig. 4.5, this plot only contains one scan at a fixed NV-micromagnet distance.

the previous configuration of the experiment (see Chapter 2.3.2). Nevertheless, we also performed field scans of micromagnets placed on empty patches of the silicon nitride substrate (not on the nanobeam). If laser demagnetization was indeed the issue, we would expect to measure higher remanences with these micromagnets, given the larger thermal conductance of the substrate versus the thin nanobeam. Some example field scans of these micromagnets on the substrate are shown in Fig. 4.7 and 4.8, also giving fitted remanences significantly lower than 0.7 T.

The micromagnets in the previous scans were magnetized after being placed onto the sample with mechanical resonators, whether they are on the nanobeams or silicon nitride substrate. To investigate whether the low remanence is due to the magnetization procedure, we performed field scans of a different batch of micromagnets. These micromagnets were magnetized separately on a bare chip, and then picked and placed onto the sample with mechanical resonators. Some example field scans are shown in Fig. 4.9 and 4.10. Once again, the fitted remanences fall significantly below 0.7 T.

Combining the field scans from the three aforementioned conditions (micromagnet on string, on nitride substrate, and magnetized on a different sample), we plot the remanences against the magnet diameter in Fig. 4.11, which reveals an increase in remanence with magnet diameter up to 3 µm. We also consulted data from a different levitation experiment in the group also using the same micromagnets [57]. The historical data of the levitated magnets and the frequencies of their mechanical modes offer an alternative way to calculate the magnetic remanences. We find a similar trend in remanences for similar magnet diameters, and that the magnetic remanences are typically ~ 0.7 T for magnet diameters > 10 µm. This suggests that a layer of non-magnetic (or less magnetic) oxidation on the neodymium micromagnet's surface, which becomes less relevant for larger micromagnets. This finding also agrees with informal discussions with researchers in MRFM and literature [86, 140].

Additional measurements such as X-ray photoelectron spectroscopy (XPS) are needed to confirm that the effect of surface oxidation on the reduced remanence of neodymium

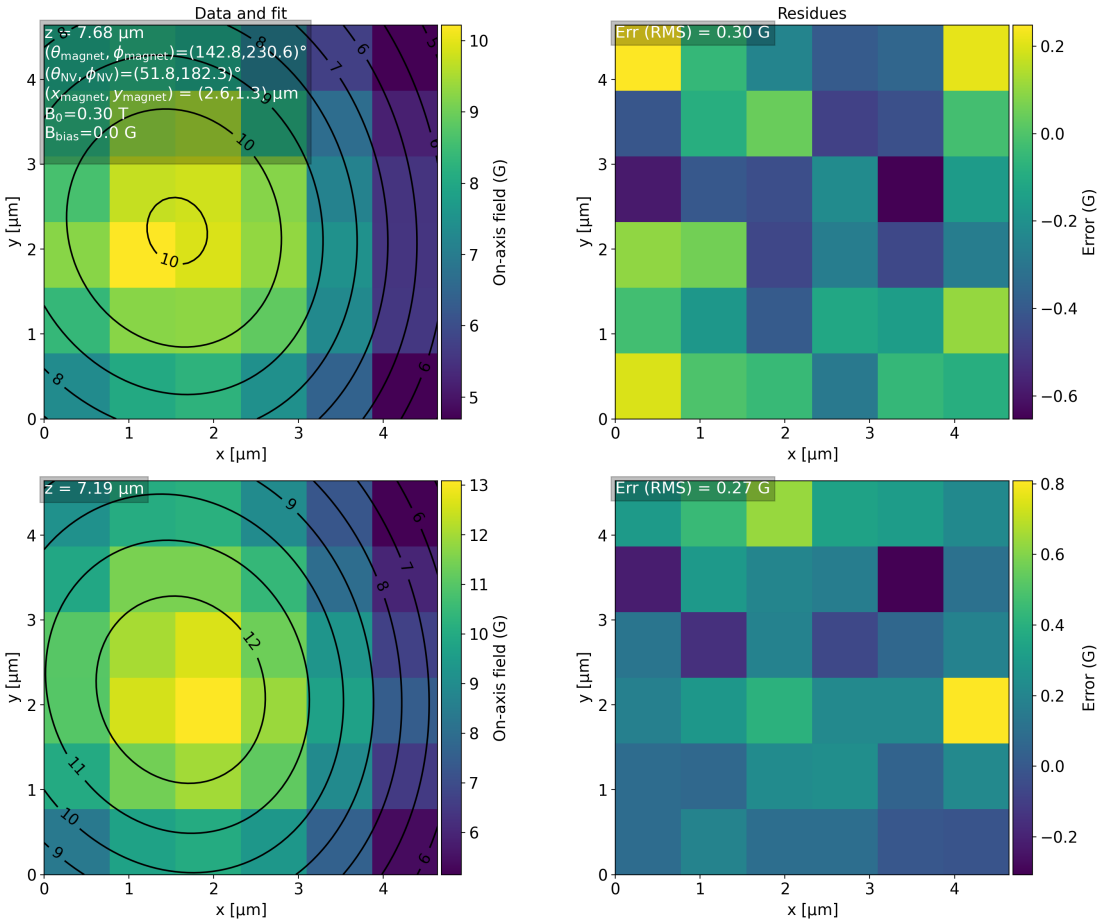


Figure 4.7: Left: field scans of a micromagnet (3.0 µm diameter) on a bare patch of silicon nitride (not on a nanobeam), with each scan taken at a different NV-micromagnet separation z. The fitting parameters are shown on the upper left of the plot, θ_{magnet} and ϕ_{magnet} being the azimuthal and polar angles of the micromagnet's magnetization orientation (with the Z axis pointing out of the page), x_{magnet} and y_{magnet} being the lateral position of the micromagnet's center, B_0 being the remanent magnetization, and B_{bias} being the background bias field. The fitting parameters are obtained by fitting all two scans together (global fitting). The step size in z between each scan is a fixed parameter (from calibration of the nanopositioner's displacement), but the offset is obtained from fitting. Right: residuals, i.e. the difference between the fit and data.

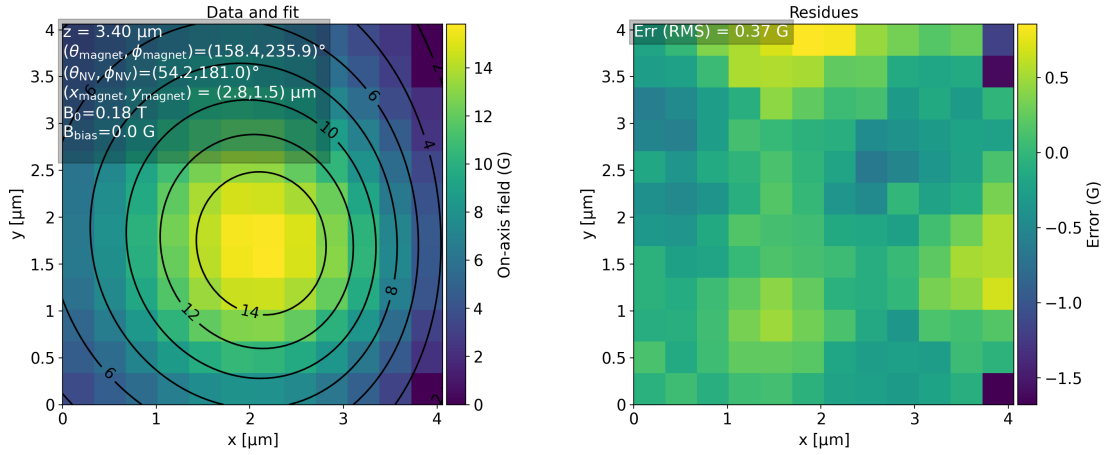


Figure 4.8: Field scan of a micromagnet (1.8 µm diameter) on a nanobeam. Unlike Fig. 4.7, this plot only contains one scan at a fixed NV-micromagnet distance.

micromagnets. Going forward, one can consider alternative materials for micromagnets, in particular SmCo, which has been used in MRFM experiments. SmCo has similar remanence, is less prone to surface oxidation [140], and has a higher Curie temperature, making it less prone to demagnetization from laser heating. Instead of buying these micromagnets from commercial vendors, we can fabricate them in-house and add a capping layer to avoid surface oxidation. Efforts are underway to develop a recipe for depositing thin-film magnets with high-remanence materials such as SmCo. For now, we are able to fabricate iron thin-film magnets. While the remanence of iron is lower than that of neodymium alloy, in principle, one can take advantage of its high saturation magnetization of 2.1 T by applying a relatively low external field of 400 G [156, 79].

4.5 Field Misalignment and Compensation with External Bias Field

The contour scans described in 4.3 are indispensable for locating the point of maximum field gradient. As mentioned earlier, the point of maximum field gradient is typically very close to the point of maximum field. However, we have found a significant loss of NV contrast and fluorescence as the NV center approaches the micromagnet. In a contour scan, this shows up as a dark region near the micromagnet, with an example shown in Fig. 4.12.

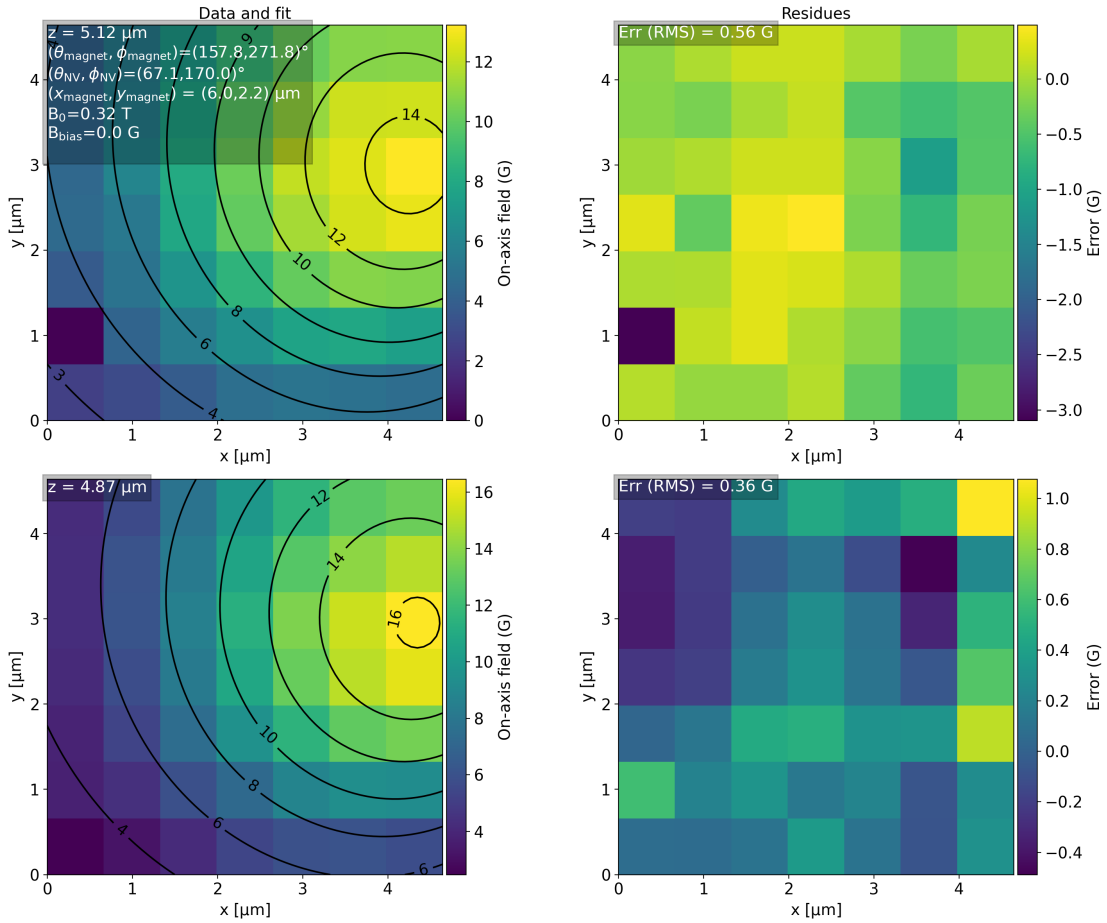


Figure 4.9: Left: field scans of a micromagnet (2.3 μm diameter) on a bare patch of silicon nitride (not on a nanobeam), with each scan taken at a different NV-micromagnet separation z. The fitting parameters are shown on the upper left of the plot, θ_{magnet} and ϕ_{magnet} being the azimuthal and polar angles of the micromagnet's magnetization orientation (with the Z axis pointing out of the page), x_{magnet} and y_{magnet} being the lateral position of the micromagnet's center, B_0 being the remanent magnetization, and B_{bias} being the background bias field. The fitting parameters are obtained by fitting all two scans together (global fitting). The step size in z between each scan is a fixed parameter (from calibration of the nanopositioner's displacement), but the offset is obtained from fitting. Right: residuals, i.e. the difference between the fit and data.

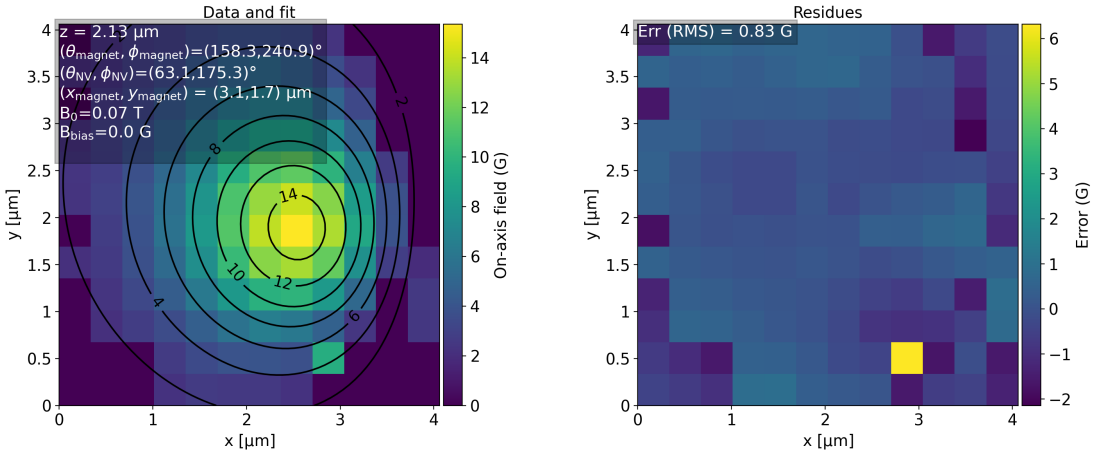


Figure 4.10: Field scan of a micromagnet (1.5 µm diameter) on a nanobeam. Unlike Fig. 4.5, this plot only contains one scan at a fixed NV-micromagnet distance.

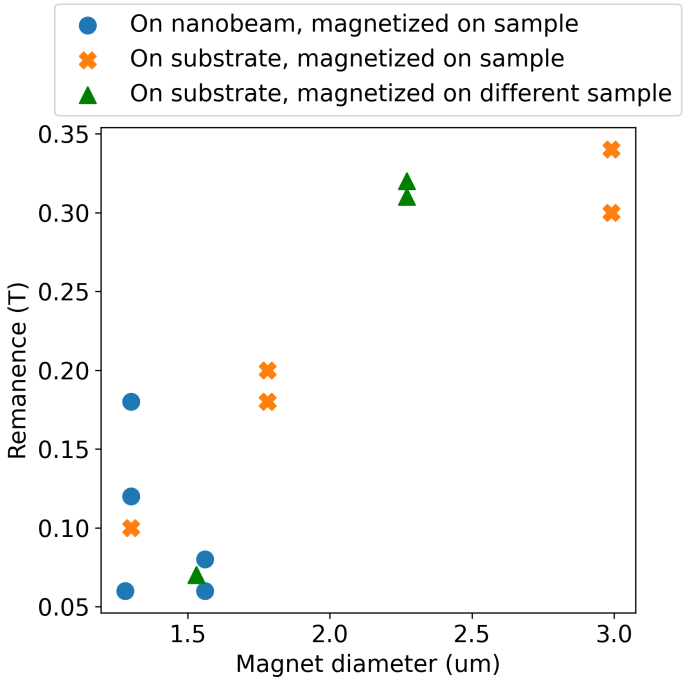
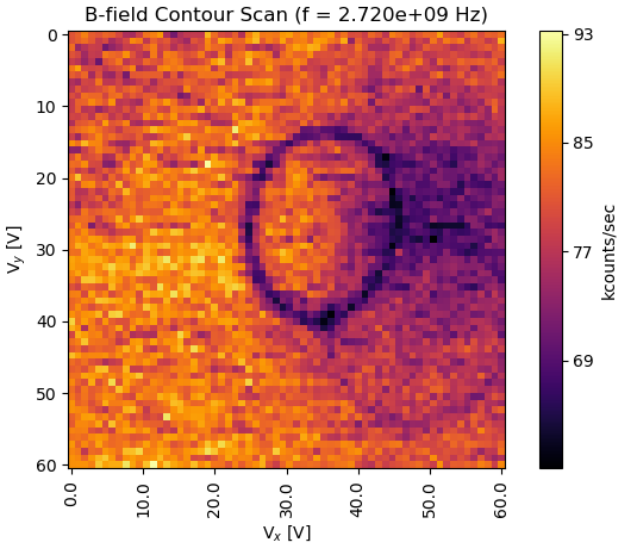
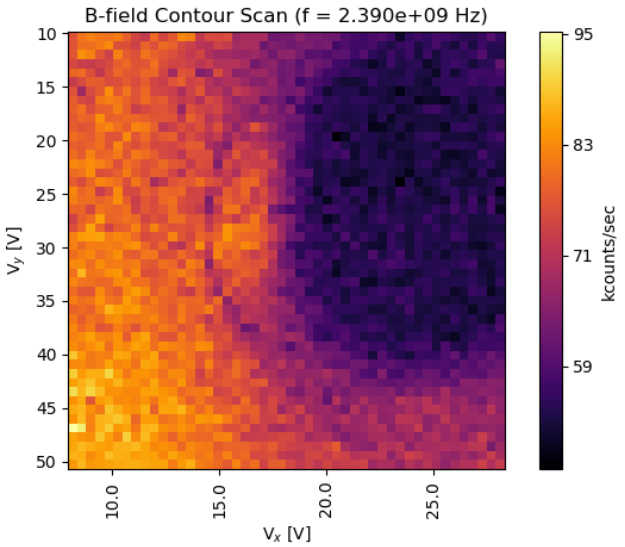


Figure 4.11: Plot of the effective magnetic remanences of spherical neodymiyum micromagnets as a function of their diameters. The effective magnetic remanence is defined as the remanence assuming that the entire micromagnet is magnetized uniformly, and is extracted from dipole fitting of the field scans. There is a clear dependence of the effective remanence on magnet diameter. Given that even larger micromagnets have shown effective remanences of $\sim 0.7\,\mathrm{T}$ (data not shown), it is likely that the reduced remanence for small micromagnets is due to a constant layer of surface oxidation with reduced/no magnetism.



(a)



(b)

Figure 4.12: (a) Contour scan above a spherical neodymium micromagnet, with the microwave frequency fixed at 2.720 GHz, corresponding to a field of about 50 G. A high-contrast contour is visible, alongside another one on the bottom right with lower contrast. The low-contrast contour is due to a second NV center in the nanopillar in the same confocal volume. The dark blob in the middle right indicates a region with low NV spin contrast. (b) After decreasing the NV-magnet distance, the dark blob indicating low spin contrast expands in size. Note the different microwave frequency of 2.390 GHz, which corresponds to a field of about 170 G.

To confirm that this dark region indicates low NV spin contrast, we can retake the contour scan with the microwaves turned off as a reference measurement. By normalizing the contour scans to this reference measurement, we can eliminate any spin-unrelated optical effects, for example due to the Purcell effect and interferometric reflections between the nanopillar and sample [76, 12]. Some normalized contour scans are shown in Fig. 4.13, where the contour disappears in the same dark region in Fig. 4.12 (b). Additional ESR measurements confirm that the NV experiences a loss of contrast in the dark region.

The loss of spin contrast and fluorescence can be explained by the presence of a large magnetic field perpendicular to the NV center's quantization axis. This causes spin mixing, reducing the efficiency of the optical polarization process and the contrast of the spin-dependent fluorescence [147]. Since this typically happens with an off-axis field $\gtrsim 100\,\mathrm{G}$, this quenching mechanism can act as qualitative method to image high off-axis field distributions [61]. In our experiment, the low-contrast region acts as a qualitiative indicator that the NV center is close to the micromagnet ($\lesssim 1\,\mu\mathrm{m}$ away, depending on the magnet diameter).

A challenge thus arises. A small NV-magnet distance is required to achieve high coupling, but large off-axis fields and the associated reduction in spin contrast degrade the spin properties. This challenge is in part due to the fact that we use (100)-diamond nanopillars, where the NV axis is at a 55° angle relative to the pillar length, while the micromagnet is magnetized vertically out of the sample plane. Due to this geometry, the point of highest field gradient typically has very poor field alignment.

Fortunately, this challenge can be addressed with an external bias field to cancel out the off-axis field from the micromagnet. For example, as shown in Fig. 4.14 (a), with just the field from the micromagnet, the high gradient region is located mostly inside the dark region with low NV contrast. However, with the addition of a large bias field ($> 100\,\mathrm{G}$) perpendicular to the NV center's axis, the contour scan changes dramatically, as shown in Fig. 4.15. A bright spot appears near the center of the contour, where the field and gradient is typically the highest. The recovery in NV fluorescence at this spot indicates successful

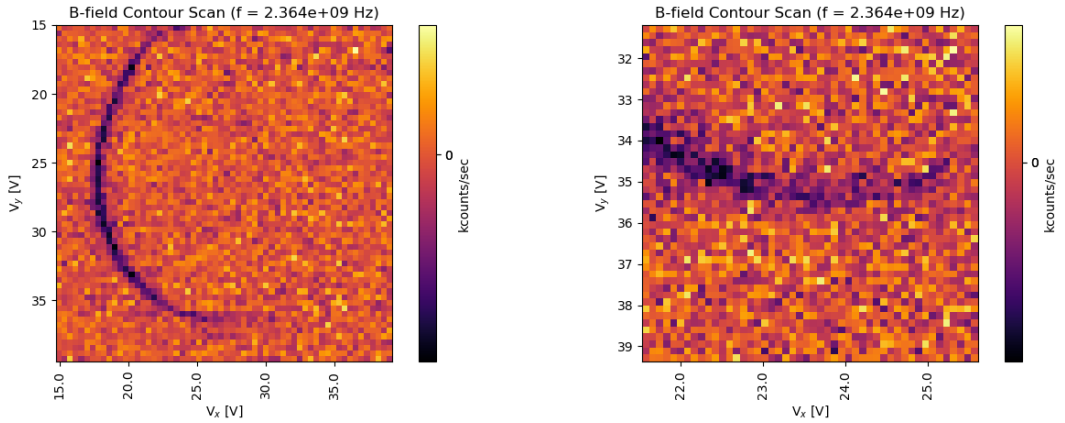
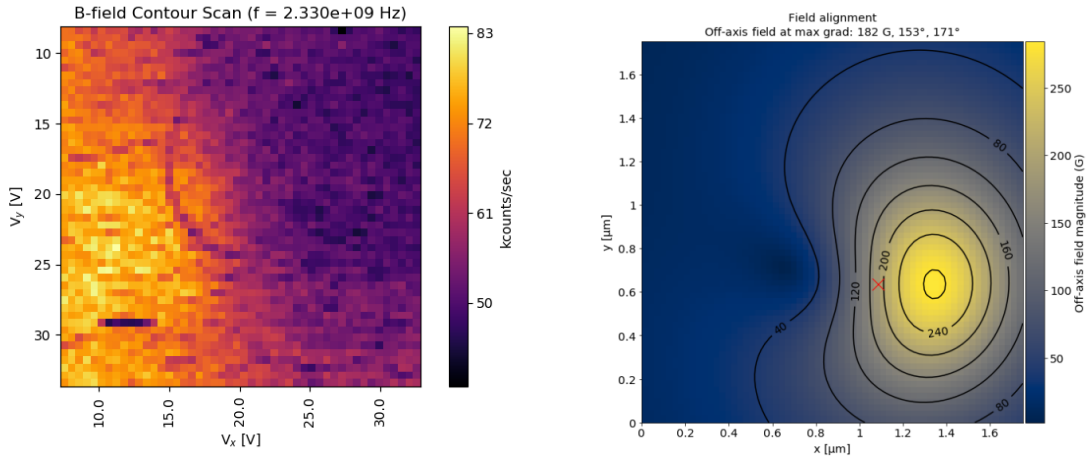


Figure 4.13: (a) Normalized contour scan in the same scan area as Fig. 4.12. The contour disappears in the same region as the dark blob in Fig. 4.12. (b,c) Zoom-in of the tail of the contour, where it disappears due to low spin contrast.



(a) **(b)**

Figure 4.14: (a) Contour scan showing a large region where the NV center experiences large off-axis fields from the micromagnet. (b) Using fitted parameters from a field scan (see 4.2), we compute the expected off-axis fields from the micromagnet. We see that the off-axis fields can exceed 200 G in the right part of the plot. This matches qualitatively with the dark region in (a). The red cross indicates the point of maximum gradient, where the off-axis field exceeds 100 G.

cancellation of the off-axis field.

Because of the high magnetic field gradient ($> 1 \times 10^4$ T/m), the off-axis field is only canceled (or substantially reduced) by the constant bias field in a limited region. With changes in the magnet-NV separation, the extent and position of the cancellation region also changes, as shown in Fig. 4.17.

4.6 Demagnetization Issues

4.6.1 Temperature-related Demagnetization Issues

We have observed temperature-related effects on the micromagnet. In particular, we have observed a change in the magnetic field distribution of neodymium spherical micromagnets after cooling down to ~ 13 K and warming up. A comparison between the magnetic field contours before and after the cool-down, both taken at room temperature is shown in Fig. 4.18. The magnetic field contours have noticeably changed after the cool-down; we also

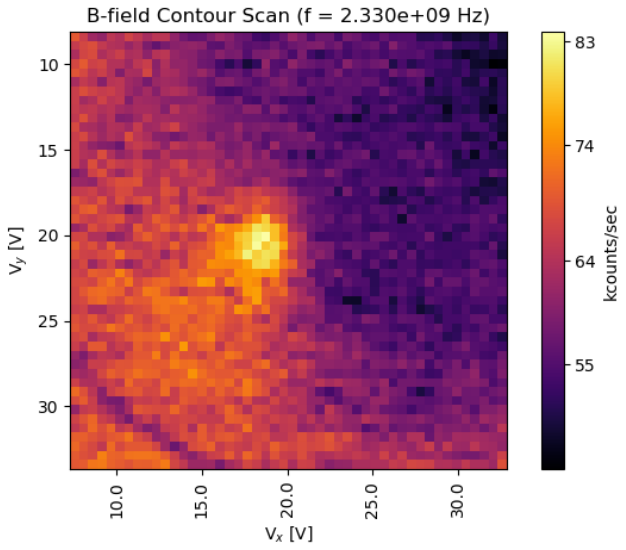


Figure 4.15: With an external bias field, the contour scan changes dramatically, with a bright spot appearing at the center of the contour in Fig. 4.14(a). The bright spot indicates where the off-axis field from the micromagnet is canceled by the external field, leading to a recovery in NV fluorescence.

find that a smaller NV-magnet distance is required to see contours corresponding to the same microwave frequency, indicating a lower effective remanence of the micromagnet. Note that we did not perform any NV measurements with the nanopillar near this micromagnet during the cool-down, thus ruling out the green laser as the cause for demagnetization.

Given that we have not observed this issue for similar micromagnets on some previous samples, the exact cause for this temperature-related change in magnetization warrants further investigation. It has been reported in literature that NdFeB undergoes a spin reorientation at low temperatures: below 135 K, NdFeB changes from an easy-axis material to an easy-cone material, with a cone angle of $< 30^\circ$ [52, 108]. Another potential explanation is that the hypothesized oxide layer on the micromagnet has irreversible temperature-dependent magnetic properties.

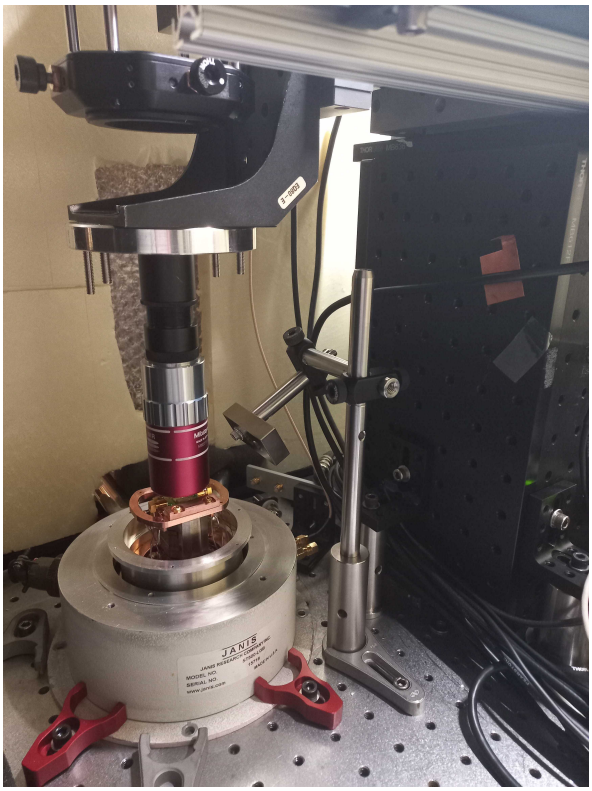
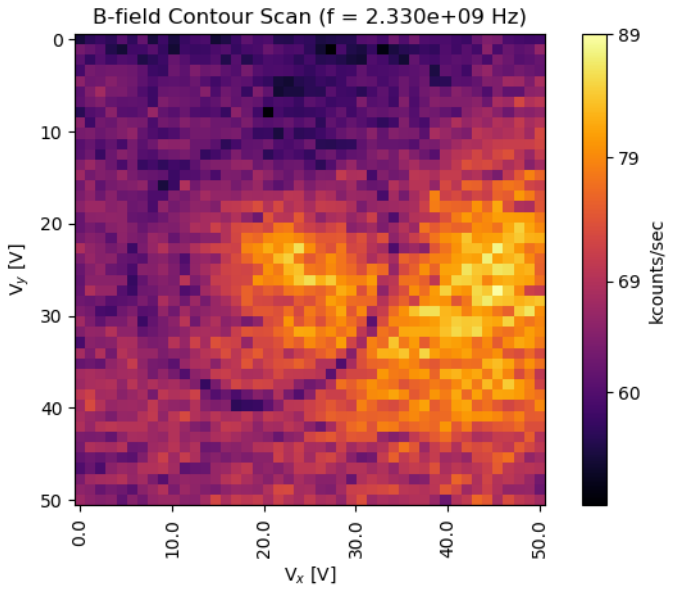
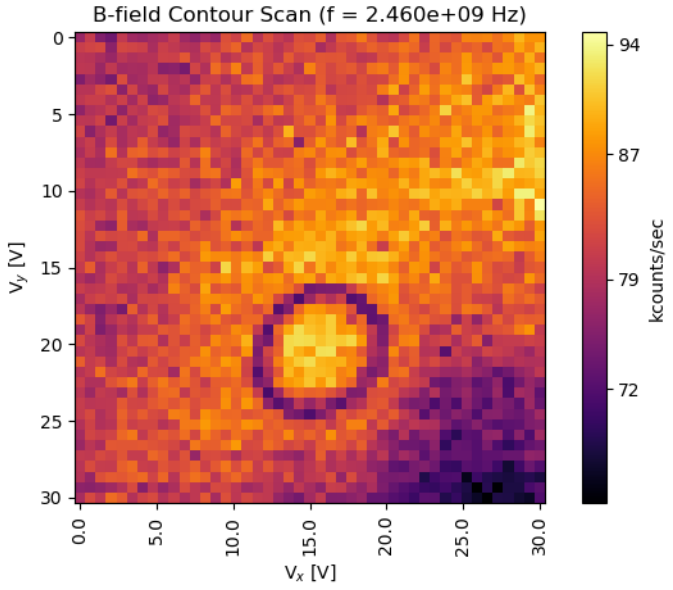


Figure 4.16: Experimental setup to demonstrate cancellation of off-axis fields from the micromagnet using an external bias field. To make this configuration compatible with the cryostat, a pocket inside the cryostat vacuum shroud was added to accommodate the external magnet (Fig. 3.1).

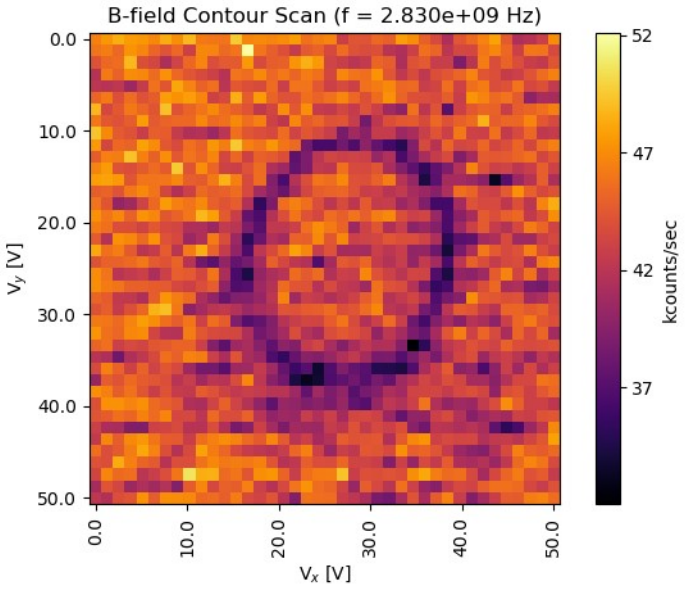


(a)

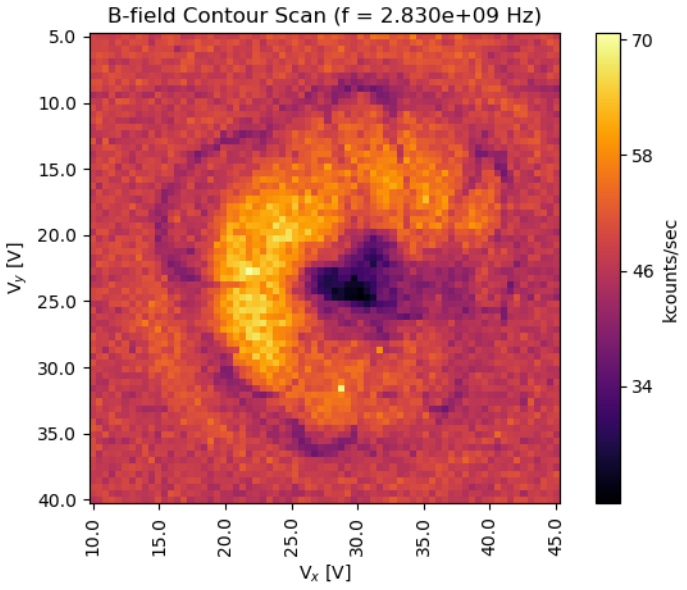


(b)

Figure 4.17: (a) Contour scan after retracting the sample away from the NV center by $\sim 200\,\text{nm}$, which resulted in a change to the shape of the cancellation region. (b) Contour scan after positioning the external magnet at the opposite side of the sample, which results in a much larger cancellation region where the ESR contrast recovers to 20%.



(a)



(b)

Figure 4.18: (a) Contour scan of a spherical neodymium magnet, with the microwave frequency fixed at 2.83 GHz, corresponding to an on-axis field of 14 G. (b) Contour scan of the same micromagnet, with the same microwave frequency. The NV-magnet distance is also smaller than in (a), as evidenced by the onset of optical effects (dark spot) near the center of the scan associated with small separations.

4.6.2 Laser-related Demagnetization Issues

In Sec. 2.3.2, we discussed how the micromagnet is prone to overheating and demagnetization from the green laser in vacuum, in part due to the low thermal conductance of the nanobeam. This issue is mitigated with the use of diamond nanopillars, which due to their waveguide structure have much higher excitation efficiency of the NV center, allowing us to use $\sim 4\times$ lower laser power ($\sim 50\,\mu W$ measured at the objective's back focal plane) than in the case of a bulk diamond crystal. This is one of the improvements that allowed us to eventually measure a spin-mechanical coupling, as outlined in Chapter 5.

However, the use of reduced green laser power does not entirely eliminate the issue of laser demagnetization. At low sample temperatures ($\sim 13\,K$, we have found that the magnetic field from the micromagnet at the NV center's location changes with the green laser duty cycle. This is indicated by a change in the ESR splitting, as shown in Fig. 4.19.

The ESR is measured with pulsed ODMR (optically detected magnetic resonance), and both the measurement sequence and microwave pulse durations are kept constant. As shown in Fig. 4.19 (a,b), there is a general trend where the ESR splitting decreases with increasing laser duty cycle, suggesting that the green laser pulses are demagnetizing the micromagnet. In Fig. 4.19 (a), we identify a threshold laser duty cycle of ~ 0.2, above which decreases in the ESR splitting become irreversible (i.e. does not recover to higher value after decreasing the duty cycle). However, after repositioning the micromagnet with respect to the NV center, this threshold appears to have increased to > 0.5, as shown in Fig. 4.19(b).

Subsequent measurements on the same micromagnet show some surprising results. Fig. 4.19(c) and (d) show that the ESR splitting increases with laser duty cycle and power. This would appear to suggest that somehow the magnet's effective remanence is somehow increased by the laser.

We reconcile these observations by noting that the neodymium micromagnet is not necessarily uniformly magnetized at cryogenic temperatures (see Sec. 4.6.1). In the case of a uniformly magnetized sphere that is also uniformly heated and demagnetized by the green laser, one can expect that the ESR splitting will always decrease with higher laser

duty cycle. However, if the micromagnet is not uniformly magnetized, the magnetic fields from its differently-oriented domains might interfere with each other. As the laser duty cycle increases, local laser heating might only affect some of these domains, which could explain an increase in the overall field at the NV center's location.

To avoid laser demagnetization, we thus have to lower the laser duty cycle to avoid overheating of the micromagnet. However, as shown in Fig. 4.19, the threshold at which irreversible demagnetization happens is unclear and appears to depend sensitively on the micromagnet's position relative to the nanopillar. To be safe, we would have to restrict the laser duty cycle to < 0.1, which drastically increases the time for all NV measurements. At such a duty cycle, a contour scan and ESR measurement with decent signal-to-noise ratio now require $\sim 5\,\mathrm{min}$ and $\sim 1.5\,\mathrm{min}$ respectively. Given that tens of contour scans and hundreds of ESR measurements are typically needed during the initial NV-magnet approach, the increased measurement time becomes a big challenge, especially considering the limited run-time of the flow cryostat.

Finally, we note that the above measurements on both laser and temperature-related demagnetization were all performed on neodymium micromagnets placed on 50 nm-thick silicon nitride nanobeams. In the next chapter, we describe the first spin-mechanical coupling measurements in this work, where 150 nm-thick nanobeams were used. We did not observe laser-caused demagnetization during those measurements. Further investigation is needed to determine whether this is because of the higher thermal conductance of the thicker nanobeam, or because of some unknown changes in the sample fabrication or magnet properties between the coupling measurements and laser duty cycle measurements.

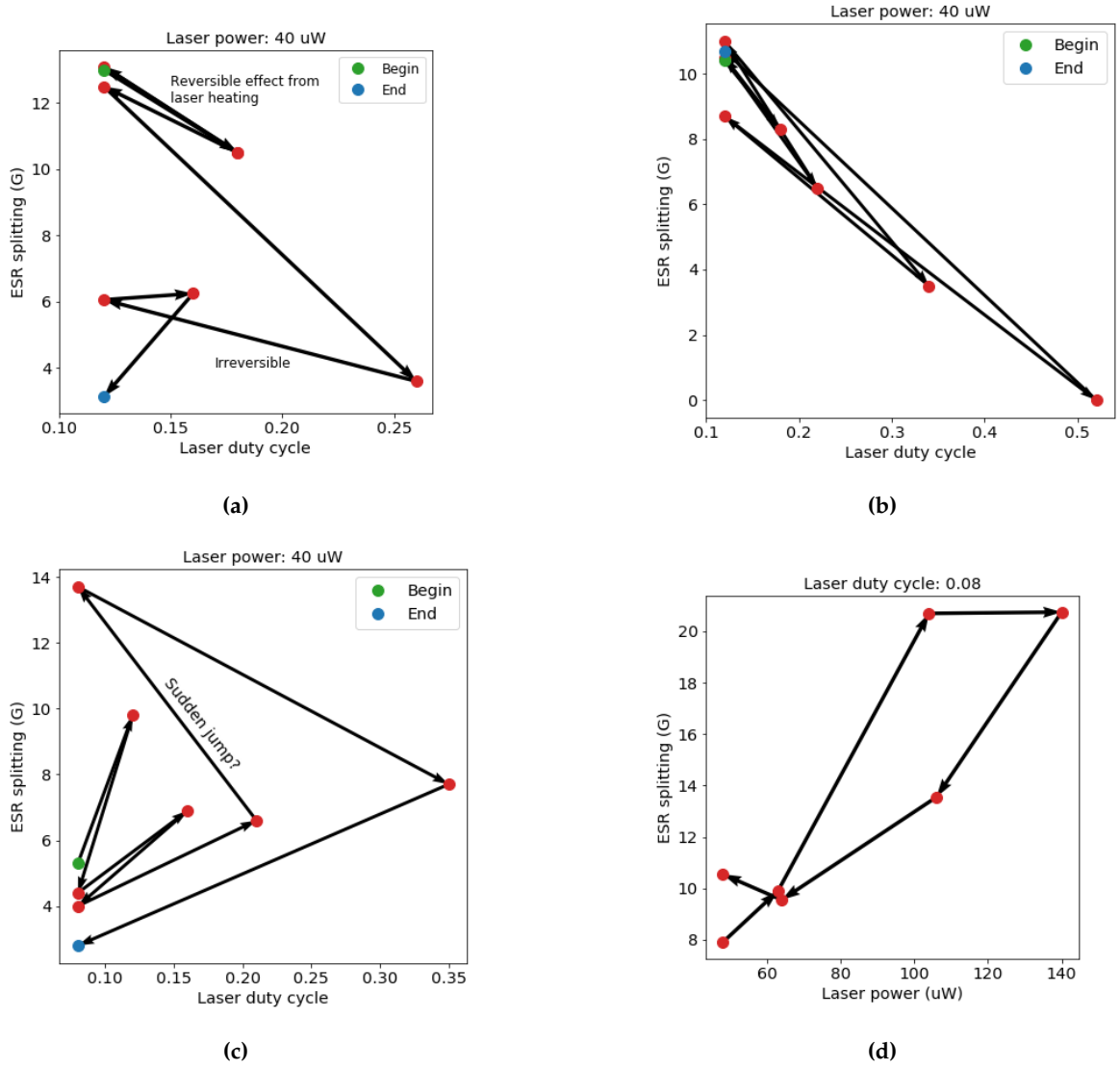


Figure 4.19: (a) Measurements of the NV center's ESR splitting as a function of laser duty cycle. The ESR measurement sequence is kept constant at 5 µs. To illustrate the irreversible and reversible effects of the laser pulses, the measurements are connected with arrows, with the initial and final measurement marked with green and blue dots respectively. With higher laser duty cycle, the ESR splitting decreases, suggesting demagnetization of the micromagnet due to laser heating. (b) The measurement in (a) is repeated after repositioning the micromagnet to regain a larger splitting. This time, even with a laser duty cycle > 0.5, changes in the ESR splitting appears reversible. (c) The ESR measurement sequence duration is changed to 7.5 µs. Interestingly, the ESR splitting increases with the laser duty cycle. (d) The ESR splitting is measured as a function of laser power, while the sequence duration is kept constant at 7.5 µs.

Chapter 5

Towards Programmable Quantum Processors based on Spin Qubits with Mechanically-Mediated Interactions and Transport

5.1 Introduction

Isolated spin defects in the solid state, such as nitrogen vacancy (NV) centers in diamond, have long been considered as promising candidates for quantum information processing, owing to their extended coherence times even at elevated temperatures [16, 91, 155, 9, 139]. While small spin registers have been realized using coupled electronic and nuclear spins [43, 6, 30], such demonstrations rely on magnetic dipole-dipole interactions, which limit the distance between spins to tens of nanometers. The short-range nature of these interactions and imprecision of defect fabrication at these length scales make it challenging to control systems containing large arrays of spin qubits.

Several approaches are currently being explored to address this challenge, including long-range entanglement based on photonic [25, 73] and mechanical systems [117, 82].

In particular, nanomechanical resonators have been proposed as a mesoscopic interface between distant and otherwise isolated spin qubits. Such a hybrid quantum system can be realized by combining electronic spins with magnetically functionalized mechanical resonators [11, 20, 80, 100, 127, 145, 112, 84, 92, 102, 57, 88]. Mechanical resonators can be engineered to have very high quality factors with flexible, compact geometric realizations, and feature low crosstalk relative to their electromagnetic counterparts [36]. Using mechanical modes as a quantum transducer, distant spin qubits can be entangled deterministically, even when the mechanical mode is in a thermal, highly excited state [117, 132, 124]. Furthermore, spin qubits can be used to cool the mechanical resonator to its ground state [116, 115] and subsequently prepare non-Gaussian states of motion [107]. Despite these intriguing proposals, realizing the necessary strong coupling between mechanical systems and individual spin qubits is a challenging task, requiring deterministic positioning of spin qubits in close proximity to magnetized mechanical resonators. Moreover, even though transducers extend the spin-spin interaction range, the system connectivity remains local, limiting its programmability and scalability.

In this Letter, we introduce a novel platform for realizing programmable interactions between distant spin qubits. The key idea of our architecture is illustrated in Fig. 5.1(a). In our approach, individual NV centers in diamond nanopillars are coupled to silicon nitride nanobeam mechanical resonators in a scanning probe geometry. A micromagnet attached to the nanobeam provides the magnetic field gradient for the spin-mechanical coupling. Pairs of NV centers can be moved close to a mechanical resonator which in turn mediates entanglement between the former [124, 132]. For example, following the proposal in [124], the NV centers can be used to conditionally excite the motion of the mechanical resonator, which is then measured to project the spins into an entangled state, even if the spins are across disparate teeth in each nanopillar comb.

Ultra-high quality factors $Q > 10^9$ have been demonstrated in silicon nitride mechanical resonators through a combination of techniques such as soft-clamping, dissipation dilution, and strain engineering [150, 55, 22, 65, 23]. At the same time, the nanoscale footprint

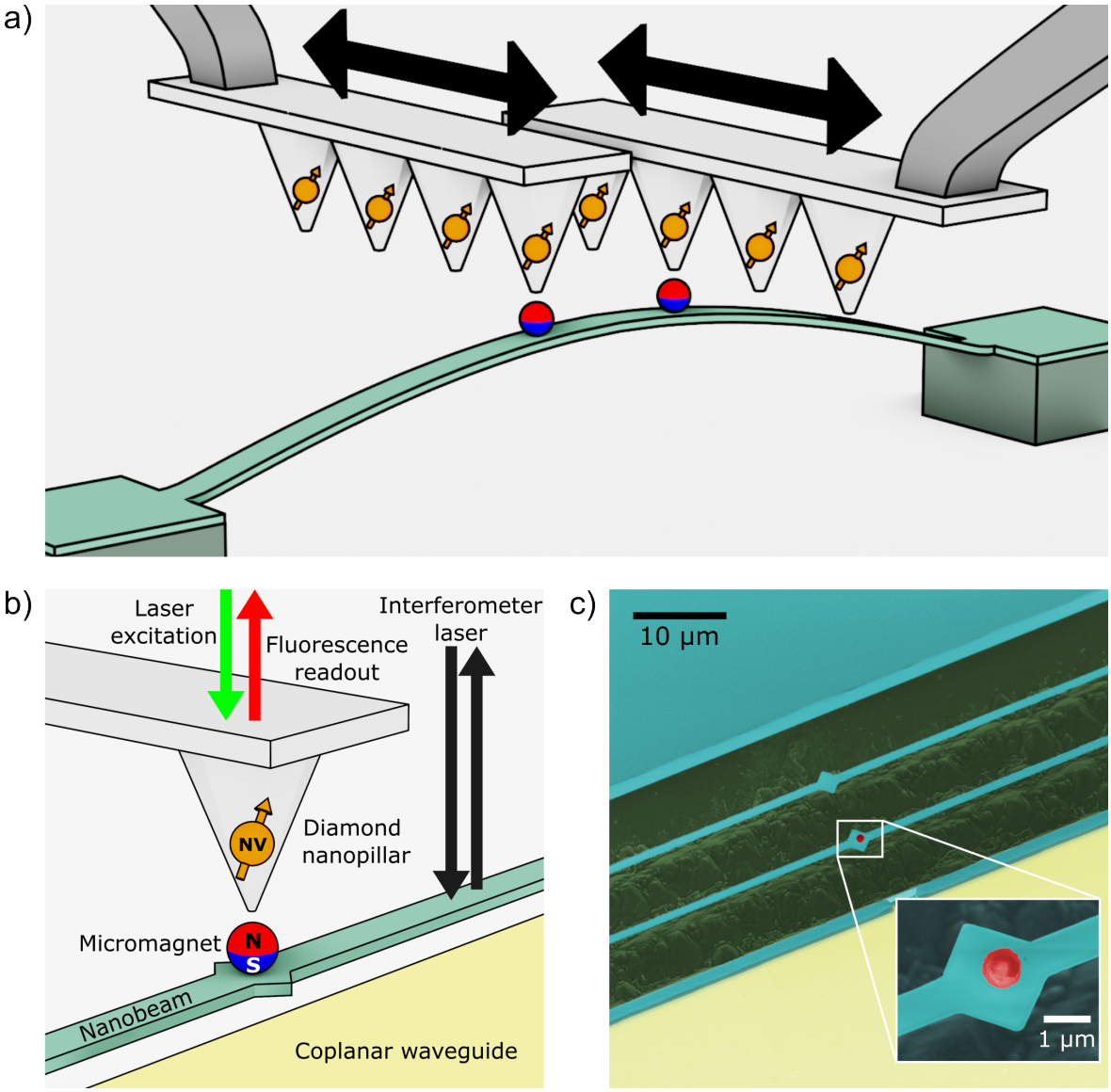


Figure 5.1: (a) Conceptual diagram for programmable interactions within arrays of nanopillars containing spin qubits. Spin qubits (orange) can be micro-manipulated (black arrows) to interact with a common mechanical mode of a magnetically-functionalized resonator (turquoise), enabling mechanically-mediated spin-spin interactions. (b) Our current experimental realization: a diamond nanopillar containing a single NV center at its tip is positioned above an NdFeB spherical micromagnet at the center of a doubly clamped silicon nitride nanobeam. A coplanar waveguide on the same chip facilitates coherent microwave control of the NV center's electronic spin. The chip is mounted on a 3-axis nanopositioner stack, while the diamond nanopillar is kept fixed. (c) False-color scanning electron microscope image of the nanobeam (turquoise lines, two shown) with a micromagnet (red sphere) placed on a pad at the antinode of motion. Gold area at the bottom of the image is the coplanar waveguide. Inset: zoom-in image of the micromagnet.

of the diamond nanopillar enables small separations between the NV center and the micromagnet [163, 89], providing access to high magnetic field gradients required for large spin-mechanical coupling. Remarkably, spin qubits confined in nanopillars can be moved mechanically in and out of the near-field of the magnetized resonators. Moreover, they can be transported across relatively long (10-100 μm) distances, enabling non-local connectivity between distant qubits [29, 104, 90, 113, 95, 37]. Further improvements in coherence time can be obtained by making use of a nuclear spin quantum memory. Since the latter is less sensitive to magnetic fields, such storage can be used for long-distant qubit transport even in the presence of proximal magnetic gradients, enabling reconfigurable quantum processing architecture similar to that demonstrated recently for neutral atom array qubits [29].

5.2 Experimental Setup and Static Magnetic Field Characterization

Our experimental platform consists of a scanning probe setup, where a (100)-diamond nanopillar containing a single NV center is positioned near a micromagnet placed at the center of the nanobeam (Fig. 5.1(b, c)). In addition to improving the optical collection efficiency, the nanopillar has a small surface area at its apex, allowing for nanoscale magnet-NV center distances [89]. Fabrication details can be found in references [163, 158].

The presence of a magnetic field perpendicular to the NV center quantization axis limits NV spin readout contrast, photoluminesence intensity, and coherence time $T_{2,e}$ in a natural-abundance ^{13}C diamond [138]. To align the magnetic field and characterize the field distribution, we scan the micromagnet with respect to the diamond nanopillar with a 3-axis stack of piezoelectric nanopositioners. At each position, we optically measure the electron spin resonance (ESR) and calculate the magnetic field along the NV center quantization axis [1]; an example map of the magnetic field around a micromagnet is shown in Fig. 5.2(a). With our current smallest micromagnet-NV distance of $\sim 1.0\,\mu$m, we estimate gradients exceeding $1.5 \times 10^4\,\mathrm{T/m}$, corresponding to an expected single-phonon spin-mechanical coupling strength of $\lambda/2\pi \sim 5\,$Hz (Fig. 5.2(b)).

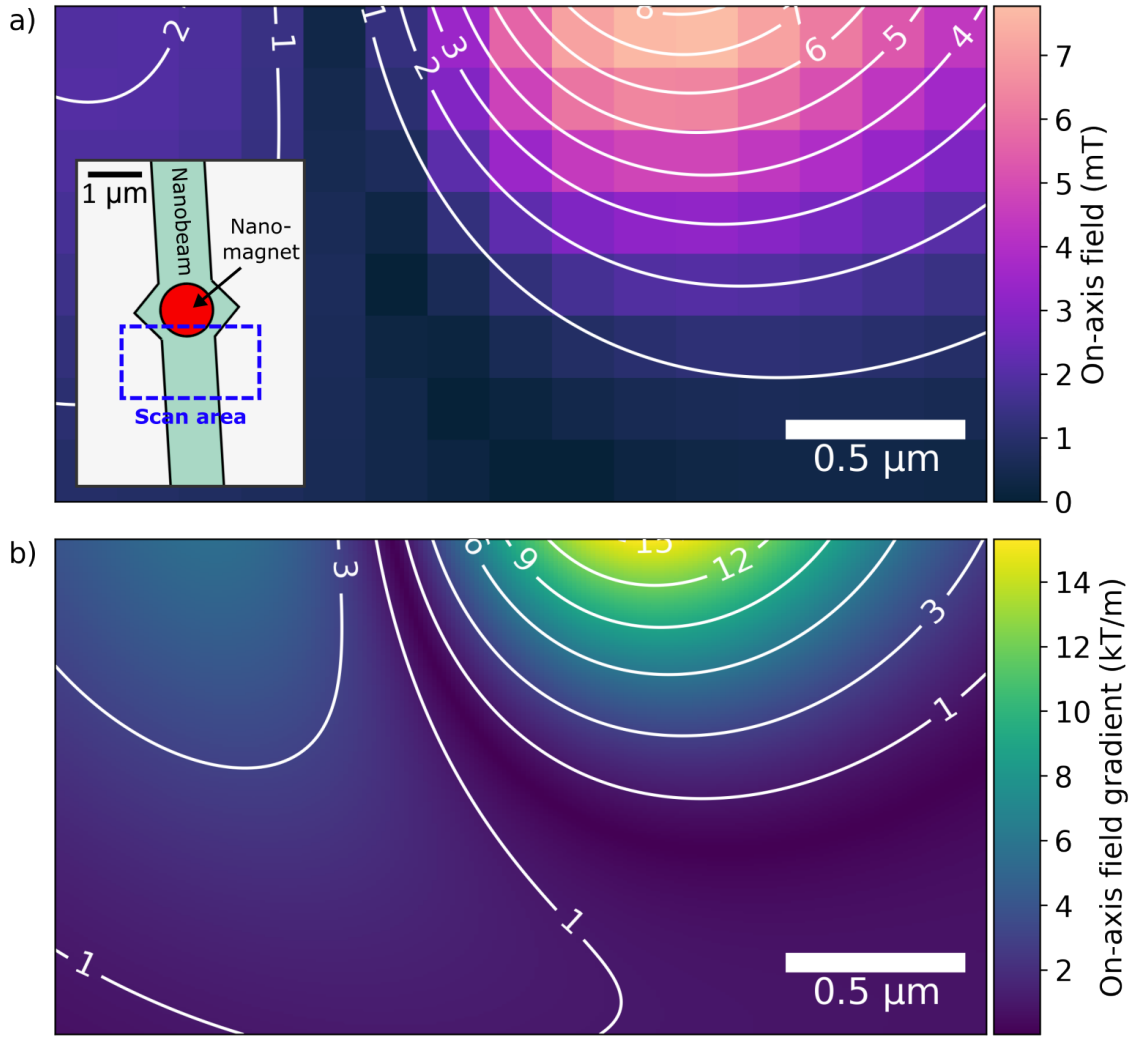


Figure 5.2: Magnetic field imaging of a micromagnet. (a) Magnetic field near the micromagnet, with a vertical NV-magnet separation of about 1 µm. For each position of the diamond nanopillar, we measure the electron spin resonance (ESR) frequencies, from which we extract the magnetic field along the NV center's axis [1]. The field from the spherical micromagnet is well-approximated by a dipole model, with the fit (contours) deviating from the measured fields by less than 3 G at any point. The orientations of the NV center and magnet are consistent with the fabrication process of the nanopillar and magnetization direction respectively. These measurements were performed in air at room temperature, without any external driving of the mechanical resonator. Inset: Diagram showing the scanning area around the micromagnet on the nanobeam. (b) Reconstructed magnetic field gradients based on fit to dipole model. The maximum gradient is $\sim 1.5 \times 10^4$ T/m.

5.3 Preservation of Spin Coherence in Proximity of a Transported Micromagnet

Next, to investigate whether the spin coherence can be maintained during qubit transport, we perform a proof-of-principle experiment in which we move the micromagnet $1.7(2)$ µm away from the diamond nanopillar and then back to its original position. Pulsed ESR measurements at different times during the movement sequence (Fig. 5.3 (a)) reveal a significant change in the magnetic field environment, as evidenced by a shift of $9.8(1)$ MHz in the ESR frequency [1].

We demonstrate the preservation of spin coherence in proximity of a transported micromagnet, using the pulse sequence in Fig. 5.3(b) synchronized with the movement sequence in Fig. 5.3(a). Since the total movement time of 1.7 ms is significantly longer than the electronic spin coherence time of $0.95(4)$ ms [1], we use the NV center's intrinsic ^{15}N nuclear spin as a quantum memory [111, 161].

Specifically, in our demonstration the electron and ^{15}N nuclear spin are first initialized in a two-qubit register $|-1\rangle_e \otimes |\downarrow\rangle_n$ [1], followed by a $\pi/2$-pulse which puts the ^{15}N nuclear spin in a superposition $|-1\rangle_e \otimes (|\downarrow\rangle + |\uparrow\rangle)_n$. Subsequently, we apply a C_nNOT_e gate which fully entangles the electron-nucleus pair $-|0\rangle_e |\downarrow\rangle_n + |-1\rangle_e |\uparrow\rangle_n$.

During the subsequent free evolution time τ, the entangled electron-nucleus pair accumulates a phase $\phi(\tau)$. For the particular NV center in our measurements, hyperfine interactions with a nearby ^{13}C nuclear spin lead to phase accumulation at a rate of ~ 0.9 MHz. A second C_nNOT_e gate then disentangles the electron-nuclear pair and the phase information $\phi(\tau)$ is now entirely stored in the ^{15}N nuclear spin $|-1\rangle_e \otimes \left(-|\downarrow\rangle + e^{i\phi(\tau)}|\uparrow\rangle\right)_n$.

As shown in Fig. 5.3(a), the field at the nanopillar changes significantly during the movement sequence, leading to an additional phase accumulation on the ^{15}N. We eliminate this additional phase by applying a π-pulse on the ^{15}N near the middle of the movement sequence [1]. Finally, a $\pi/2$-pulse at the end of the movement sequence converts the stored phase information $\phi(\tau)$ into the probability of finding the ^{15}N in either $|\downarrow\rangle_n$ or $|\uparrow\rangle_n$, which

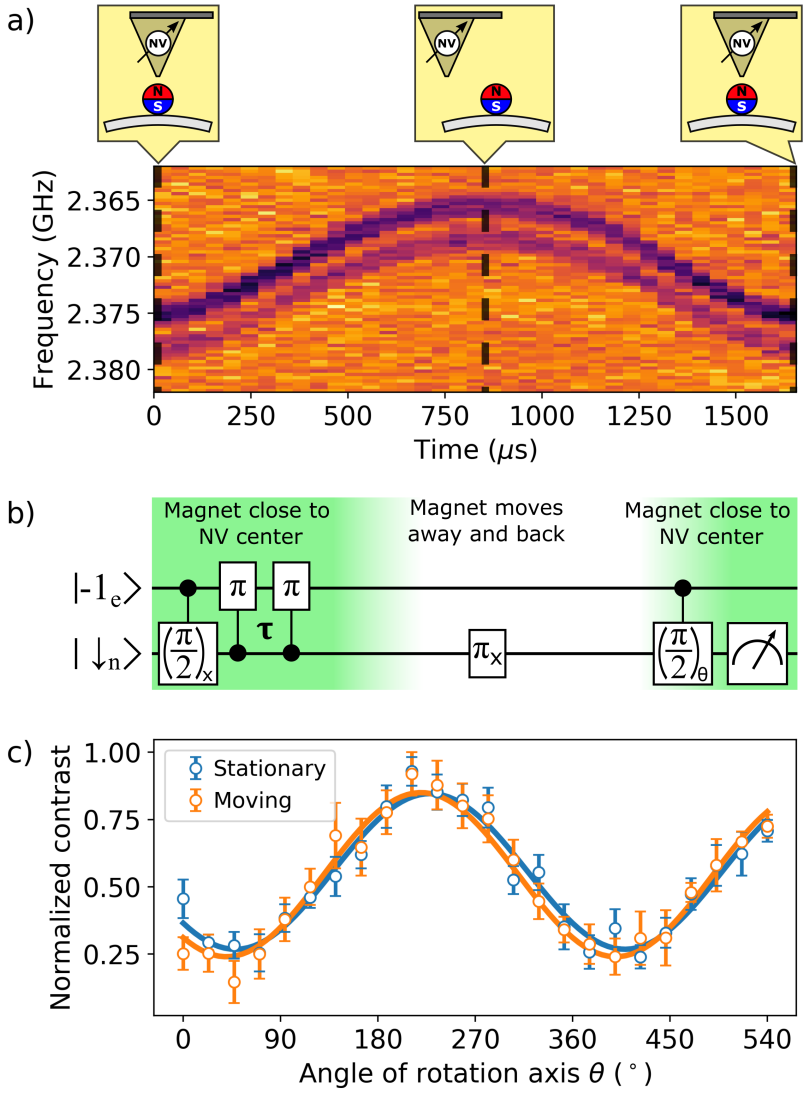


Figure 5.3: Preservation of spin coherence in proximity of a transported micromagnet. (a) The nanobeam along with the micromagnet is moved 1.7(2) µm from the NV center and then back to its original position over 1.7 ms. Pulsed ESR measurements at different times during the movement sequence show the changing field from the moving micromagnet. The 3 MHz hyperfine splitting from the NV center's intrinsic ^{15}N nuclear spin is clearly visible; an additional hyperfine splitting from a nearby ^{13}C nuclear spin is not shown here due to the microwave pulse duration used [1]. (b) Pulse sequence used to demonstrate storage and retrieval of coherent information, synchronized with the movement sequence shown in (a). (c) Fixing the phase accumulation time $\tau = 900$ ns, we measure the coherence of the nuclear spin at the end of the movement sequence by varying the rotation axis angle θ of the final $\pi/2$-pulse, for both cases where the micromagnet is moved (orange) and kept stationary (blue).

can be measured with a boost in signal-to-noise ratio (SNR) using repetitive readout [77].

By fixing $\tau = 900\,\text{ns} < T^*_{2,e}$ and varying the rotation axis angle of the final $\pi/2$-pulse, we can quantify the spin coherence preservation. The results, shown in 5.3(c) demonstrate that the normalized contrasts for cases where the micromagnet is moved (orange) and kept stationary (blue) are $0.61(3)$ and $0.57(3)$ respectively, indicating that the nuclear spin coherence is unaffected by the significant change in magnetic field.

5.4 Mechanical Motion and Single-phonon Coupling Strength

Finally, we characterize the spin-mechanical coupling by exciting the nanobeam and characterizing its mechanical motion via independent measurements with both an interferometer and the nearby NV center. To take advantage of higher quality factors at low temperatures, we use the scanning probe setup in a helium cryostat. The interferometric measurements, shown in Fig. 5.4(a,b), reveal a quality factor of $8.25(6) \times 10^5$ (Fig. 5.4(b)), demonstrating that the quality factor remains high despite magnetic functionalization [1]. The mechanical frequency $\omega_r/2\pi \sim 1.4\,\text{MHz}$ (Fig. 5.4(a)) corresponds to a period of $0.7\,\mu\text{s}$. As a result, the mechanical resonator can undergo multiple oscillations during the spin coherence time $T_{2,e}$, which is around several microseconds. The readily accessible high mechanical frequency of the nanobeam compares favorably to other spin-mechanical platforms, such as those featuring cantilevers, nanowires, and magnetic levitation [127, 11, 57].

Near the micromagnet, the NV center experiences a Zeeman shift, which can be expanded in the resonator displacement to give the interaction Hamiltonian $\mathcal{H}_{\text{int}} = \gamma_e z_p \nabla_z (\hat{a} + \hat{a}^\dagger)$, where γ_e is the NV center electronic spin gyromagnetic ratio, ∇_z is the magnetic field gradient along the NV center quantization axis, z_p is the mechanical zero-point motion, and a is the mechanical mode annihilation operator. To quantify the single-phonon spin-mechanical coupling strength $\lambda = \gamma_e z_p \nabla_z$, we excite the nanobeam with an external broadband drive and detect the field from the oscillating micromagnet with the nearby NV center. We use a Hahn echo pulse sequence, which results in frequency-dependent detection of the magnetic spin environment [1]. Sweeping the time τ between the π pulses

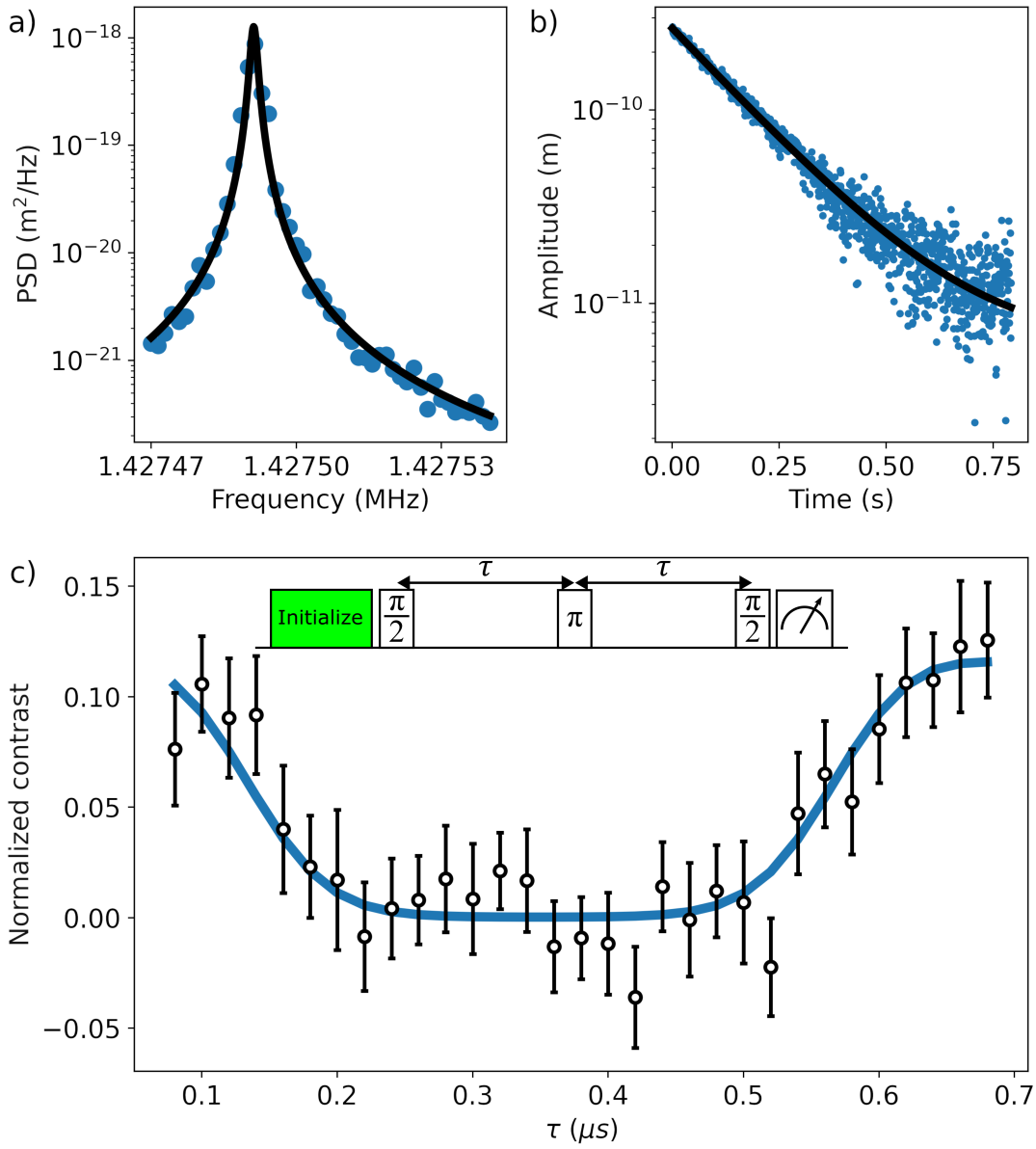


Figure 5.4: Sensing the mechanical motion of the nanobeam. (a) Power spectral density (PSD) of the mechanical mode, measured using an interferometer. From the Lorentzian fit (black line) we extract a resonance frequency of $\sim 1.4\,\mathrm{MHz}$ and a linewidth of $\kappa/2\pi = 1.5(2)\,\mathrm{Hz}$. (b) After switching off an external drive from a piezoelectric chip, we measure the amplitude decay of the mechanical motion and obtain $Q = 8.25(6) \times 10^5$. **(c)** Sensing of the mechanical motion with the NV center. We perform a Hahn echo pulse sequence on the NV center with and without the mechanical drive, and plot their ratio (black circles) such that we can neglect the NV center's decoherence in our model for the fit ($\chi(\tau)$, blue line). We fit the signal $S(\tau, \lambda, \Delta_x)/e^{-\chi(\tau)}$ (see eq. (5.1)) to find $\lambda/2\pi = 7.7(9)\,\mathrm{Hz}$. Due to drift in the cryogenic setup, the sweep of τ is limited to 700 ns to capture the first collapse in coherence due to the effect of the mechanical motion.

and assuming a Gaussian distribution of the mechanical state, the spin contrast can be approximated as

$$S(\tau, \lambda, \Delta_x) = \alpha e^{-8\Delta_x^2\lambda^2 \sin^4(\omega_r\tau/2)/\omega_r^2 z_p^2} e^{-\chi(\tau)} \tag{5.1}$$

where Δ_x is the root-mean-squared (RMS) amplitude of motion, α is the spin readout contrast, and $\chi(\tau)$ describes the coherence decay from other noise sources in the diamond, such as the bath of ^{13}C nuclear spins [138] [1].

To determine λ, we first independently quantify Δ_x by integrating the interferometer signal of the mechanical response from the wideband drive, and assign ω_r to the center frequency. For the data corresponding to figure 5.4(a), we find that $\Delta_x = 1.86(1)$ nm, far above the RMS thermal motion of 9 pm. We then fit the Hahn echo data, normalized to a baseline Hahn echo measurement (without driving the mechanical resonator) to compensate for intrinsic NV decoherence $e^{-\chi(\tau)}$ (Fig. 5.4(c), black dots). For the fit (blue line), λ is the only free parameter, while ω_r and Δ_x are fixed, and $z_p = \sqrt{\hbar/2m_{\text{eff}}\omega_r} = 11$ fm for an effective mass $m_{\text{eff}} = 4.6 \times 10^{-14}$ kg. We find that $\lambda/2\pi = 7.7(9)$ Hz (Fig. 5.4(c), corresponding to a gradient of $2.4(1) \times 10^4$ T/m, similar to the gradients from the static field imaging of the same magnet (Fig. 5.2(b)).

5.5 Discussion and Outlook

Our experiments demonstrate the feasibility of the proposed architecture for programmable mechanically-mediated interactions between distant spins. Specifically, we showed that the NV center's intrinsic nuclear spin memory is not degraded by transport of a nearby micromagnet, if the proper decoupling pulse sequences are applied. The demonstrated movement distance of 1.7(2) µm in Fig. 5.3(a-c) significantly exceeds the range of magnetic dipole-dipole interactions between spins, and is limited by the moving speed of 1 mm/s and nuclear spin coherence time $T_{2,n} \sim 5$ ms [1]. The speed can be increased by using a nanopositioner with a higher bandwidth and minimizing residual vibrations caused by the scanning motion. By decoupling the nuclear spin from its local environment or cooling to

cryogenic temperatures, $T_{2,n}$ can be extended to $> 1\,\mathrm{s}$ [91, 110], which would extend the possible distance to $> 1\,\mathrm{mm}$ even with the current speed.

At the same time, achieving quantum coherent spin-mechanical coupling [115, 20, 152, 151, 132, 124] requires increasing the coupling strength while minimizing noise. Specifically, the onset of coherent quantum phenomena is generally marked by the spin-mechanical cooperativity $C \equiv \frac{\lambda^2}{\Gamma \kappa n_{th}} \gtrsim 1$, which compares the coherent coupling rate λ to the dissipation rates $\Gamma, \kappa n_{th}$ of the spin and mechanical mode respectively. While the cooperativity of our present experiment exceeds previous spin-mechanical platforms involving NV centers [1], its value of 10^{-7} remains far below the coherent coupling regime. However, significant improvements can be made. Drift of the NV-magnet distance causes significant variations of the ESR frequency at high magnetic field gradients, limiting our current gradient to $2.4 \times 10^4\,\mathrm{T/m}$ at a distance of $1.0\,\mu\mathrm{m}$. With improvements to the setup stability and the use of atomic-force microscopy (AFM) feedback [13, 163], positioning the NV center at a reduced distance of 50 nm from the surface of a 1 µm-diameter micromagnet should yield gradients $\sim 1.4 \times 10^6\,\mathrm{T/m}$, or a spin-mechanical coupling of $\lambda/2\pi \sim 800\,\mathrm{Hz}$. The doubly clamped nanobeam can be replaced with recent designs that utilize strain engineering and soft-clamping, which have demonstrated $Q \sim 10^9$ at MHz frequencies [150, 55, 23, 65, 21]. Even higher quality factors have been demonstrated or predicted, by replacing silicon nitride with crystalline materials such as silicon and diamond [19, 133]. For a coupling strength of $\lambda/2\pi = 800\,\mathrm{Hz}$, an NV center electronic spin coherence time $T_{2,e}$ of 10 ms [6, 17], and a quality factor of 10^9 at 4 K, the coherent coupling regime is possible with $C \sim 75$. Under such conditions, mechanics-mediated entanglement of electronic spins with fidelity exceeding 95 % should be feasible according to the proposal in [124]. Although we expect $T_{2,e}$ to improve with larger NV implantation depth, further investigation into diamond fabrication and surface termination might be required to increase $T_{2,e}$ to the 10 ms regime for NV centers in diamond nanopillars [87, 129].

Compared to previous work involving on-chip, circuit-based hybrid quantum systems [117, 107], a spin-mechanical architecture featuring dynamical qubit transport has the advan-

tage of being able to generate programmable, non-local interactions, similar to reconfigurable platforms based on neutral atoms and trapped ions. The long coherence time of the nuclear spin allows multiple distant spins to be dynamically transported to interact with the same mechanical bus. While Fig. 5.1 only shows one mechanical resonator for clarity, the architecture can also be parallelized, with multiple mechanical resonators simultaneously mediating interactions within large arrays of spins. We also note that, unlike most other hybrid quantum systems [57, 107], both the mechanical and spin components of our platform are highly coherent even at room temperature. With a nanomagnet diameter of 0.3 µm, an NV-magnet separation of 20 nm, spin coherence time of $T_{2,e} = 2$ ms [72], and $Q = 1 \times 10^9$, reaching the coherent-coupling regime at room temperature appears feasible. We note that while our work focuses on NV centers, the core concept applies to other solid-state spin qubits such as silicon-vacancy centers in diamond and color centers in silicon carbide, which have been incorporated into nanopillar-like structures [149, 126, 162, 119]. The above considerations indicate that with realistic improvements, our platform can enable programmable interactions between distant spins, opening up a new avenue towards scalable quantum information processing with solid-state spin qubits. The ability to generate scalable long-range interactions between quantum sensors also presents new opportunities in entanglement-enhanced sensing with applications in condensed matter studies. Finally, the present approach can be extended to realize other hybrid systems by coupling spin qubits to quantum systems such as superconducting qubits and optical photons [38, 36, 18, 26].

5.6 Acknowledgements

We thank M. Markham and Element Six for providing diamond samples, R. Walsworth and M. Turner for annealing diamonds, K. Van Kirk, D. Bluvstein, A. Mulski, and E. Polzik for helpful discussions, B. Machielse for assistance with fabrication, R. Riedinger for comments on the manuscript, S. Y. F. Zhou and A. Cui for assistance with sample magnetization, and A. S. Zibrov and J. MacArthur for technical assistance. This work was supported by NSF, Center for Ultracold Atoms, and DOE Quantum Systems Accelerator Center (contract

no. 7568717). E. R. acknowledges support from the NSF Graduate Research Fellowship Program. A. K. acknowledges support from the DOD through the NDSEG Fellowship Program. J. G. acknowledges support by the European Union (SEQOO, H2020-MSCA-IF-2014, No. 655369). Diamond and resonator sample fabrication were performed at the Center for Nanoscale Systems (CNS), a member of the National Nanotechnology Coordinated Infrastructure, which is supported by the NSF under award no. ECCS -1541959. CNS is part of Harvard University. T. X. Z is an affiliate to Center for Quantum Network (CQN) established by NSF to facilitate collaboration within CQN to advance quantum research. T.M. acknowledges support from the NSF Graduate Research Fellowship Program (grant 2140743). N.A. acknowledges support from the Alexander von Humboldt Foundation and by the Federal Ministry of Education and Research (BMBF, project “13N16297”).

Chapter 6

Characterization of High-Q Mechanical Resonators

6.1 Introduction

In Sec. 2.2.1 and 5.4, we presented some characterization measurements of the mechanical resonator's frequency and quality factor. In particular, the quality factor of our doubly-clamped silicon nitride nanobeams is about 1×10^6 at cryogenic temperatures. As mentioned in Sec. 5.5, the quality factors of silicon nitride mechanical resonators reported in literature have increased by orders of magnitude over the past decade, with the highest exceeding 1×10^{10}. In this section, we outline our efforts to take advantage of new resonator designs to obtain higher quality factors. We also discuss some of the technical challenges related to the resonator functionalization and frequency drift at cryogenic temperatures.

6.2 Frequency Drift at Cryogenic Temperatures

We have observed significant drift in the frequency of the nanobeam after cooling the sample down. The drift rate is roughly constant over a timescale of several minutes. Four example measurements are shown in Fig. 6.1, from which we can extract drift rates ranging from $-0.1\,\mathrm{Hz/s}$ to $-2.0\,\mathrm{Hz/s}$. The geometries and functionalization details of the

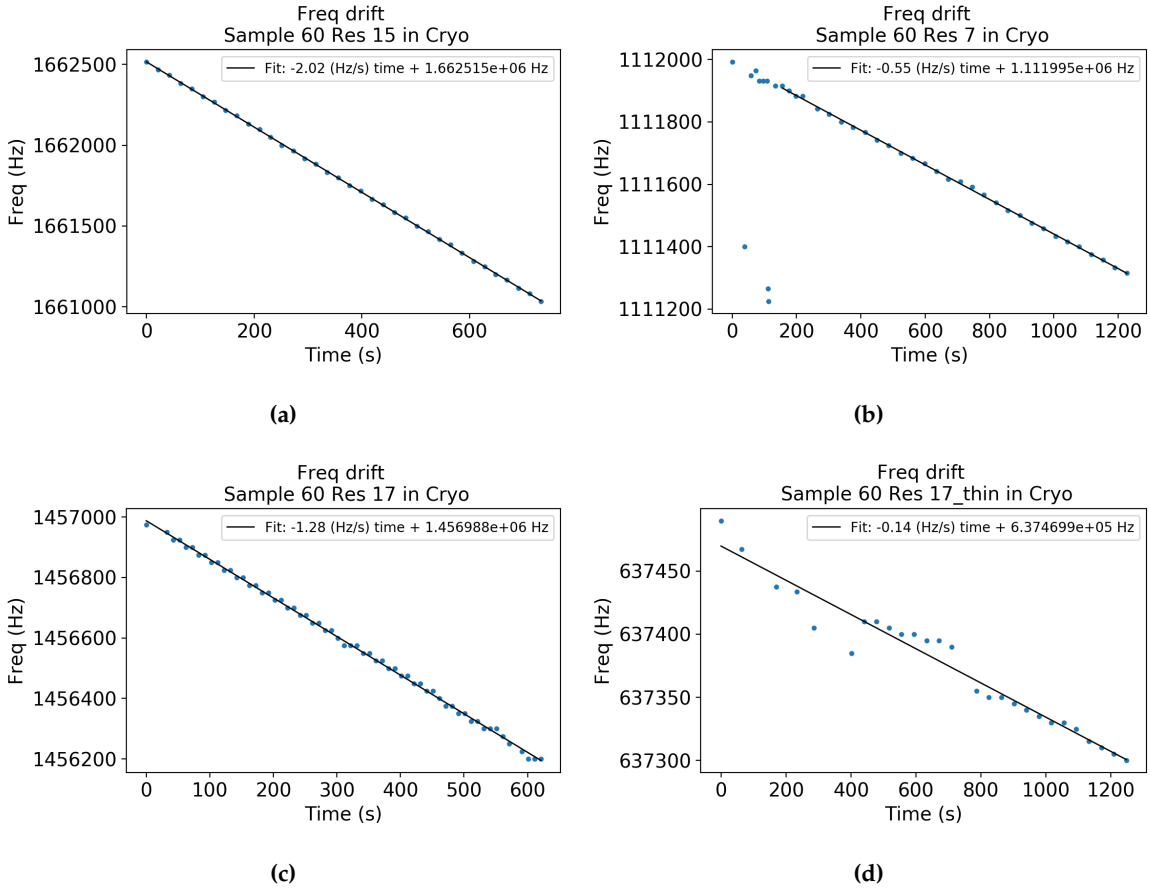


Figure 6.1: Frequency drift of four nanobeams with varying geometries and magnetic functionalization at cryogenic temperatures ($\sim 20\,\mathrm{K}$). The resonance frequency is tracked by repeatedly taking frequency sweeps and fitting the mechanical response to a Lorentzian lineshape.

corresponding nanobeams are presented in Table 6.1. In Fig. 6.2, we plot the drift rates against the resonators' initial frequencies, revealing an exponential relationship between the two variables. Further investigation is needed to determine the cause of this relationship.

Fig. 6.3 shows a measurement of the frequency drift over almost an entire day, where the frequency drops to 1.35 MHz, a 18% decrease from its initial value of 1.65 MHz. As expected, the drift rate does not stay constant over this longer timescale and decreases gradually following an exponential decay.

Similar observations have been reported in literature and discussions with our collabora-

Resonator	Initial frequency (MHz)	Drift rate (Hz/s)	Drift rate (%/s)	Magnet radius (μm)	Resonator width (um)
15	1.663	-2.02	1.2E-4	0	5
7	1.112	-0.55	4.9E-5	2.2	5
17	1.457	-1.28	8.8E-5	1.3	5
17_thin	0.638	-0.14	2.2E-5	1.8	1

Table 6.1: Drift rates (absolute and relative) are tabulated alongside the dimensions and functionalization details of each resonator shown in Fig. 6.1.

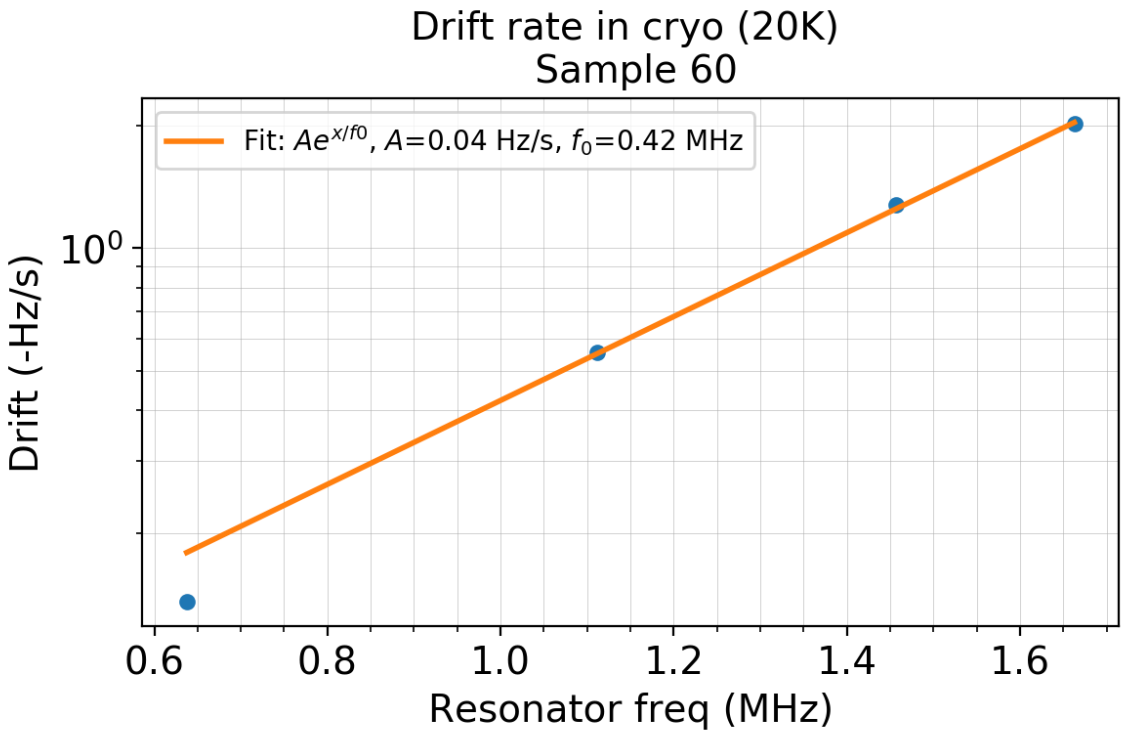


Figure 6.2: Drift rate of the mechanical frequency plotted against their initial frequencies.

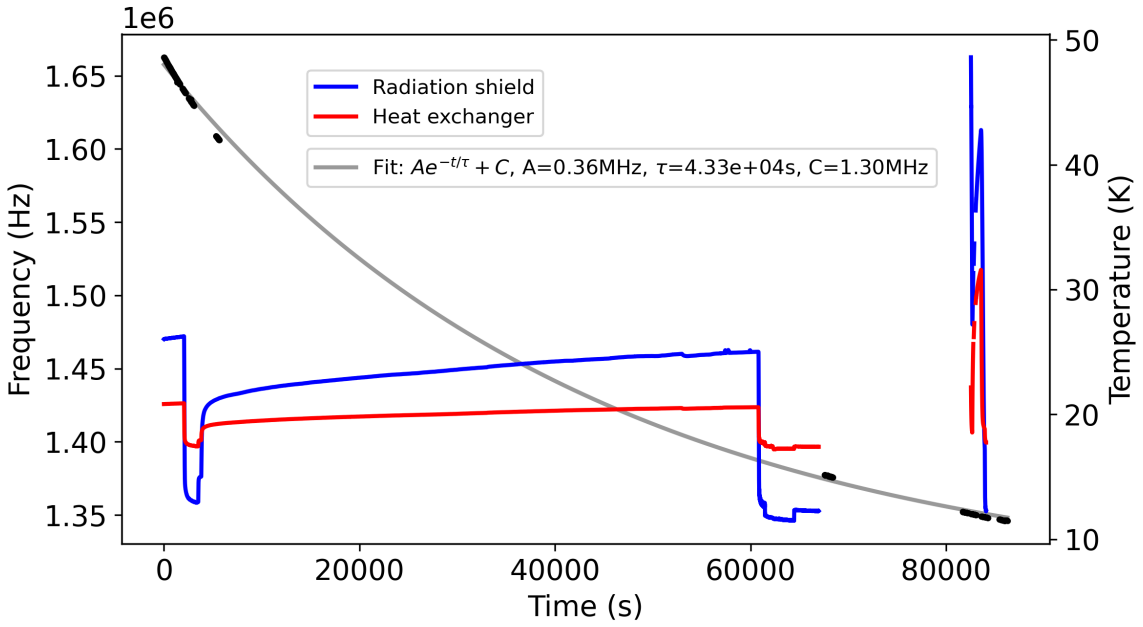


Figure 6.3: The mechanical frequency of a nanobeam is plotted over about 22 h, alongside the cryostat temperature. Note that data for the sample mount temperature was unavailable at the time of the measurement; it can be estimated as an intermediate value between the temperature of the heat exchanger and the radiation shield. The abrupt temperature changes are due to user intervention in attempts to affect the frequency drift.

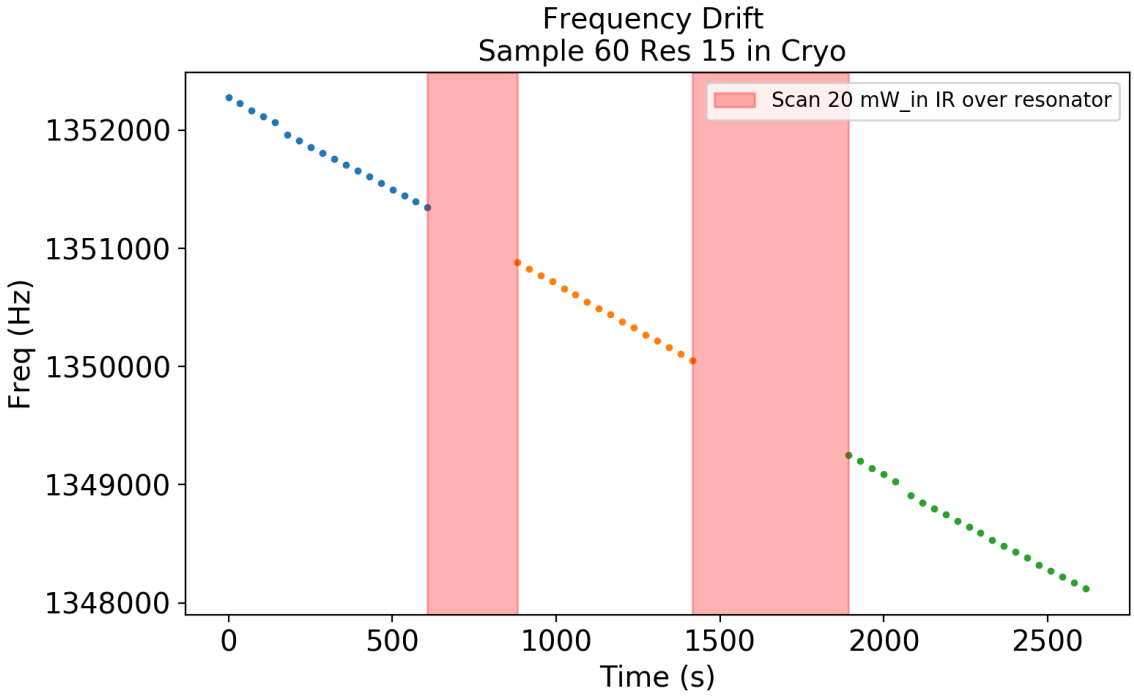


Figure 6.4: Measurement of the frequency drift over time, interrupted by scans of the nanobeam with the same laser used for the interferometer measurements (1064 nm). The setting for the laser is 20 mW, corresponding to several hundred µW at the objective back focal plane.

tors in Prof. Simon Gröblacher's group. In particular, Ref [97] reports a similar drift rate at 3 K for MHz mechanical resonators. A common hypothesis is that particles are cryopumped onto the nanobeam, resulting in added mass which decreases the mechanical frequency. To test this hypothesis, we tried scanning the 1064 nm laser used for the mechanics measurements over the nanobeam to see if we can "burn off" some of these adsorbed contaminants, which should result in a recovery of the mechanical frequency. The results are shown in Fig. 6.4. We do not observe any appreciable changes in the mechanical frequency after this procedure. However, this measurement is only meant as a quick test; for a more thorough investigation, the laser power should be increased further and multiple laser wavelengths should be tested.

We note that the frequency decrease is not permanent, and that the downwards drift of

the resonator frequency can be reversed in two ways. In the first case, one can simply warm the sample back to room temperature, whereupon the frequency recovers to its initial value.

In the second case (Fig. 6.5), we have noticed that after decreasing the cryostat temperature from 30 K to 20 K, the resonator frequency increases for a few minutes before resuming the usual downward drift. We attribute this to the non-uniform cooling rates of different parts of the cryostat. Upon lowering the cryostat temperature (measured at the heat exchanger), it is possible that some parts of the cryostat, such as the radiation shield, cool down at a higher rate than the sample, momentarily decreasing the cryopumping effect of the sample. This effect goes away after the temperatures of the sample and the rest of the cryostat settle into equilibrium, whereupon the mechanical frequency resumes its downward drift.

After discussions with our collaborators in the Gröblacher group, we designed and installed an extension (parts 7 and 8 in Fig. 3.1) to the original radiation shield. The result is a much larger surface area of cold metal surrounding the sample area, which intercepts and "traps" contaminants via cryopumping before they reach the sample. This radiation shield extension decreases the frequency drift rate by two orders of magnitude to about $-0.02\,\mathrm{Hz/s}$, as show in Fig. 6.6.

However, even with the greatly reduced drift rate, the frequency still changes by more than its linewidth every few seconds (assuming a quality factor of 1×10^6), an issue that becomes more acute with even higher quality factors. We attribute the remaining frequnecy drift to two design issues. The first one is the opening at the top of the radiation shield, which is necessary for the high-NA objective. However, the objective is at room temperature and cannot be thoroughly cleaned given its delicate optical coatings. It therefore presents an obvious source of contaminants which get cryopumped onto the nanobeam. Future modifications to the cryostat can be made to mitigate this issue. For example, a thin glass slide can be inserted between the objective and the sample, acting as a transparent radiation shield (See Fig. 3.5 in [85]). However, given the large NA of the objective, even a thin cover slip will lead to significant spherical aberrations, requiring the use of an objective with a

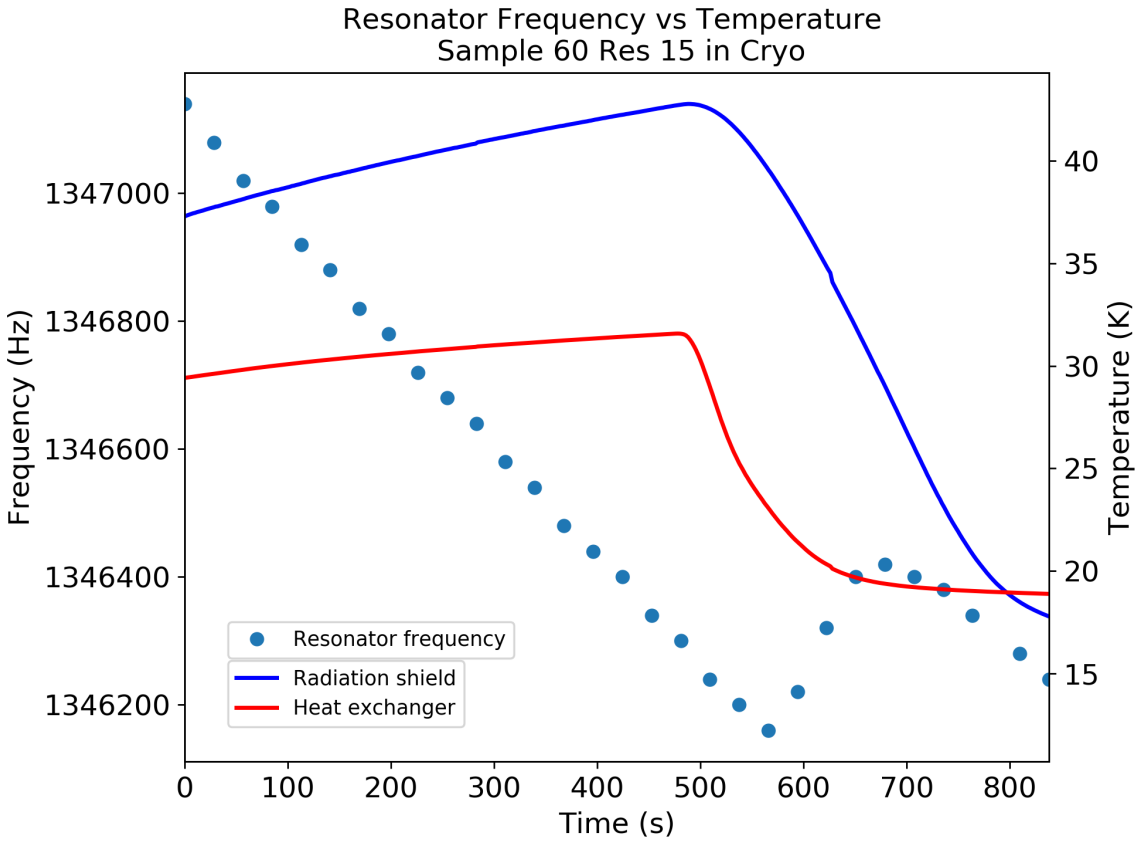
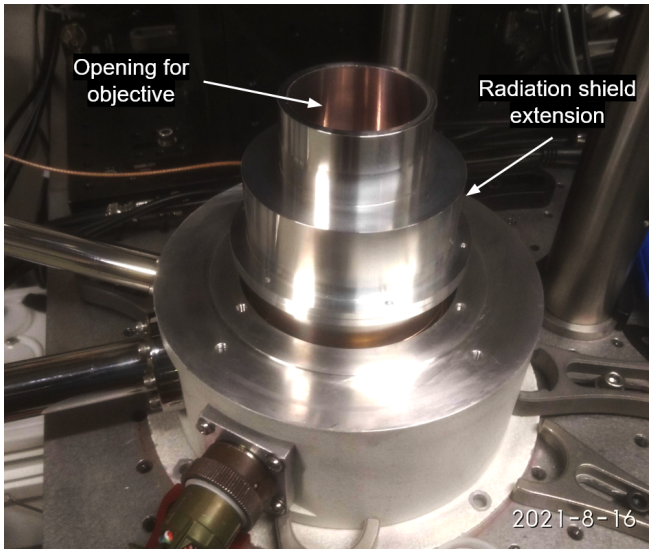
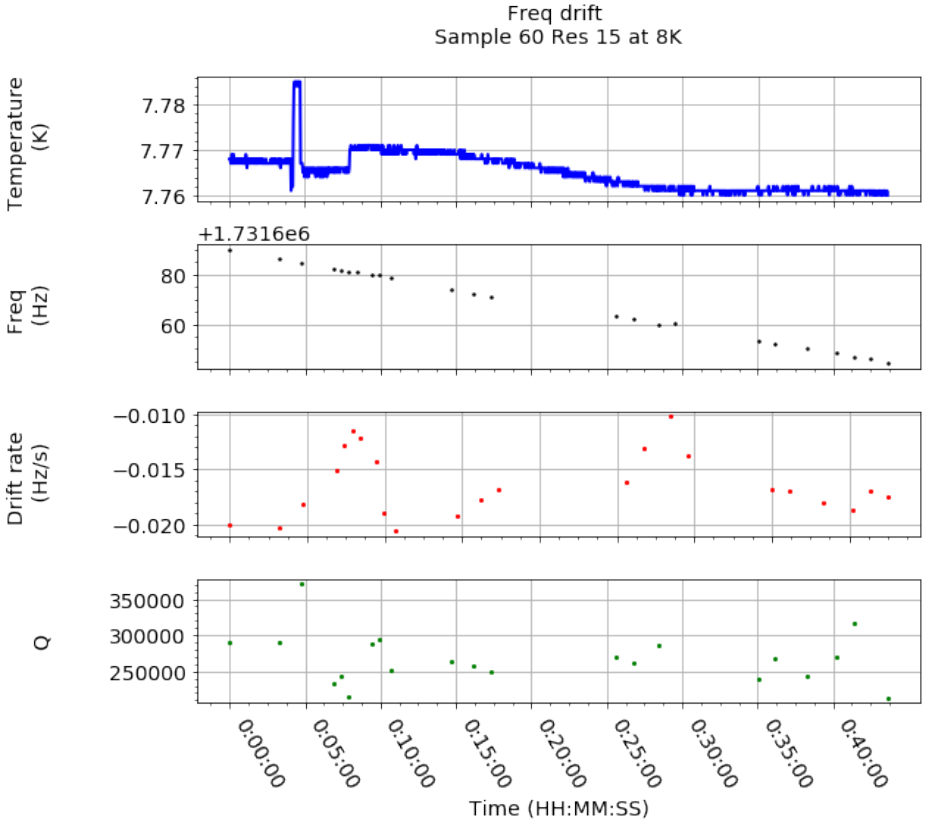


Figure 6.5: Upon cooling the cryostat from 30 K to 20 K, the resonator frequency momentarily increases before resuming its downward drift.



(a)



(b)

Figure 6.6: (a) Photo of the radiation shield extension. (b) The frequency drift rate is reduced by 2 orders of magnitude for the same nanobeam after the installation of the shield extension.

correction collar. The correction collar will have to be adjusted before pumping down the cryostat; alternatively, the cryostat can be modified such that the objective is no longer in vacuum. The second approach is to cool down the objective as well. Unfortunately, the current selection of high-NA, broadband, cryo-compatible objectives with long working distance is limited.

The second design issue concerns the temperature distribution inside the cryostat. In general, it is good practice, especially during the cooldown process, to ensure that the sample is not the coldest part inside the cryostat, to avoid cryopumping contaminants onto it. In the future, a heater can be integrated onto the sample mount to allow for independent control of the sample temperature, such that it is several degrees hotter than the base temperature.

6.3 Magnetically Functionalized Soft-Clamped Resonators

6.3.1 Hierarchical Resonators

As mentioned in the introduction to this chapter, the previous decade has seen remarkable increases in the quality factors of silicon nitride resonators. This development might be somewhat counterintuitive, given the relatively high intrinsic mechanical loss ($Q_{int} \sim 1 \times 10^3$) compared to crystalline materials such as silicon and diamond ($Q_{int} \sim 1 \times 10^5$) [46]. The saving grace of silicon nitride is its versatility in nanofabrication: in particular, highly stressed thin films of silicon nitride can be fabricated easily. The high tensile stress gives rise to a phenomenon known as dissipation dilution, allowing for quality factors much higher than the nitride's intrinsic quality factor [46].

For dissipation dilution to be effective, care must be taken to reduce so-called bending losses near the clamping points. For a simple nanobeam, the finite bending rigidity leads to a high curvature near the clamping points and correspondingly high clamping bending losses. Several approaches to reduce bending losses have been taken. The first is phononic crystal (PnC) soft-clamped devices: a single defect inside the crystal gives rise to an isolated

mode inside the crystal's bandgap. The PnC serves two purposes: the bandgap structure reduces losses from the defect mode into the substrate (i.e. radiative loss), while the extent of the crystal reduces the bending curvature at the clamping points (i.e. soft-clamping). Such PnC devices have achieved quality factors of 8×10^9 at room temperature [55].

A more recent approach takes inspiration from hierarchical structures that often appear in nature, such as in coastlines, blood vessels, and spiderwebs [134]. A nanobeam is embedded inside a binary-tree structure; contrary to a simple nanobeam, the nanobeam is subdivided into pairs of branches repeatedly, such that the clamping points are spread out to achieve soft-clamping. Such resonators have achieved quality factors of 1×10^9 at 8 K [23]. Notably, it is the fundamental mode that is soft-clamped, with large frequency separation from higher-order modes. This is in contrast to PnCs, where the defect mode can be affected by thermomechanical noise from other high-order modes outside of the bandgap.

Fig. 6.7 shows one of such fractal resonators from our collaborators in Prof. Simon Gröblacher's group. Details of the fabrication can be found in [64, 63]. For a bare resonator (before functionalization), the effective mass is calculated to be about 1.6×10^{-14} kg, with measured frequency of roughly 1 MHz and quality factors up to 4×10^7 at cryogenic temperatures (see Fig. 6.8) [63].

Just as we did for simple nanobeams, we can also functionalize the fractal resonators by pick-and-placing neodymium micromagnets onto them, following the procedure in Chapter B. While the functionalization process causes about an order-of-magnitude decrease in the quality factor at room temperature, the quality factor recovers significantly at $\sim$ 10 K and approaches 1×10^7 [78]. We have measured the quality factors of resonators functionalized using different epoxies (or none), but have not found an obvious difference in the resulting quality factors at cryogenic temperatures. The results are presented in Fig. 6.9.

Effect of IR Laser on Mechanics

We have also seen that the IR laser can affect the quality factor of these fractal resonators [19]. In Fig. 6.10, we plot the quality factor of a functionalized fractal resonator with respect

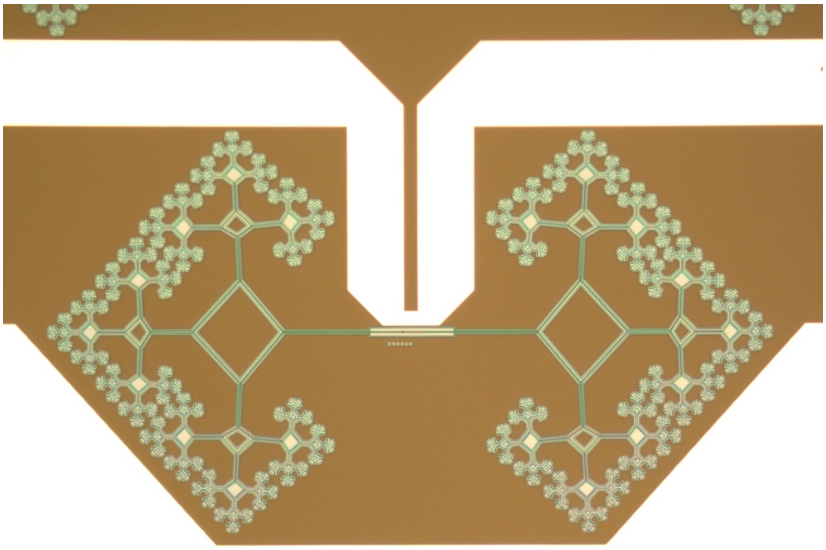


Figure 6.7: Photo of a fractal resonator fabricated in Simon Gröblacher's group, taken with an optical microscope. A coplanar waveguide is fabricated on the same chip, with constrictions near the center of the resonator, to deliver microwaves for manipulating the NV center's spin state.

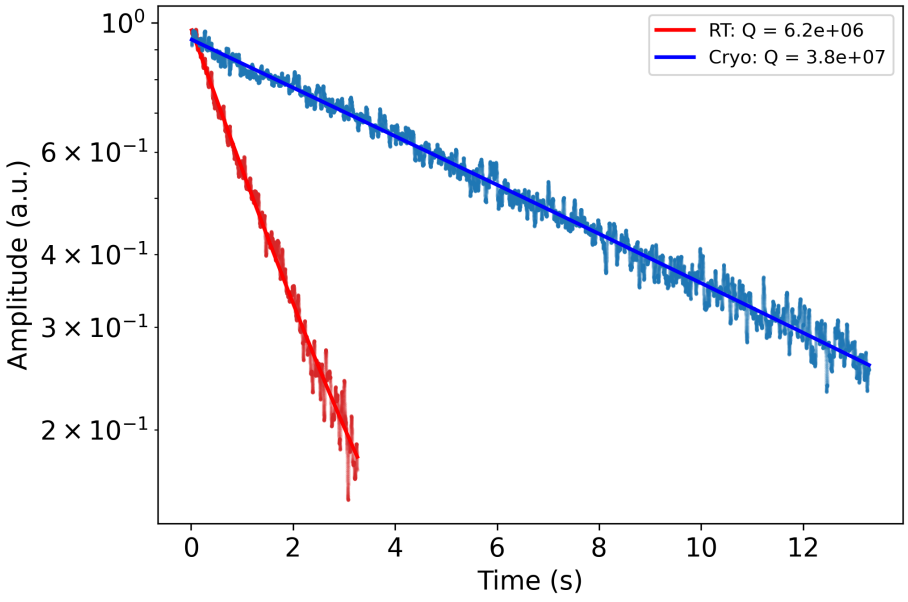


Figure 6.8: Ringdown measurements of a bare (not functionalized) resonator at room and cryogenic temperatures.

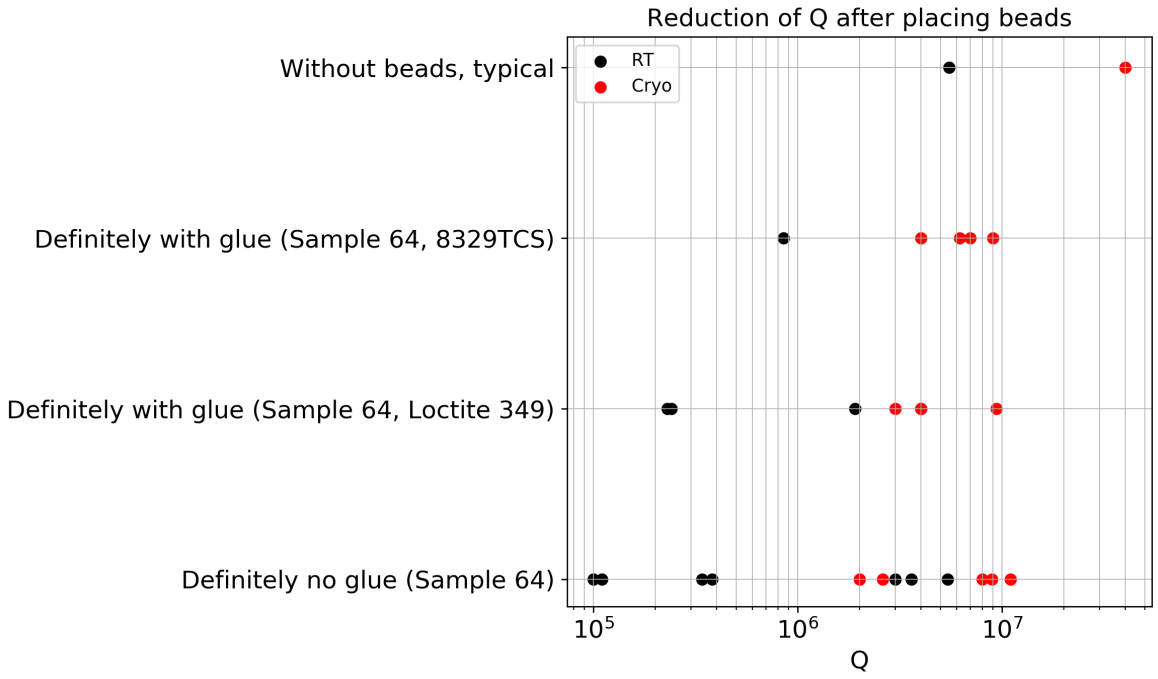
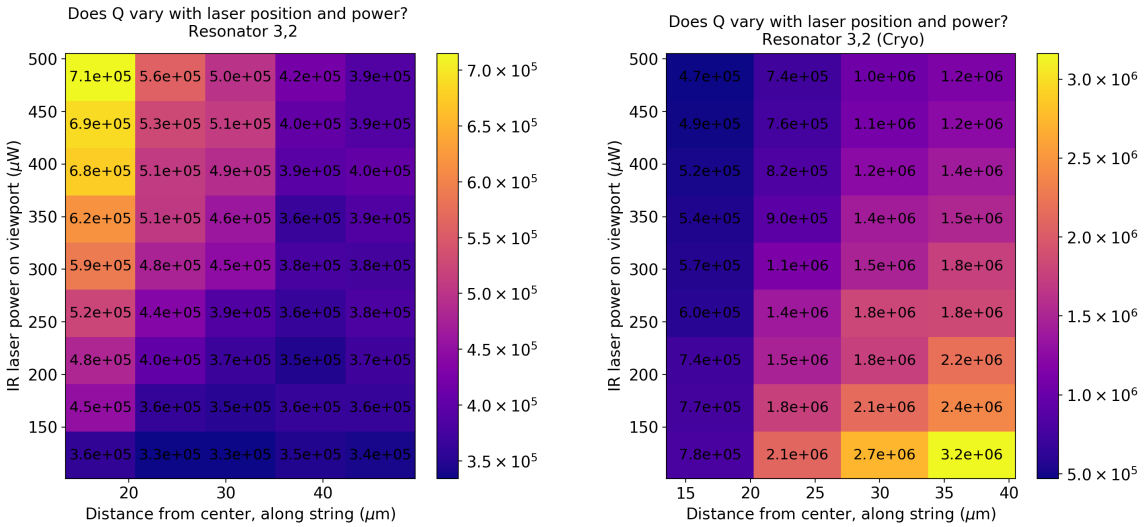


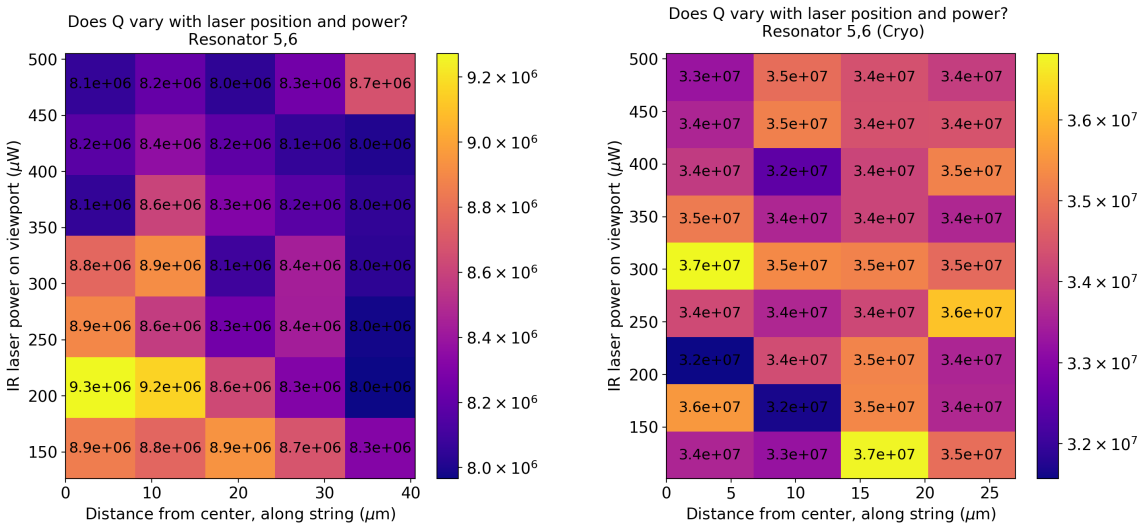
Figure 6.9: Quality factors of multiple fractal resonators functionalized with neodymium micromagnets. The micromagnets are attached with different types of epoxy, or simply with electrostatic forces. In particular, the two epoxies are 8329TCS (MG Chemicals), which is heat-cured and has high thermal conductivity, and Loctite 349, which is UV-cured. For about half of the functionalized resonators, the quality factor approaches or even exceeds 1×10^7 at $\sim 10\,\mathrm{K}$.



(a) **(b)**

Figure 6.10: (a) The quality factor of a magnetically functionalized (with neodymium microsphere) fractal resonator is plotted as a function of the interferometer's laser power and the laser spot's position relative to the center of the resonator. We see that with increasing laser power and a laser spot close to the magnet, the quality factor is at its maximum (i.e. laser has an anti-damping effect). (b) The same measurement is repeated at cryogenic temperature ($\sim 14\,\mathrm{K}$), showing an opposite effect. The quality factor is maximized with low laser power and the laser spot far away from the magnet (i.e. laser has a damping effect).

to both the interferometer's infrared (IR) laser power and the laser spot position. At room temperature, the IR laser appears to have an optical damping effect, such that the quality factor decreases with higher laser power and a laser spot closer to the magnet. At 14 K, the effect is reversed: the IR laser appears to have an anti-damping effect. Such damping and anti-damping effects can be rather significant, with the quality factor varying by several times its minimum in the plotted measurements. We also note that this effect is likely related to the magnet, as shown in a reference measurement of a bare resonator, where such optical damping effects are not noticeable (Fig. 6.11).



(a) **(b)**

Figure 6.11: The measurements in Fig. 6.10 are repeated for a bare resonator at room temperature (a) and $\sim 14\,\mathrm{K}$ (b). No clear relationship is observed between the quality factor and the laser power and spot position.

6.3.2 Nanobeam Resonators with Torsional Supports

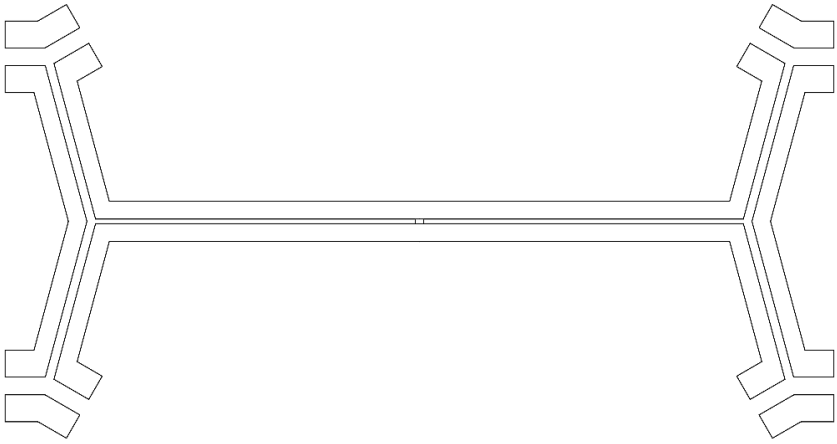
While the quality factor measurements are encouraging, we have unfortunately been unable to utilize the fractal resonators functionalized with neodymium micromagnets. The main issue is the demagnetization of the neodymium caused by the green laser used for the NV spin state initialization and readout, as explained in Sec. 4.6.1. To address this issue, we have begun work on adapting the fabrication process to incorporate iron thin film magnets (see Sec.7.2). A notable challenge is that the original recipe uses SF6 gas to release the resonators. However, due to cleanroom limitations and concerns about SF6 attacking the iron, we have been limited to using XeF2 gas for the release. The XeF2 etch is isotropic and the etch rate is highly sensitive to the exposed area of silicon. While this aspect can be easily managed with the geometry of a single nanobeam, it becomes much harder with the complicated geometry of the fractal design. The significantly different exposed areas of silicon at different parts of the fractal design means that some parts are released much earlier than others. As a result,

we have had difficulty releasing a fractal resonator without significant overetching in some areas, which leads to low quality factors ($< 1 \times 10^4$).

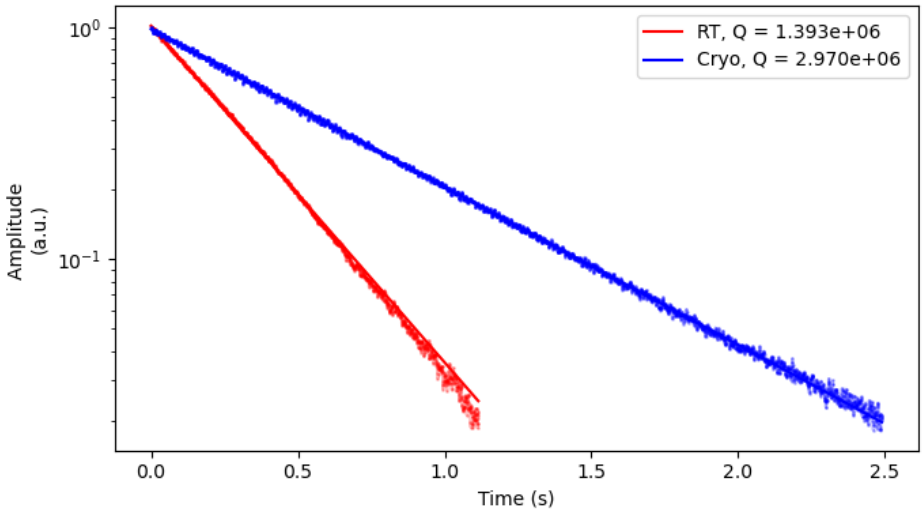
There are several potential solutions. One is to adjust the geometry of the exposed silicon to achieve a more uniform release process. Another is to test the SF6 release on resonators with iron thin film magnets deposited on top, and check if the magnet properties suffer any degradation.

In the mean time, we have initiated another effort to redesign the fractal resonators from the ground up. The idea is that we would test the release process with a one-layer fractal design, and if the resulting quality factor is satisfactory, repeat the process with an extra layer. The rationale is that we might be able to obtain large increases in the quality factor using a fractal design with only 1 or 2 layers, with a relatively small increase in the complexity of the fabrication.

For a simple nanobeam with torsional supports, we have obtained quality factors of 1.3×10^6 at 14 K. For a two-layer fractal design, we have obtained quality factors of 3.0×10^6 at similar temperatures (Fig. 6.12).



(a)



(b)

Figure 6.12: (a) Design of a double fractal resonator. The width of the nanobeam at the center is 1 µm. The rectangle at the center of the nanobeam is the iron thin-film magnet, measuring 2 µm long and 1 µm wide. (b) Ringdown measurement of a double fractal resonator, with quality factor of 3×10^6 at 14 K.

Chapter 7

Nanomechanical Sensing of a Single NV Center

7.1 Introduction

In the previous chapter, we discussed how we were able to use the NV center to sense the mechanical motion via AC magnetometry, and thereby extract the spin-mechanical coupling strength. A question then arises: is it possible to swap the two elements, and use the mechanical resonator to sense the state of the NV center? In other words, is it possible to detect single-spin "backaction" on the mechanical resonator?

There are several reasons why this measurement would be interesting and worthwhile. For one, this is very much related to the field of magnetic resonance force microscopy (MRFM), where nanomechanical resonators are used to image spins. First proposed in 1991, MRFM can be thought of as the mechanical analog of magnetic resonance imaging (MRI) [136]. In MRI, the precession of a collection of spins is detected by pickup coils, and spatial resolution is achieved by applying a magnetic field gradient of tens of mT/m. In MFRM, a magnetically functionalized cantilever is brought close to a collection of spins, and by flipping their magnetic moments at the cantilever's resonant frequency, the spins can be detected in the form of a mechanical excitation. Spatial resolution is determined by the

magnetic field gradient from the cantilever, which can be on the order of $1 \times 10^6\,\mathrm{T/m}$. To date, MRFM has demonstrated sensitivity down to a single electron spin, and a spatial resolution of less than 1 nm [127, 60].

While most MRFM experiments to date have used cantilevers, there have been proposals to use alternative mechanical resonators such as membranes and nanobeams. Recent advances in nanofabrication and resonator design have led to mechanical resonators with ultrahigh quality factors reaching 1×10^{10} and force sensitivities down to $4 \times 10^{-19}\,\mathrm{N}/\sqrt{\mathrm{Hz}}$ [19, 21]. These alternative resonators also offer interesting new modalities: for example, coupled modes in a single membrane or between different nanobeams can be used to frequency-upconvert a low-frequency spin signal [81, 21]. The detection of a single NV center with a nanobeam will therefore be a convincing demonstration of the utility of these alternative resonators for MRFM and force sensing in general.

Another aspect is the spin in question. The tour de force demonstration of single-spin detection in 2004 uses singly occupied silicon dangling bonds, known as E′ centers [127]. However, E′ centers are not widely considered for quantum information processing, in part due to their low coherence times on the order of µs [8, 56, 142]. On the other hand, NV centers are well-suited for quantum information processing, with coherence times up to seconds and well-established control methods [9, 6]. A demonstration of single-NV detection via mechanical readout offers an alternative readout mechanism for not just NV centers, but also other "dark" solid-state spin qubits without an optical readout mechanism.

A sufficiently strong spin-dependent force is required to realize proposals that use the spin to cool the mechanics or prepare non-classical mechanical states [116, 115, 107]. Moreover, as we will show in subsequent sections, the experimental scheme used to detect the backaction of a single NV center is very similar to the protocol used to generate spin-spin entanglement via projective mechanical readout. Substantial technical improvements are needed to enable single-NV detection, in particular increases in the spin-mechanical coupling strength and mechanical quality factor. Another challenge, which might not be obvious at first glance, is the careful design of the pulse sequence to control the spin, such

that the pulses do not cause spurious classical effects on the mechanical resonator. Both the improvement in system parameters and design of spin-control pulse sequences are also critical to the eventual goal of enabling mechanically-mediated spin-spin interactions.

7.2 High Gradients with Iron Thin Film Magnets

In Chapters 3 and 4, most of the mechanical resonators were functionalized with neodymium micromagnets. However, there are a few limitations to these magnets. Their effective magnetic remanence is usually less than 20% of their theoretical value of 0.7 T, likely due to the previously reported problem of surface oxidation (Sec. 4.4). Furthermore, they are highly prone to demagnetization from the green laser needed to perform initialization and readout of the NV center (Sec. 4.6.2). The method of functionalization, which involves manually gluing neodymium microspheres onto the nanobeam, is also not scalable and often contaminates the sample, leading to inconsistent mechanical frequencies and quality factors.

These experimental challenges led us to return to the iron thin-film magnets used in Chapter 2. Given that the magnets are directly fabricated onto the nanobeam, the mechanical frequencies and quality factors are much more consistent. Importantly, the shape and thickness of the iron magnets can be defined precisely using electron beam lithography, allowing us to optimize for the highest gradients. The fabrication process can eventually be adapted for better magnet materials such as SmCo for even higher gradients and addition of reflective capping layers for resilience against oxidation and laser demagnetization.

7.2.1 Coupling Measurement

In this section we outline a measurement of the spin-mechanical coupling between the NV center and a nanobeam functionalized with an iron thin-film magnet, similar to the previous measurement in Sec. 5.4.

After cooling down the cryostat, we approach the sample with the nanopillar, guided by a series of contour scans to locate the high-field region of the micromagnet. Some example

scans are shown in Fig. 7.1, showing the high-field regions to be localized around the corners of the magnet.

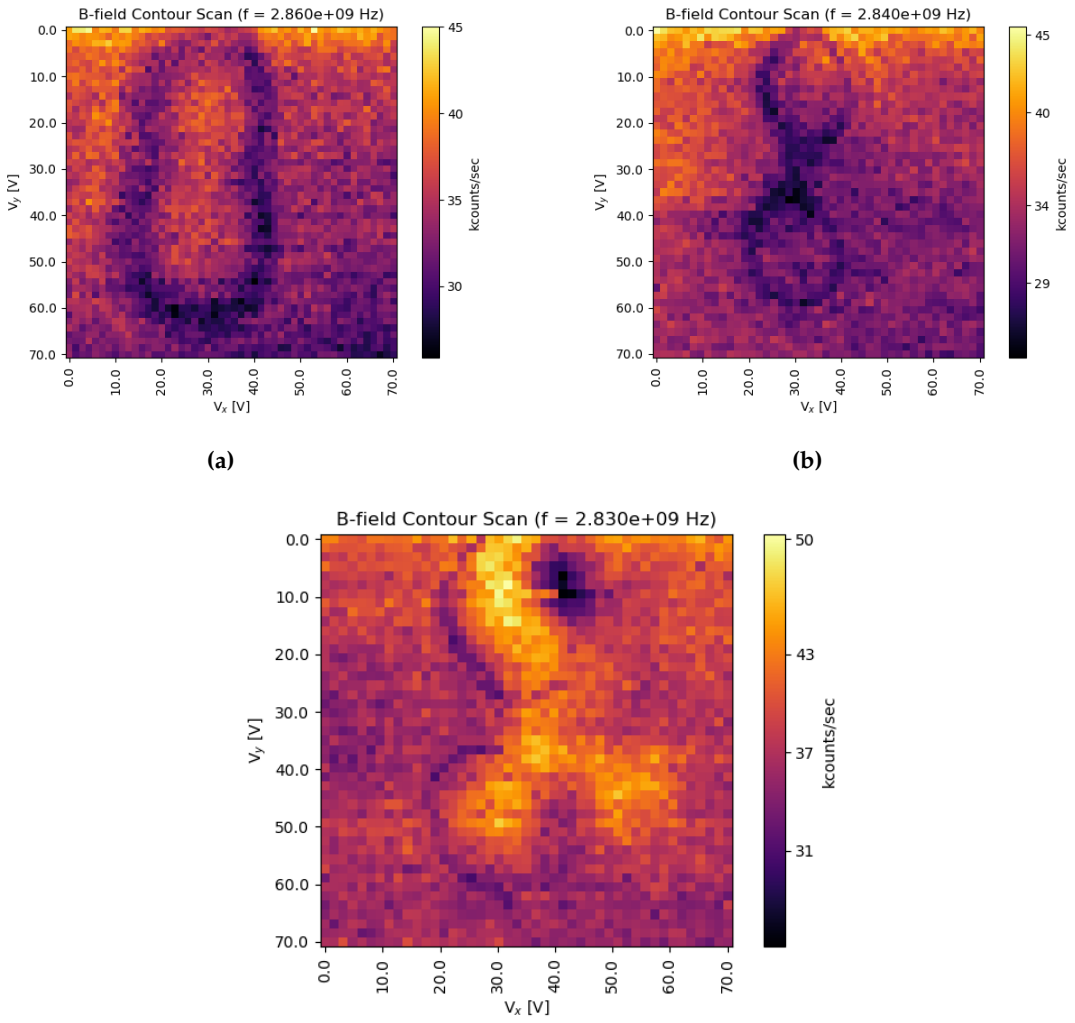
Parking the nanopillar at one of the two contours, we measure the magnetic field gradient at the NV center's location, by monitoring the ESR frequency as we decrease the NV-magnet distance. The results are plotted in Fig. 7.2, showing a maximum gradient of $1.3 \times 10^5\,\mathrm{T/m}$, which is more than 6 times the gradient measured in Chapter 5.

At these high gradients, we can readily excite the nanobeam such that the oscillating micromagnet broadens the NV center's ESR. Examples of the broadened ESRs are shown in Fig. 7.3 (a,b). Assuming that the micromagnet's motion is purely sinusoidal, one can fit the broadened ESR lineshape to an analytical function and obtain the amplitude of the oscillating magnetic field along the NV center's axis.

A plot of the magnetic field oscillation amplitude versus the mechanical drive amplitude is shown in Fig. 7.3(c), with a linear fit giving $0.46\,\mathrm{G/mV}$. For the measurements in the plot, the ESR is centered at 2.64 GHz, corresponding to a field of 88 G. Referring back to Fig. 7.2, the expected gradient at this point is about $1 \times 10^5\,\mathrm{T/m}$. This then allows us to obtain a calibration of the physical (peak-to-peak) displacement of the nanobeam versus drive amplitude: $(0.46\,\mathrm{G/mV})/(1 \times 10^5\,\mathrm{T/nm}) = 0.46\,\mathrm{nm/mV}$.

Afterwards, we measure the mechanical motion by performing AC magnetometry using the NV center. A clear effect on the spin-echo signal is seen as we increase the driven amplitude of the nanobeam, as shown in Fig. 7.4. Just as in Fig. 5.4, we normalize the spin-echo signal to a baseline measurement with the mechanical drive turned off, resulting in the plot in Fig. 7.5.

Unlike the measurement in Fig. 5.4, however, the resonator is driven coherently and not with a broadband drive. This is made possible due to upgrades in the experimental setup, which allows us to drive the resonator on resonance in the presence of frequency drift using a phase-locked loop (PLL). Fitting the normalized spin-echo measurement to an analytical function, we extract the spin-mechanical coupling strength to be 30 Hz, a factor of ~ 4 increase from the measurement in Fig. 5.4.



(a) **(b)**

(c)

Figure 7.1: (a,b,c) A series of Contour scans of the iron micromagnet during the NV-magnet approach (NV-magnet distance reduces from top to bottom). Two separate contours emerge, corresponding to two corners of the rectangular magnet.

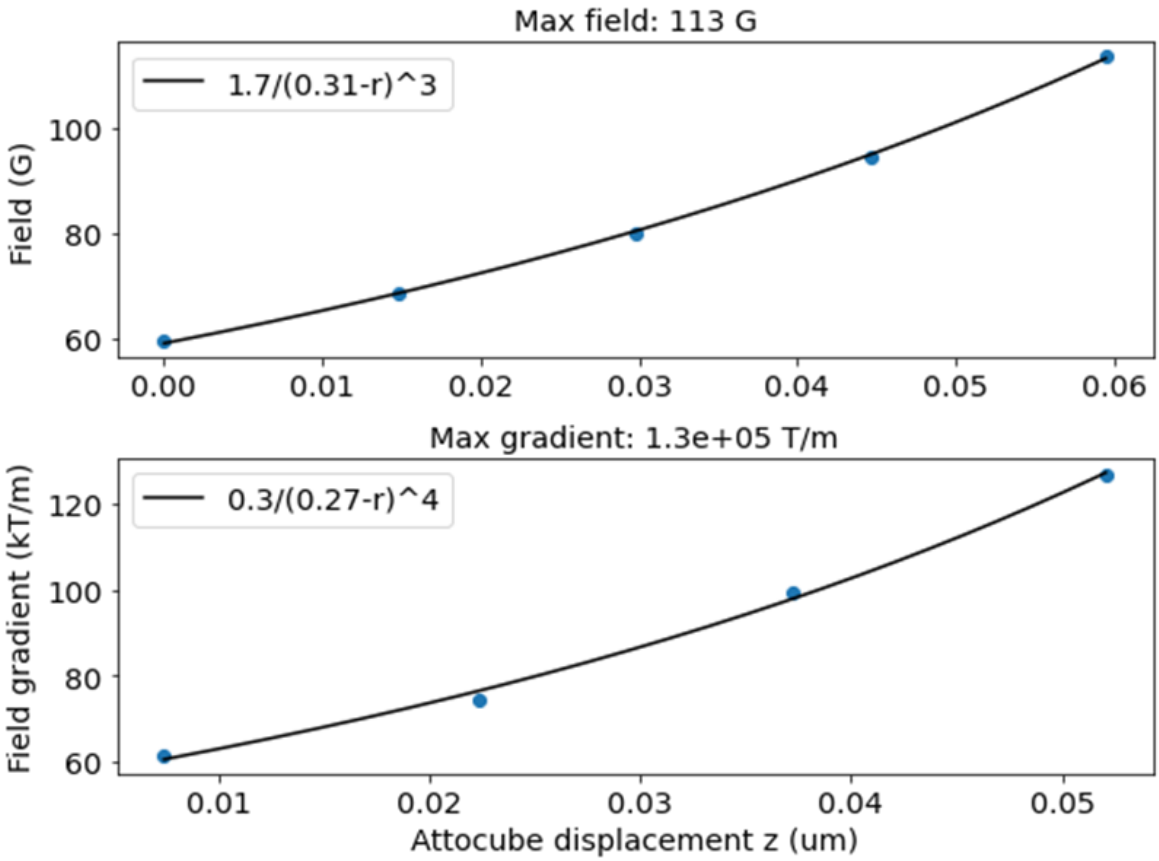


Figure 7.2: By monitoring the NV center's ESR frequency as we decrease the NV-magnet distance, we can measure changes in the magnetic field and therefore the field gradient.

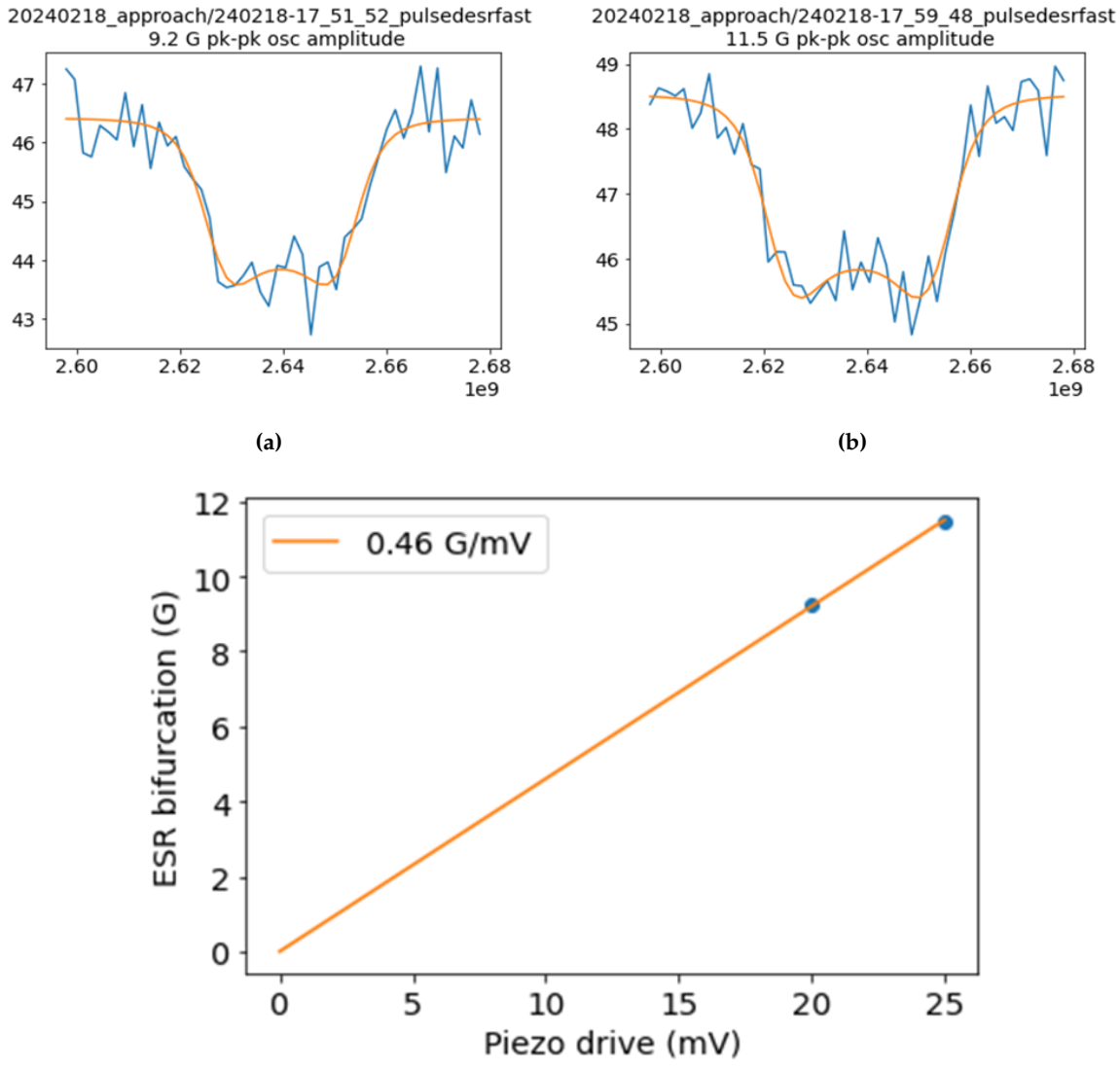
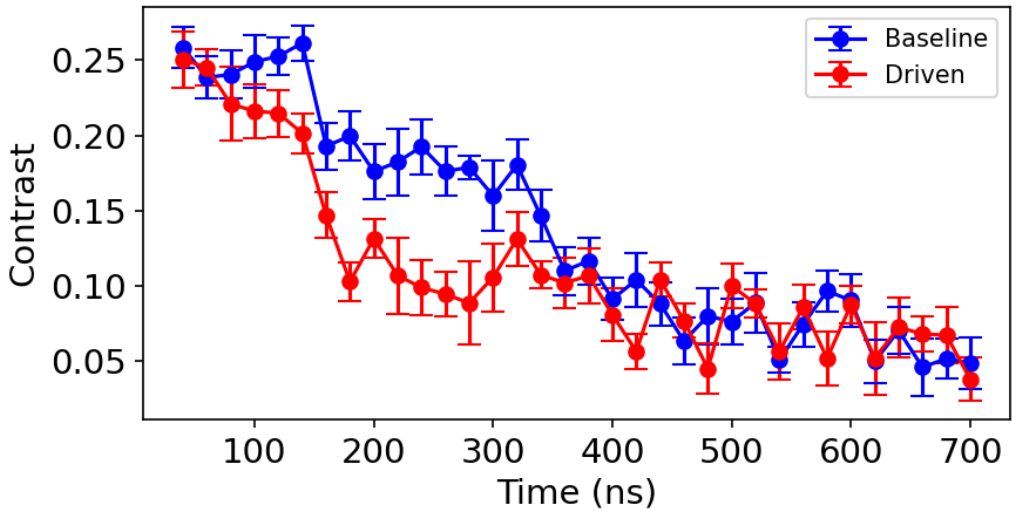
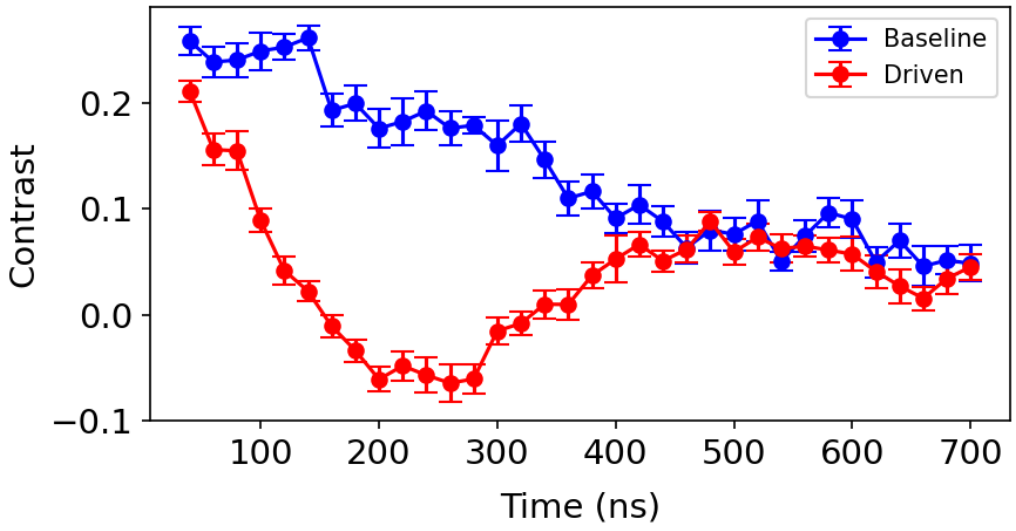


Figure 7.3: (a,b) ESR measurements for different drive amplitudes of the nanobeam. As the nanobeam is driven with a higher drive amplitude, the oscillating micormagnet causes the ESR lineshape to broaden. For the two drive amplitudes 20 mV (a) and 25 mV (b), we can fit the broadened lineshape to determine the magnetic field oscillation amplitude to be 9.2 G and 11.5 G respectively. (c) Plotting the magnetic field oscillation amplitude as a function of the external piezo drive, we can fit the results using a linear function with zero intercept.



(a)



(b)

Figure 7.4: (a,b) Spin-echo measurement of the mechanical motion. As the amplitude of the mechanical drive is increased (1 mV and 2 mV for (a) and (b) respectively), the effect of the oscillating micromagnet has a more prominent effect on the echo signal. The baseline measurement is taken with the mechanical drive turned off.

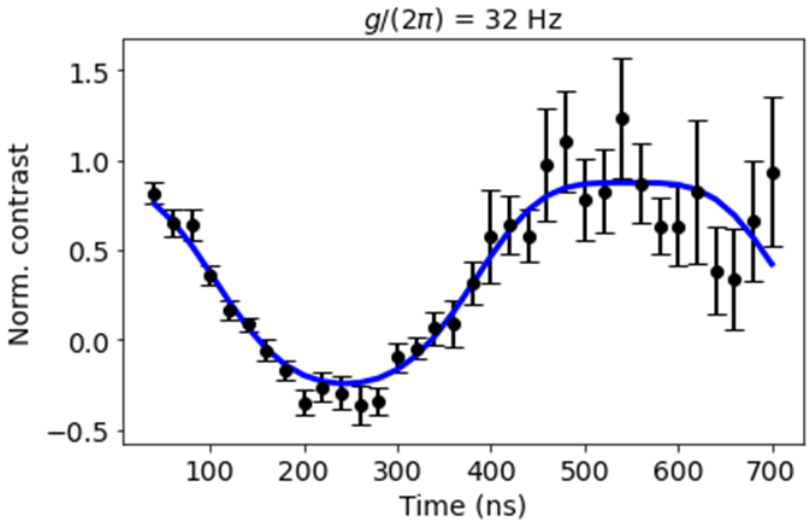


Figure 7.5: Normalized spin-echo signal, with a drive amplitude of 2 mV, which corresponds to a nanobeam displacement amplitude of 0.92 nm. Fitting the normalized signal to an analytical function, we obtain a coupling strength of 30 Hz.

7.2.2 Additional Gradient Measurements

Higher magnetic field gradients have been measured on iron micromagnets since the results in the previous section. An exemplary measurement is shown in Fig. 7.6, showing gradients approaching 3×10^5 T/m, corresponding to a coupling strength of ~ 110 Hz.

7.3 General Detection Scheme

7.3.1 Pulse Sequence

To excite the mechanical resonator with the spin, one simple scheme is to flip the latter's magnetic moment at twice the mechanical frequency. Since the mechanical resonator is coupled to the spin via a magnetic field gradient, the spin flips will drive the mechanic mode on resonance. The resulting mechanical excitation can then be detected via interferometric readout.

A simple sequence to achieve this is shown in Fig. 7.7. A series of microwave (MW) π pulses are applied on the NV center, causing the spin state to flip between $|0\rangle$ and $|1\rangle$ at

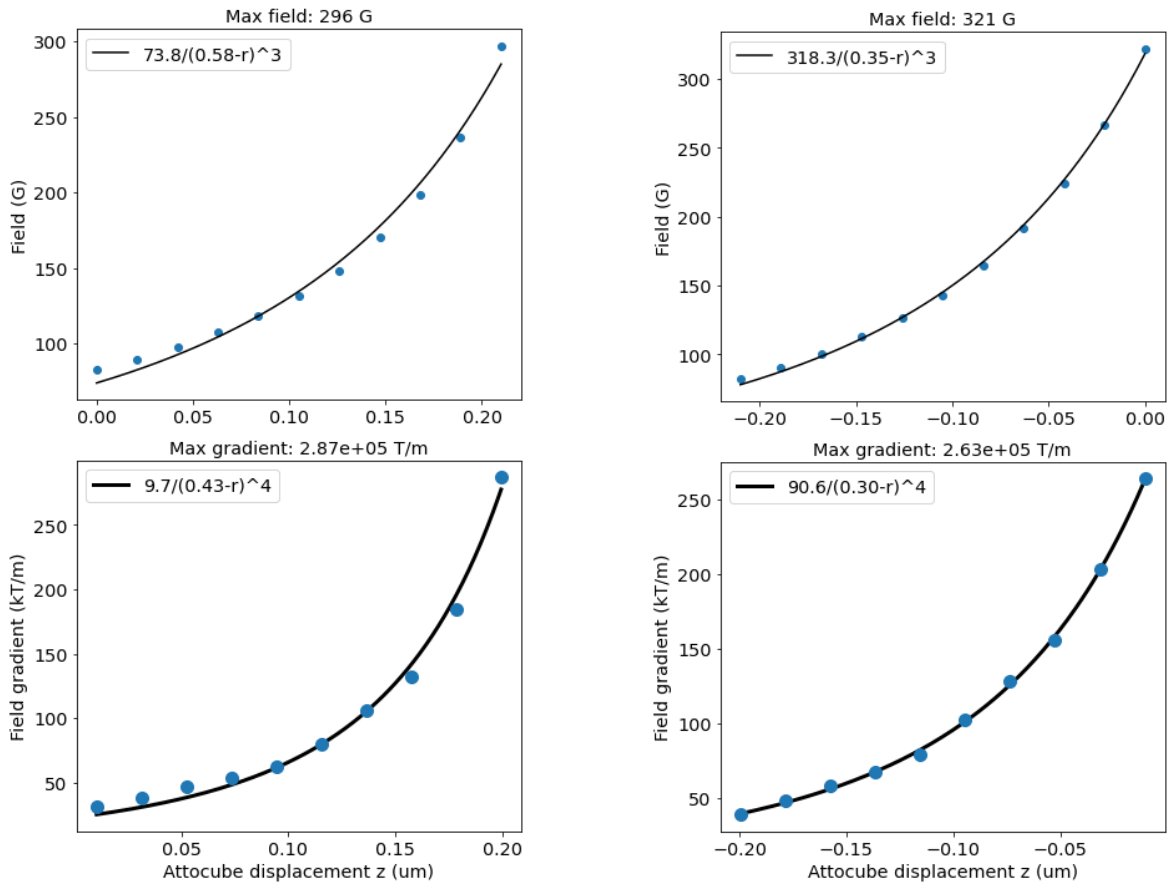


Figure 7.6: (a,b) By monitoring the NV center's ESR frequency as we change the NV-magnet distance, we can measure changes in the magnetic field and therefore the field gradient. To avoid misleading measurements due to drift during the gradient measurement, we measure the gradient as we approach (a) and then retract (b) the nanopillar from the micromagnet. By confirming that both field curves look similar, we can also confirm that "snap-in" did not occur at the rightmost data point, where the nanopillar is the closest to the magnet. "Snap-in" is a phenomenon in AFM where the tip snaps into contact with the sample at small separation distances [141]. In the context of this experiment, "snap-in" would result in misleadingly large gradients. If "snap-in" did occur, the field will instead remain "stuck" at the maximum value in the retraction curve.

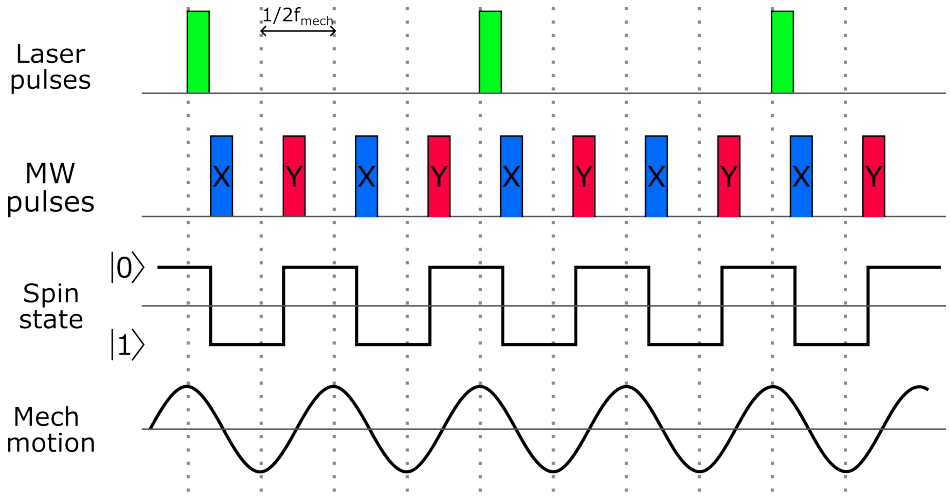


Figure 7.7: Basic pulse sequence (LX Y X Y) for performing spin flips to excite the mechanical resonator. At each mechanical half-period, a trigger signal (gray dashed line) is sent to the pulse generator, which sends a combination of laser and MW π pulses.The phase of the MW pulses is alternated by 90° (X and Y) to mitigate pulse errors. Laser pulses are applied periodically to correct for pulse errors and mitigate lifetime decay of the spin state. Note that they must be applied every even number of mechanical half-periods, such that the reinitialization to spin state $|0\rangle$ is in sync with the spin drive.

twice the mechanical frequency. To reduce errors, we follow the well-known XY scheme, where the phase of the π pulses is alternated between 0° (X) and 90° (Y). However, even with perfect pulses, we expect the amplitude of spin flips to decay over time, due to the NV center's finite coherence time. Given that the quality factor of the nanobeam is on the order of 1×10^6, we would need roughly the same number of MW pulses to excite the nanobeam to its full amplitude. For a typical π pulse time of 50 ns, the total duration of these pulses will be on the order of 50 ms, which is much longer than the usual spin coherence time.

To maintain the average amplitude of the spin flips, we periodically reinitialize the NV center with green laser pulses. Since the reinitialization brings the spin state back to the $|0\rangle$ state, to maintain the phase coherence of the spin flips, we must apply these pulses every $2n$ MW pulses. For example, if we were to apply a green laser pulse every $2n + 1$ MW pulses, the spin flips will occur with an opposite phase after every laser pulse, leading to self-cancellation of the spin's effect on the nanobeam.

For the rest of this chapter, pulse sequences will be labeled according to the following

convention (using the above sequence, shown graphically in Fig. 7.7, as an example):

$$\text{LX Y X Y} \tag{7.1}$$

where L, X, and Y denote a laser pulse, a MW X pulse (0°), and a MW Y pulse (0°). It is implied that the pulses in the label will be repeated indefinitely. Each segment in the label represents the pulses within a mechanical half-period. For example, LX means that a laser pulse followed by a MW X pulse is applied within the same mechanical half-period. Additionally, we denote the absence of a MW pulse with 0, which will be useful later in this chapter.

7.3.2 Sideband Modulation

The pulse sequence in Fig. 7.7 flips the NV center's electron spin periodically to excite the mechanical resonator. A crucial requirement is that the spin must flip at precisely twice the mechanical frequency. However, as discussed in Sec. 6.2, the mechanical frequency drifts by more than a linewidth every few seconds in cryogenic temperatures. As a result, the spin drive will also become off-resonant with the mechanical resonator within a similar time scale.

It is therefore crucial to lock the repetition frequency of the π pulses to the mechanical frequency. This can be accomplished with a phase-locked loop (PLL) on the lock-in amplifier used to read out the mechanical motion. A coherent excitation is used to drive the mechanics, either with a piezo chip or the sample's coplanar waveguide. When the drive is on resonance with the mechanics, the mechanical resonator's motion and the drive differs in phase by 90°. By monitoring the phase of the mechanical motion and adjusting the drive frequency to maintain the phase of the mechanical motion at 90°, we can ensure that the drive is always on resonance. In practice, the phase on resonance will differ from 90°, due to the finite length of cables between the lock-in amplifier and the cryostat, as well as the phase response of the driving element. The correct phase setpoint can be determined by sweeping the drive frequency around the mechanical resonance and noting the phase where the driven

amplitude is at its maximum.

With the PLL enabled, we can also configure the lock-in amplifier to output a sinusoidal signal at twice the tracked mechanical frequency. This signal at $2f_{mech}$ is then converted into a square wave using a home-built Schmidt trigger, before being sent to the PulseBlaster which generates the gating pulses for the laser and microwaves (Fig. 3.8). This configuration ensures that the π pulses will be sent at twice the mechanical frequency in the presence of frequency drift.

However, we are now confronted with another problem, as illustrated by Fig. 7.8. For the PLL to lock properly to the mechanical resonance, we have found that we typically need to drive the mechanical motion to several nanometers. In the frequency domain, this external coherent drive leads to a large narrow peak (blue) at the mechanical resonance. On the other hand, the contribution to the driven motion from the spin is on the order of $z_p g/\kappa$, where g, z_p and κ are the spin-mechanical coupling strength, mechanical zero-point motion and linewidth respectively. For $g = 100\,\mathrm{Hz}$, and $z_p \sim 1 \times 10^{-14}\,\mathrm{m}$, the spin-driven motion is only about 1 pm. Detecting such a small signal on top of a large background represents a significant experimental challenge, notwithstanding the typical large amount of $1/f$ noise near the resonance, due to factors such as slow drift of the detection sensitivity and instabilities in the PLL.

One solution to this problem is to shift the spin signal away from the resonance via amplitude modulation (Fig. 7.9). The spin force is turned on and off at frequency f_{mod}. This can be achieved by, for example, changing the frequency of the MW pulses to be on-resonant and off-resonant every $1/f_{mod}$. As a result of this amplitude modulation of the spin force, the spin signal shows up as two sidebands around the mechanical resonance. Care must be taken in choosing f_{mod}. It cannot be too low, otherwise the sidebands will be too close to the large peak from the external coherent drive. As mentioned earlier, $1/f$ fluctuations can cause leakage of the large peak into surrounding frequencies, resulting in a higher noise background. On the other hand, f_{mod} cannot be too high. We note that both the spin signal and thermal noise scale the same with frequency (following the mechanical

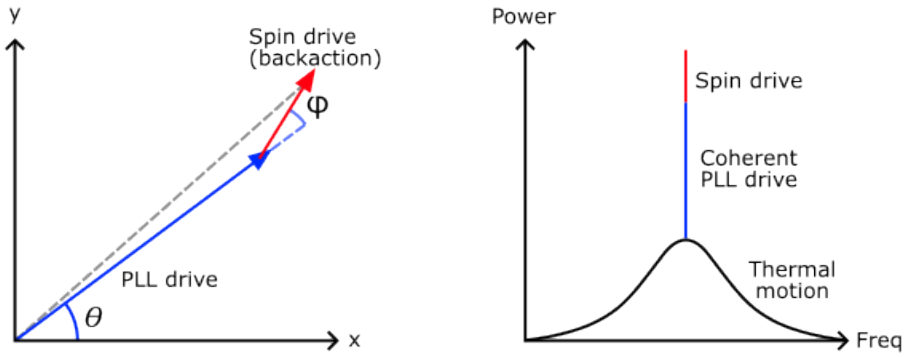


Figure 7.8: Spin signal in phase space and the frequency domain. Left: The external coherent drive for the PLL is shown in blue. Flipping the NV center's magnetic moment at twice the mechanical frequency results in an additional excitation of the mechanical resonator, indicated by the red arrow. The phase of the "spin drive" relative to the PLL drive is denoated ϕ, and can be adjusted with the delay of the MW π pulses on the NV center. To maximize the spin signal, ϕ should be either 0° or 180°. Right: Mechanical motion in the frequency domain. The thermal motion is shown as a Lorentzian (black), and the excitations from the PLL and spin drives are shown in blue and red respectively.

susceptibility), resulting in the same signal-to-noise ratio (SNR). However, this is only true when the thermal noise dominates over the measurement noise. For a f_{mod} much higher than the mechanical linewidth, the measurement noise dominates and stays somewhat constant, while the spin signal is drastically reduced, resulting in poor SNR. Based on our calculations and typical linewidths of 1 Hz, we typically choose f_{mod} to be about 3 Hz.

The spin signal can be further enhanced by modulating the phase of the spin force. Instead of turning on and off the spin force at f_{mod}, its phase can be toggled between ϕ and $\phi + 180^\circ$, where ϕ is the phase between the spin force and the external coherent drive required for the PLL. ϕ can be adjusted within the lock-in amplifier, by changing the phase delay between the mechanical motion and the trigger signals for the MW and laser pulses. Toggling between ϕ and $\phi + 180^\circ$ can be done via the same principle. Another way to do this is to shift the pulse sequence by one mechanical half-period, as showin in Fig. 7.11.

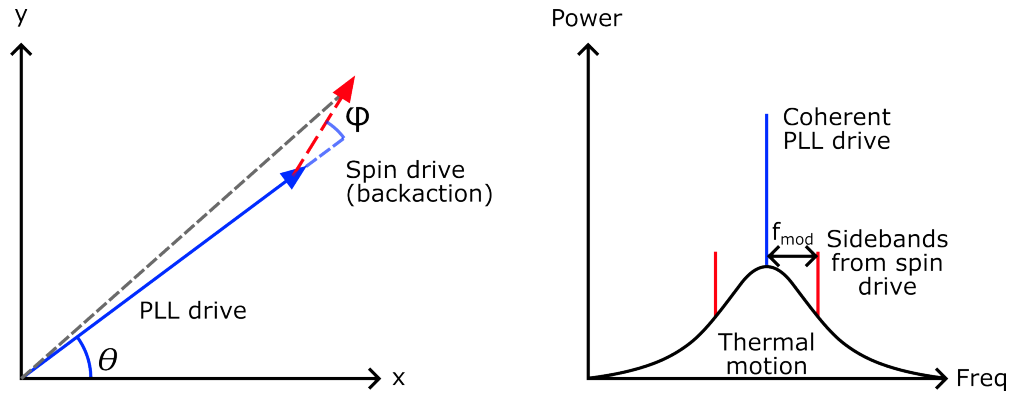


Figure 7.9: Amplitude modulation of the spin signal. Left: The additional excitation from the spin is turned on and off periodically at frequency f_{mod}, as indicated by the dashed red arrow. Right: Because of the amplitude modulation of the spin drive, the spin signal now appears as two symmetrical sidebands around the coherent PLL drive.

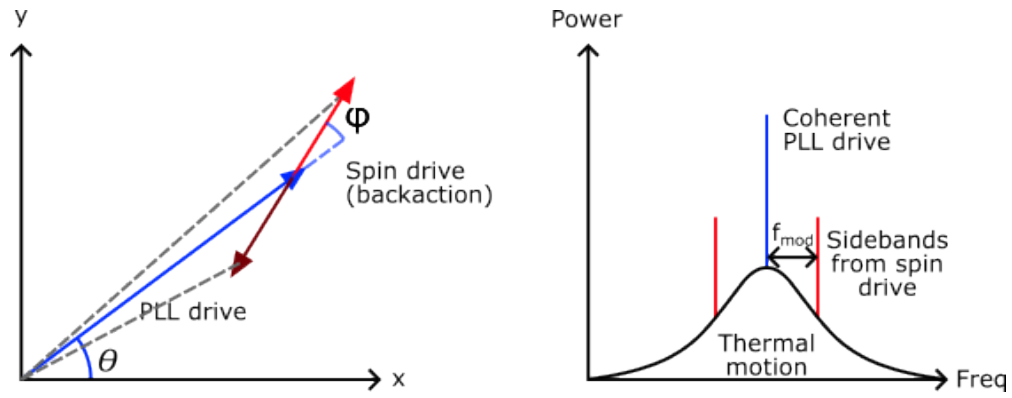


Figure 7.10: Phase modulation of the spin signal. Left: The phase of the spin drive is toggled at frequency f_{mod} between ϕ and $\phi + 180°$, as indicated by the bright and dark red arrows. This effectively doubles the spin signal.

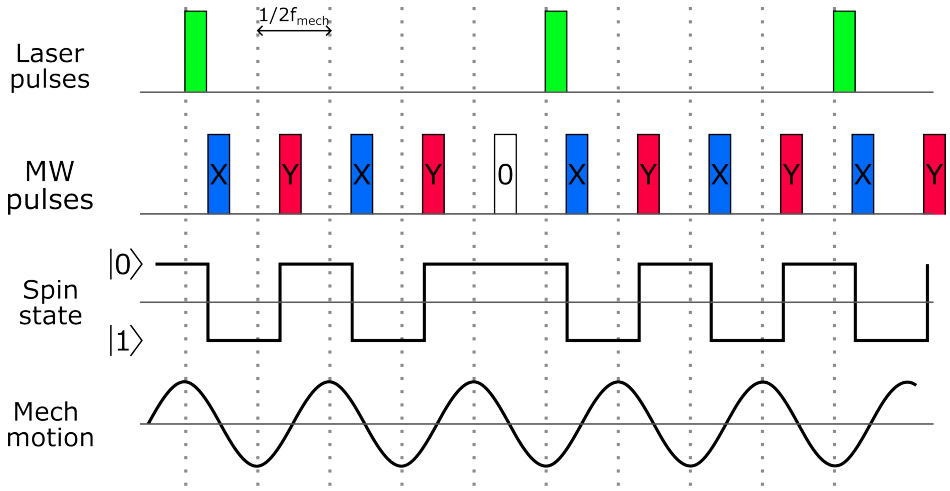


Figure 7.11: Phase modulation of spin control sequence. Every $1/2f_{mod}$, the pulse sequence skips over one mechanical half-period (indicated by the empty pulse labeled 0). Since the laser pulse always initializes the spin to the $|0\rangle$ state, it sets the phase of the spin drive relative to the mechanical motion. By shifting the pulse sequence (and therefore the laser pulses) by one mechanical half-period, the spin drive changes its phase by 180°.

7.3.3 Spurious Classical Effects of Microwave and Laser Pulses

Effects of Microwave Pulses

The sequence shown in Fig. 7.7 suffers from a major issue, in that both the laser and MW pulses cause large spurious excitations of the mechanical resonator. These excitations are hard to distinguish from the small spin signal, because they both react to the modulation mechanism (e.g. changing the frequency of MW pulses) in similar ways. In this section, the effects of the laser and MW pulses are discussed separately. Unless otherwise specified, measurements in this section and the next were performed in cryogenic temperatures. Also, the sample was retracted from the nanopillar; thus we can assume that the spurious effects are from the pulses and not the NV center.

A measurement to determine whether MW pulses can drive the mechanical resonators is set up as follows:

- A coherent drive with fixed amplitude from a piezo is used to excite the mechanical resonator using a phase-locked loop (PLL), resulting in a driven amplitude of 1.5 mV

on the lock-in amplifier.

- A train of MW π pulses, with repetition rate equal to the mechanical frequency f, is delivered via the coplanar waveguide (CPW) next to the mechanical resonator.

In Fig. 7.12(a), the phase ϕ of the π pulse train (with "clock" given by $\sin(2\pi ft + \phi)$) is swept relative to the phase of the mechanical motion, for different MW powers. The phase-dependent amplitude is symmetric around 1.5 mV, indicating that the MW pulses act as a coherent drive on top of the piezo drive. In Fig. 7.12(b), we plot the peak-to-peak amplitude of the phase-dependent amplitude as a function of the MW pulse power, revealing a linear relationship. This suggests that the force from the MW pulses scales with the square of the magnetic or electric field from the CPW at the resonator's location.

A measurement to investigate parametric effects of the MW pulses is set up as follows (Fig. 7.13(a)):

- Coherent PLL drive from a piezo.
- A train of MW π pulses, with repetition rate equal to $2f$.

The results are shown in Fig. 7.13(b). Sweeping the phase ϕ of the MW pulse train (with "clock" given by $\sin(4\pi ft + \phi)$) relative to the mechanical motion, we see that the total driven amplitude follows a periodic dependence that is not centered around the driven amplitude from only the piezo. The periodicity of 360° also suggests that the MW pulses are not behaving as a simple coherent drive on top of the piezo drive. This is made clear by Fig. 7.13(c), where we repeat the measurement in Fig. 7.13(b) with different piezo drive amplitudes, and plot the total excitation amplitude at $\phi = 132°$. Comparing the cases with and without MW pulses, we see that the added excitation amplitude from the MW pulses is not constant, but rather depends linearly with the piezo drive. This is strong evidence for parametric amplification from the MW pulses repeating at $2f$.

The plot in Fig. 7.13(b) can be compared to similar measurements in literature on parametric amplification of mechanical resonators [45, 128, 153], with an example reproduced in Fig. 7.14. The phase dependence is similar (note the different definitions of ϕ in Fig. 7.13(b)

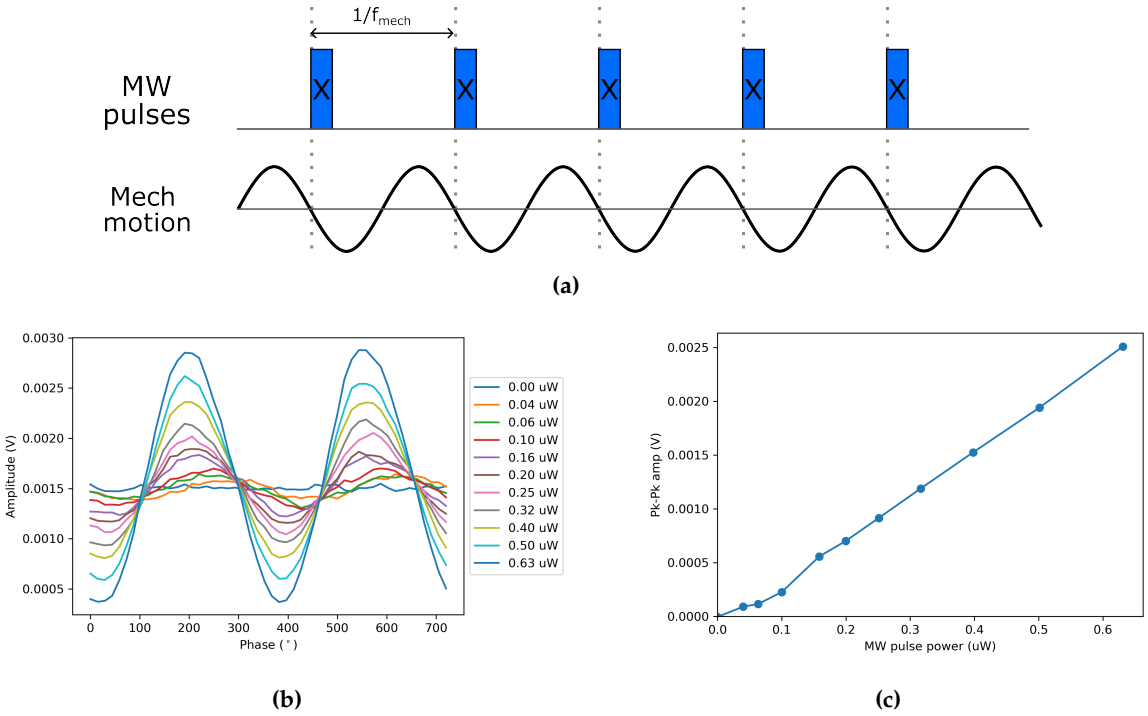


Figure 7.12: (a) A 80 ns MW pulse is sent every mechanical period. There are no laser pulses. The gray dashed line indicates when the pulse generator is triggered. (b) Phase dependence of the vibration amplitude of the mechanical resonator, with the phase being that between the mechanical motion and the pulse train. The different colors correspond to measurements with varying MW power. (c) MW power dependence of the peak-to-peak amplitude of the phase-dependent driven amplitude in (b).

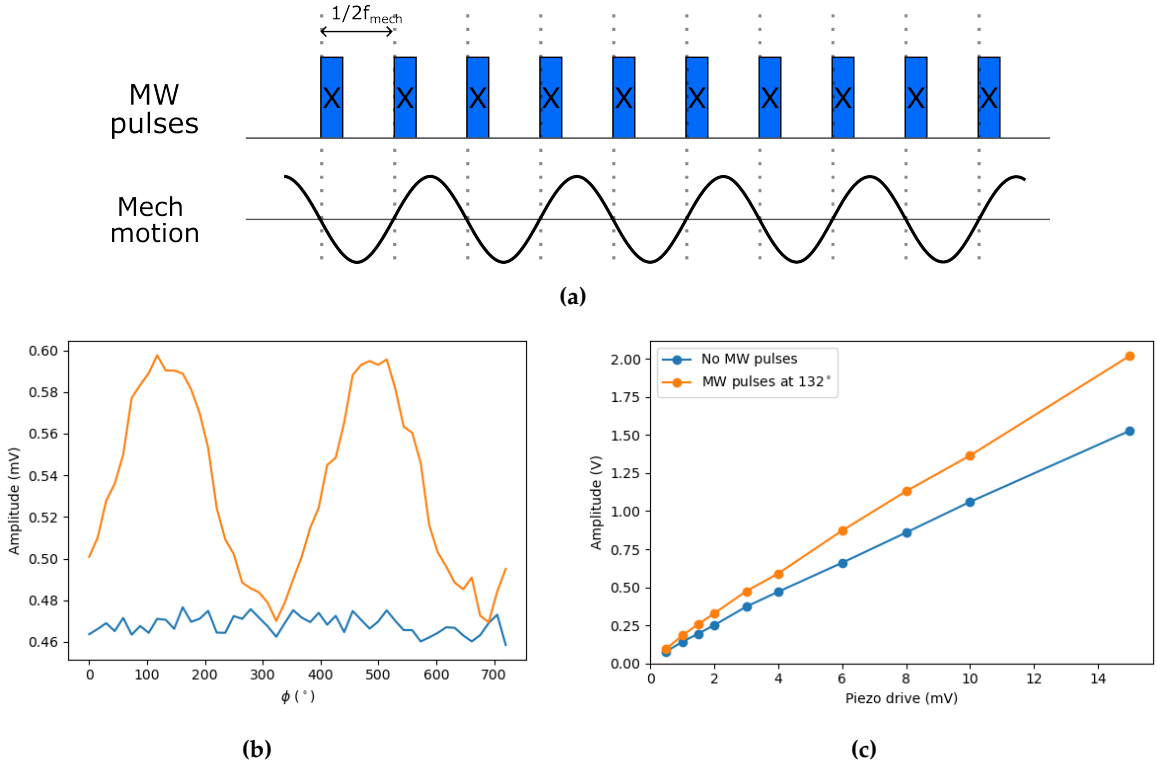


Figure 7.13: (a) A 80 ns MW pulse is sent every mechanical half-period (X-X). There are no laser pulses. The gray dashed line indicates when the pulse generator is triggered. (b) Phase dependence of the vibration amplitude of the mechanical resonator, with the phase ϕ being that between the mechanical motion and the pulse train. Blue (orange): MW pulses are disabled (enabled). Note that we also drive the mechanical resonator with a piezo in a PLL to sync the pulse train with the mechanics, hence the non-zero amplitude even with the microwaves disabled (blue). (c) The measurement in (b) is repeated with different drive amplitudes of the piezo. Blue (orange): total driven amplitude at $\phi = 132^\circ$ with MW pulses disabled (enabled).

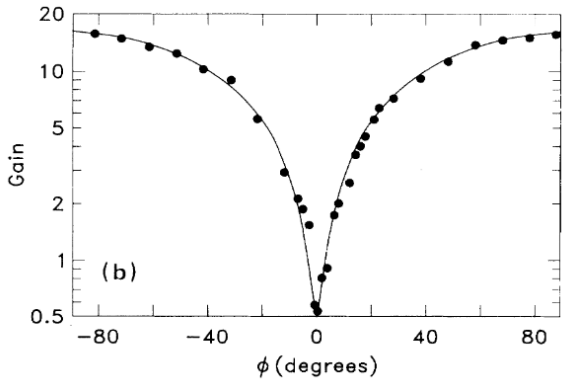


Figure 7.14: Mechanical parametric amplification. A coherent excitation $\sin(2\pi ft + \phi)$ is amplified by a parametric pump at $\sin(4\pi ft)$. The gain G varies from amplification ($G > 1$ to deamplfication (limited to $1 > G > 0.5$). Plot reproduced from reference [128].

and Fig. 7.14, which differ by a factor of 2). One difference is that the gain does not fall below 1 (i.e. deamplification) in our measurement. We attribute this to the fact that our pump drive is from a train of MW π pulses repeating at $2f$, which differs from a pure sinusoid following $\sin(4\pi ft)$.

Effects of Laser Pulses

We now turn our attention to the effects of the laser pulses on the mechanical resonator. A measurement to investigate whether laser pulses excite the mechanical resonator is set up as follows (Fig. 7.15(a)):

- No coherent drive from a piezo.
- A train of laser π pulses, with one laser pulse sent every n mechanical half-periods.

Fig. 7.15(b) shows the driven amplitude of the resonator as a function of n. We find that, for even values of n, the laser pulses strongly excite the mechanics, such that it can replace the piezo drive entirely to complete the PLL. This can be explained by the laser pulse acting as a "kick". With the kicks occurring every even n mechanical half-periods, there is always a Fourier component at the mechanical frequency. Conversely, with the kicks occurring every odd n mechanical half-periods, each pulse gives the resonator a kick in and

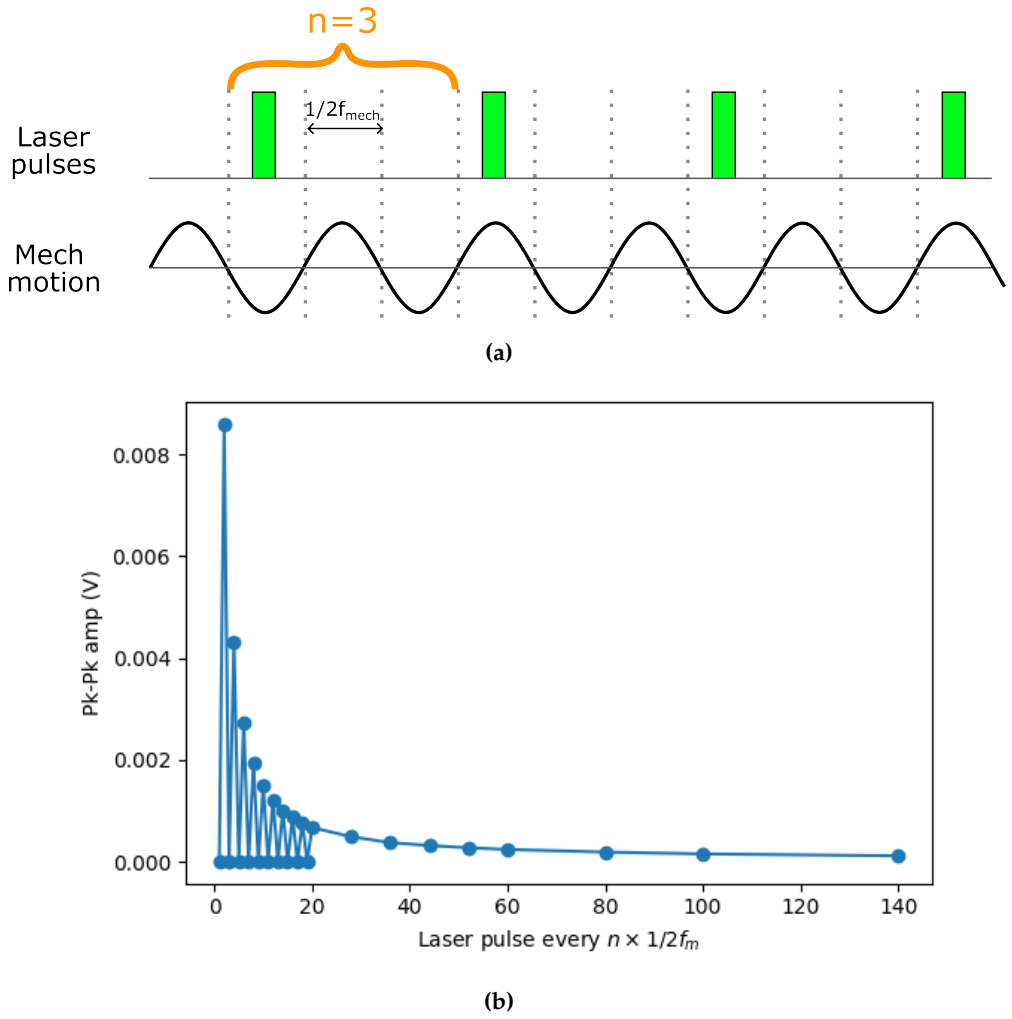


Figure 7.15: (a) A laser pulse is sent every n mechanical half-periods (L0 0^{n-1}). (b) For each value of n, we plot the driven amplitude of the mechanical resonator.

out of phase alternatively, leading to an overall cancellation of their effects. For even n, the excitation amplitude decays with n according to $1/n$, consistent with a simple model where the excitation amplitude scales inversely with the laser duty cycle.

The drastic effect of the laser pulses for even values of n can also be shown in the frequency domain, as plotted in Fig. 7.16. For odd n, the laser pulses do not change the spectrum of the mechanical motion significantly, except for some added noise within a few Hz near the resonance for small n. For even n, the laser pulses changes the spectrum dramatically, raising the noise floor orders of magnitude above the thermal noise.

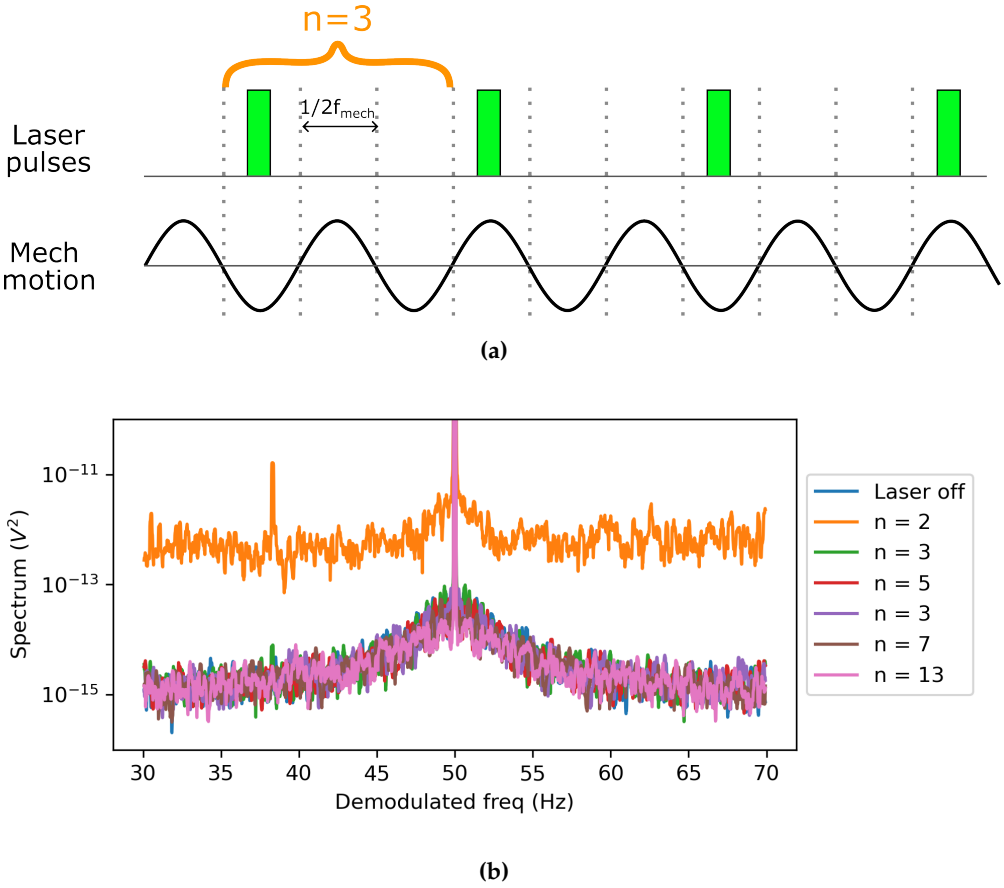


Figure 7.16: (a) A laser pulse is sent every n mechanical half-periods. (b) For each value of n, we plot the spectrum of the mechanical motion. Note that the mechanical resonance has been demodulated to 50 Hz, and that the data for $n = 3$ was taken twice. It is clear that when $n = 2$, the excitation from the laser pulses raises the noise floor significantly above the thermal noise.

However, as we saw previously in Fig. 7.7, the laser pulses must be applied every even number of mechanical half-periods, such that the reinitialization of the spin state is in sync with the spin flips. It would appear that this constraint on the control sequence means that spurious excitations caused by laser pulses are unavoidable. Fortunately, as we will see later, we can modify the spin control sequence to manage these conflicting requirements.

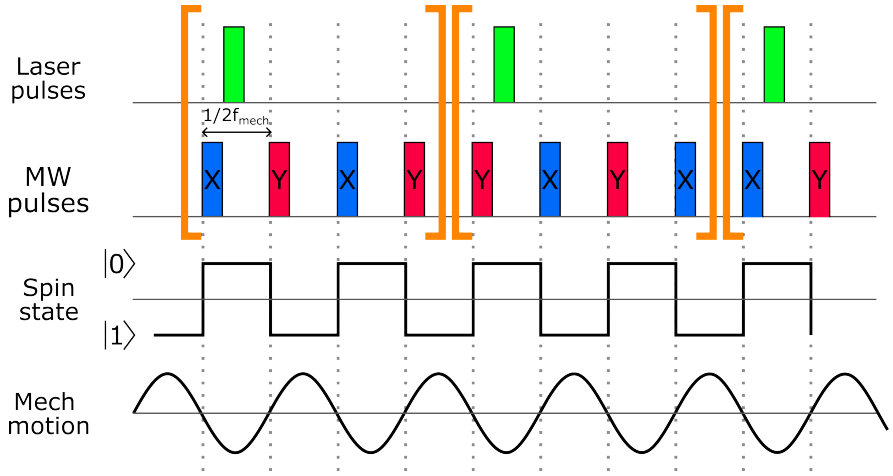


Figure 7.17: XYYX pulse sequence. The order of the XY pulses is flipped periodically, which leads to self-cancellation of the excitation due to the MW pulses.

7.3.4 Pulse Sequences to Mitigate Classical Spurious Effects

Design Guidelines

In the previous sections 7.3.3 and 7.3.3, we saw that MW and laser pulses can excite the mechanical resonator. In particular, applying a MW or laser pulse every even n mechanical half-periods is the equivalent of applying a coherent drive on the resonator. On the other hand, applying MW pulses every odd n mechanical half-periods causes parametric (de)amplification of the mechanical motion. These effects pose significant challenges in designing a pulse sequence that does not lead to spurious classical excitation of the mechanics unrelated to the NV center.

Consider the simple pulse sequence LX Y X Y, shown in Fig. 7.7 . Since a laser pulse is applied every 4 mechanical half-periods, the laser will cause significant excitation of the mechanics. On the other hand, any slight imbalance between the X and Y pulse amplitudes (e.g. due to variations in the separate switches used for X and Y pulses) leads to a Fourier component at $1f$, also leading to excitation of the mechanics. We can then consider what happens when we try to modulate the spin signal, for example, by toggling the MW frequency at f_{mod}. Any frequency dependence in the amplitude of the MW generator or

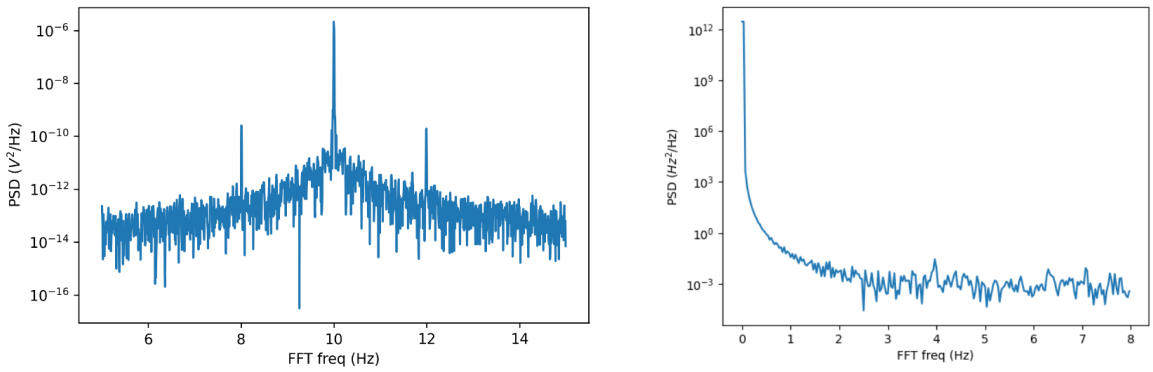
the transmission of the CPW will also cause modulation of the classical spurious excitation at f_{mod}, exactly where we would expect the spin signal. Similarly, if we were to modulate the spin signal by skipping a mechanical half-period in the pulse sequence (Fig. 7.10) every $1/f_{mod}$, the spurious effects will also be phase modulated at the same frequency, also resulting in sidebands unrelated to the spin.

Self-cancellation: the XYYX Sequence

A solution to mitigate the spurious effects of the MW pulses is an LX Y Y X sequence, shown in Fig. 7.17. The idea is that by switching the order of the X Y pulses, the phase of the spurious effects is also reversed periodically, leading to self-cancellation. The reversal should happen at a rate much higher than the mechanical linewidth, such that the spurious effects do not significantly excite the mechanics between reversals. We can generalize this sequence to LX Y $(\mathrm{X\ Y})^{\mathrm{m}}(\mathrm{Y\ X})^{\mathrm{m}}$, where $4m+2$ denotes the total number of MW pulses in each repetition block.

The LX Y $(\mathrm{X\ Y})^{\mathrm{m}}(\mathrm{Y\ X})^{\mathrm{m}}$ sequence greatly reduces the spurious effects of the MW pulses. However, it does not mitigate the effects of the laser pulses, which are sent every even number of mechanical half-periods. A simple solution is to simply increase m, which reduces the effective laser duty cycle and the spurious effects according to $1/m$ (Fig. 7.15). However, we are constrained by how large m can be, given that the laser reinitialization pulses are required periodically to correct for pulse errors and decoherence during the pulses.

An example of these spurious classical effects is shown in Fig. 7.18. In both measurements in the figure, the MW pulse frequency is modulated at f_{mod}. The pulse sequence significantly excites the mechanical resonator with an amplitude depending on the MW frequency. This results in sidebands spaced at f_{mod} around the mechanical resonance in the amplitude spectrum, as well as a peak at f_{mod} in the fast Fourier Transform (FFT) of the PLL's frequency spectrum. Given that the NV center was placed far away from the micromagnet in these measurements, we conclude that the sidebands result from classical spurious effects of the



(a) (b)

Figure 7.18: (a) The mechanical motion is measured with a lock-in amplifier and demodulated down to 10 Hz, such that both sides of the thermal spectrum can be seen in the Fourier transform. Symmetric sidebands at f_{mod} around the resonance can be seen, where f_{mod} is the modulation frequency of the MW pulse frequency. The sidebands can be seen even when the NV center is far away ($\sim 1\,\mu$m) from the micromagnet, indicating that they are due to classical spurious excitation from the laser and MW pulses. (b) The Fourier transform of the PLL's frequency is plotted. A peak is also seen at f_{mod} (2 Hz in this measurement). However, just as with the amplitude sideband in (a), this signal in the mechanical frequency's FFT also persists when the NV center is far away from the micromagnet.

pulse sequence and are unrelated to the NV center.

To investigate the frequency dependence of the spurious driving due to the MW pulses, we measure the sideband amplitude as we sweep the center frequency of the MW pulses, while modulating the frequency at f_{mod}. The results for both the sidebands in the FFT of the mechanical amplitude and frequency are shown in Fig. 7.19 (a). The data was taken at ~ 14 K, with the NV center close to the resonator and a magnetic field gradient of $\sim 1 \times 10^5$ T/m. A clear dependence of the sideband amplitude on the MW frequency is seen, featuring peaks with linewidths of ~ 50 MHz. Given that the MW pulse frequency is modulated between two values, we expect to see only sidebands at two MW frequencies separated by the modulation depth of 40 MHz. In this particular measurement, we would expect a peak in the sideband amplitude at the ESR frequency f_{ESR} and $f_{\mathrm{ESR}} + 40$ MHz. While we do see a peak close to f_{ESR}, we do not observe a second peak at $f_{\mathrm{ESR}} + 40$ MHz. We also observe peaks with comparable amplitudes at frequencies far-detuned from the

ESR frequency.

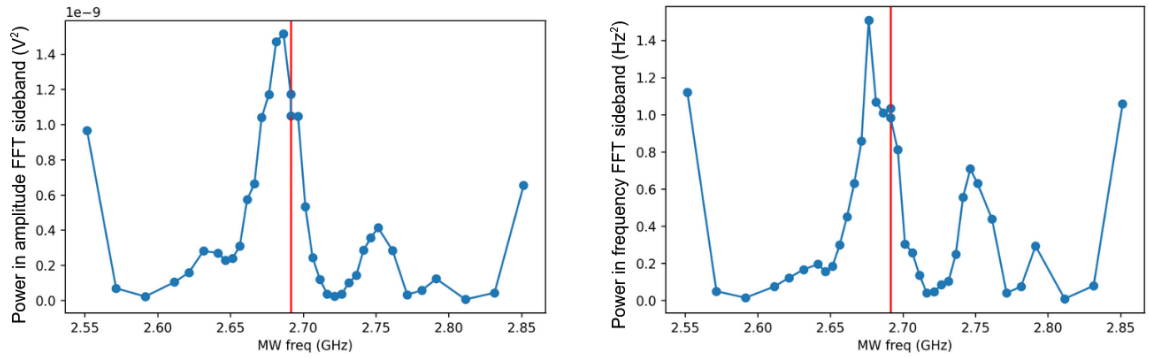
Fig. 7.19 (b) shows the same measurement performed at room temperature, with the NV center placed far away from the micromagnet on the resonator. However, the same MW frequency dependence of the sideband amplitude can be seen. This is strong evidence that the sidebands in Fig. 7.19 (a) are mostly not due to the NV center, but from spurious driving due to the MW pulses. As mentioned earlier, the frequency dependence of this spurious driving can be attributed to frequency-dependent performance of different electronic components. Ref [41] (Fig. 3 in supplementary material) also reports a strong dependence of the CPW's transmission on the MW frequency, with features showing similar linewidths.

Monitoring Sequence

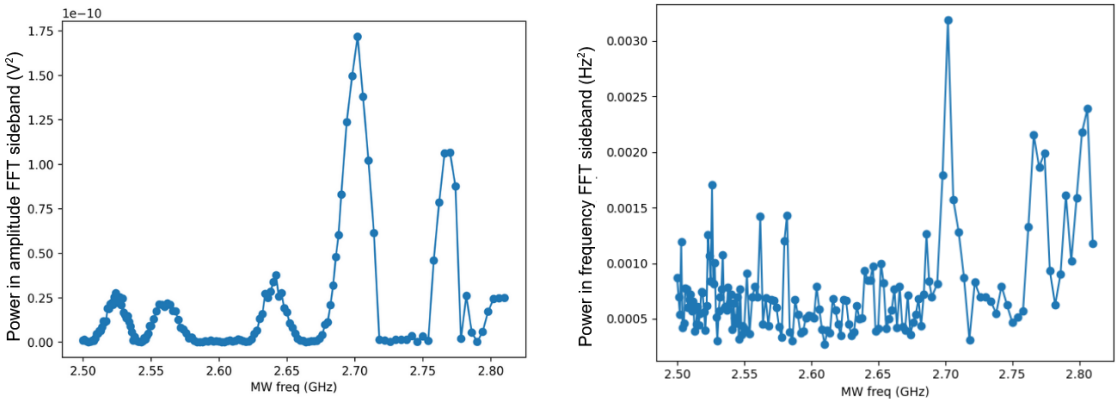
After testing many different pulse sequences, we have concluded that a pulse sequence will not result in spurious coherent excitation of the mechanics, as long as the minimum repetition block is an odd number of mechanical half-periods. For example, the following pulse sequences have been tested to confirm that they do not lead to spurious excitation:

- L 0 0
- X $(\mathrm{Y\ X})^{\mathrm{n}}$
- LX $(\mathrm{Y\ X})^{\mathrm{n}}$

This simple rule is known in the community as the "principle of success" (PoS). It also presents a challenge for designing a pulse sequence that simultaneously flips the spin continuously with the same phase while eliminating spurious classical excitations. Consider the sequence LX $(\mathrm{Y\ X})^{\mathrm{n}}$, which has a minimum repetition block size of $2n+1$ mechanical half-periods, and its effect on the spin as shown in Fig. 7.20. In the first repetition block of LX (Y X), the spin is flipped in phase with the mechanical motion, whereas in the second repetition block, it is flipped out of phase with the motion. This results in self-cancellation of the spin's effect on the mechanical resonator.



(a)



(b)

Figure 7.19: (a) The power contained in the sideband (due to MW frequency modulation) in the mechnaical amplitude and frequency FFT is shown as a function of the MW center frequency. The measurements were taken at $\sim 14\,\mathrm{K}$ with the NV center close to the resonator with a magnetic field gradient of $\sim 1 \times 10^5\,\mathrm{T/m}$. The red line indicates the ESR frequency. (b) The power contained in the sideband is shown as a function of the MW center frequency, with data taken at room temperature, with the NV center placed far away from the micromagnet on the mechanical resonator.

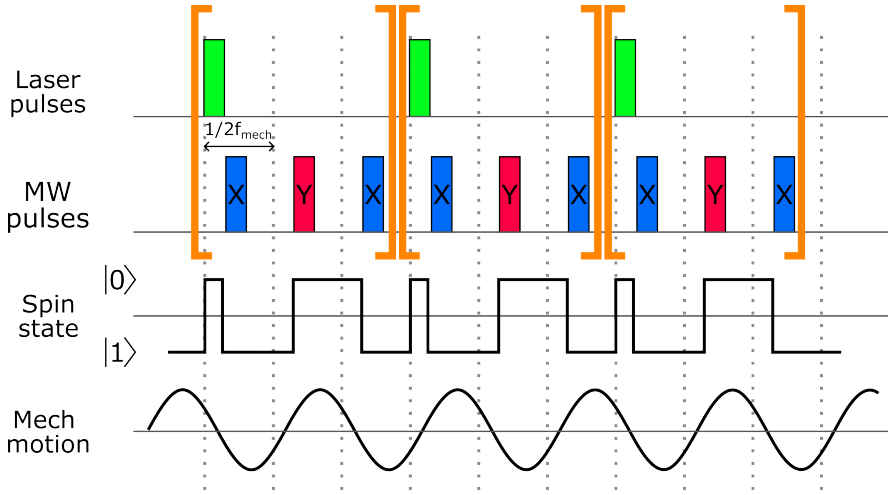


Figure 7.20: The LX $(\mathrm{Y\ X})^{\mathrm{n}}$ sequence, with $n = 1$. As clearly shown, in the first repetition block of LX (Y X), the spin state is $|0\rangle$ when the mechanical displacement is positive (in phase), whereas in the second repetition block, the spin state is $|1\rangle$ when the mechanical displacement is positive (in phase). This leads to self-cancellation of the spin's effect on the mechanics.

A compromise between the two conflicting requirements (flipping the spin continuously and no spurious classical excitation) can be made with the sequence LX $(\mathrm{Y\ X})^{\mathrm{n}}$ L0 $(\mathrm{Y\ X})^{\mathrm{n}}$, which is illustrated in Fig. 7.21. The removal of one of the X pulses (indicated by the 0) ensures that the spin is flipped continuously with the same phase relative to the mechanics. However, the price to pay is that the PoS has been violated, as the minimum repetition block size is now an even number, which results in experimentally observed spurious driving of the mechanics. In principle, the blank pulse can be replaced with a far-detuned MW pulse to approximate the classical effect of the missing X pulse without flipping the spin. As we have found experimentally, with fine-tuning of the amplitude of this detuned pulse, the spurious driving can be greatly reduced but not eliminated entirely.

However, there is one important feature of the aforementioned sequence. As one can see in Fig. 7.21, each laser pulse "sees" a different previous spin state before reinitializing it back to $|0\rangle$. For example, the first and third laser pulses "see" the spin state $|0\rangle$, while the second laser pulse "sees" $|1\rangle$; each successive laser pulse can be used to read out an alternating spin state. By simply collecting the fluorescence at each laser pulse, we can monitor the spin

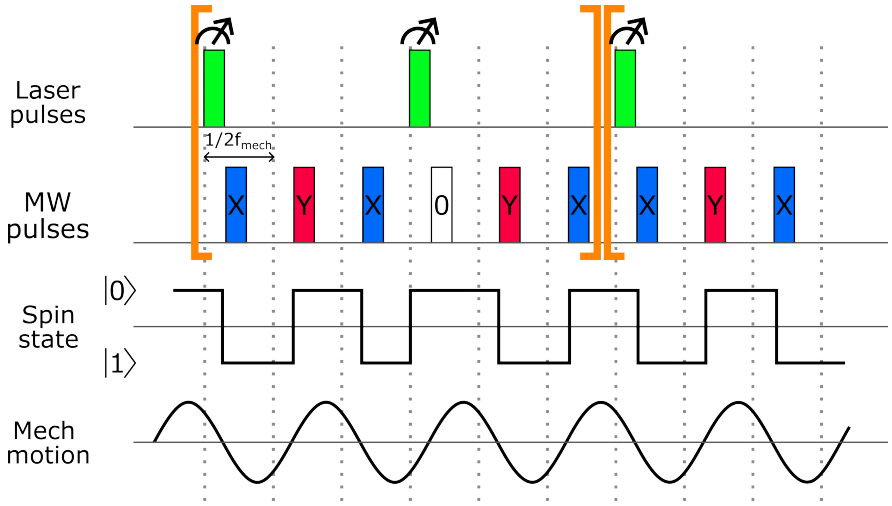


Figure 7.21: The monitoring sequence given by LX $(\mathrm{Y\ X})^{\mathrm{n}}$ L0 $(\mathrm{Y\ X})^{\mathrm{n}}$, with $n = 1$. Unlike the LX (Y X) sequence shown in Fig. 7.20, the spin state in this sequence always flips with the same phase (in phase in this figure) relative to the mechanical motion, which results in a spin-induced change in the overall motion. Additionally, the spin state can be read out at the beginning of each laser pulse before it gets fully reinitialized to the $|0\rangle$ state.

contrast during a long mechanics measurement, and confirm that it is flipping with high fidelity. For this reason, the sequence is named the "monitoring" sequence.

An example measurement with the monitoring sequence (with $n = 20$) is shown in Fig. 7.22. The photon counts from the laser pulses are averaged together to form a clear zigzag pattern, with a contrast of $\sim 15\%$ (compared to an ESR contrast of 20%). For this particular measurement, the total number of laser pulses is 2×10^5. Given the averaging method, the high contrast of the zigzag indicates that the spin flips maintain the same phase over this entire duration. Furthermore, we have seen this zigzag persist over tens of minutes, indicating that the laser indeed reinitializes the spin well enough to maintain a high spin contrast for the whole duration.

Furthermore, this real-time monitoring sequence allows us to tune certain pulse settings to optimize the spin flip fidelity, or to compensate for drift. Two example measurements are shown in Fig. 7.23, where we sweep the MW pulse frequency and power respectively. As a result, we were able to obtain a spin flip contrast close to the 20% from a typical ESR measurement.

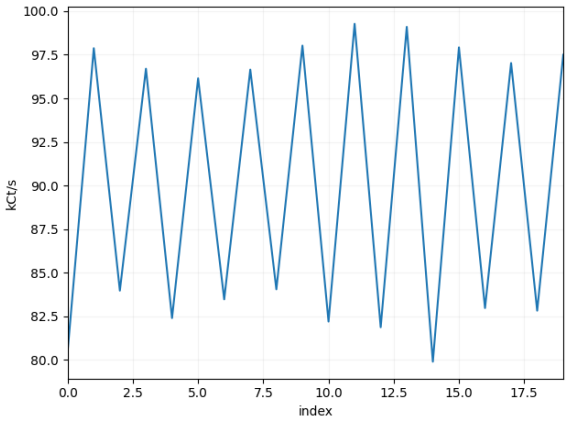
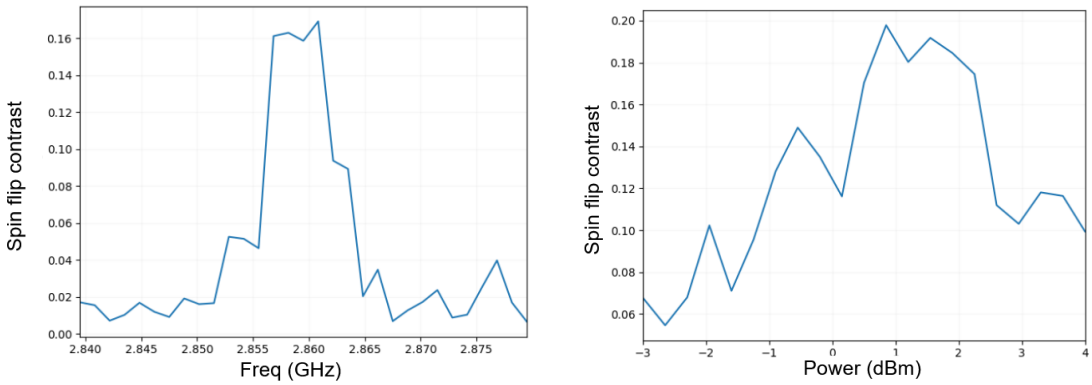


Figure 7.22: Zigzag pattern in the NV fluorescence collected from the monitoring sequence ($n = 20$), indicating that the spin is flipped continuously with decent fidelity. For this particular measurement, 2×10^5 laser pulses were used, with a single read-out performed for each pulse. The fluorescence data is then divided into sets of 20 successive measurements, stacked together and then averaged to give the plot shown. Because of this method of averaging, the zigzag pattern indicates that spin flips maintain their phase throughout 4×10^6 flips.

Finally, we note that the NV measurements with the monitoring sequence have only been done so far at room temperature in air. We are currently in the process of repeating these measurements at low temperatures.

7.4 Preliminary Results

Preliminary results suggesting detection of the NV center with the mechanical resonator are shown in Fig. 7.24. A sequence following $((\mathrm{LX\,Y})\ (\mathrm{X\,Y})^9)^8\ ((\mathrm{LY\,X})\ (\mathrm{Y\,X})^9)^8$ is used, i.e. with 80 consecutive pairs of X Y pulses and then Y X pulses, and a laser pulse weaved in every 10 MW pulses. The measured magnetic field gradient exceeds $3 \times 10^5\,\mathrm{T/m}$, with a mechanical quality factor of 7×10^5. To generate the sidebands shown in Fig. 7.9, an external bias field is modulated according to a 3.9 Hz square wave to bring the MW pulses on and off resonance with the ESR transition. For a given DC offset of the bias field, we expect the spin signal to appear when the MW frequency matches the ESR frequency during part of the square wave modulation. With adjustments to the bias field's DC offset, the



(a) **(b)**

Figure 7.23: (a) The spin contrast is measured using the monitoring sequence ($n = 20$) as the MW pulse frequency is varied. For a π time of 90 ns, the monitoring sequence appears to be effective at inducing spin flips within 10 MHz of the ESR frequency. (b) The spin contrast is measured with the same monitoring sequence, while the MW power is swept.

spin signal appears when the MW frequency matches the new ESR frequency. Plotting the sideband amplitude in a 2D plot where the X and Y axes are the bias field DC offset and MW pulse frequency respectively, we see a faintly visible signal in the form of a line with a slope equal to the NV center's gyromagnetic ratio of 2.8 MHz/G. The reason for the noisy background is due to the aforementioned spurious classical driving from the pulse sequence, which leads to a "background" sideband even when the MW pulses are far off-resonant. Additional measurements are needed to increase the signal-to-noise ratio and confirm that the signal on top of this noisy background is due to the NV center. Such measurements include changing the direction of the bias field, which would cause the slope to have the opposite sign; reducing the MW pulse duration such that it is only a $\pi/2$ pulse, which would eliminate the signal; reproducing this signal for both spin transitions $|0\rangle \leftrightarrow |1\rangle$ and $|0\rangle \leftrightarrow |-1\rangle$.

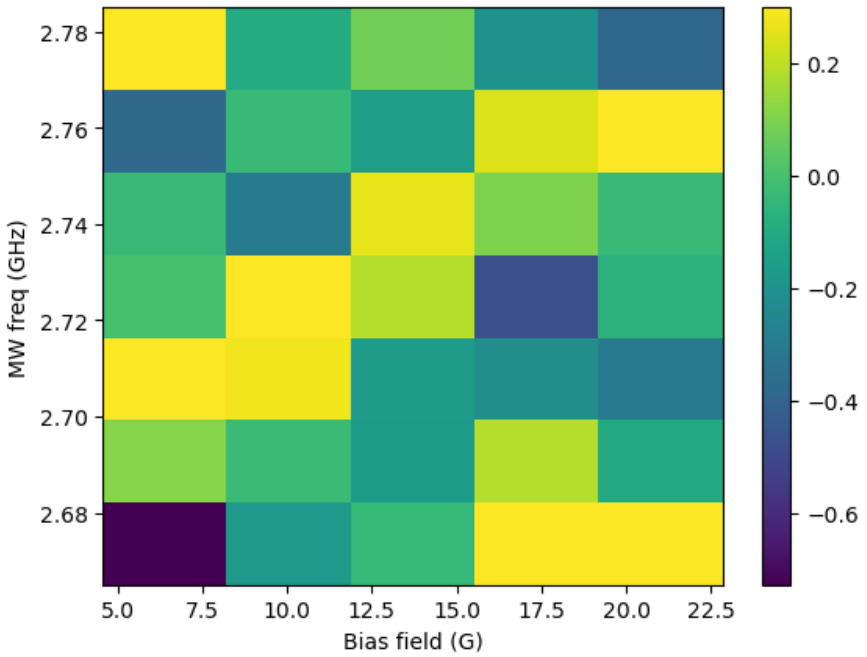


Figure 7.24: Preliminary results suggesting the detection of single-spin backaction on the mechanical resonator. The color indicates the sideband amplitude (a.u.) in the amplitude FFT, after row-wise mean subtraction followed by column-wise mean subtraction.

References

[1] See Supplemental Material.

[2] `https://qzabre.com`, 2025.

[3] `https://qnami.ch/`, 2025.

[4] `https://alconox.com/product/citranox/`, 2025.

[5] B. P. Abbott, R. Abbott, T. D. Abbott, M. R. Abernathy, F. Acernese, K. Ackley, C. Adams, T. Adams, P. Addesso, R. X. Adhikari, et al. Observation of gravitational waves from a binary black hole merger. *Phys. Rev. Lett.*, 116(6):061102, 2016.

[6] M. H. Abobeih, J. Cramer, M. A. Bakker, N. Kalb, M. Markham, D. J. Twitchen, and T. H. Taminiau. One-second coherence for a single electron spin coupled to a multi-qubit nuclear-spin environment. *Nat. Commun.*, 9(1):2552, 2018.

[7] T. Akiyama, U. Staufer, N. De Rooij, P. Frederix, and A. Engel. Symmetrically arranged quartz tuning fork with soft cantilever for intermittent contact mode atomic force microscopy. *Rev. Sci. Instrum.*, 74(1):112–117, 2003.

[8] K. Ambal, A. Payne, D. Waters, C. Williams, and C. Boehme. Spin-relaxation dynamics of é centers at high density in sio 2 thin films for single-spin tunneling force microscopy. *Phys. Rev. Appl.*, 4(2):024008, 2015.

[9] C. P. Anderson, E. O. Glen, C. Zeledon, A. Bourassa, Y. Jin, Y. Zhu, C. Vorwerk, A. L. Crook, H. Abe, J. Ul-Hassan, et al. Five-second coherence of a single spin with single-shot readout in silicon carbide. *Sci. Adv.*, 8(5):eabm5912, 2022.

[10] P. Appel, E. Neu, M. Ganzhorn, A. Barfuss, M. Batzer, M. Gratz, A. Tschöpe, and P. Maletinsky. Fabrication of all diamond scanning probes for nanoscale magnetometry. *Rev. Sci. Instrum.*, 87(6), 2016.

[11] O. Arcizet, V. Jacques, A. Siria, P. Poncharal, P. Vincent, and S. Seidelin. A single nitrogen-vacancy defect coupled to a nanomechanical oscillator. *Nat. Phys.*, 7(11):879–883, 2011.

[12] A. Ariyaratne, D. Bluvstein, B. A. Myers, and A. C. B. Jayich. Nanoscale electrical conductivity imaging using a nitrogen-vacancy center in diamond. *Nat. Commun.*, 9(1):2406, 2018.

[13] A. Ariyaratne, D. Bluvstein, B. A. Myers, and A. C. B. Jayich. Nanoscale electrical conductivity imaging using a nitrogen-vacancy center in diamond. *Nat. Commun.*, 9(1):2406, 2018.

[14] R. L. Badzey, G. Zolfagharkhani, A. Gaidarzhy, and P. Mohanty. A controllable nanomechanical memory element. *Appl. Phys. Lett.*, 85(16):3587–3589, 10 2004.

[15] G. Balasubramanian, I. Chan, R. Kolesov, M. Al-Hmoud, J. Tisler, C. Shin, C. Kim, A. Wojcik, P. R. Hemmer, A. Krueger, et al. Nanoscale imaging magnetometry with diamond spins under ambient conditions. *Nature*, 455(7213):648–651, 2008.

[16] G. Balasubramanian, P. Neumann, D. Twitchen, M. Markham, R. Kolesov, N. Mizuochi, J. Isoya, J. Achard, J. Beck, J. Tissler, V. Jacques, P. R. Hemmer, F. Jelezko, and J. Wrachtrup. Ultralong spin coherence time in isotopically engineered diamond. *Nat. Mat.*, 8(5):383–387, 2009.

[17] N. Bar-Gill, L. M. Pham, A. Jarmola, D. Budker, and R. L. Walsworth. Solid-state electronic spin coherence time approaching one second. *Nat. Commun.*, 4(1):1743, 2013.

[18] S. Barzanjeh, A. Xuereb, S. Gröblacher, M. Paternostro, C. A. Regal, and E. M. Weig. Optomechanics for quantum technologies. *Nat. Phys.*, 18(1):15–24, 2022.

[19] A. Beccari, D. A. Visani, S. A. Fedorov, M. J. Bereyhi, V. Boureau, N. J. Engelsen, and T. J. Kippenberg. Strained crystalline nanomechanical resonators with quality factors above 10 billion. *Nat. Phys.*, 18(4):436–441, 2022.

[20] S. D. Bennett, S. Kolkowitz, Q. P. Unterreithmeier, P. Rabl, A. C. B. Jayich, J. G. E. Harris, and M. D. Lukin. Measuring mechanical motion with a single spin. *New J. Phys.*, 14(12):125004, 2012.

[21] M. J. Bereyhi, A. Arabmoheghi, A. Beccari, S. A. Fedorov, G. Huang, T. J. Kippenberg, and N. J. Engelsen. Perimeter modes of nanomechanical resonators exhibit quality factors exceeding 10 9 at room temperature. *Phys. Rev. X*, 12(2):021036, 2022.

[22] M. J. Bereyhi, A. Beccari, S. A. Fedorov, A. H. Ghadimi, R. Schilling, D. J. Wilson, N. J. Engelsen, and T. J. Kippenberg. Clamp-tapering increases the quality factor of stressed nanobeams. *Nano Lett.*, 19(4):2329–2333, 2019.

[23] M. J. Bereyhi, A. Beccari, R. Groth, S. A. Fedorov, A. Arabmoheghi, T. J. Kippenberg, and N. J. Engelsen. Hierarchical tensile structures with ultralow mechanical dissipation. *Nat. Commun.*, 13(1):3097, 2022.

[24] H. Bernien, B. Hensen, W. Pfaff, G. Koolstra, M. S. Blok, L. Robledo, T. H. Taminiau, M. Markham, D. J. Twitchen, L. Childress, et al. Heralded entanglement between solid-state qubits separated by three metres. *Nature*, 497(7447):86–90, 2013.

[25] M. K. Bhaskar, R. Riedinger, B. Machielse, D. S. Levonian, C. T. Nguyen, E. N. Knall, H. Park, D. Englund, M. Lončar, D. D. Sukachev, et al. Experimental demonstration of memory-enhanced quantum communication. *Nature*, 580(7801):60–64, 2020.

[26] A. Bienfait, K. J. Satzinger, Y. P. Zhong, H.-S. Chang, M.-H. Chou, C. R. Conner, É. Dumur, J. Grebel, G. A. Peairs, R. G. Povey, and A. N. Cleland. Phonon-mediated quantum state transfer and remote qubit entanglement. *Science*, 364(6438):368–371, 2019.

[27] G. Binnig and H. Rohrer. Scanning tunneling microscopy. *Surf. Sci.*, 126(1-3):236–244, 1983.

[28] R. Blatt and C. F. Roos. Quantum simulations with trapped ions. *Nature Physics*, 8(4):277–284, 2012.

[29] D. Bluvstein, H. Levine, G. Semeghini, T. T. Wang, S. Ebadi, M. Kalinowski, A. Keesling, N. Maskara, H. Pichler, M. Greiner, V. Vuletić, and M. D. Lukin. A quantum processor based on coherent transport of entangled atom arrays. *Nature*, 604(7906):451–456, Apr 2022.

[30] C. E. Bradley, J. Randall, M. H. Abobeih, R. C. Berrevoets, M. J. Degen, M. A. Bakker, M. Markham, D. J. Twitchen, and T. H. Taminiau. A ten-qubit solid-state spin register with quantum memory up to one minute. *Phys. Rev. X*, 9(3):031045, 2019.

[31] A. Browaeys and T. Lahaye. Many-body physics with individually controlled rydberg atoms. *Nature Physics*, 16(2):132–142, 2020.

[32] Y. Cao, J. Romero, and A. Aspuru-Guzik. Potential of quantum computing for drug discovery. *IBM Journal of Research and Development*, 62(6):6–1, 2018.

[33] R. J. Celotta, S. B. Balakirsky, A. P. Fein, F. M. Hess, G. M. Rutter, and J. A. Stroscio. Invited article: Autonomous assembly of atomically perfect nanostructures using a scanning tunneling microscope. *Rev. Sci. Instrum.*, 85(12), 2014.

[34] Y.-C. Chen, P. S. Salter, S. Knauer, L. Weng, A. C. Frangeskou, C. J. Stephen, S. N. Ishmael, P. R. Dolan, S. Johnson, B. L. Green, et al. Laser writing of coherent colour centres in diamond. *Nat. Photonics*, 11(2):77–80, 2017.

[35] J. Chow, J. Gambetta, J. Koch, B. Johnson, J. Schreier, L. Frunzio, D. Schuster, et al. Coupling superconducting qubits via a cavity bus. *Nature*, 449(7161):443–447, 2007.

[36] Y. Chu and S. Gröblacher. A perspective on hybrid quantum opto-and electromechanical systems. *Appl. Phys. Lett.*, 117(15):150503, 2020.

[37] J. I. Cirac and P. Zoller. A scalable quantum computer with ions in an array of microtraps. *Nature*, 404(6778):579–581, 2000.

[38] A. A. Clerk, K. W. Lehnert, P. Bertet, J. R. Petta, and Y. Nakamura. Hybrid quantum systems with circuit quantum electrodynamics. *Nat. Phys.*, 16(3):257–267, 2020.

[39] L. Dania, D. S. Bykov, F. Goschin, M. Teller, A. Kassid, and T. E. Northup. Ultrahigh quality factor of a levitated nanomechanical oscillator. *Phys. Rev. Lett.*, 132:133602, Mar 2024.

[40] C. Degen. Scanning magnetic field microscope with a diamond single-spin sensor. *Appl. Phys. Lett.*, 92(24), 2008.

[41] C. Du, T. Van der Sar, T. X. Zhou, P. Upadhyaya, F. Casola, H. Zhang, M. C. Onbasli, C. A. Ross, R. L. Walsworth, Y. Tserkovnyak, et al. Control and local measurement of the spin chemical potential in a magnetic insulator. *Science*, 357(6347):195–198, 2017.

[42] L.-M. Duan, M. D. Lukin, J. I. Cirac, and P. Zoller. Long-distance quantum communication with atomic ensembles and linear optics. *Nature*, 414(6862):413–418, 2001.

[43] M. V. G. Dutt, L. Childress, L. Jiang, E. Togan, J. Maze, F. Jelezko, A. Zibrov, P. Hemmer, and M. Lukin. Quantum register based on individual electronic and nuclear spin qubits in diamond. *Science*, 316(5829):1312–1316, 2007.

[44] S. Ebadi, A. Keesling, M. Cain, T. T. Wang, H. Levine, D. Bluvstein, G. Semeghini, A. Omran, J.-G. Liu, R. Samajdar, et al. Quantum optimization of maximum independent set using rydberg atom arrays. *Science*, 376(6598):1209–1215, 2022.

[45] A. Eichler, J. Chaste, J. Moser, and A. Bachtold. Parametric amplification and self-oscillation in a nanotube mechanical resonator. *Nano Lett.*, 11(7):2699–2703, 2011.

[46] N. J. Engelsen, A. Beccari, and T. J. Kippenberg. Ultrahigh-quality-factor micro-and nanomechanical resonators using dissipation dilution. *Nat. Nanotechnol.*, 19(6):725–737, 2024.

[47] S. Ernst, P. J. Scheidegger, S. Diesch, L. Lorenzelli, and C. L. Degen. Temperature dependence of photoluminescence intensity and spin contrast in nitrogen-vacancy centers. *Phys. Rev. Lett.*, 131(8):086903, 2023.

[48] E. Farhi, J. Goldstone, and S. Gutmann. A quantum approximate optimization algorithm. *arXiv preprint arXiv:1411.4028*, 2014.

[49] R. P. Feynman. Simulating physics with computers. In *Feynman and computation*, pages 133–153. cRc Press, 2018.

[50] M. Fujiwara, R. Tsukahara, Y. Sera, H. Yukawa, Y. Baba, S. Shikata, and H. Hashimoto. Monitoring spin coherence of single nitrogen-vacancy centers in nanodiamonds during ph changes in aqueous buffer solutions. *RSC Adv.*, 9(22):12606–12614, 2019.

[51] F. Fung, E. Rosenfeld, J. D. Schaefer, A. Kabcenell, J. Gieseler, T. X. Zhou, T. Madhavan, N. Aslam, A. Yacoby, and M. D. Lukin. Toward programmable quantum processors based on spin qubits with mechanically mediated interactions and transport. *Phys. Rev. Lett.*, 132:263602, Jun 2024.

[52] L. García, J. Chaboy, F. Bartolomé, and J. Goedkoop. Orbital magnetic moment instability at the spin reorientation transition of nd 2 fe 14 b. *Phys. Rev. Lett.*, 85(2):429, 2000.

[53] E. Gavartin, P. Verlot, and T. J. Kippenberg. A hybrid on-chip optomechanical transducer for ultrasensitive force measurements. *Nat. Nanotechnol.*, 7(8):509–514, 2012.

[54] I. M. Georgescu, S. Ashhab, and F. Nori. Quantum simulation. *Rev. Mod. Phys.*, 86(1):153–185, 2014.

[55] A. H. Ghadimi, S. A. Fedorov, N. J. Engelsen, M. J. Bereyhi, R. Schilling, D. J. Wilson, and T. J. Kippenberg. Elastic strain engineering for ultralow mechanical dissipation. *Science*, 360(6390):764–768, 2018.

[56] B. T. Ghim, S. Eaton, G. R. Eaton, R. W. Quine, G. Rinard, and S. Pfenninger. Magnetic field and frequency dependence of electron spin relaxation times of the é center in irradiated vitreous silica. *J. Magn. Reson., Ser. A*, 115(2):230–235, 1995.

[57] J. Gieseler, A. Kabcenell, E. Rosenfeld, J. D. Schaefer, A. Safira, M. J. A. Schuetz, C. Gonzalez-Ballestero, C. C. Rusconi, O. Romero-Isart, and M. D. Lukin. Single-spin magnetomechanics with levitated micromagnets. *Phys. Rev. Lett.*, 124(16):163604, 2020.

[58] D. Goll, M. Seeger, and H. Kronmüller. Magnetic and microstructural properties of nanocrystalline exchange coupled prfeb permanent magnets. *Journal of Magnetism and Magnetic Materials*, 185(1):49–60, 1998.

[59] W. J. Greenleaf, M. T. Woodside, and S. M. Block. High-resolution, single-molecule measurements of biomolecular motion. *Annu. Rev. Biophys. Biomol. Struct.*, 36(1):171–190, 2007.

[60] U. Grob, M.-D. Krass, M. Héritier, R. Pachlatko, J. Rhensius, J. Kosata, B. Moores, H. Takahashi, A. Eichler, and C. L. Degen. Magnetic resonance force microscopy with a one-dimensional resolution of 0.9 nanometers. *Nano Lett.*, 19(11):7935–7940, 2019.

[61] I. Gross, W. Akhtar, A. Hrabec, J. Sampaio, L. Martínez, S. Chouaieb, B. Shields, P. Maletinsky, A. Thiaville, S. Rohart, et al. Skyrmion morphology in ultrathin magnetic films. *Phys. Rev. Mater.*, 2(2):024406, 2018.

[62] D. N. Guerra, M. Imboden, and P. Mohanty. Electrostatically actuated silicon-based nanomechanical switch at room temperature. *Appl. Phys. Lett.*, 93(3), 2008.

[63] J. Guo, J. Chang, X. Yao, and S. Gröblacher. Active-feedback quantum control of an integrated low-frequency mechanical resonator. *Nat. Comm.*, 14(1):4721, 2023.

[64] J. Guo and S. Gröblacher. Integrated optical-readout of a high-q mechanical out-of-plane mode. *Light:Sci. Appl.*, 11(1):282, 2022.

[65] J. Guo and S. Gröblacher. Integrated optical-readout of a high-Q mechanical out-of-plane mode. *Light Sci. Appl.*, 11(1):282, 2022.

[66] O. Gutfleisch. High-temperature samarium cobalt permanent magnets. *Nanoscale magnetic materials and applications*, pages 337–372, 2009.

[67] J. Hadden, J. Harrison, A. C. Stanley-Clarke, L. Marseglia, Y.-L. Ho, B. Patton, J. L. O'Brien, and J. Rarity. Strongly enhanced photon collection from diamond defect centers under microfabricated integrated solid immersion lenses. *Appl. Phys. Lett.*, 97(24), 2010.

[68] G. C. Hadjipanayis and M. Bonder. *Rare Earth Magnets and Their Applications: Proceedings of the Seventeenth International Workshop on Rare Earth Magnets and Their Applications, 18-22 August 2002, Newark, Delaware*, volume 1. Ave Maria Press, 2002.

[69] U. Hartmann. Magnetic force microscopy. *Annu. Rev. Mater. Sci.*, 29(1):53–87, 1999.

[70] N. Hedrich, D. Rohner, M. Batzer, P. Maletinsky, and B. J. Shields. Parabolic diamond scanning probes for single-spin magnetic field imaging. *Phys. Rev. Appl.*, 14(6):064007, 2020.

[71] B. Hensen, H. Bernien, A. E. Dréau, A. Reiserer, N. Kalb, M. S. Blok, J. Ruitenberg, R. F. Vermeulen, R. N. Schouten, C. Abellán, et al. Loophole-free bell inequality violation using electron spins separated by 1.3 kilometres. *Nature*, 526(7575):682–686, 2015.

[72] E. D. Herbschleb, H. Kato, Y. Maruyama, T. Danjo, T. Makino, S. Yamasaki, I. Ohki, K. Hayashi, H. Morishita, M. Fujiwara, et al. Ultra-long coherence times amongst room-temperature solid-state spins. *Nat. Commun.*, 10(1):3766, 2019.

[73] S. L. N. Hermans, M. Pompili, H. K. C. Beukers, S. Baier, J. Borregaard, and R. Hanson. Qubit teleportation between non-neighbouring nodes in a quantum network. *Nature*, 605(7911):663–668, 2022.

[74] A. A. Houck, H. E. Türeci, and J. Koch. On-chip quantum simulation with superconducting circuits. *Nature Physics*, 8(4):292–299, 2012.

[75] W. S. Huxter, M. L. Palm, M. L. Davis, P. Welter, C.-H. Lambert, M. Trassin, and C. L. Degen. Scanning gradiometry with a single spin quantum magnetometer. *Nat. Commun.*, 13(1):3761, 2022.

[76] N. M. Israelsen, S. Kumar, M. Tawfieq, J. S. Neergaard-Nielsen, A. Huck, and U. L. Andersen. Increasing the photon collection rate from a single nv center with a silver mirror. *Journal of optics*, 16(11):114017, 2014.

[77] L. Jiang, J. S. Hodges, J. R. Maze, P. Maurer, J. M. Taylor, D. G. Cory, P. R. Hemmer, R. L. Walsworth, A. Yacoby, A. S. Zibrov, and M. D. Lukin. Repetitive readout of a single electronic spin via quantum logic with nuclear spin ancillae. *Science*, 326(5950):267–272, 2009.

[78] S. K. Keshava. Understanding the quality factor of mass-loaded tensioned resonators. *Phys. Rev. Appl.*, 19(3):L031006, 2023.

[79] P. Kim, B. Hauer, T. Clark, F. Fani Sani, M. Freeman, and J. Davis. Magnetic actuation and feedback cooling of a cavity optomechanical torque sensor. *Nat. Commun.*, 8(1):1355, 2017.

[80] S. Kolkowitz, A. C. B. Jayich, Q. P. Unterreithmeier, S. D. Bennett, P. Rabl, J. G. E. Harris, and M. D. Lukin. Coherent sensing of a mechanical resonator with a single-spin qubit. *Science*, 335(6076):1603–1606, 2012.

[81] J. Košata, O. Zilberberg, C. L. Degen, R. Chitra, and A. Eichler. Spin detection via parametric frequency conversion in a membrane resonator. *Phys. Rev. Appl.*, 14(1):014042, 2020.

[82] M. C. Kuzyk and H. Wang. Scaling phononic quantum networks of solid-state spins with closed mechanical subsystems. *Phys. Rev. X*, 8(4):041027, 2018.

[83] D. Lee, K. W. Lee, J. V. Cady, P. Ovartchaiyapong, and A. C. B. Jayich. Topical review: spins and mechanics in diamond. *J. Opt.*, 19(3):033001, 2017.

[84] K. W. Lee, D. Lee, P. Ovartchaiyapong, J. Minguzzi, J. R. Maze, and A. C. B. Jayich. Strain coupling of a mechanical resonator to a single quantum emitter in diamond. *Phys. Rev. Appl.*, 6(3):034005, 2016.

[85] K. W. Lee III. *Coherent dynamics of a hybrid quantum spin-mechanical oscillator system*. University of California, Santa Barbara, 2017.

[86] J. G. Longenecker, H. Mamin, A. W. Senko, L. Chen, C. T. Rettner, D. Rugar, and J. A. Marohn. High-gradient nanomagnets on cantilevers for sensitive detection of nuclear magnetic resonance. *ACS Nano*, 6(11):9637–9645, 2012.

[87] L. Luan, M. S. Grinolds, S. Hong, P. Maletinsky, R. L. Walsworth, and A. Yacoby. Decoherence imaging of spin ensembles using a scanning single-electron spin in diamond. *Sci. Rep.*, 5(1):8119, 2015.

[88] S. Maity, L. Shao, S. Bogdanović, S. Meesala, Y.-I. Sohn, N. Sinclair, B. Pingault, M. Chalupnik, C. Chia, L. Zheng, K. Lai, and M. Lončar. Coherent acoustic control of a single silicon vacancy spin in diamond. *Nat. Commun.*, 11(1):193, 2020.

[89] P. Maletinsky, S. Hong, M. S. Grinolds, B. Hausmann, M. D. Lukin, R. L. Walsworth, M. Loncar, and A. Yacoby. A robust scanning diamond sensor for nanoscale imaging with single nitrogen-vacancy centres. *Nat. Nanotechnol.*, 7(5):320–324, 2012.

[90] O. Mandel, M. Greiner, A. Widera, T. Rom, T. W. Hänsch, and I. Bloch. Coherent transport of neutral atoms in spin-dependent optical lattice potentials. *Phys. Rev. Lett.*, 91(1):010407, 2003.

[91] P. C. Maurer, G. Kucsko, C. Latta, L. Jiang, N. Y. Yao, S. D. Bennett, F. Pastawski, D. Hunger, N. Chisholm, M. Markham, D. J. Twitchen, J. I. Cirac, and M. D. Lukin. Room-temperature quantum bit memory exceeding one second. *Science*, 336(6086):1283–1286, 2012.

[92] S. Meesala, Y.-I. Sohn, H. A. Atikian, S. Kim, M. J. Burek, J. T. Choy, and M. Lončar. Enhanced strain coupling of nitrogen-vacancy spins to nanoscale diamond cantilevers. *Phys. Rev. Appl.*, 5(3):034010, 2016.

[93] S. A. Momenzadeh, R. J. Stohr, F. F. De Oliveira, A. Brunner, A. Denisenko, S. Yang, F. Reinhard, and J. Wrachtrup. Nanoengineered diamond waveguide as a robust bright platform for nanomagnetometry using shallow nitrogen vacancy centers. *Nano Lett.*, 15(1):165–169, 2015.

[94] C. Monroe, W. C. Campbell, L.-M. Duan, Z.-X. Gong, A. V. Gorshkov, P. W. Hess, R. Islam, K. Kim, N. M. Linke, G. Pagano, et al. Programmable quantum simulations of spin systems with trapped ions. *Reviews of Modern Physics*, 93(2):025001, 2021.

[95] C. Monroe, R. Raussendorf, A. Ruthven, K. R. Brown, P. Maunz, L.-M. Duan, and J. Kim. Large-scale modular quantum-computer architecture with atomic memory and photonic interconnects. *Phys. Rev. A*, 89(2):022317, 2014.

[96] J. Moser, J. Güttinger, A. Eichler, M. J. Esplandiu, D. Liu, M. Dykman, and A. Bachtold. Ultrasensitive force detection with a nanotube mechanical resonator. *Nat. Nanotechnol.*, 8(7):493–496, 2013.

[97] J. T. Muhonen, G. R. La Gala, R. Leijssen, and E. Verhagen. State preparation and tomography of a nanomechanical resonator with fast light pulses. *Phys. Rev. Lett.*, 123(11):113601, 2019.

[98] D. J. Muller. Afm: a nanotool in membrane biology. *Biochemistry*, 47(31):7986–7998, 2008.

[99] J. N. Neethirajan, T. Hache, D. Paone, D. Pinto, A. Denisenko, R. Stöhr, P. Udvarhelyi, A. Pershin, A. Gali, J. Wrachtrup, et al. Controlled surface modification to revive shallow nv–centers. *Nano Lett.*, 23(7):2563–2569, 2023.

[100] J. M. Nichol, E. R. Hemesath, L. J. Lauhon, and R. Budakian. Nanomechanical detection of nuclear magnetic resonance using a silicon nanowire oscillator. *Phys. Rev. B*, 85:054414, Feb 2012.

[101] H. Noh, S.-B. Shim, M. Jung, Z. G. Khim, and J. Kim. A mechanical memory with a dc modulation of nonlinear resonance. *Appl. Phys. Lett.*, 97(3), 2010.

[102] T. Oeckinghaus, S. A. Momenzadeh, P. Scheiger, T. Shalomayeva, A. Finkler, D. Dasari, R. Stöhr, and J. Wrachtrup. Spin–phonon interfaces in coupled nanomechanical cantilevers. *Nano Lett.*, 20(1):463–469, 2020.

[103] F. Ohnesorge and G. Binnig. True atomic resolution by atomic force microscopy through repulsive and attractive forces. *Science*, 260(5113):1451–1456, 1993.

[104] T. Đorđević, P. Samutpraphoot, P. L. Ocola, H. Bernien, B. Grinkemeyer, I. Dimitrova, V. Vuletić, and M. D. Lukin. Entanglement transport and a nanophotonic interface for atoms in optical tweezers. *Science*, 373(6562):1511–1514, 2021.

[105] J. S. Otterbach, R. Manenti, N. Alidoust, A. Bestwick, M. Block, B. Bloom, S. Caldwell, N. Didier, E. S. Fried, S. Hong, et al. Unsupervised machine learning on a hybrid quantum computer. *arXiv preprint arXiv:1712.05771*, 2017.

[106] P. Ovartchaiyapong, K. W. Lee, B. A. Myers, and A. C. B. Jayich. Dynamic strain-mediated coupling of a single diamond spin to a mechanical resonator. *Nat. Commun.*, 5(1):4429, 2014.

[107] A. D. O'Connell, M. Hofheinz, M. Ansmann, R. C. Bialczak, M. Lenander, E. Lucero, M. Neeley, D. Sank, H. Wang, M. Weides, J. Wenner, J. M. Martinis, and A. N. Cleland. Quantum ground state and single-phonon control of a mechanical resonator. *Nature*, 464(7289):697–703, 2010.

[108] Y. G. Pastushenkov, A. Forkl, and H. Kronmüller. Temperature dependence of the domain structure in fe14nd2b single crystals during the spin-reorientation transition. *J. Magn. Magn. Mater.*, 174(3):278–288, 1997.

[109] A. E. Pelling, S. Sehati, E. B. Gralla, J. S. Valentine, and J. K. Gimzewski. Local nanomechanical motion of the cell wall of saccharomyces cerevisiae. *Science*, 305(5687):1147–1150, 2004.

[110] M. Pfender, N. Aslam, P. Simon, D. Antonov, G. Thiering, S. Burk, F. Fávaro de Oliveira, A. Denisenko, H. Fedder, J. Meijer, et al. Protecting a diamond quantum memory by charge state control. *Nano Lett.*, 17(10):5931–5937, 2017.

[111] M. Pfender, N. Aslam, H. Sumiya, S. Onoda, P. Neumann, J. Isoya, C. A. Meriles, and J. Wrachtrup. Nonvolatile nuclear spin memory enables sensor-unlimited nanoscale spectroscopy of small spin clusters. *Nat. Commun.*, 8(1):834, 2017.

[112] B. Pigeau, S. Rohr, L. Mercier de Lépinay, A. Gloppe, V. Jacques, and O. Arcizet. Observation of a phononic mollow triplet in a multimode hybrid spin-nanomechanical system. *Nat. Commun.*, 6(1):8603, 2015.

[113] J. M. Pino, J. M. Dreiling, C. Figgatt, J. P. Gaebler, S. A. Moses, M. S. Allman, C. H. Baldwin, M. Foss-Feig, D. Hayes, K. Mayer, et al. Demonstration of the trapped-ion quantum ccd computer architecture. *Nature*, 592(7853):209–213, 2021.

[114] M. Poot and H. S. van der Zant. Mechanical systems in the quantum regime. *Phys. Rep.*, 511(5):273–335, 2012.

[115] P. Rabl. Cooling of mechanical motion with a two-level system: The high-temperature regime. *Phys. Rev. B*, 82(16):165320, 2010.

[116] P. Rabl, P. Cappellaro, M. V. G. Dutt, L. Jiang, J. R. Maze, and M. D. Lukin. Strong magnetic coupling between an electronic spin qubit and a mechanical resonator. *Phys. Rev. B*, 79(4):041302, 2009.

[117] P. Rabl, S. J. Kolkowitz, F. Koppens, J. Harris, P. Zoller, and M. D. Lukin. A quantum spin transducer based on nanoelectromechanical resonator arrays. *Nat. Phys.*, 6(8):602–608, 2010.

[118] P. Rabl, S. J. Kolkowitz, F. H. L. Koppens, J. G. E. Harris, P. Zoller, and M. D. Lukin. A quantum spin transducer based on nanoelectromechanical resonator arrays. *Nat. Phys.*, 6(8):602–608, 2010.

[119] M. Radulaski, M. Widmann, M. Niethammer, J. L. Zhang, S.-Y. Lee, T. Rendler, K. G. Lagoudakis, N. T. Son, E. Janzén, T. Ohshima, et al. Scalable quantum photonics with single color centers in silicon carbide. *Nano Lett.*, 17(3):1782–1786, 2017.

[120] F. Ricci, M. T. Cuairan, G. P. Conangla, A. W. Schell, and R. Quidant. Accurate mass measurement of a levitated nanomechanical resonator for precision force-sensing. *Nano Lett.*, 19(10):6711–6715, 2019.

[121] R. Riedinger, A. Wallucks, I. Marinković, C. Löschnauer, M. Aspelmeyer, S. Hong, and S. Gröblacher. Remote quantum entanglement between two micromechanical oscillators. *Nature*, 556(7702):473–477, 2018.

[122] L. Robledo, L. Childress, H. Bernien, B. Hensen, P. F. Alkemade, and R. Hanson. High-fidelity projective read-out of a solid-state spin quantum register. *Nature*, 477(7366):574–578, 2011.

[123] L. Rondin, J.-P. Tetienne, P. Spinicelli, C. Dal Savio, K. Karrai, G. Dantelle, A. Thiaville, S. Rohart, J.-F. Roch, and V. Jacques. Nanoscale magnetic field mapping with a single spin scanning probe magnetometer. *Appl. Phys. Lett.*, 100(15), 2012.

[124] E. Rosenfeld, R. Riedinger, J. Gieseler, M. Schuetz, and M. D. Lukin. Efficient entanglement of spin qubits mediated by a hot mechanical oscillator. *Phys. Rev. Lett.*, 126(25):250505, 2021.

[125] E. L. Rosenfeld, L. M. Pham, M. D. Lukin, and R. L. Walsworth. Sensing coherent dynamics of electronic spin clusters in solids. *Phys. Rev. Lett.*, 120(24):243604, 2018.

[126] A. E. Rugar, C. Dory, S. Sun, and J. Vučković. Characterization of optical and spin properties of single tin-vacancy centers in diamond nanopillars. *Phys. Rev. B*, 99:205417, May 2019.

[127] D. Rugar, R. Budakian, H. J. Mamin, and B. W. Chui. Single spin detection by magnetic resonance force microscopy. *Nature*, 430(6997):329–332, 2004.

[128] D. Rugar and P. Grütter. Mechanical parametric amplification and thermomechanical noise squeezing. *Phys. Rev. Lett.*, 67(6):699, 1991.

[129] S. Sangtawesin, B. L. Dwyer, S. Srinivasan, J. J. Allred, L. V. H. Rodgers, K. De Greve, A. Stacey, N. Dontschuk, K. M. O'Donnell, D. Hu, et al. Origins of diamond surface noise probed by correlating single-spin measurements with surface spectroscopy. *Phys. Rev. X*, 9(3):031052, 2019.

[130] E. Schaefer-Nolte, F. Reinhard, M. Ternes, J. Wrachtrup, and K. Kern. A diamond-based scanning probe spin sensor operating at low temperature in ultra-high vacuum. *Rev. Sci. Instrum.*, 85(1), 2014.

[131] P. J. Scheidegger, S. Diesch, M. L. Palm, and C. L. Degen. Scanning nitrogen-vacancy magnetometry down to 350 mk. *Appl. Phys. Lett.*, 120(22), 2022.

[132] M. J. A. Schuetz, G. Giedke, L. M. K. Vandersypen, and J. I. Cirac. High-fidelity hot gates for generic spin-resonator systems. *Phys. Rev. A*, 95:052335, May 2017.

[133] L. Sementilli, E. Romero, and W. P. Bowen. Nanomechanical dissipation and strain engineering. *Adv. Funct. Mater.*, 32(3):2105247, 2022.

[134] D. Shin, A. Cupertino, M. H. de Jong, P. G. Steeneken, M. A. Bessa, and R. A. Norte. Spiderweb nanomechanical resonators via bayesian optimization: inspired by nature and guided by machine learning. *Adv. Mat.*, 34(3):2106248, 2022.

[135] P. W. Shor. Polynomial-time algorithms for prime factorization and discrete logarithms on a quantum computer. *SIAM Rev.*, 41(2):303–332, 1999.

[136] J. A. Sidles. Noninductive detection of single-proton magnetic resonance. *Appl. Phys. Lett.*, 58(24):2854–2856, 1991.

[137] B. Smeltzer, L. Childress, and A. Gali. 13c hyperfine interactions in the nitrogen-vacancy centre in diamond. *New J. Phys.*, 13(2):025021, 2011.

[138] P. L. Stanwix, L. M. Pham, J. R. Maze, D. Le Sage, T. K. Yeung, P. Cappellaro, P. R. Hemmer, A. Yacoby, M. D. Lukin, and R. L. Walsworth. Coherence of nitrogen-vacancy electronic spin ensembles in diamond. *Phys. Rev. B*, 82(20):201201, 2010.

[139] P.-J. Stas, Y. Q. Huan, B. Machielse, E. N. Knall, A. Suleymanzade, B. Pingault, M. Sutula, S. W. Ding, C. M. Knaut, D. R. Assumpcao, et al. Robust multi-qubit quantum network node with integrated error detection. *Science*, 378(6619):557–560, 2022.

[140] R. A. Steward. *Fabrication and characterization of ferromagnetic tips for magnetic resonance force microscopy*. PhD thesis, The Ohio State University, 2008.

[141] T. Stowe, K. Yasumura, T. Kenny, D. Botkin, K. Wago, and D. Rugar. Attonewton force detection using ultrathin silicon cantilevers. *Appl. Phys. Lett.*, 71(2):288–290, 1997.

[142] M. Stutzmann and D. Biegelsen. Electron-spin-lattice relaxation in amorphous silicon and germanium. *Phys. Rev. B*, 28(11):6256, 1983.

[143] J. Sun, J. Ren, J. Li, and Y. Huang. Measurement and analysis of magnetic properties of permalloy for magnetic shielding devices under different temperature environments. *Materials*, 16(8):3253, 2023.

[144] T. H. Taminiau, J. Cramer, T. van der Sar, V. V. Dobrovitski, and R. Hanson. Universal control and error correction in multi-qubit spin registers in diamond. *Nature nanotechnology*, 9(3):171–176, 2014.

[145] J. Teissier, A. Barfuss, P. Appel, E. Neu, and P. Maletinsky. Strain coupling of a nitrogen-vacancy center spin to a diamond mechanical oscillator. *Phys. Rev. Lett.*, 113(2):020503, 2014.

[146] J.-P. Tetienne, T. Hingant, L. Martínez, S. Rohart, A. Thiaville, L. H. Diez, K. Garcia, J.-P. Adam, J.-V. Kim, J.-F. Roch, et al. The nature of domain walls in ultrathin ferromagnets revealed by scanning nanomagnetometry. *Nat. Commun.*, 6(1):6733, 2015.

[147] J. P. Tetienne, L. Rondin, P. Spinicelli, M. Chipaux, T. Debuisschert, J.-F. Roch, and V. Jacques. Magnetic-field-dependent photodynamics of single nv defects in diamond: an application to qualitative all-optical magnetic imaging. *New J. Phys.*, 14(10):103033, 2012.

[148] C. Timberlake, G. Gasbarri, A. Vinante, A. Setter, and H. Ulbricht. Acceleration sensing with magnetically levitated oscillators above a superconductor. *Appl. Phys. Lett.*, 115(22), 2019.

[149] M. E. Trusheim, B. Pingault, N. H. Wan, M. Gündoğan, L. De Santis, R. Debroux, D. Gangloff, C. Purser, K. C. Chen, M. Walsh, et al. Transform-limited photons from a coherent tin-vacancy spin in diamond. *Phys. Rev. Lett.*, 124:023602, Jan 2020.

[150] Y. Tsaturyan, A. Barg, E. S. Polzik, and A. Schliesser. Ultracoherent nanomechanical resonators via soft clamping and dissipation dilution. *Nat. Nanotechnol.*, 12(8):776–783, 2017.

[151] J. Van Wezel and T. H. Oosterkamp. A nanoscale experiment measuring gravity's role in breaking the unitarity of quantum dynamics. *Proc. R. Soc. A.*, 468(2137):35–56, 2012.

[152] A. Vinante, M. Bahrami, A. Bassi, O. Usenko, G. Wijts, and T. H. Oosterkamp. Upper bounds on spontaneous wave-function collapse models using millikelvin-cooled nanocantilevers. *Phys. Rev. Lett.*, 116:090402, Mar 2016.

[153] A. Vinante and P. Falferi. Feedback-enhanced parametric squeezing of mechanical motion. *Phys. Rev. Lett.*, 111(20):207203, 2013.

[154] R. G. West, K. Kanellopulos, and S. Schmid. Photothermal microscopy and spectroscopy with nanomechanical resonators. *J. Phys. Chem. C*, 127(45):21915–21929, 2023.

[155] M. Widmann, S.-Y. Lee, T. Rendler, N. T. Son, H. Fedder, S. Paik, L.-P. Yang, N. Zhao, S. Yang, I. Booker, et al. Coherent control of single spins in silicon carbide at room temperature. *Nat. Mat.*, 14(2):164–168, 2015.

[156] E. P. Wohlfarth. *Handbook of magnetic materials*, volume 2. Elsevier, 1986.

[157] A. L. Woodcraft. Recommended values for the thermal conductivity of aluminium of different purities in the cryogenic to room temperature range, and a comparison with copper. *Cryogenics*, 45(9):626–636, 2005.

[158] L. Xie, T. X. Zhou, R. J. Stöhr, and A. Yacoby. Crystallographic orientation dependent reactive ion etching in single crystal diamond. *Adv. Mat.*, 30(11):1705501, 2018.

[159] S. Yamada, S. Schmid, T. Larsen, O. Hansen, and A. Boisen. Photothermal infrared spectroscopy of airborne samples with mechanical string resonators. *Anal. Chem.*, 85(21):10531–10535, 2013.

[160] T. Yamada, T. Tomaru, T. Suzuki, T. Ushiba, N. Kimura, S. Takada, Y. Inoue, and T. Kajita. High performance thermal link with small spring constant for cryogenic applications. *Cryogenics*, 116:103280, 2021.

[161] S. Zaiser, T. Rendler, I. Jakobi, T. Wolf, S.-Y. Lee, S. Wagner, V. Bergholm, T. Schulte-Herbrüggen, P. Neumann, and J. Wrachtrup. Enhancing quantum sensing sensitivity by a quantum memory. *Nat. Commun.*, 7(1):12279, 2016.

[162] J. L. Zhang, K. G. Lagoudakis, Y.-K. Tzeng, C. Dory, M. Radulaski, Y. Kelaita, K. A. Fischer, S. Sun, Z.-X. Shen, N. A. Melosh, et al. Complete coherent control of silicon vacancies in diamond nanopillars containing single defect centers. *Optica*, 4(11):1317–1321, Nov 2017.

[163] T. X. Zhou, R. J. Stöhr, and A. Yacoby. Scanning diamond nv center probes compatible with conventional afm technology. *Appl. Phys. Lett.*, 111(16), 2017.

Appendix A

Fabrication of Mechanical Resonator Chip

The full recipe for making a chip containing mechanical resonators along a coplanar waveguide is described below. The fabrication of iron thin-film magnets is covered in this recipe. If one were to pick-and-place neodymium magnets instead, A.3 can be skipped and the neodymium magnets can be placed after the resonator release following the procedure in B.

A.1 Coplanar Waveguide Fabrication

A.1.1 Cleaning

- 5-minute AMI clean
  - Sonicate wafer in acetone, methanol, and isopropyl alcohol (IPA) for 5 min each.
  - This step is optional; no need to do this if wafer is straight out of the box from vendor.

A.1.2 Spinning Resist

- Dynamic clean
  - Use a spin sequence of 500 RPM (5 s) followed by 3500 RPM (45 s). (From now on, unless specified otherwise, all spin sequences start with a 500 RPM pre-spin for 5 s, followed by a subsequent spin at high speed for 45 s.)
  - During the first part (500 RPM) of the sequence, spray acetone at the center of the wafer for a few seconds, and then spray IPA until the spinner ramps up to full speed (3500 RPM) in the second step.
- Dehydration bake at 180 °C for 5 min. Cool down the wafer by running a spin sequence without resist.
- Spin LOR 20B at 4000 RPM.
  - Dispense LOR20B directly from cup to cover at least 2/3 of wafer
- Bake at 180 °C for 4 min. Cool down the wafer by running a spin sequence without resist.
- Spin S1805 at 4000 RPM.
  - Dispense to center of wafer using plastic pipette.
  - Skip the 500 RPM ramp of the spin sequence.
  - After spinning, remove beads of resist on the edges by using a swab soaked with acetone.
- Soft bake at 115 °C for 1 min.

A.1.3 Optical Lithography

We use a masklesss optical lithography tool (Heidelberg MLA150) to define the coplanar waveguide. The wafers come pre-scored on the backside so that we can break them apart

easily into roughly 1×1 cm^2. These score-lines can also be used to perform backside alignment of the CPW to the wafer. We use a dose of 65 mJ/cm^2 and laser wavelength of 405 nm. The entire pattern write takes about 1.25 h.

The development is done according to the following steps:

- Wear full protection: nitrile gloves, apron, and face shield.
- Develop in tray of CD-26 for 45 s. Agitate bath by gently moving tray left and right.
- Halt the development by placing wafer under low-pressure running deionized (DI) water.
- Submerge in DI water for about 1 min.
- Blow dry with nitrogen.
- Inspect under optical microscope. Develop more in 10 s increments if necessary.

A.1.4 Metal Deposition

We use an electron-beam evaporator (Denton Vacuum) to deposit 7 nm titanium followed by 200 nm gold. We typically wait for the vacuum to pump down to $\approx 10^{-6}$ Torr before starting the evaporation.

A.1.5 Liftoff

- Place wafer in Remover PG (Kayaku).
  - Some metal will start lifting off right away. You can blow them off the wafer with a plastic pipette to speed up the process.
- Leave wafer in Remover PG at 80 °C overnight.
- Use plastic pipette to remove any remaining metal stuck on the wafer.
- Immerse wafer in acetone and then IPA for 5 min each.
- Blow dry with nitrogen.

A.2 Nanobeam Definition

A.2.1 Spinning Resist

- Dynamic clean (see first step in Sec. A.1.2).
- Dehydration bake at 180 °C for 5 min. Cool down the wafer by running a spin sequence without resist.
- Spin ZEP520A (Zeon) at 4000 RPM.
- Bake at 180 °C for 1 min. Cool down the wafer by running a spin sequence without resist.
- Spin ESPACER (Resonac) at 1000 RPM.
  - Transfer chip to e-beam lithography machine within the next 20 min.

A.2.2 E-beam Lithography

To define the resonator with high resolution, we perform electron beam lithography using ELS-HS50 (Elionix). The pattern of resonators is aligned to the CPW using 4 alignment marks. The dose used is 160 $\mu C/cm^2$.

The development is done according to the following steps:

- Submerge chip in DI water for 1 min to remove ESPACER.
- Submerge chip in o-Xylene for 1 min.
- Submerge chip in IPA for 1 min.
- Blow dry with nitrogen.

A.2.3 Nitride Etching

- Clean an 8-in carrier wafer with IPA and load it into the reactive ion etcher (STS).

- Run an O_2 plasma clean and silicon etch conditioning recipe, each for 10 min.
- Place the chip onto the carrier wafer, after applying a small drop of oil for thermal anchoring.
- Run the nitride etch recipe, which uses a C_4H_8/SF_6 chemistry, for 2 min 15 s.
  - This step etches through the nitride layer and also etches about 1 µm into the silicon, which helps with the subsequent release with XeF_2.
- Retrieve chip and remove any residual oil on the backside with IPA.

A.3 Magnet Definition and Deposition

A.3.1 Spinning Resist

- Dynamic clean (see first step in Sec. A.1.2).
- Dehydration bake at 180 °C for 5 min. Cool down the chip by running a spin sequence without resist.
- Spin MMA EL-11 (Kayaku) at 5000 RPM.
- Bake at 180 °C for 5 min. Cool down the chip by running a spin sequence without resist.
- Spin PMMA C-4 at 5000 RPM.
- Bake at 180 °C for 5 min.

A.3.2 Defining Micromagnets

To define the magnets, we perform electron beam lithography using ELS-HS50 (Elionix). The pattern of magnets is aligned to the resonators using 4 alignment marks. The dose used is 2000 µC/cm^2.

The development is done according to the following steps:

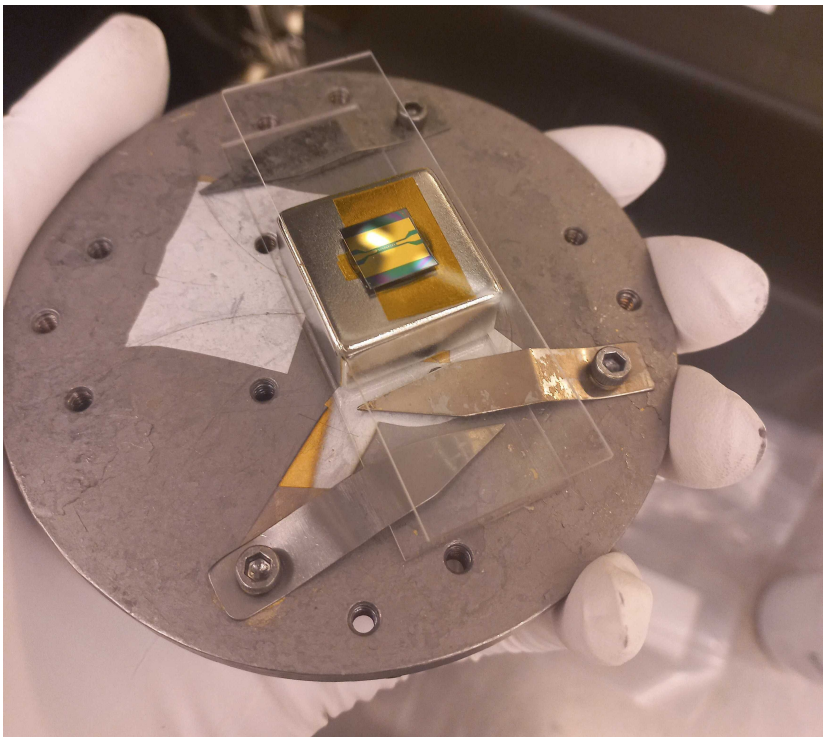


Figure A.1: A neodymium magnet is placed next to the sample inside the e-beam evaporator to magnetize the deposited iron thin-film in-situ.

- Submerge chip in a solution of MIBK:IPA (1:3) for 100 s while gently agitating the solution.
- Submerge chip in IPA for 30 s.
- Blow dry with nitrogen.

A.3.3 Magnet Deposition

We deposit thin-film magnets using an e-beam evaporator (Sharon), following the steps below:

- Load evaporator with crucibles (KJ Lesker FABMATE) containing chromium and iron (99.99% purity) pellets.
- Load evporator with chip(s) and a large neodymium magnet to magnetize the iron

in-situ (Fig. A.1).

  - Clamp down a glass slide onto substrate holder.
  - Attach the large magnet onto the glass slide using double-sided Kapton tape.
  - Cover the magnet by taping another glass slide on top of it.
  - Attach chip(s) onto the topmost glass slide using double-sided Kapton tape.

- Pump down chamber to $\approx 10^{-6}$ Torr.
- Evaporate 8 nm chromium at 1 Å/s.
- Evaporate 182 nm iron at 1 Å/s.
- Evaporate 10 nm chromium at 1 Å/s.

A.3.4 Liftoff

- Place chip(s) into PG Remover at 80 °C overnight.
- Use pipette to remove any metal still stuck to the chip.
- Immerse the chip(s) in IPA and then DI water for 5 min each.
- Blow dry with nitrogen.

A.4 Nanobeam Release

We use XeF2 to release the resonators. XeF2 is used in the MEMS industry because of its high selectivity to a variety of materials such as silicon nitride, silicon oxide, and various metals. It is also a dry process, which eliminates problems with stiction associated with wet processes. As for the downsides, the process is very sensitive to the surface chemistry, and the etch rate depends on the aperture size, which places constraints on the complexity of the mechanical resonator's shape.

The steps are as follows:

- Clean XeF2 etcher (Xactix) with IPA.
- Condition the chamber by running a continuous flow recipe, with XeF2 pressure of 0.8 Torr, flow rate of 0.5 sccm, and process time of 1.5 min.
- Etch using a continuous flow recipe, with XeF2 pressure of 0.8 Torr, flow rate of 0.5 sccm, and process time of 1.0 min.
  - We have previously tried a pulsed flow recipe, which alternates between pulses of XeF2 and nitrogen to reduce the etch roughness and improve selectivity. However, we have noticed residual filaments connecting the nanobeam and the underlying silicon in SEM images. This issue was solved by using a continuous flow recipe.
- Perform additional etches with same pressure and flow parameters, using a shorter process time of 0.2 min, until all features have been released.
  - A nanobeam is most likely released if the nitride overhang on the sides is wider than the nanobeam itself. Overetching can decrease the mechanical quality factor.

Appendix B

Magnetic Functonalization of Nanobeams with Neodymium Microspheres

In this section we outline the steps and equipment needed to magnetically functionalize nanobeams.

B.1 Setup and Components

A micromanipulator setup (Fig. B.1) is used to pick and place neodymium micropsheres onto nanobeams. The key components are:

- 3-axis flexure stage (Thorlabs MAX312D)
- Tungsten probe tips (Electron Microscopy Sciences 75960-02)
- Fiber clamps (Thorlabs T711-250)
- Epoxy (Loctite 349)
- UV curing system (Thorlabs CS20K2)

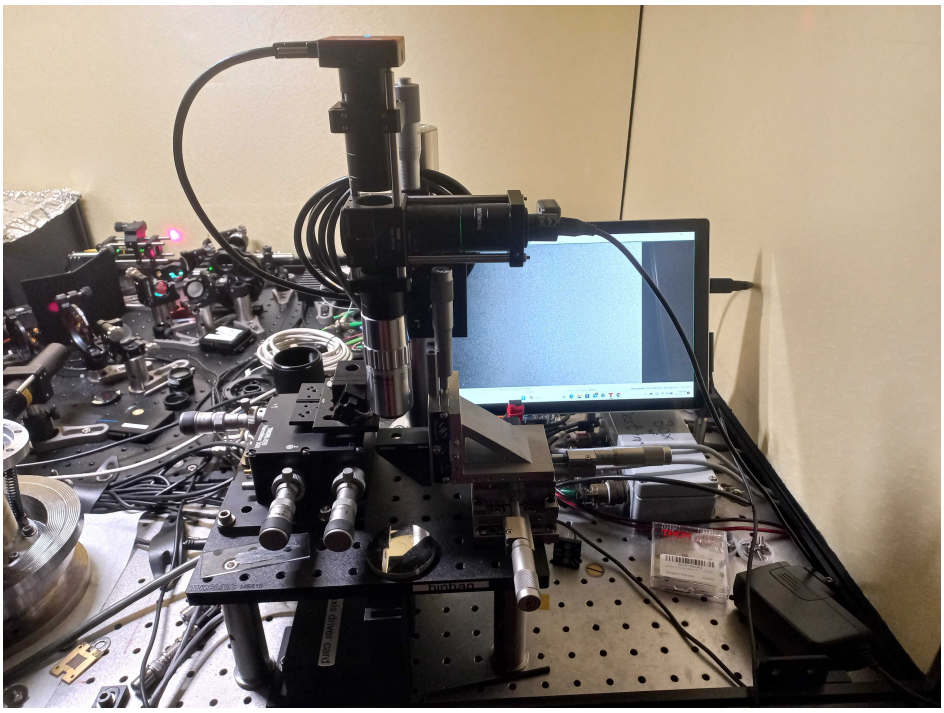


Figure B.1: Micromanipulator setup

B.2 Preparation

1. Prepare two new needles, each mounted inside a fiber clamp; one for applying glue and the other for placing micromagnets.

    - Adjust the fiber clamps so that both needles will be mounted at a steep angle to the substrate. Keep the angle and needle location in both clamps to be as close as possible to save time refinding the focus when switching between the two.

2. Use a spatula to place a small amount of micromagnets onto a substrate, such as a copper piece or glass slide cleaned with isopropyl alcohol (IPA). Do this in a fume hood to avoid breathing in microparticles. Tap the substrate a few times to scatter the magnets around the substrate.

3. Smear epoxy onto a clean glass slide using a razor blade.

B.3 Applying Glue to Needle

1. Mount the glue needle onto the flexure stage.
2. Mount the glass slide with epoxy onto the coarse translation stage.
3. Use the flexure stage to bring the needle's tip into focus on the camera.
    - The tip is only about 1 µm wide, so it is easier to focus on the thicker part of the needle before following the taper to the tip.
    - If the tip is bent or not at the lowest point relative to the rest of the needle, use a different needle.
4. Use the coarse stage to approach the tip with the sample, checking the focii of the needle and glue periodically to avoid crashing
5. When focii of sample and tip are sufficiently close (i.e. you can see the shadow of tip on the glue), use the flexure stage's Z-axis fine knob to gently touch the epoxy with the needle.
6. Move the needle around in the epoxy in all 3 axes to make sure the epoxy gets onto some part of the needle.

B.4 Applying Epoxy to Sample

1. Take out the glass slide with epoxy.
2. Mount the sample chip onto the coarse translation stage.
3. Use the coarse stage to approach the glue tip with the sample, checking the focii of the needle and sample periodically to avoid crashing.
    - Make sure to focus on some obvious feature (e.g. CPW) on the sample, rather than an empty area, to avoid missing the focus and crashing

4. Once the tip of the needle is a few microns above the sample, use the coarse stage to move to an empty area on the side of the sample (far away from the CPW and strings), and push down the needle onto the sample, until you see the needle move horizontally along the sample surface. This should deposit a big blob of epoxy from the thicker part of the needle.

5. Use the tip of the needle to pick up epoxy from this big blob. From now on, you can use this big blob of epoxy as your "reservoir". This not only saves time switching back between the sample chip and the glass slide with epoxy, but also helps ensure that there is epoxy on the needle's tip.

6. Use the flexure stage to gently touch the string with the epoxy needle.

    - The string should move/change its shade when the needle touches it
    - The deposited epoxy should show up as a darker spot on the string. If not, try smearing the epoxy a bit along the string or use the thicker part of the needle.

7. Transfer epoxy to a few more strings. Transfer to as many strings as you think you can functionalize before the working time (roughly 2 hours) of the epoxy runs out.

B.5 Picking up a Micromagnet

1. Take out sample chip and epoxy needle.

2. Mount the slide with scattered micromagnets onto the coarse translation stage.

3. Mount the magnet needle onto the flexure stage.

4. Similar to the glue deposition procedure, approach the sample with the needle. When the focii of sample and tip are sufficiently close (i.e. can see the shadow of the needle's tip on the sample), use the flexure stage to touch the magnet's top surface with the needle tip and pick it up.

    - Do not apply too much pressure on the magnet or it will fly away.

- The magnet should stick to the bottom of the needle tip. If it is stuck to the needle's side, slam down the needle onto the substrate to remove the magnet and try again.
- If the magnet seems to be repulsed by the needle, or if it seems to snap back to the glass slide, replace the needle. If that fails to fix the problem, try changing the substrate material from an insulator to a conductor (or vice versa).

5. After confirming that the magnet is stuck under the needle tip, retract the substrate using the coarse translation stage.
6. Unmount the substrate with magnets and mount the sample chip.
7. Place the magnet onto the nanobeam. Just like with the epoxy, use minimal force to avoid damaging the nanobeam.
    - You should be able to get the magnet to stick by just bringing down the needle vertically and then lifting it back up.
    - If that fails, try making contact between the magnet and the nanobeam, and then gently drag the needle away perpendicular to the nanobeam.
    - If all else fails, slam the needle down onto an empty part of the sample to get it off, pick it back up and try putting it on the nanobeam again.

B.6 Curing the Epoxy (heat)

For epoxy that requires heat cure:

1. Cover a hot plate with clean foil and place sample on top.
2. Set hot plate temperature to 65 °C for 2 hours. Adjust temperature and time according to the datasheet. Err on the side of over-curing, by adding >5 °C to account for the temperature difference between the surface of the sample and hot plate.
3. Cover the sample with a glass beaker to protect it from dust.

4. Wait in person until the hot plate reaches desired temperature and then come back later to retrieve sample.

B.7 Curing the Epoxy (UV)

For epoxy that requires UV cure:

1. Wear appropriate eye protection.

2. Shine UV light at maximum power onto the sample for 10 – 30 minutes. Keep the lamp about 1 – 2 cm away from the sample.

Appendix C

Attempts to revive diamond probes

Multiple methods have been developed to revive “dead” NV centers with either no contrast or very low fluorescence. The methods are unconventional and we encourage the reader to think of them as acts of heroic struggle and desperation, similar to how one might punch a vending machine to dislodge a snack stuck inside. In a lot of cases, we were expecting new probes to arrive soon, so we did not spend the time to systematically test the effectiveness of each method.

The first method involves placing the nanopillar in a “sauna”, which was based on previous work showing that adsorption of water could revive shallow NV centers [99]. The procedure is as follows:

- Cool the diamond probe in a domestic fridge (in lab) overnight.
- Heat up ultrapure DI water in glass beaker using a domestic microwave (in lab).
- Place the cold diamond probe next to the beaker with hot water, and cover both with a big beaker to "steam" it for a minute or two (Fig. C.1).
- Put diamond probe in a nitrogen box for drying.

We have used this method on three probes with low contrast, but this method has only worked once, where the ESR contrast increased from 8% to 20%.



(a) (b)

Figure C.1: (a) A diamond probe (on copper probe mount) and a beaker of hot water are enclosed in a "sauna". (b) Condensation on the diamond probe and probe holder.

The second method involves acid-cleaning the diamond nanopillar. We were inspired to try this because acid-cleaning is a standard procedure for diamond-cleaning, and there is some literature on its effectiveness on diamond nanopillars (page 199 in [85]). However, the diamond nanopillar is typically glued onto either a cantilever or tuning fork typically made of silicon, and it is unclear whether the standard tri-acid mixture of sulfuric, nitric, and perchloric acid will dissolve the glue or the rest of the probe support such as the PCB or AFM chip. Our solution is to use the micromanipulator (same one used to place micromagnets on nanobeams) to dip only the diamond inside a small drop of acid (Fig. C.2a).

Another consideration is that the micromanipulator is located on an optics table in our lab, and it would be unwise to bring such a dangerous mixture of acid there. We therefore use Citranox as the acid instead, which is a much safer option. However, Citranox only contains about 10 – 20% of citrix acid by weight [4], and there is scant literature on its effectiveness for diamond-cleaning [50]. In the future, one might consider moving the

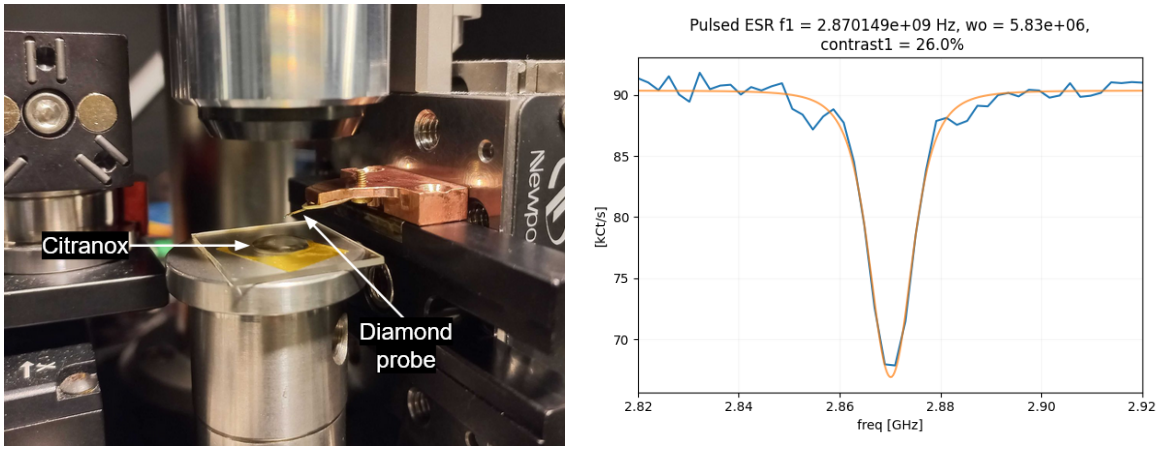
micromanipulator setup to a wet lab and use a tri-acid mixture instead.

The procedure is as follows:

- Use a pipette to deposit a drop of Citranox onto a glass slide.
- Mount diamond probe on translation stage such that the nanopillar is pointing down.
- Lower probe to approach acid drop
  - When the nanopillar is close to the acid, the reflection of the former can be seen in the acid.
  - The focii of the reflection and actual nanopillar will merge; that is when the tip is very close to the acid.
- Dip entire nanopillar inside acid.
- Move the diamond probe around in the field of view of the microscope.
- Leave the nanopillar in the acid for about 30 min, and lower it further as the acid evaporates.
- Retract probe.

The procedure is then repeated with a drop of DI water to remove residue from the acid.

In our first attempt to revive an NV center with low contrast ($\sim 8\%$), the fluorescence counts increased to 200 kCt/s after the acid-cleaning. After touching the coplanar waveguide of a sample with a nanopillar to neutralize surface charges, the counts returned to the normal 80 kCt/s but the contrast stayed the same. Afterwards, we ran CW ESR and galvo scans around the NV center's location for a few hours, during which the contrast gradually recovered to 26% (Fig. C.2b).



(a) **(b)**

Figure C.2: (a) The same micromanipulator setup used for placing micromagnets on nanobeams (Sec. B) can also be used for "acid-cleaning" diamond nanopillars. (b) Pulsed ESR contrast reaches 26% after acid-cleaning and scanning the laser over the NV center for a few hours.

Appendix D

Experimental Setup and Methods for Chapter 5

D.1 Experimental setup

The experiment is performed inside a modified Janis ST-500 continuous flow cryostat, which also serves as a vacuum chamber for room temperature measurements shown in Fig. 2 and 3. The AFM chip containing the diamond nanopillar is attached to a glass slide which is then mounted on a fixed copper block. The sample containing the nanobeams is mounted on a 3-axis Attocube stack (ANPz101 and ANPx101), which allows for fine control over the position of the diamond nanopillar relative to nanobeam.

We use a home-built confocal microscope to perform NV measurements. A Mach-Zehnder interferometer (Fig. D.1) integrated into the optical path is used to characterize the mechanical properties of the nanobeams.

D.2 Sample Fabrication

We start with a 4-inch, 525 µm-thick, high resistivity ($\geq 10^4\ \Omega \cdot \mathrm{cm}$) $\langle 100 \rangle$ silicon wafer obtained from Silicon Valley Microelectronics (SVMI). These wafers have 150 mm of high stress (~ 1 GPa) silicon nitride deposited on one side using LPCVD. The backside is also

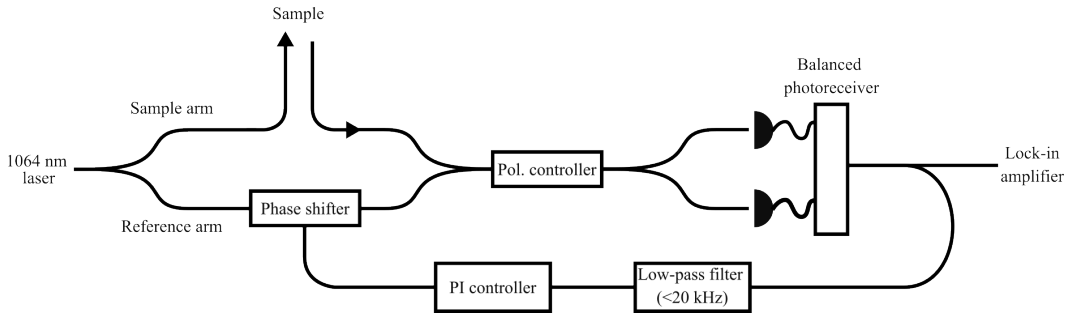


Figure D.1: Schematic of the interferometer. A 1064 nm laser is split into a sample and reference arm. Power in the sample arm is reflected off a nanobeam and then recombined with the reference arm. The light is then split off again by a polarization beam splitter to be detected by a balanced photoreceiver (Newport 2117-FC), where the output is sent for lock-in detection (Zurich Instruments HF2) and also used to phase-stabilize the reference arm against low-frequency noise.

scored $\sim 200\,\text{nm}$ deep according to a 1 cm square grid.

First, we fabricate the coplanar waveguide (CPW) using optical lithography, electron-beam evaporation, and a liftoff process. The CPW consists of 200 nm of gold evaporated on a 7 nm sticking layer of titanium. Next, the mechanical resonators are defined with electron-beam lithography and the corresponding areas are etched with reactive ion etching, resulting in nanobeams that are 145 µm long and 1 µm wide. Then the resonators are released using either a wet KOH etch or a dry XeF_2 isotropic etch. Finally, the sample chip is wire-bonded to a printed circuit board (PCB) for microwave delivery.

We magnetically functionalize the nanobeam using a home-built micromanipulator setup. The sample is placed on a 3-axis translation stage, while a tungsten tip (75960-02, Electron Microscopy Sciences) is mounted on a nearby micromanipulator. This allows us to move both the sample and tip independently under a microscope objective (100X Mitutoyo Plan Apo SL). We first deposit a small volume of UV epoxy (Loctite 349) on the center of the beam using the tungsten tip. Then we use another tungsten tip to pick up a NdFeB micromagnet, put it on the glue, and cure the epoxy with UV light. Since we have observed that the glue remains tacky even after prolonged UV exposure, we put the sample on a hot plate at 80 °C for 8 hours to eliminate any "tackiness". A comparison of the quality factors

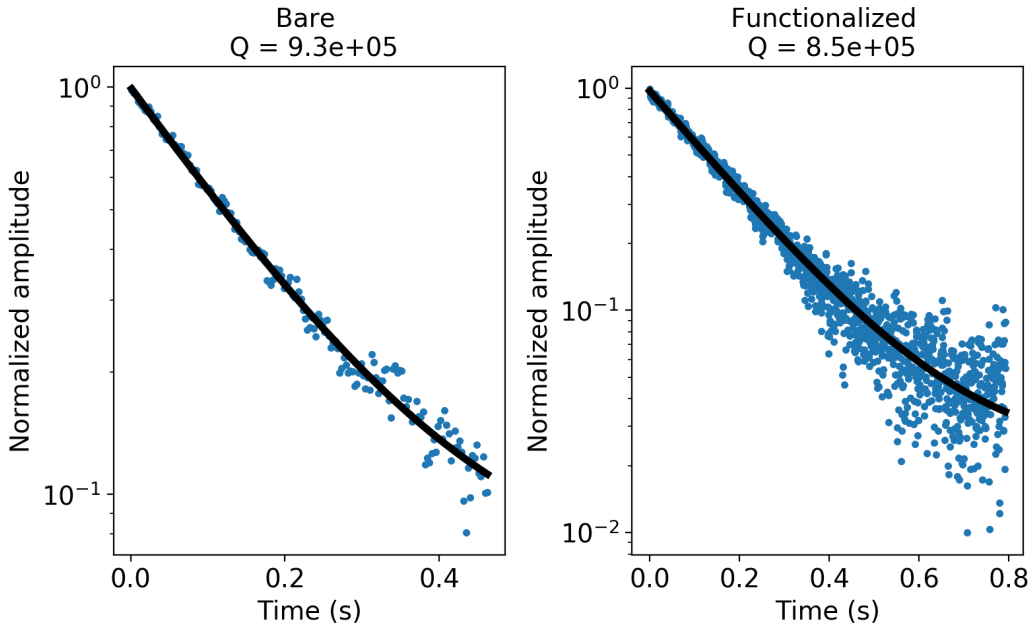


Figure D.2: Ringdown measurements of a bare resonator (left) and a functionalized resonator (right, same as Fig. 4(b) of the main text), taken at cryostat base temperature of 20 K and 10 K respectively.

of a functionalized and bare resonator is shown in Fig. D.2.

Details on fabrication of the diamond nanopillars can be found in references [158, 163].

D.3 Magnetic Field Imaging

The scan in Fig. 2(a) in the main text was done in air at room temperature without an external field. At each position in the scan, we perform an electron spin resonance (ESR) measurement by sweeping a microwave frequency and observing changes in the NV center photoluminescence. Since we are not driving the mechanical resonator and the measurement time is much longer than the mechanical period, we can neglect the mechanics. The spin Hamiltonian is given by:

$$\mathcal{H}/\hbar = DS_z^2 + \gamma_e(S_z \cdot B_z + S_x \cdot B_x) \tag{D.1}$$

where $D = 2.8707\,\text{GHz}$ is the zero-field splitting and $\gamma_e = 2.8\,\text{MHz/G}$ is the NV gyromagnetic ratio. By diagonalizing $\mathcal{H}$, we can extract the magnetic field component B_z from the micromagnet that is parallel to the NV center quantization axis.

Two pixels are missing because the ESR frequencies exceeded the frequency sweep range. We do not consider the missing pixels in the fit to the dipole model. For display in the figure, we fill in these pixels by interpolating from nearby pixels.

D.4 Analytical Form of Hahn Echo Contrast in the Presence of Mechanical Motion

For our analysis we consider only the $|S_z = +1\rangle$ and $|S_z = 0\rangle$ eigenstates, and model our spin-mechanical system using the following Hamiltonian:

$$\mathcal{H}/\hbar = \frac{\omega_s}{2}\sigma_z + \omega_r a^\dagger a + \lambda\sigma_z(a + a^\dagger) \tag{D.2}$$

where a is the annihilation operator for the mechanical mode, $S_z = \frac{1}{2}\sigma_z$ is the spin-$\frac{1}{2}$ operator, and $\lambda = 2\pi\gamma_e z_p G$ is the spin-mechanical coupling strength for gradient G and zero-point motion z_p. For our system, we find typical values of $z_p \sim 10\,\text{fm}$.

Considering a Hahn echo pulse sequence, we calculate the signal in the limit of no intrinsic spin decoherence. Since λ is small, we use a semi-classical approximation, where the resonator quadrature $x = z_p(a + a^\dagger)$ is independent of the spin state.

After initializing the spin into $|0\rangle$, we put it into a coherent superposition with a $\pi/2$ pulse. We then let it evolve over time τ, resulting in the following spin state, up to a global phase:

$$|\psi\rangle = \frac{1}{\sqrt{2}}\left(|0\rangle + e^{-i\int_0^\tau \frac{\lambda}{z_p}x(t)dt}\,|1\rangle\right) \tag{D.3}$$

After the π pulse and evolution for another time τ, the spin state becomes

$$|\psi\rangle = \frac{1}{\sqrt{2}}\left(|0\rangle + e^{-i\phi(\tau)}\,|1\rangle\right) \tag{D.4}$$

where $\phi(\tau) \equiv \int_{\tau}^{2\tau} \frac{\lambda}{z_p} x(t)dt - \int_0^{\tau} \frac{\lambda}{z_p} x(t)dt$ is the phase difference accumulated due to the mechanical motion. After the last $\pi/2$ pulse to convert the coherence into population, the measured contrast is $\alpha \cos(\phi(\tau))$, where α is a constant determined by the spin-dependent optical initialization and readout, as well as the background fluorescence. We assume that the quality factor is high, $Q \gg 1$, such that the signal is highly correlated during the pulse sequence, and can be given by a specific point in phase space with amplitude x_0 and phase ϕ_0, such that $x(t) = x_0 \cos(\omega_r t + \phi_0)$. For a given run of the pulse sequence with phase ϕ_0 and amplitude x_0 the accumulated phase on the spin is:

$$\phi(\tau) = \frac{\lambda}{z_p \omega_r} x_0 \left(\sin(2\omega_r \tau + \phi_0) - 2\sin(\omega_r \tau + \phi_0) + \sin(\phi_0)\right) \tag{D.5}$$

The resonator frequency drifts over the duration of the Hahn echo measurement, so we apply a wide-band drive to ensure that the resonator is always driven on resonance. Because the wide-band drive effectively raises the temperature of the mechanical mode and the measurement is longer than the dissipation time, we incoherently average over the statistical distribution for $x(t)$. From the statistics of thermal states, we assume that ϕ_0 is uniformly distributed, and that the energy E of the resonator follows a Boltzmann distribution:

$$p(E)dE = \frac{1}{kT} e^{\frac{E}{kT}} dE \tag{D.6}$$

where $E = \frac{1}{2} m_{\text{eff}} \omega_r^2 x_0^2$ and $\frac{1}{2} k_B T = \frac{1}{2} m_{\text{eff}} \omega_r^2 \Delta_x^2$ according to the equipartition theorem; m_{eff} is the effective mass of the resonator, k_B is the Botlzmann constant, T is the effective temperature of the mechanical mode, and Δ_x^2 is the variance of the mechanical motion.

Averaging over the phase ϕ_0 first, we find the equivalent signal under a coherent drive with amplitude x_0:

$$\alpha \langle \cos(\phi(\tau)) \rangle_{\phi_0} = \alpha \mathcal{J}_0 \left(\frac{2\lambda x_0}{z_p \omega_r} \left(\cos(\omega_r t) - 1\right) \right), \tag{D.7}$$

where $\mathcal{J}_0$ is the zeroth order Bessel function of the first kind. Note that this would be the form of the signal under a coherent state assumption. Averaging over the amplitudes:

$$\alpha \langle \cos(\phi(\tau)) \rangle_{A,\phi_0} = \alpha \int_0^{\infty} \frac{1}{\Delta_x^2} e^{-x_0^2/2\Delta_x^2} \langle \cos(\phi(\tau)) \rangle_{\phi_0} x_0 \, \mathrm{d}x_0 = \alpha e^{-q(\tau)} \tag{D.8}$$

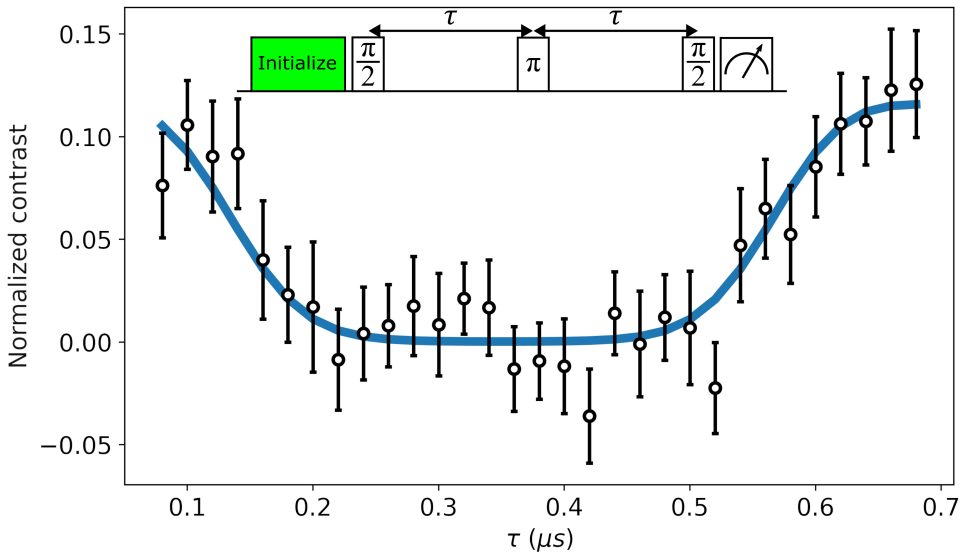


Figure D.3: Hahn echo contrast without normalizing to a baseline measurement (without driving mechanical resonator),

where $q(\tau) = 8\Delta_x^2\lambda^2 \sin^4(\omega_r\tau/2)/(\omega_r^2 z_p^2)$ as reported in the main text [20]. To account for spin decoherence, we include an additional phenomenological term $e^{\chi(\tau)}$ and factor it out with a baseline Hahn echo measurement in the absence of mechanical driving.

Fig. 4c of the main text shows the Hahn echo data normalized to a baseline measurement (without driving the mechanical resonator). In Fig. D.3, we also plot the raw Hahn echo contrast without the normalization.

D.5 Preservation of Coherent Information while Moving inside a Field Gradient

D.5.1 Experimental Setup

The measurements in Fig. 3 in the main text were performed in air at room temperature. An external field of about 180 G from a bar magnet is aligned within 1° to the quantization axis of the NV center. To drive radiofrequency (RF) pulses on nuclear spins, we use an external

coil consisting of magnet wire wound in two layers with 7 turns each.

The sample is placed on a 3-axis Attocube stack, which in turn is placed on top of a single-axis flexure stage (Thorlabs NFL5DP20S). To move the sample containing the mechanical resonators horizontally relative to the nanopillar during the movement sequence, we drive the flexure stage with a signal from an arbitrary function generator (Tektronix AFG3021) amplified by a piezo driver (Thorlabs BPC301). The signal is chosen to be a simple sinusoid to avoid exciting higher harmonics of the setup (e.g. resonances of the Attocube stack).

D.5.2 Nuclear and Electronic Spin Control

The RF signals are synthesized with an arbitrary function generator (Tektronix AFG3022) and amplified (Mini Circuits LZY-22+). With the RF coil placed between the nanopillar and long working distance objective (LU Plan 100X/0.90), we obtain minimum π-pulse durations of $\sim 20\,\mu s$.

The same on-chip coplanar waveguide (CPW) in Fig. 1 of the main text is used to drive microwave (MW) transitions of the electronic spin. We generate two MW signals at the fixed frequencies $MW_{\uparrow}$ and $MW_{\downarrow}$, which correspond to the upper and lower ^{15}N hyperfine transitions (Fig. D.4). The two MW signals are combined using a power combiner, gated with a switch, and then amplified (Mini Circuits ZHL 16W 43+).

During the movement sequence, the micromagnet begins near the NV center, moves away, and finally returns to its original position. The pulse sequences for the coherence measurements are synchronized with the movement sequence. While the hyperfine frequencies shift significantly over the entire movement sequence, we expect from the sinusoidal driving signal that the shift will be insignificant during the beginning and end, which are the only times where C_nNOT_e pulses are applied. We estimate from our field profile measurement in Fig. 3(a) that during the time between the two entangling/disentangling gates, the hyperfine frequencies do not deviate by more than 15 kHz, corresponding to an estimated phase accumulation of less than $0.01\,\pi$ over a maximum accumulation time of

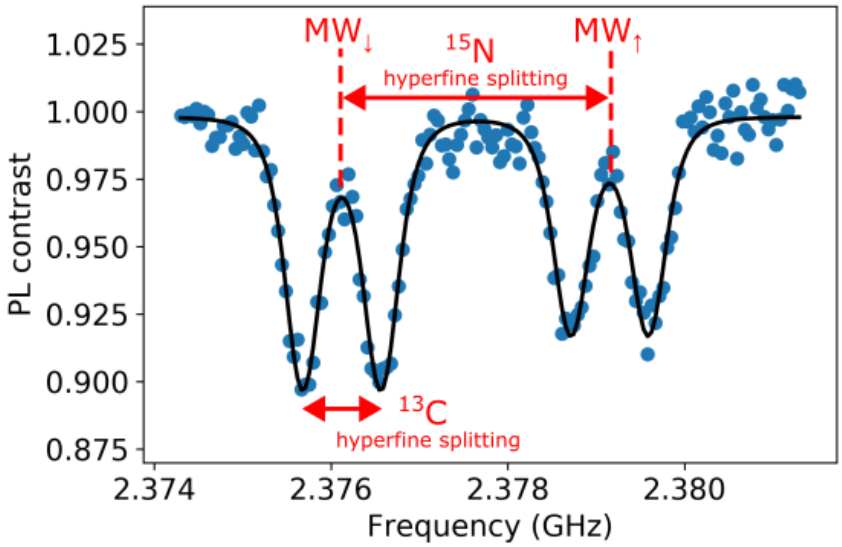


Figure D.4: Pulsed ESR measurement taken with the NV center being near a stationary micromagnet and an external field. We see four dips as a result of hyperfine interactions with both the ^{15}N and ^{13}C nuclear spins. We choose frequencies $\mathrm{MW}_{\downarrow}$ and $\mathrm{MW}_{\uparrow}$ such that they are equally detuned from the two nearby hyperfine transitions attributed to a nearby ^{13}C nuclear spin.

4.5 µs.

D.5.3 Pulse Sequence for ESR Measurements during Movement Sequence

To monitor the field experienced by the NV center during the movement of the micromagnet (Fig. 3(a) in main text), we take pulsed ESR measurements at different times and MW frequencies during the movement sequence (Fig. D.5). By initializing the NV center electronic spin and then applying a π pulse, we expect to see a drop in the NV photoluminescence if the MW frequency coincides with the ESR frequency. To obtain a better signal-to-noise ratio, we repeat for $n = 11$ times the initialization and π-pulse pair, for each time segment ($\sim 46\,\mu$s) of the entire movement duration of 1.7 ms.

Due to the long read times of our data acquisition card, we use a single long readout window for each time segment, which results in faster data acquisition at the expense of lower photoluminescence contrast, as the readout window now includes times where the

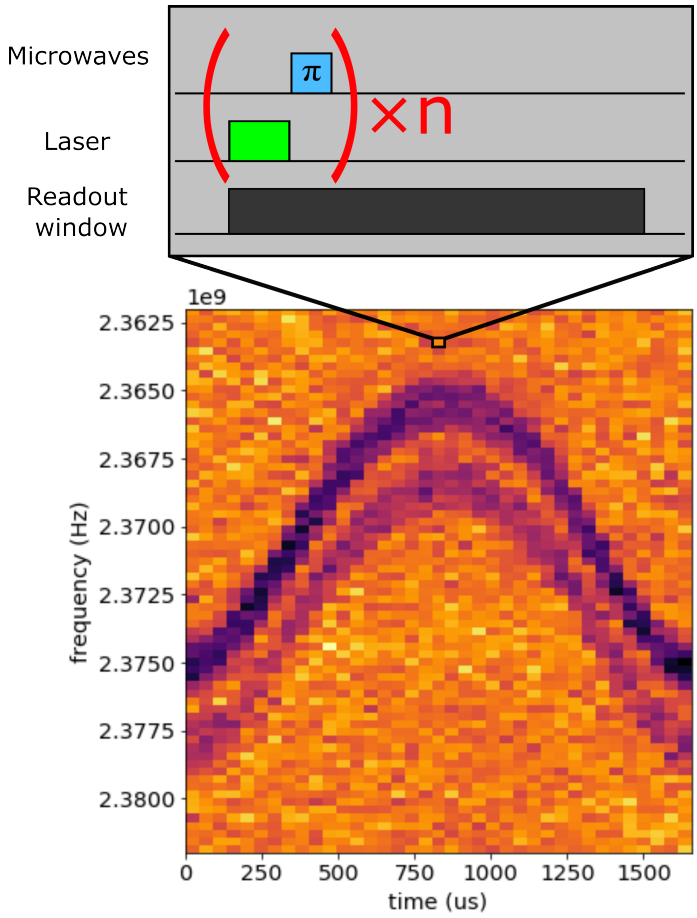


Figure D.5: Pulse sequence for taking ESR measurements during movement. For each microwave frequency, we divide the total movement time by a number of time segments (number of pixels along the x-axis). In each time segment we run the pulse sequence shown inside the gray box.

NV center is being reinitialized.

D.5.4 Pulse Sequence for Coherence Measurement

The detailed version of the pulse sequence in Fig. 3(b) in the main text is shown in Fig. D.6. At the beginning of the pulse sequence, we polarize the ^{15}N nuclear spin by first polarizing the electron spin and then transferring the polarization to the nuclear spin via a SWAP operation [77]. A pulsed ESR measurement after ^{15}N polarization is shown in Fig. D.7, where the polarization is $\sim 78\,\%$.

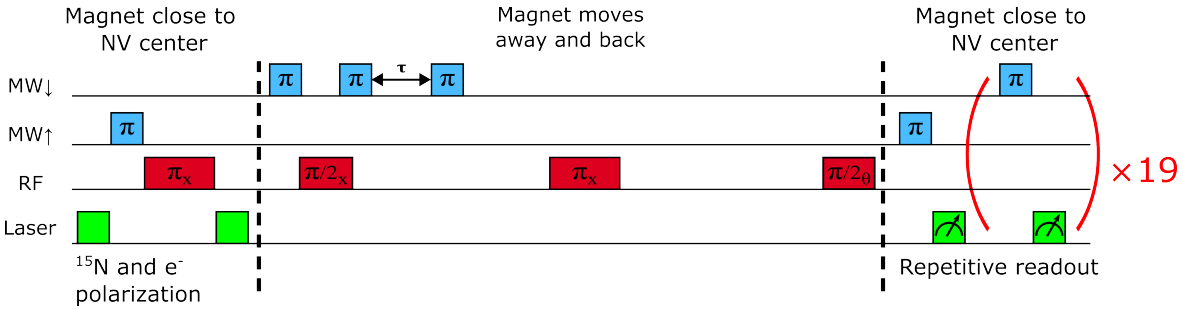


Figure D.6: Full pulse sequence for the measurements in Fig. 3(c) in the main text, with the part between the dashed lines corresponding to the pulse sequence in Fig. 3(b).

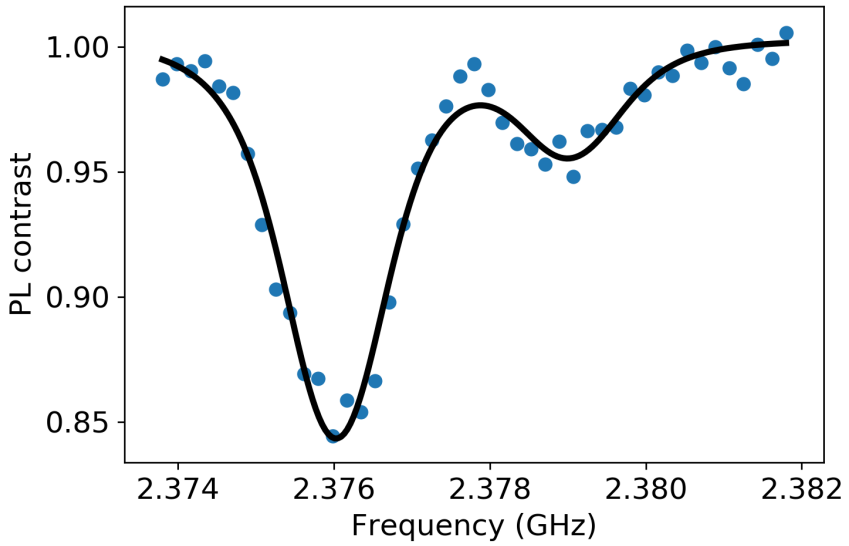


Figure D.7: Pulsed ESR taken after nuclear spin polarization.

To normalize the measurement in Fig. 3(c) in the main text, we use the same pulse sequence, but without the two entangling and disentangling C_nNOT_e gates. Setting the rotation axis angle of the final nuclear $\pi/2$ pulse to be $\theta = 0$ and π, we obtain the upper and lower bounds for the fluorescence levels, which we use to normalize the measurements where we vary θ.

Despite the small gyromagnetic ratio of the the ^{15}N nuclear spin, the field change during the movement sequence is large enough to cause significant phase accumulation ($> 2\pi$) on the nuclear spin (see Fig. D.8. To cancel out this phase, we apply a π-pulse on the ^{15}N

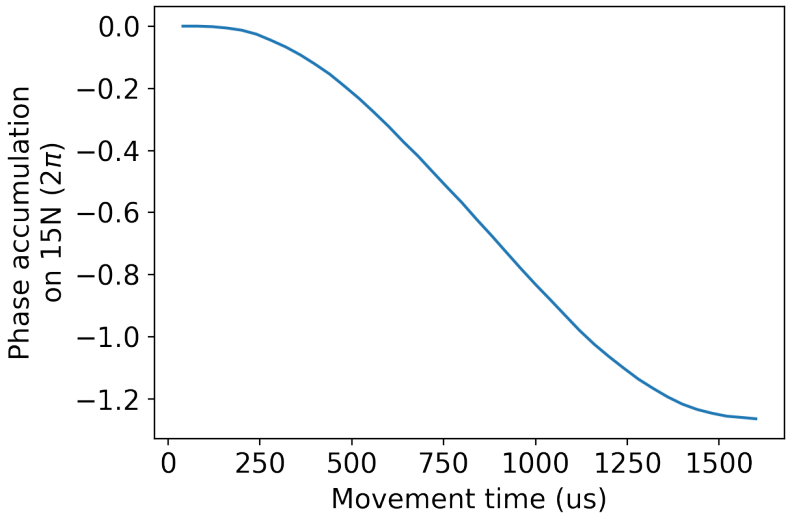


Figure D.8: Estimation of the phase accumulated on the ^{15}N nuclear spin during the movement sequence. From the ESR plot in Fig. 3(a) in the main text, one can integrate the magnetic field change over time to obtain the total phase accumulated on the nuclear spin.

nuclear spin. Since the field changes symmetrically during the movement sequence, the optimal time for this π-pulse is around the middle of the movement sequence, when the micromagnet is the furthest away from the NV center.

One can calculate the optimal T_π by measuring the ESR frequencies of the electronic spin during the movement sequence (Fig. 3(a) in the main text). As the micromagnet moves away from the diamond nanopillar, the ESR frequencies become positively detuned relative to their initial values due to the Zeeman interaction; as the micromagnet moves back, the detunings of the ESR frequencies decrease back to 0. The nuclear magnetic resonance (NMR) frequency of the ^{15}N nuclear spin also experiences the same detuning as the electron spin, scaled by the ratio of their respective gyromagnetic ratios $\gamma_\mathrm{n}/\gamma_e$. We then solve for T_π such that the total phase accumulated ϕ_n is 0:

$$\phi_\mathrm{n} = \int_0^{T_\pi} \gamma_\mathrm{n}\delta_\mathrm{n}(t)dt - \gamma_\mathrm{n}\int_{T_\pi}^{T_\mathrm{move}} \gamma_\mathrm{n}\delta_\mathrm{n}(t)dt = 0 \tag{D.9}$$

where $T_\mathrm{move} = 1.7\,\mathrm{ms}$ is the duration of the entire movement sequence; $\delta_n(t)$ is the time-dependent detuning of the ^{15}N NMR frequency from its frequency at the beginning of the

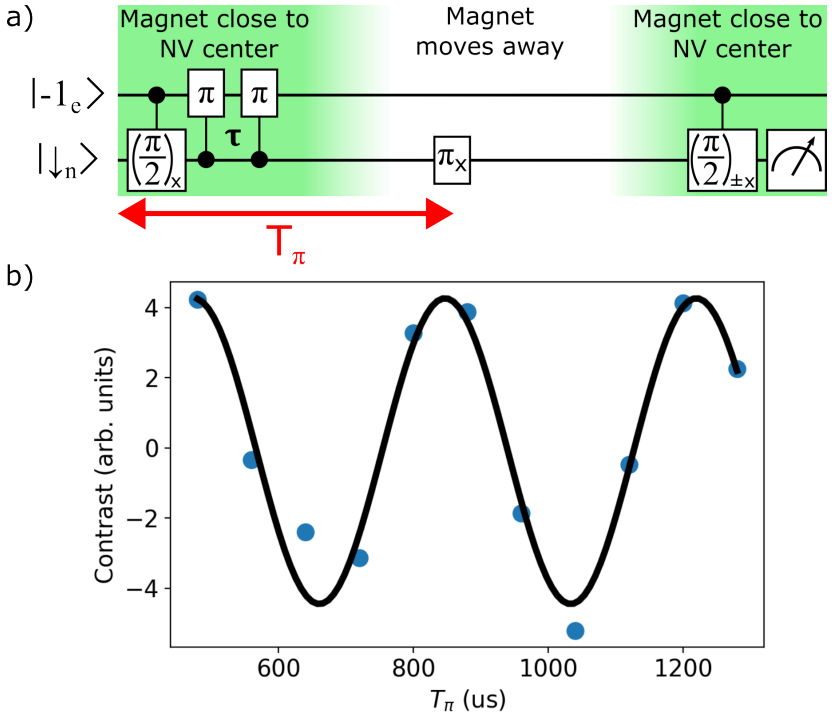


Figure D.9: (a) Pulse sequence for determining the optimal time of the ^{15}N nuclear spin echo π-time. (b) We observe fringes in the readout contrast as we sweep T_π, where the maxima correspond to times when the phase accumulation is cancelled out to 0 by the nuclear π-pulse. The contrast is defined as the difference between the readout fluorescence when the final $\pi/2$-pulse rotation axis is set to $+x$ and $-x$.

movement sequence.

To experimentally determine T_π, we use the pulse sequence in Fig. D.9, where we vary the π-pulse time T_π and observe the resulting change in readout photoluminescence. As expected, as we vary T_π, the total phase accumulation also changes, resulting in the fringes in Fig. D.9. The maxima of the fringe correspond to the times when the total phase accumulation is 0. The maximum at $\sim 853\,\mu s$ is roughly half the time of the movement sequence and agrees with the calculated result using Equation D.9.

D.5.5 Phase Information $\phi(\tau)$

In fig. 3(c) of the main text, we quantify the preservation of spin coherence by fixing $\tau = 900\,ns$ and varying the rotation axis angle of the final $\pi/2$ pulse. We also show in

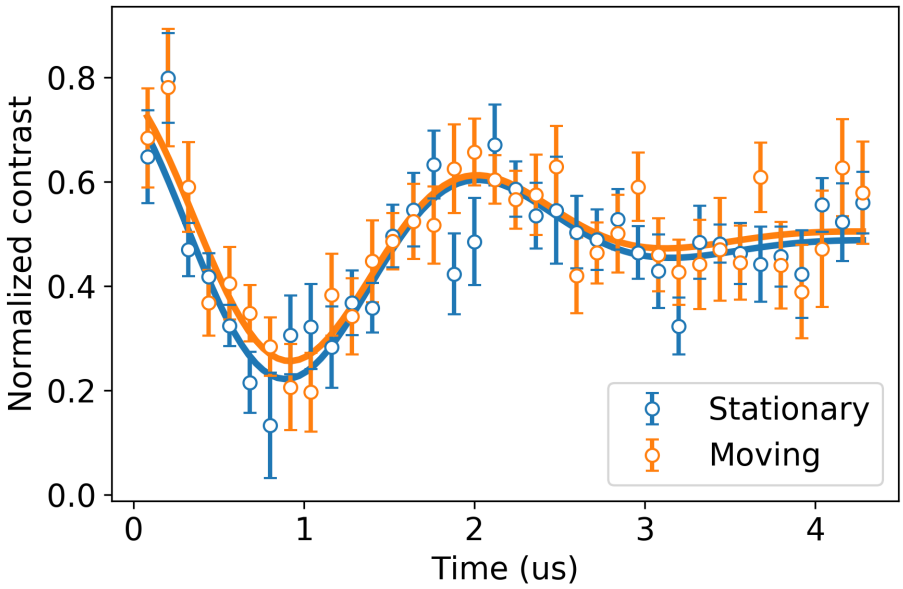


Figure D.10: Phase information stored inside the nuclear spin. The fringe contrast is not degraded by movement inside the magnetic field gradient.

Fig. D.10 a measurement where we keep the rotation axis angle of the final $\pi/2$ pulse same as all the other nuclear pulses, and vary τ instead. As expected, we observe Ramsey fringes due to the C_nNOT_e gate having an equal detuning from the two ^{13}C transitions.

D.6 NV center Electronic and Nuclear Spin Coherence Times

In Fig. D.11, we show measurements of the electron spin coherence time ($T_{2,e}$), lifetime ($T_{1,e}$), and the ^{15}N nuclear spin coherence time ($T_{2,n}$). These measurements are performed in air at room temperature in the presence of an external bias magnetic field of $\sim 180\,G$. With an XY8-4 sequence, $T_{2,e}$ exceeds $0.95(4)$ ms (middle). We expect that NV centers implanted with more energy than the 6 keV used in this diamond nanopillar would have improved coherence times. Furthermore, we measure the nuclear spin coherence time $T_{2,n} \sim 5\,ms$ (right), similar to $T_{1,e}$, suggesting that it is limited by the electron spin lifetime.

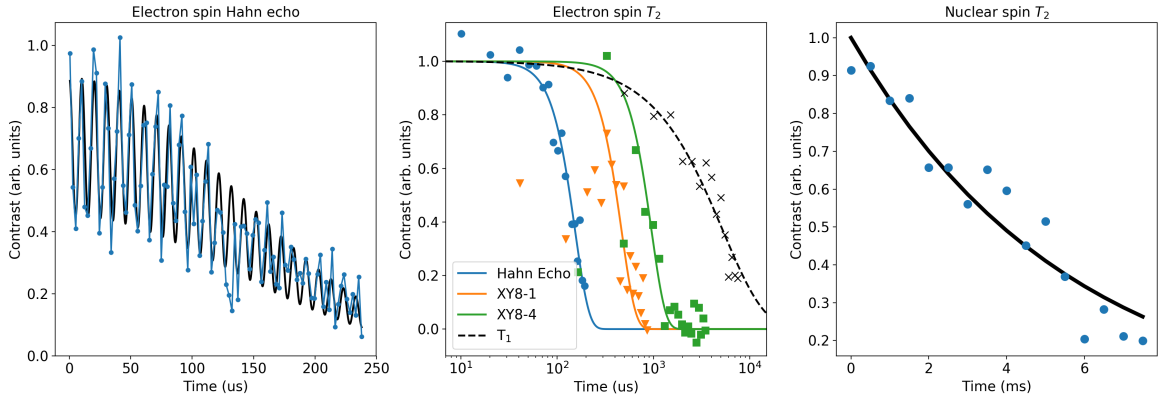


Figure D.11: Left: coherence of a single NV in the nanopillar, measured using a Hahn echo sequence, showing collapse and revivals of the 13C bath due to an external bias magnetic field. Middle: coherence times measured using different dynamic decoupling sequences. The electron spin T_1 is also plotted (black) for comparison. Right: coherence of the nuclear spin, measured using a Hahn echo sequence.

Work	$\omega/(2\pi)$ (Hz)	$g/(2\pi)$ (Hz)	T (K)	$n\kappa/(2\pi)$ (Hz)	T_2 (s)	C
This work	1.4×10^6	7.7	20	5×10^5	8.8×10^{-4}	1.0×10^{-7}
Gieseler *et al.* [57]	1.4×10^2	4.8×10^{-2}	4	8×10^4	1.0×10^{-2}	2.8×10^{-10}
Arcizet *et al.* [11]	1.0×10^6	1.4×10^2	300	4×10^{10}	4.0×10^{-4}	1.8×10^{-10}
Oeckinghaus *et al.* [102]	8.6×10^5	7.7	5	2×10^5	1.2×10^{-6}	2.8×10^{-10}

Table D.1: Comparison of spin-mechanical cooperativities with previous works. Optimistic estimates (highlighted) are given for unreported values. We also note the large coupling strength (> 700 Hz) reported in a related work where a cantilever is coupled to unpaired electron spins [127]; however, the spin coherence time and quality factor were not reported.

D.7 Comparisons of Cooperativity for Previous Works

In Table D.1 we compare the spin-mechanical cooperativity of our current system with those of previous works involving NV centers. We note that some of the previous works do not explicitly report parameters necessary to calculate the cooperativity; we give optimistic estimates (highlighted) where appropriate.